In vitro Studies of Improvement in Treatment Efficiency of Photodynamic Therapy of Cancers through Near-Infrared/Bioluminescent Activation

by

Ting Luo

A thesis

presented to the University of Waterloo

in fulfillment of the

thesis requirement for the degree of

Doctor of Philosophy

in

Physics

Waterloo, Ontario, Canada, 2014

AUTHOR'S DECLARATION

I hereby declare that I am the sole author of this thesis. This is a true copy of the thesis, including any required final revisions, as accepted by my examiners.

I understand that my thesis may be made electronically available to the public.

ABSTRACT

Cancer is a leading cause of death that affects millions of people across the globe each year. Photodynamic therapy (PDT) is a relatively new treatment approach for cancer in which anticancer drugs are activated by light at an appropriate wavelength to generate highly cytotoxic reactive oxygen species (ROS) and achieve tumor destruction. Compared with conventional chemo- and radiotherapy, PDT can be performed with minimal invasiveness, local targeting and reduced side effects. However, most of the currently available PDT drugs mainly absorb in the visible part of the spectrum, where light penetration depth into human tissues is very limited. Therefore, increasing the treatment depth of PDT has been considered to be an important approach to improve the effectiveness of PDT for treating larger and thicker tumor masses. In this thesis, we present our investigation into the potential of two-photon activated PDT (2-γ PDT), combination therapy of PDT and chemotherapy, and bioluminescence-activated PDT as a means to increase the treatment depth of this modality.

In 2-γ PDT, the photosensitizing agents are activated through simultaneous absorption of two photons. This approach allows the use of near-infrared (NIR) light that can penetrate deeper into tissues and thus, has the potential of treating deep-seated tumors and reducing side effects, while the non-linear nature of two-photon excitation (TPE) may improve tumor targeting. We have evaluated the PDT efficacy of a second-generation photosensitizer derived from chlorophyll *a*, pyropheophorbide a methyl ester (MPPa), through both one- and two-photon activation. We observed that MPPa had high one-photon (1-γ) PDT efficacy against both cisplatin-sensitive human cervical (HeLa) and cisplatin-resistant human lung

(A549) and ovarian (NIH:OVCAR-3) cancer cells when activated by femtosecond (fs) laser pulses at 674 nm. At a low light dose of 0.06 J cm^{-2}, the MPPa concentration required to produce a 50% cell killing effect (IC_{50}) was determined to be 5.3 ± 0.3, 3.4 ± 0.3 and 3.6 ± 0.4 μM in HeLa, A549 and NIH:OVCAR-3 cells, respectively. More significantly, we also found that MPPa could be effectively activated at the optimal tissue-penetrating wavelength of 800 nm through TPE. At a light dose of 886 J cm^{-2}, where no measurable photodamage was observed in the absence of MPPa, the IC_{50} values were measured to be 4.1 ± 0.3, 9.6 ± 1.0 and 1.6 ± 0.3 μM in HeLa, A549 and NIH:OVCAR-3 cells, respectively. We obtained corresponding LD_{50} (the light dose required to produce a 50% killing effect) values of 576 ± 13, 478 ± 18 and 360 ± 16 J cm^{-2} for 10 μM MPPa, which were approximately 3-5 times lower than the published 2-γ LD_{50} of Visudyne® and 20-30 times lower than that of Photofrin®. These results indicate that MPPa may serve as a photosensitizer for both 1- and 2-γ activated PDT treatment of difficult-to-treat tumors by conventional therapies.

Indocyanine green (ICG), a dye having an absorption maximum near 800 nm, has been considered to be a potential NIR PDT agent. However, the PDT efficacy of ICG has been found to be very limited probably due to the low yield of cytotoxic ROS. In the present work, we have evaluated the combination effects of ICG-mediated PDT with conventional chemotherapy mediated by two types of chemotherapeutic drugs, namely the type II topoisomerase (TOPII) poisons etoposide (VP-16)/teniposide (VM-26) and the platinum-based drugs cisplatin (CDDP)/oxaliplatin (OXP). Synergistic enhancement of cytotoxicity and increased yields of DNA double strand breaks (DSBs) were observed in HeLa, A549 and

NIH:OVCAR-3 cancer cells treated with the combination of ICG-PDT and VP-16. The presence of VP-16 during the laser irradiation process was found to be critical for producing a synergistic effect. An electron-transfer-based mechanism, in which ICG could increase the yield of highly cytotoxic VP-16 metabolites, was proposed for the observed synergistic effects, although direct spectroscopic detection of the reaction products was found to be very challenging. Moreover, we observed a much lower degree of synergy in the human normal fibroblast GM05757 cells than that in the three cancer cell lines investigated. Synergistic effects were also observed in A549 cells treated with the combination of ICG-PDT and VM-26 (i.e. an analog of VP-16). Furthermore, the combination of low-dose CDDP/OXP and ICG-PDT was demonstrated to produce an additive or synergistic effect in selected cancer cell lines. These preliminary results suggest that the combination of ICG-PDT with VP-16/VM-26 or CDDP/OXP chemotherapy may offer the advantages of enhancing the therapeutic effectiveness of ICG-PDT and lowering the side effects associated with the chemotherapeutic drugs.

Bioluminescence, the generation of light in living organisms through chemical reactions, has been explored as an internal light source for PDT in recent years. This approach, in principle, does not suffer from the limited tissue penetration depth of light. In the present project, we have evaluated the effectiveness of luminol bioluminescence in activating the porphyrin photosensitizers meso-tetra(4-sulfonatophenyl)porphine dihydrochloride ($TPPS_4$) and Fe(III) meso-tetra(4-sulfonatophenyl)porphine chloride (FeTPPS). The combination treatment induced significant killing of HeLa cells, while additive effects were observed in two normal human fibroblast cell lines (GM05757 and

MRC-5). Our observations indicate that bioluminescence of luminol may generate sufficient light for intracellular activation of PDT sensitizers. Furthermore, the combination treatment may have intrinsic selectivity towards cancerous tissues.

In summary, we have demonstrated effective killing of cancer cells by MPPa-mediated 1- and 2-γ PDT, combination of ICG-PDT and VP-16/VM-26 or CDDP/OXP chemotherapy, and bioluminescence of luminol activated PDT mediated by $TPPS_4$/FeTPPS. These positive preliminary results indicate that all these three approaches have the potential of increasing the treatment depth of PDT and facilitating the development of more effective PDT treatment strategies.

ACKNOWLEDGEMENTS

First and foremost, I would like to express my sincere appreciation and gratitude to my supervisor Professor Qing-Bin Lu for his invaluable guidance and constant support during the course of my study at the University of Waterloo. I am also very grateful for the countless opportunities he has provided me on this journey of personal and academic growth. I am thankful to Professor Brain Wilson, who has given me many helpful research suggestions. I also like to thank Professors Dayan Ban, Qiyin Fang, Bae-Yeun Ha, Kesen Ma and Hart Peemoeller, for serving as my committee members. Their valuable comments and suggestions are very important for improving the quality of this thesis. I thank Professor Juewen Liu for allowing me to use their laboratory equipment. Thanks to Ms. Judy McDonnell for her help and support over the past few years.

Sincere thanks to all my colleagues in Professor Qing-Bin Lu's laboratory for their kind assistance and generous sharing of their own experience with me.

I would like to thank all my friends at Waterloo for their friendship during various stages of my stay here.

Financial support through the Ontario Graduate Scholarship, Ontario Graduate Scholarship in Science and Technology, Queen Elizabeth II. Graduate Scholarship in Science and Technology, President's Graduate Scholarship from the University of Waterloo, and other forms of support provided by the department, faculty and university are gratefully acknowledged.

DEDICATION

To my parents, husband and sons.

TABLE OF CONTENTS

LIST OF FIGURES

LIST OF TABLES

LIST OF ABBREVIATIONS

5FdUr	5-fluoro-2'-deoxyuridine
ABC	ATP-binding cassette
ABCB1	ATP-binding cassette sub-family B member 1
ABCC2	ATP-binding cassette sub-family C member 2
ALA	delta-aminolevulinic acid or 5-aminolaevulinic acid
$AlPcS_4$	aluminium tetrasulfonated phthalocyanine
$AlPcS_2$	aluminium disulfonated phthalocyanine
AMD	age-related macular degeneration
ATCC	American Type Culture Collection
BBO	barium borate
BCC	basal cell carcinoma
BPD-MA	benzoporphyrin derivative monoacid ring A
BRET	bioluminescence resonant energy transfer
CDDP	cisplatin
Ce6-PVP	chlorin e6-polyvinypyrrolidone
CW	continuous-wave
DET	dissociative electron-transfer
DHI	5,6-dihydroxyindole
DHICA	5,6-dihydroxyindole-2-carboxylic acid
DMSO	dimethyl sulfoxide
Dox	doxorubicin
DSB	double strand break

EGF	epidermal growth factor
MEM	minimum essential medium Eagle
ER	endoplasmic reticulum
ESR	electron spin resonance
eV	electron volt
F12K	nutrient mixture F12 Ham Kaighn's modification
FBS	fetal bovine serum
FDA	Food and Drug Administration
FeTPPS	Fe(III) meso-tetra(4-sulfonatophenyl)porphine chloride
fLuc	firefly luciferase
FRET	fluorescence resonance energy transfer
fs	femtosecond
fs-TRLS	femtosecond time-resolved laser spectroscopy
FWHM	full width at half maximum
GM	Goeppert-Mayer unit
GSH	glutathione
Hb	deoxyhaemoglobin
HbO_2	oxyhaemoglobin
H_2O_2	hydrogen peroxide
Hp	haematoporphyrin
HpD	haematoporphyrin derivative
HPPH	2-(1-hexyloxyethyl)-2-devinyl pyropheophorbide-a
IC_{50}	the drug dose required to produce a 50% cell killing effect

IC	internal conversion
ICG	indocyanine green
ISC	intersystem crossing
Labview	Laboratory Virtual Instrument Engineering Workbench
LD_{50}	the light dose required to produce a 50% cell killing effect
LED	light-emitting diode
MACE	mono-(L)-aspartylchlorin-e6
MAL	methyl aminolaevulinate
MDR1	multidrug resistance protein 1
mM	millimolar
μM	micromolar
MPO	myeloperoxidase
MPPa/PPME	pyropheophorbide-a methyl ester
MRP	multi-drug resistance protein
MRP2	multi-drug resistance protein 2
mTHPC	5,10,15,20-tetra(m-hydroxyphenyl)chlorin
MTT	3-(4,5-dimethylthiazol-2-yl)-2,5-diphenyltetrazolium bromide
NIR	near infrared
NSCLC	non-small-cell lung carcinoma
$^1O_2$	singlet oxygen
$O_2^{-\cdot}$	superoxide anion radical
$OH^{\cdot}$	hydroxyl radical
OPA	optical parametric amplifier

OPD	optical path difference
OPE	one-photon excitation
OXP	oxaliplatin
PBS	phosphate-buffered saline
PCD	programmed cell death
PD_{50}	the light-drug product required to produce a 50% cell killing effect
PDT	photodynamic therapy
PF	paraformaldehyde
PMT	photomultiplier tube
PS	penicillin-streptomycin antibiotics
PTT	photothermal therapy
ROS	reactive oxygen specie
SCLC	small-cell lung carcinoma
S.D.	standard deviation
SDS	sodium dodecyl sulfate
S.E.M	standard error of mean
SFG	sum frequency generation
SiPc	silicon(IV) phthalocyanine
SnEt2	tin ethyl etiopurpurin
SOSG	singlet oxygen sensor green
SOSG-EP	singlet oxygen sensor green endoperoxide
SSB	single-strand break

Tf	transferrin
TMPD	N,N,N′,N′-tetramethyl-p-phenylenediamine
TOODKAD or WST09	palladium bacteriochlorophyll derivative
TOPII	type II topoisomerase
TPE	two-photon excitation
$TPPS_4$	meso-tetra(4-sulfonatophenyl)porphine dihydrochloride
VCR	vincristine
VM-26	teniposide
VP-16	etoposide
VR	vibrational relaxation
VTP	vascular targeted photodynamic therapy
$ZnPcS_4$	Zn(II) phthalocyanine tetrasulfonic acid

1 Introduction

Cancer is not a single disease but a group of diseases characterized by unregulated growth and spread of cells. It affects millions of people around the world each year and is the second cause of death from diseases after heart disease. In Canada, an estimated 186,400 new cases and 75,700 cancer deaths occurred in 2012 (1). According to the American Cancer Society, there were over 1.66 million new cancer cases and nearly 0.6 million cancer deaths in the United States in 2013 (2).

1.1 Cancer staging

Cancer cells, also known as malignant cells, differ from their normal counterparts in a number of ways, including morphology, growth control, cell-to-cell interactions, cell-surface markers, and protein or gene expression. Cancer staging is the determination of the extent to which a cancer has developed by spreading and plays an important role in treatment planning. There are five main stages:

- **Stage 0**: carcinoma in situ. Abnormal cells are found only within the layer of cells where they began.
- **Stage I**: cancers are localized to the organ in which they developed.

- **Stage II**: cancers are locally advanced. Cancer cells can also be found in nearby lymph nodes, organs, or tissues.
- **Stage III**: cancers are also locally advanced. The specific criteria for Stages II and III are cancer type-dependent.
- **Stage IV**: metastasis. Cancers are found in organs or lymph nodes distant from the primary site.

1.2 Lung cancer

Despite great improvements in diagnosis and treatment modalities, lung cancer remains the deadliest among all the cancers. It was the second most common cancer (14%) and also the leading cause of cancer death in both men (27%) and women (26%) in Canada in 2012 (1). In the United States, it was estimated that there were 228,190 newly diagnosed cases and 159,480 deaths associated with lung and bronchus cancer in 2013, which accounted for about 14% and 27% of the total numbers (2).

The two main types of lung cancer are the small-cell lung carcinoma (SCLC) and non-small-cell lung carcinoma (NSCLC), which can be distinguished based on the appearance of the cells under a microscope. The overall 5-year survival rates for SCLC and NSCLC have been reported to be 6.1% and 17.1%, respectively (3). Radiation therapy alone or in combination with chemotherapy is the standard treatment for SCLC. Surgery is usually performed in patients with early stage NSCLC. For patients with advanced stage NSCLC, the treatment options are either chemotherapy/radiation therapy alone or in combination. In the case of advanced stages diseases, patients may receive the combination of chemotherapy and

targeted therapy. For example, an agent designed to target specific molecular pathways in lung cancer cells (bevacizumab (Avastin®)) has been approved in the United States (3). Some cases of early-stage lung cancer may also be treated with photodynamic therapy (PDT) to help relieve symptoms of a blocked airway.

1.3 Ovarian and cervical cancers

Ovarian and cervical cancers are also commonly diagnosed in women. Ovarian cancer causes more deaths than any other gynecological cancers (cancers of the female reproductive system). According to the Canadian Cancer Society, over 2,600 new cases were diagnosed and about 1,750 deaths occurred in 2012 in Canada (1). In the United States, approximately 22,240 (3%) new cases and 14,030 (5%) deaths occurred in 2013 (2). Currently, surgery, chemotherapy and radiation therapy are the three main treatment options for ovarian cancer patients. The extent of treatment depends on a number of factors, including cancer type, the stage of the disease, the patient's overall health status, and personal considerations.

The number of estimated new cases and deaths from cervical cancer were 1,350 and 390 in 2012 in Canada (1), while this disease was expected to account for 1.5% (12,340) of the new cases and 1.5% (4,030) of the deaths associated with cancer in women in 2013 in the United States (2). In patients with early stage cervical cancers, treatment options include electrocoagulation (tissue destruction by high-frequency electric current), cryotherapy (killing of abnormal cells by extremely low temperature), laser ablation, or local surgery. Surgery, chemotherapy, or radiotherapy may be applied in more advanced stages.

1.4 Conventional cancer therapies

1.4.1 Surgery

Surgery is a medical procedure in which the diseased tissue or organ is removed from the body. It may be performed for diagnosis purposes such as to determine the type, stage and extent of spread of tumors. As a treatment approach, surgery remains one of the main options for cancer, especially solid tumors. When the disease is completely contained in one area, the cancer may be cured by physical removal of the cancerous tissue. However, complete excision is impossible if the cancer cells have spread to other remote sites prior to surgery. Moreover, even a single cancer cell can regrow into a new tumor. Therefore, complete cure of the cancer often requires the combination of two or more therapies. The combination of surgery with chemotherapy or radiotherapy can greatly improve the treatment outcomes.

Side effects of cancer surgery may include anesthesia complications, infections, inflammation, loss of function, scarring, etc. Development of secondary cancers (metastasis), which is usually difficult to treat, has also been found in some cases following the removal of the primary tumor (4, 5).

1.4.2 Chemotherapy

Chemotherapy is a type of cancer treatment where one or more medicines are given either orally or intravenously to kill the cancer cells. It is one of the most important treatment

modalities currently available for cancer. Many chemotherapeutic drugs have been approved by the United States (U.S.) Food and Drug Administration (FDA). For example, 10 new drugs were approved in fiscal year 2012 for the treatment of cancer (6). Based on their chemical structures and action mechanisms, chemotherapeutic drugs may be classified into the following groups: alkylating agents, topoisomerase inhibitors, antimetabolites, mitotic inhibitors, antitumor antibiotics, corticosteroids, and some other drugs that do not fit well into any of the these categories.

1.4.2.1 Platinum-based chemotherapeutic drugs

Cisplatin (CDDP) is the first platinum-based chemotherapeutic drug that acts by causing direct and indirect damages to cellular DNA and sometimes is grouped with alkylating agents because their mechanisms of action are similar. CDDP is widely used for the treatment of a variety of cancers, including bladder, blood vessel, bone, brain, cervical, lymphoma, lung and ovarian cancers (7-9). It has been estimated that approximately 50-70% of the cancer patients have received CDDP treatment (10). Over the past decades, great efforts have been made in developing more effective platinum-based anticancer compounds. Thousands of CDDP analogues have been prepared and tested, but only two of them (carboplatin and oxaliplatin (OXP)) have been approved by FDA for clinical use.

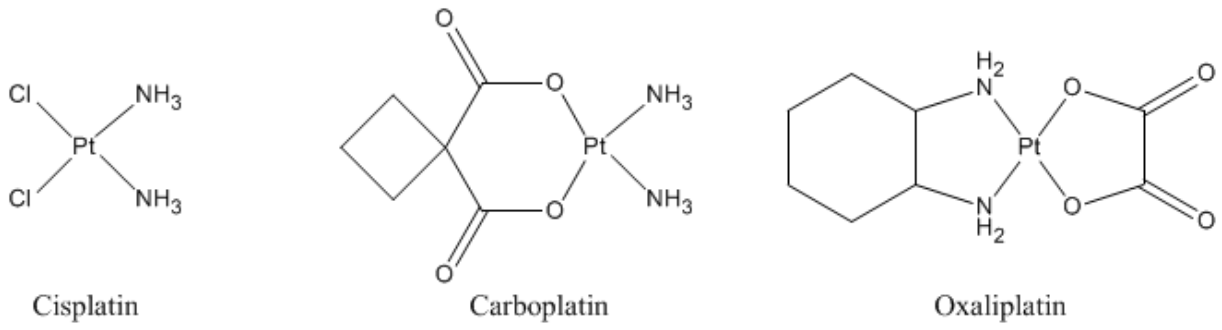

Figure 1-1: Chemical structures of cisplatin (CDDP), carboplatin and oxaliplatin (OXP).

1.4.2.2 Type II topoisomerase inhibitors

Type II topoisomerases (TOPII) are enzymes that cut both strands of one DNA double helix during replication and transcription in order to facilitate DNA untangling. A number of TOPII poisons have been developed as effective anticancer drugs and can be classified into two groups according to their mechanisms of action (11-14). The drugs etoposide (VP-16) and teniposide (VM-26) (Figure 1-2) belong to the class of interfacial poisons that interact non-covalently at the protein-DNA interface. Etoposide was first approved by FDA in 1983. It is currently used for treating acute myeloid leukemia, choriocarcinoma, small and non-small cell lung carcinoma, lymphoma, advanced ovarian carcinoma, and testicular cancers (15, 16). Teniposide was approved later in 1992 for the treatment of bladder cancer, malignant lymphoma, and central nervous system tumors. Covalent poisons can form adducts with the sulfhydryl groups on cysteine residues of TOPII. Quinones have been found to belong to this class (11, 12). The catechol and quinone metabolites of VP-16 also belong to this class and have been found to be a few times more active than the parent compound VP-16 in inducing TOPII-mediated DNA double strand breaks (DSBs) (13, 14).

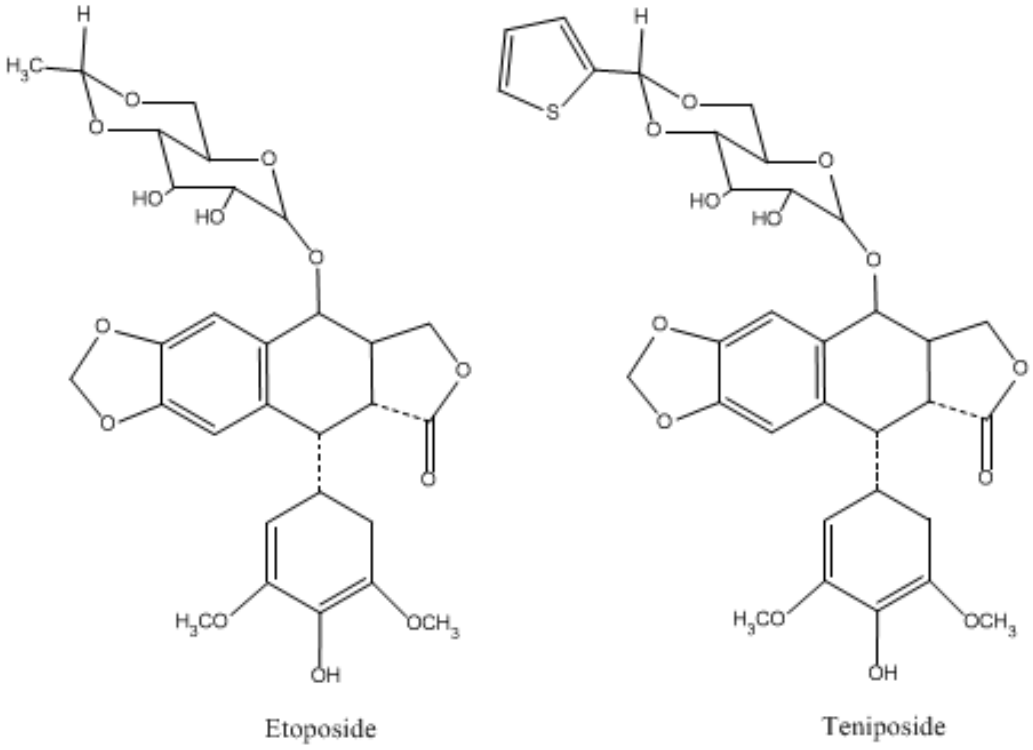

Figure 1-2: Chemical structures of etoposide (VP-16) and teniposide (VM-26).

Despite the great success of chemotherapeutic drugs, especially CDDP, in treating cancers, they destroys not only cancer cells, but also many rapidly dividing normal cells resulting in severe side effects such as nausea, vomiting, hair loss, etc. Generally speaking, chemotherapeutic drugs accumulate not only in cancer cells but also in proliferating normal cells by inhibiting DNA synthesis or interfering with cellular processes, including cell division and metabolism. As a consequence, chemotherapeutic treatments often cause damages to healthy tissues, especially bone marrow, skin, and gastro-intestinal mucosa. In addition, cancer cells readily acquire resistance to chemotherapeutic agents. The poor specificity of chemotherapeutic agents commonly prevents aggressive and effective treatment of the cancer.

1.4.3 Radiotherapy

Radiotherapy is another common cancer therapy in which ionizing radiation, such as hard X-rays, γ-rays, electron beams, or protons, is used to kill or control the growth of cancer cells. It has been estimated that ~50-60% of all cancer patients will be treated with radiotherapy either alone or together with other cancer therapies such as surgery and chemotherapy during the course of illness (17, 18). The energy of the ionizing radiation can be deposited directly into the target molecules causing excitation or direct ionization of important biological molecules such as nuclear DNA and thus, induce cell death. Ionizing radiation can also induce cell death by causing indirect damages to DNA of exposed tissue by generating free radicals, including prehydrated electrons (e_{pre}^-), hydrated electrons (e_{hyd}^-), and hydroxyl radicals ($^{\cdot}OH$), from radiolysis of water (19). It has been found that more damages are produced in the indirect pathway than the direct pathway (20).

During the process of radiation treatment, surrounding normal tissues may also be damaged due to the fact that most types of radiation lack specificity against cancer cells. Although low-dose radiation therapy causes minimal or no side effects, a number of acute side effects, such as vomiting and swelling, long-term side effects, such as secondary cancer and heart diseases, or cumulative side effects, may be caused at high doses. Therefore, radiosensitizers that can make the cancer cells more sensitive to radiation therapy are studied extensively in preclinical and clinical studies (18, 21). On the other hand, various radiation protectors are also being developed to protect normal cells from damages caused by radiation therapy (18). Although further study of these compounds in clinical trials is required, the use

of radiosensitizers and radioprotectors is believed to be crucial to improving the clinical outcomes of radiation treatment of cancer.

1.5 Photodynamic therapy

Photodynamic therapy (PDT) is a novel cancer therapy in which tumor destruction is achieved through the generation of cytotoxic reactive oxygen species (ROS) by exposing the diseased tissue to a photosensitizer and light of an appropriate wavelength. Over 100 years ago, a German student named Oscar Rabb reported the first case of cell death induced by the interaction of light and a chemical compound (22). Three years later, the first medical application of PDT was reported by von Tappeiner and Jesionkek, who used the combination of eosin and white light to treat basal cell carcinomas (BCCs) (23). However, therapeutic applications of PDT were not widely explored until 1972, when Diamond *et al.* proposed that the tumor-specificity and phototoxicity of porphyrins might be combined for the treatment of cancers (24). Later in 1975, Dougherty and coworkers successfully treated tumors in experimental animals by haematoporphyrin-mediated PDT for the first time (25). In the same year, Kelly *et al.* reported that haematoporphyrin derivative (HpD) and light could induce marked destruction of human bladder tumor transplanted into mice (26). Three years later, Dougherty *et al.* demonstrated the first case of successful treatment of more than one hundred patients by PDT (27). Since then, a large number of studies have shown the clinical effectiveness of PDT in treating various cancers and some other diseases (28-38).

1.5.1 Mechanism of photodynamic therapy

Figure 1-3 is a Jablonski diagram illustrating the major processes that may occur when a molecule absorbs a photon of appropriate energy. Upon excitation, the molecule may be promoted from its ground electronic state (usually a singlet state, S_0) to an excited singlet state S_n (n = 1, 2 …). According to the Frank-Condon principle, no significant displacement of nuclei will occur during the process of an electronic transition, which takes place on a much shorter timescale (on the order of 10^{-15} s) than that of nuclear rearrangement (on the order of 10^{-14} to 10^{-13} s) (39). If an excited singlet state higher than S_1 is reached, the molecule will undergo a fast (~ 10^{-14} – 10^{-11} s) internal conversion (IC) process to an excited vibrational state S_1 (S_1^v). The molecules in the S_1^v state may lose their excess energy through vibrational relaxation (VR), which takes place between 10^{-14} and 10^{-11} seconds. From the lowest, zero-point vibration level of S_1 state (S_1^0), the molecule may go back to its ground state via either radiation emission (fluorescence; on the order of 10^{-9} to 10^{-7} s) or IC. A crossing from S_1^0 to the excited triplet state (T_1^v) can also take place through another radiationless process, called intersystem crossing (ISC; on the order of 10^{-8} to 10^{-3} s). From T_1^0, the molecule may lose its excess energy by emitting light through a process known as phosphorescence, a slow (~ 10^{-8} – 10^{-3} s) and spin-forbidden transition, or react with other molecules such as molecular oxygen (O_2) and the solvent.

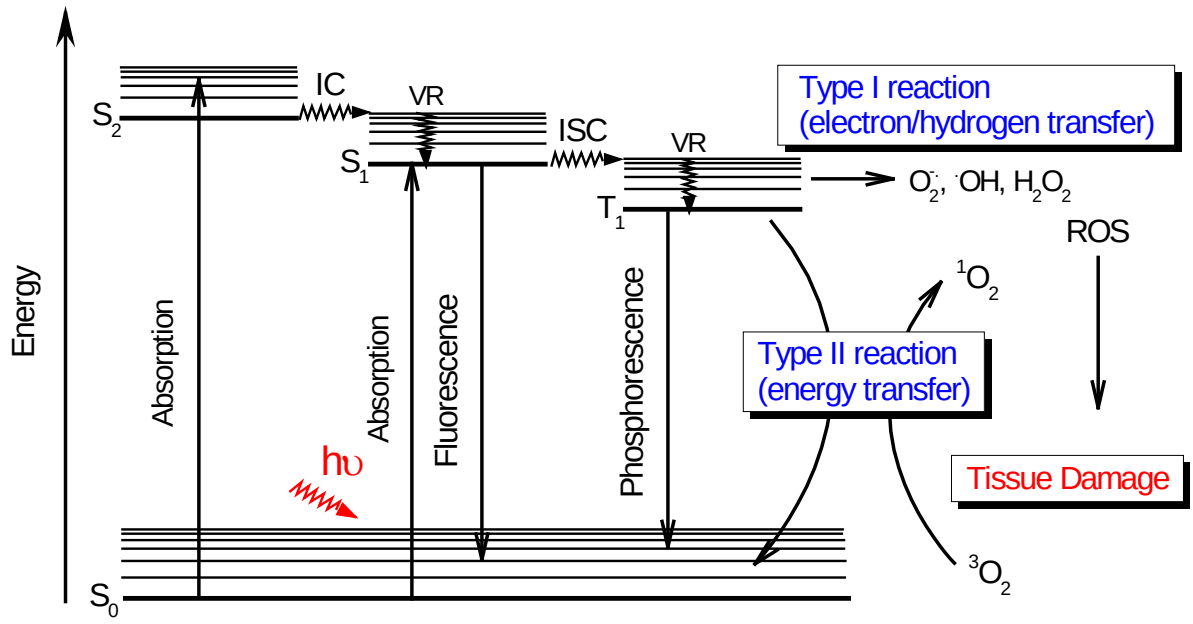

Figure 1-3: Jablonski diagram illustrating the photosensitization processes. Upon absorbing one photon of appropriate energy, a photosensitizer is promoted from its ground state (S_0) to the first excited singlet state (S_1). From S_1 state, the molecule may undergo intersystem crossing (ISC) to an excited triplet state (T_1), which can transfer its energy to an oxygen molecule ($^3O_2$) through an energy transfer reaction to form singlet oxygen ($^1O_2$) or form other free radicals through electron/hydrogen transfer reactions. The generated $^1O_2$, $O_2^{\cdot-}$, $^{\cdot}OH$ and H_2O_2 are called reactive oxygen species (ROS), which are cytotoxic. (IC: internal conversion; VR: vibrational relaxation; ISC: intersystem crossing.)

The ground state of O_2 is a triplet state ($^3\Sigma_g^-$) while the lowest excited state is a singlet state ($^1\Delta_g$), which is located at 0.98 eV above the ground state (40). It has been found that both the excited singlet and triplet states of a photosensitizer can be quenched through reactions with molecular oxygen as shown in Scheme 1 (40-48).

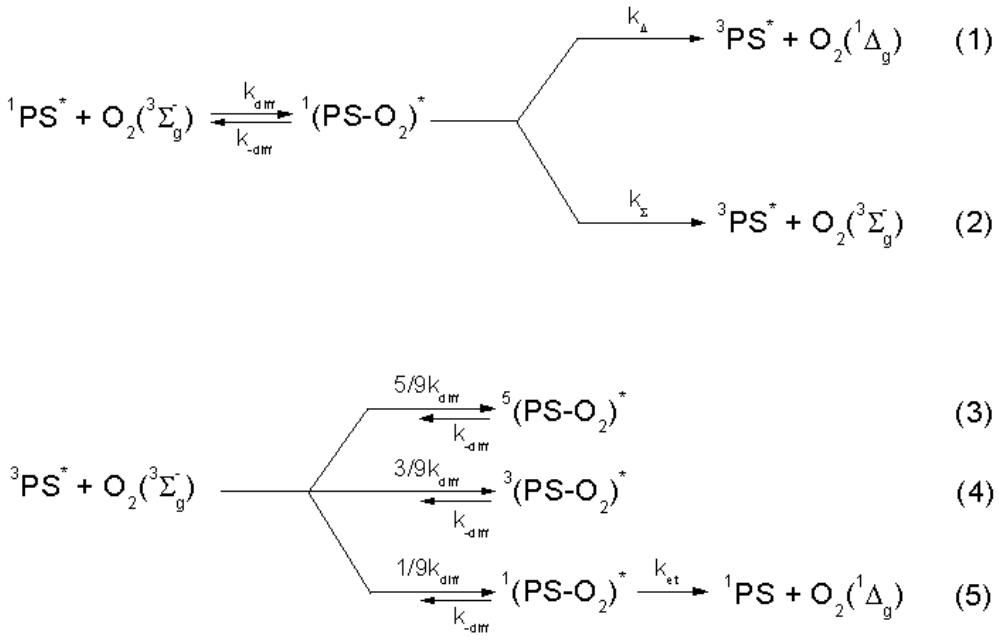

Scheme 1

where $(PS\text{-}O_2)^*$ represents an encounter complex, k_{diff} is the diffusion-controlled rate constant, k_{-diff} is the rate constant for separation of the encounter pairs, k_Δ and k_{ST} are the rate constants for quenching of the excited singlet states by oxygen via reactions (1) and (2) that result in the formation of $O_2(^1\Delta_g)$ and $O_2(^3\Sigma_g^-)$, respectively, and k_{et} is the rate constant for quenching of the excited triplet states by oxygen via reaction (5), which results in the formation of $O_2(^1\Delta_g)$. The fractions of $O_2(^1\Delta_g)$ generated from quenching of the excited singlet states (f_Δ^S) and the excited triplet states (f_Δ^T) have been determined in a number of studies (41-48). The values have been demonstrated to be dependent on the type of the compound, the type of the solvent, the energy and redox potential of the excited states, etc. In

general, the efficiency of singlet oxygen generation from the excited singlet states is much lower than that from the excited triplet states of the same compound.

In PDT, a photosensitizer in its excited triplet state ($^3PS^*$) is believed to be the major state responsible for the generation of cytotoxic species that finally cause tumor cell destruction. Due to the spin-forbidden nature of the T_1-S_0 transition, the typical lifetime of a molecule in the excited triplet state is tens of microseconds (μs) (49), which allows sufficient time for the excited photosensitizer to interact with surrounding molecules to produce cytotoxic species. There are two mechanisms that have been proposed for the reaction of $^3PS^*$ with bio-molecules, known as the Type I and Type II reactions (Figure 1-3) (49-52). In a Type I process, the $^3PS^*$ reacts with the solvent or a substrate molecule through electron/hydrogen transfer to produce highly reactive free radicals, such as hydroxyl radical ($^{\cdot}OH$), superoxide anion radical (O_2^{-*}), and hydrogen peroxide (H_2O_2). In Type II reactions, the $^3PS^*$ may transfer its energy to O_2 leading to the production of singlet oxygen ($^1O_2$). Although both Type I and Type II reactions may occur during the process of photodynamic treatment, $^1O_2$ is believed to have a higher contribution to tumor destruction than the other cytotoxic species generated in PDT.

1.5.2 Cellular and tissue responses to PDT

At the cellular and tissue levels, the ROS, including $^1O_2$, $O_2^{\cdot-}$, $^{\cdot}OH$, and H_2O_2, generated in PDT can cause direct killing of tumor cells, damage the tumor vasculature, or activate an immune response against tumor growth. Both Type I and Type II processes contribute to the

production of ROS and their relative contributions depend on various factors such as oxygen tension, light dose, and the type, concentration and subcellular localization of the photosensitizer (32). Therefore, long-term tumor control will rely on the combination of all these factors (32, 53).

1.5.2.1 Direct killing of tumor cells

The photodynamic treatment may induce apoptotic, necrotic or autophagic cell death (54-67). The primary site of photodynamic damages is generally accepted to coincide with the intracellular localization of the photosensitizer since the cytotoxic $^1O_2$ generated during PDT treatment has a very short lifetime (<~μs) and hence limited diffusion length (<~100 nm) (68). For this reason, PDT is believed to have a relatively low potential of causing DNA damages, mutations or carcinogenesis because most PDT drugs do not enter the cell nuclei (56). With a relatively low level of oxidative stress, photosensitizers that localize to the mitochondria or endoplasmic reticulum (ER) may induce apoptosis (54, 56), a form of programmed cell death (PCD) characterized by cytoplasmic membrane blebbing, cell shrinkage, chromatin condensation, chromosomal DNA fragmentation, and formation of apoptotic bodies. Those photosensitizers targeting the plasma membrane or lysosomes may favor the activation of the necrotic pathway (54, 56). In contrast to apoptosis, necrosis results in an unregulated release of cellular components into the extracellular space, which usually triggers inflammatory responses in the surrounding tissue.

Light dose is another important factor in determining the death pathway following PDT treatment. While apoptotic cell death is predominant when cells are photosensitized with low light doses, necrosis has been observed at high light doses (55). Although necrosis has been considered to be a passive, uncontrolled way of cell death, some recent studies have shown that necrosis may also be propagated through a signal transduction pathway (69-71). In PDT, a necrotic cell death pathway has not been reported yet, however, some factors, such as overload of Ca^{2+}, have been suggested to be involved (57, 62).

More recently, it has been indicated that sublethal photodynamic damages may trigger autophagy, which involves isolation of damaged cellular components within autophagosomes and subsequent fusion with the cell's own lysosomes for degradation and recycling, and lead to cancer cell death (58-60, 63-65). ROS can either stimulate cytoprotection or activate autophagic cell death depending on the type of ROS generated, level of oxidative stress induced, and the molecular targets affected during PDT treatment (59-61, 63-67, 72). Although the molecular mechanisms of autophagy modulation by ROS are still under investigation, it has been suggested that autophagy can cause cell death in apoptosis defective cells (58, 65).

1.5.2.2 Vasculature damages

The tumor vasculature represents an important target for PDT *in vivo* (37, 66, 73-83). Apart from the direct tumor cell killing effects, the ROS generated in PDT can also cause blood vessel shutdown leading to nutrient deprivation and hypoxia within the target tumor. Blood

vessel dilation has been observed in mice treated with PDT mediated by HpD (73). Elevated interstitial pressure following PDT treatment has also been reported suggesting increased blood vessel permeability (74, 75). Other effects such as blood flow stasis, thrombus formation and over-expression of angiogenic factors have also been observed following PDT treatments (66, 77-79, 83). Therefore, PDT-induced vascular damages have been considered to be one of the major mechanisms of tumor destruction. The importance of vascular effects of PDT has stimulated the development of vascular targeted photodynamic therapy (VTP) as a potential approach for improving the effectiveness of PDT (66, 80, 82).

1.5.2.3 Immune responses

Distinct from the immunologically silent genotoxic damages induced by chemotherapy or radiotherapy, rapid cell death following photo-oxidative damages induced by PDT treatment can alert host's immune system (36, 53, 84-90). It has been shown that PDT can cause acute inflammatory and immune responses such as heat shock proteins expression and leukocyte infiltration within the tumor (87). In addition, Castano *et al.* observed an increased level of tumor-derived antigen to T cells following PDT treatment (88). Other immune responses, including attraction of host leukocytes, lymphocytes and macrophages into treated cancerous tissue, have also been observed, and up-regulation of the inflammatory cytokines interleukin (IL)-6 and IL-1 and activation of the neutrophil accumulation have been found to be responsible to these responses (84, 85, 91). These results indicate that the immune responses may be very helpful in long-term tumor control in addition to the direct PDT effects that can cause destruction of the bulk of the tumor. More interestingly, some recent investigations

have demonstrated that potent vaccines may be generated by treating tumor cells of the same origin by PDT *in vitro* (36, 86, 89, 90).

1.5.3 Photosensitizers

A photosensitizer is a chemical compound that can absorb photons of energy equal to the energy difference between the ground state and an excited state leading to the production of ROS and other radicals. In 1900, acridine (Figure 1-4) was first used as a photosensitizer by Oscar Raab to kill infusoria (22), minute aquatic creatures such as unicellular algae and small invertebrates. A red crystalline derivative of fluorescein, eosin (Figure 1-4), was used in combination with visible light to treat skin tumors by Herman von Tappeiner and Albert Jesionek in 1903 (23).

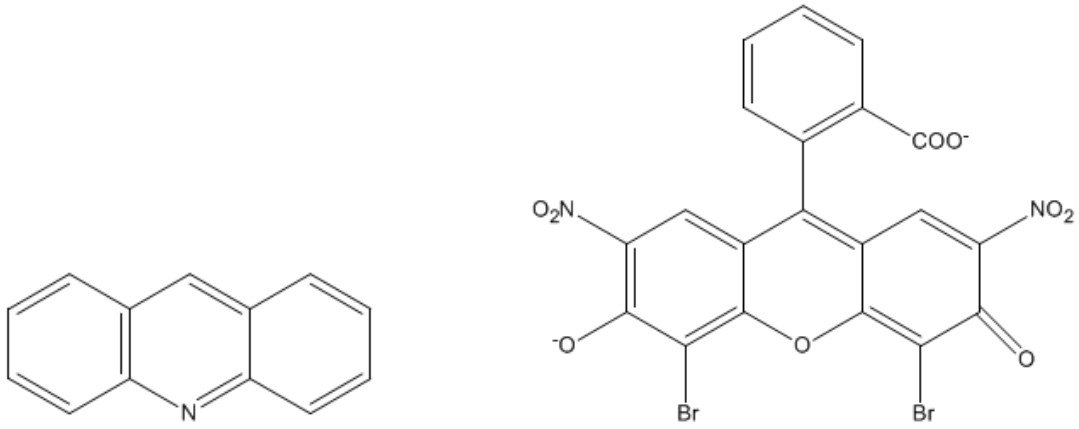

Figure 1-4: Chemical structures of acridine and eosin.

Later in 1910, W. Hausmann observed toxic effects of haematoporphyrin (Hp) (Figure 1-5) on the skin of mice after light exposure (92). Three years later, the German scientist Friedrich Meyer-Bertz tested Hp and observed pain and swelling in the treatment areas (93). In 1955 Samuel Schwartz synthesized a derivative of haem containing ferric ion-free (known as "haematoporphyrin derivative" (HpD)) (94). Although HpD was later found to be a mixture of several compounds, it was demonstrated to be able to localize in tumors and could be administrated at much lower doses than the parent compound Hp, and therefore held promise for diagnostic applications (95). In 1978, HpD-mediated PDT was successfully applied for the first time to treat skin tumors by Thomas J. Dougherty *et al.* (27). The first photosensitizer approved by FDA was a purified form of HpD known as Photofrin® (Figure 1-6), which was approved in 1995.

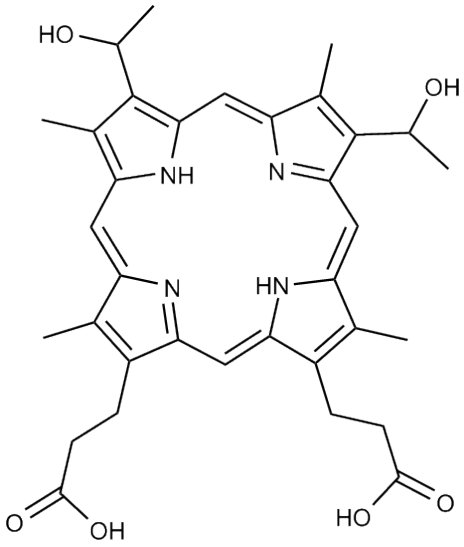

Figure 1-5: Chemical structure of haematoporphyrin (Hp).

Although Photofrin® continues to be the most widely used drug for PDT, the "first-generation photosensitizers", including Photofrin® and other commercial HpD variants Photosan®, Photogem® and Photocarcinorin®, have several disadvantages. First, they are not pure compounds but complex mixtures of monomeric and oligomeric non-metallic porphyrins. Second, the patient will have to avoid direct exposure to sunlight and bright indoor light up to several weeks after PDT treatment due to prolonged skin sensitivity. Third, they are activated by light around 630 nm, where the tissue penetration and resulting effective treatment depth are limited (96).

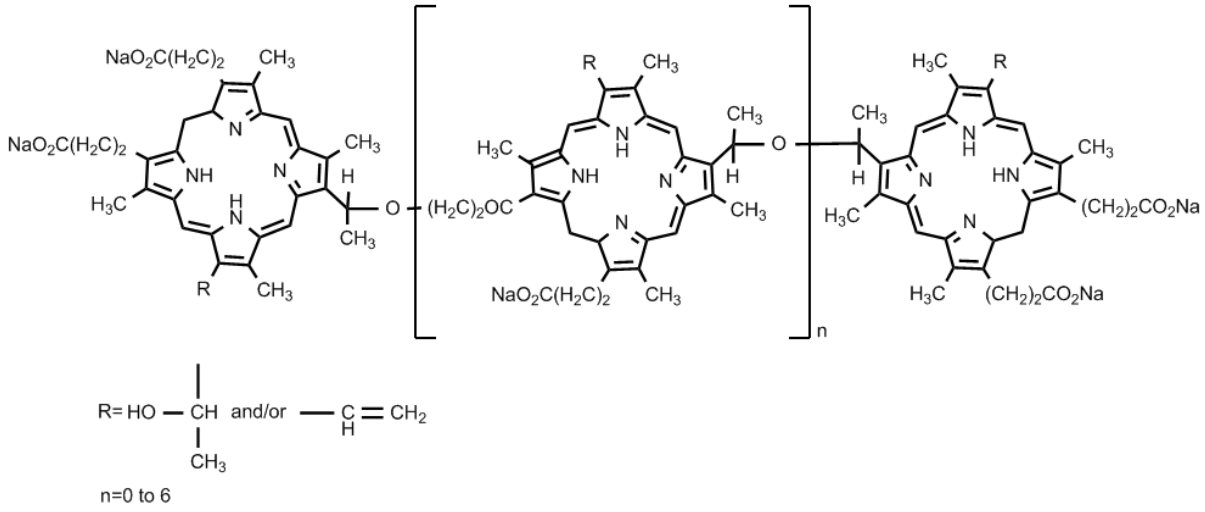

Figure 1-6: Chemical structure of Photofrin®.

To overcome these limitations of the "first-generation photosensitizers", many new compounds have been synthesized and some of them have been found to be promising (37, 97-100). Table 1-1 is a summary of photosensitizers that have been approved for use in humans. In the 1990s, several "second-generation photosensitizers", including 5-

aminolaevulinic acid (ALA; Figure 1-7) and its methyl ester (methyl aminolaevulinate, MAL; Figure 1-7), benzoporphyrin derivatives (Figure 1-8), chlorins (Figure 1-8), phthalocyanines (Figure 1-8), porphycenes (Figure 1-8) and others were developed. These synthetic dyes are more pure, efficient, selective and safe than the "first-generation photosensitizers". In addition, the skin photosensitivity of these compounds lasts for relatively short times. Among them, a few new drugs have been approved for use in PDT.

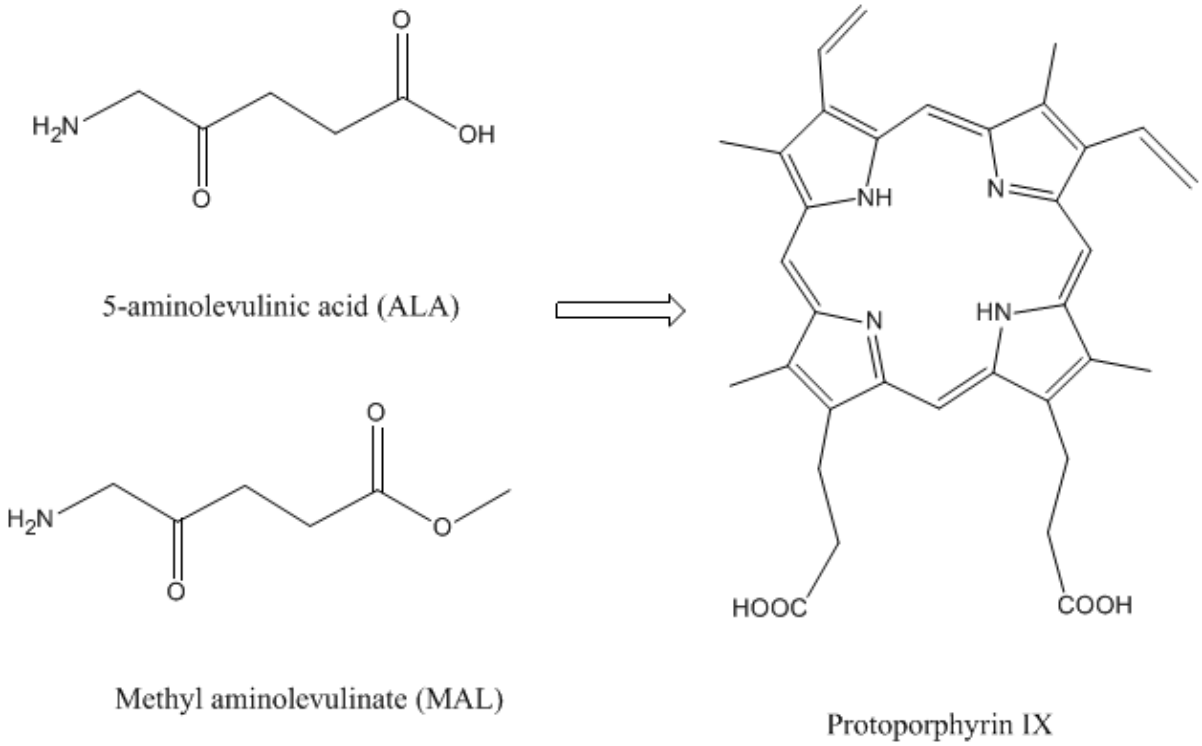

Figure 1-7: Chemical structures of 5-aminolaevulinic acid (ALA), methyl aminolevulinate (MAL) and protoporphyrin IX.

Delta-aminolevulinic acid (ALA; Levulan®), also known as 5-aminolevulinic acid, was approved in 1999 by FDA for the treatment of cancerous lesions. This is a biosynthetic "pro-drug", which needs to be converted to the active photosensitizer protoporphyrin IX (Figure

1-7). In 2004, FDA approved the methyl ester of ALA, methyl aminolevulinate (MAL; Metvix®), for the treatment of BCCs and actinic keratosis. The drug benzoporphyrin derivative monoacid ring A (BPD-MA; verteporfin), has gained approval in the liposomal formulation known as Visudyne® for treating age-related macular degeneration (AMD) in Canada, the U.S., most European Union (EU) countries and Japan. Although the approval of 5,10,15,20-tetra(m-hydroxyphenyl)chlorin (mTHPC; temoporfin; Foscan®) has been declined in the U.S., it has been approved for treating head and neck cancer in the EU, Norway and Iceland. Mono-(L)-aspartylchlorin-e6 (MACE; LS11; NPe6; talaporfin; Aptocine™) is available for lung cancer treatment in Japan.

Recently, strategies to improve the efficiency and selectivity of PDT have also been investigated extensively (101-121). Direct linking of the photosensitizers with molecules that have some affinity for tumor cells, such as antibodies (121), small peptides (122), proteins (e.g. transferrin (104, 123, 124), epidermal growth factor (EGF) (125), etc.) and many others (116), have been found to be able to either increase the uptake of the drugs by tumor cells or make the drugs become active in response to specific tumor activities. The photosensitizers can also be encapsulated within drug delivering vehicles, such as liposomes, polymeric nanoparticles and gold nanoparticles, which may be further functionalized with the above mentioned tumor-targeting molecules (102, 106, 107, 115, 126-130). These biologically or chemically modified novel drugs can be classified as belonging to the “third-generation photosensitizers”. Visudyne® is a successful example of using liposomes as the delivery vehicles for a PDT drug and has been approved for treating AMD.

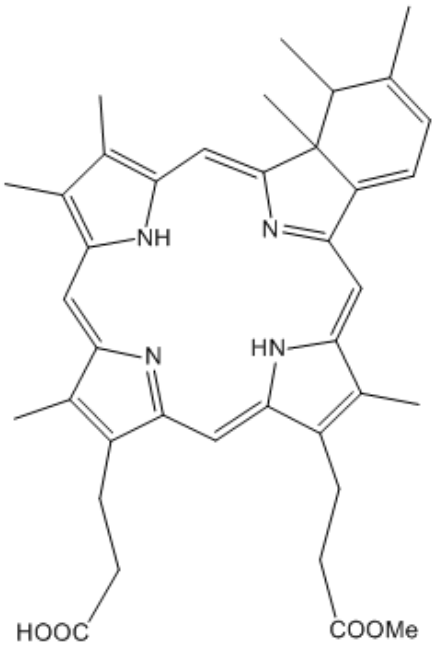

Benzoporphyrin derivative

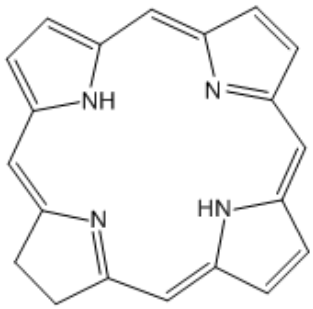

Chlorin

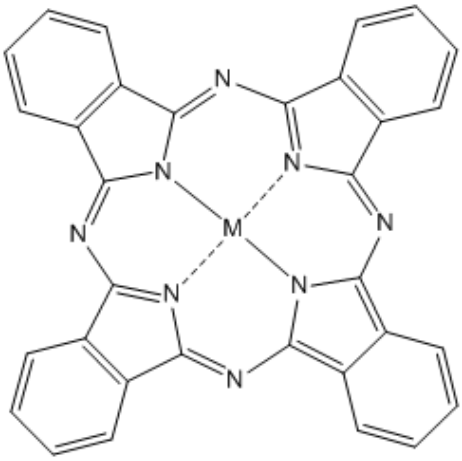

Phthalocyaines

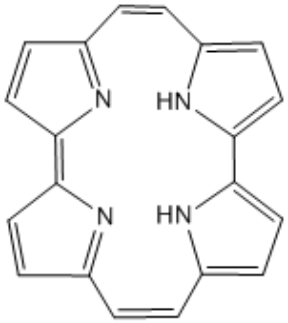

Porphycene

Figure 1-8: Chemical structures of benzoporphyrin derivative, chlorin, phthalocyanines and porphycene.

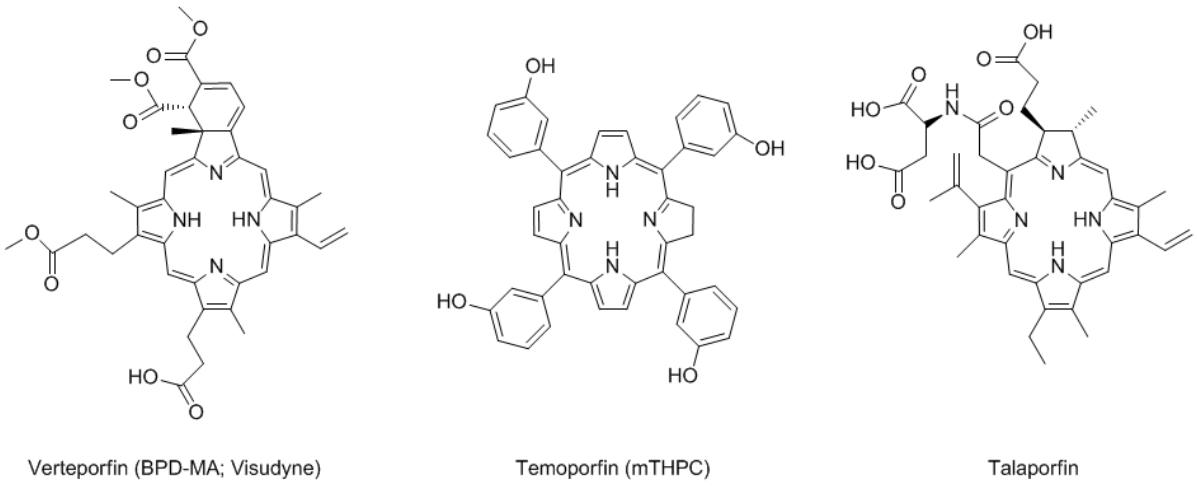

Figure 1-9: Chemical structures of verteporfin, temoporfin and talaporfin

Table 1-1: Photosensitizers approved for use in humans.

Photosensitizer	Wavelength	Description	Type of diseases	Country
Photofrin®	630 nm	Haematoporphyrin monomers/di-, oligomers	Barrett‘s dysplasia	U.S., Canada, EU, UK
			Bladder cancer	Canada
			Cervical cancer	Japan
			Endobronchial cancer	Canada, Most EU Countries, Japan, U.S.
			Esophageal cancer	Canada, Most EU Countries, Japan, U.S.
			Gastric cancer	Japan
			Early- and late-stage lung cancer	Japan (early-stage), Netherlands
			Papillary bladder cancer	Canada
			Stomach	Japan
Levulan®	635 nm	5-aminolevuinate (5-ALA), precursor of endogenous porphyrins	Actinic keratosis, Basal cell carcinoma	U.S., EU
Metvix®	635 nm	ALA methyl ester	Some types of actinic keratoses of the face and scalp	U.S.
Foscan®	652 nm	Tetra(m-hydroxyphenyl)chlorin (m-THPC), Temoporfin	Advanced head and neck squamous cell carcinoma	EU, Norway, Iceland
Visudyne ®	690 nm	Benzoporphyrin derivative monoacid ring A, Verteporfin	Age-related macular degeneration	Canada, Most EU Countries, Japan, U.S.
Aptocine™	660 nm	Mono-(L)-aspartylchlorin-e6 (MACE, LS11, NPe6), Talaporfin	Lung cancer	Japan

1.5.4 Tissue "optical window" for PDT and near-infrared photosensitizers

The tissue "optical window" for PDT, also known as the therapeutic window, defines the wavelength range 700 - 950 nm, where light absorption by biological molecules is relatively low (96). Figure 1-10 shows that the endogenous chromophores haemoglobin and melanin are highly absorbing below ~700 nm, while light absorbance by water becomes dominant at wavelengths longer than 900 nm (96, 131).

- **Haemoglobin:** There are two types of haemoglobin in blood, namely deoxyhaemoglobin (Hb) and oxyhaemoglobin (HbO_2). Hb has two absorption maxima at 420 and 580 nm, while HbO_2 has three major absorption peaks at 410, 550 and 600 nm. Above 600 nm, the molar extinction coefficient of both Hb and HbO_2 gradually decreases as light wavelength increases.
- **Melanin:** Melanin is a natural pigment found in most organisms. In humans, the two major forms of melanin are eumelanin, a polymer of 5,6-dihydroxyindole (DHI) and 5,6-dihydroxyindole-2-carboxylic acid (DHICA) having a brown-black color, and pheomelanin, which is a red-brown polymer of benzothiazine and benzothiazole.

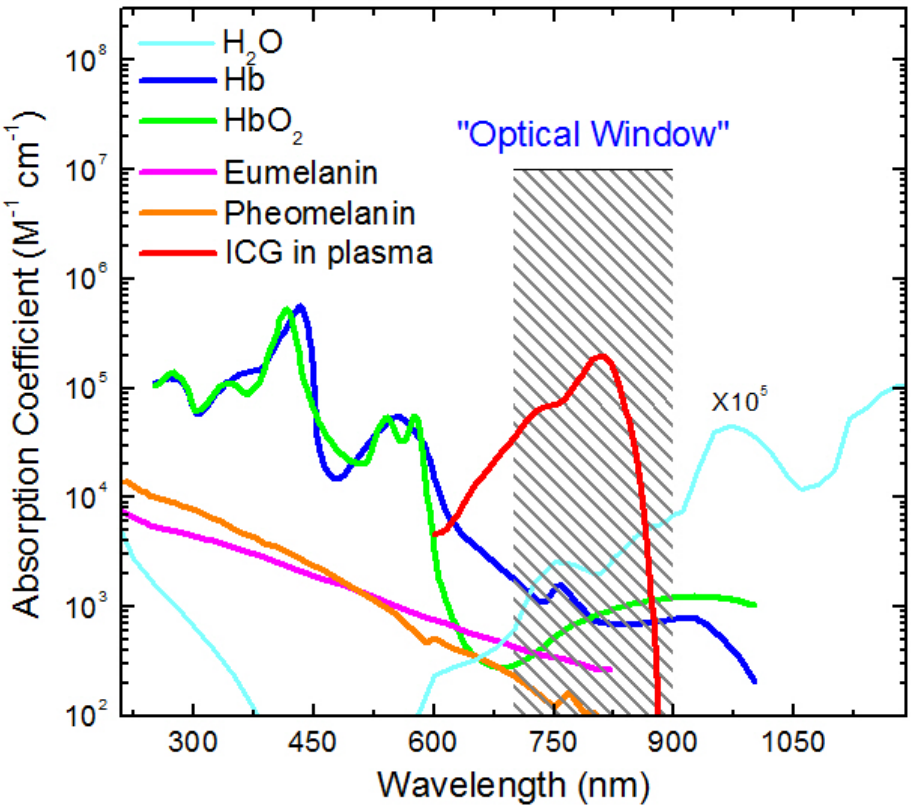

Figure 1-10: UV-Vis absorption spectra of water, deoxyhaemoglobin (Hb), oxyhaemoglobin (HbO_2), eumelanin, pheomelanin and a potential near-infrared photosensitizer indocyanine green (ICG). The shaded area indicates the "optical window". The absorption coefficient data were obtained from http://omlc.ogi.edu/spectra/. (Note: the absorption coefficient of water has been multiplied by 10^5.)

As shown in Table 1-1, the absorption peaks of all the clinically approved photosensitizers are outside the "optical window". The spectral mismatch between the photosensitizer absorption spectrum and the optimum wavelength for tissue penetration has hindered the widespread adoption of PDT into clinical practice, especially in the treatment of larger or thicker solid tumor masses. Hence, one approach to improve the clinical effectiveness of PDT is to develop new photosensitizers that are sensitive to light at near-

infrared (NIR) wavelengths (52, 100, 132-136). Table 1-2 is a summary of new photosensitizers that are currently in clinical trials.

Table 1-2: Photosensitizers in clinical trials.

Photosensitizer	**Wavelength**	**Description**	**Type of diseases**	**Country**
Rostaporfin	660 nm	Tin ethyl etiopurpurin (SnEt2), Purlytin	Skin, breast cancers, macular degeneration	U.S.
Talaporfin	660 nm	Mono-(L)-aspartylchlorin-e6 (MACE, LS11, NPe6)	Liver, colon, brain cancers	U.S
Fotolon	660 nm	Chlorin e6-polyvinypyrrolidone (Ce6-PVP)	Malignancy of skin, mucosal malignancies of hollow organs	Belarus, Russia
Radachlorin	660 nm	Ce6 derivatives	Nasopharyngeal, sarcoma, brain cancers	Russia
Photodithazine	660 nm	Ce6 derivatives	Nasopharyngeal, sarcoma, brain cancers	Russia
Photochlor	665 nm	2- (1-hexyloxyethyl)-2-devinyl pyropheophorbide-a (HPPH)	Head and neck, esophagus, lung cancers	U.S.
SiPcS	675 nm	Silicon phthalocyanine	Lymphoma, non-melanomatous, skin cancer, precancerous condition	U.S.
Lutex	732 nm	Lutetium texaphyrin (motexafin lutetium)	Breast cancer	U.S.
Padoporfin	762 nm	Palladium bacteriochlorophyll derivative (TOOKAD, WST09)	Prostate cancer	U.S.

In this thesis project, we have investigated the potential of increasing the treatment depth of PDT through three different approaches, namely two-photon activated PDT,

combination of NIR light activated PDT with chemotherapy, and bioluminescence-activated PDT, which will be discussed in the following sections.

1.6 Two-photon activated PDT

Two-photon excitation (TPE) is a non-linear optical process originally predicted by the Nobel Laureate Maria Goeppert-Mayer in the 1930s (137). In a TPE process, a molecule absorbs two photons simultaneously leading to the formation of an excited state molecule with energy equal to the total energy of the two incident photons. In other words, in a TPE process, photons with half the energy (i.e. longer wavelength) required for one-photon excitation (OPE) can promote the molecule to the same energy state as that reached in a OPE process. In confocal fluorescence microscopy, the concept of TPE has been used successfully since 1990 (138-140). Possible applications of TPE in PDT have also been explored over the past two decades (141-152). Two-photon activated PDT, denoted here as 2-γ PDT, has several potential advantages over conventional one-photon activated PDT (1-γ PDT) using (quasi) continuous-wave (CW) illumination, including greater treatment depth in tissue (149, 152), minimized side effects, and improved spatial targeting (148).

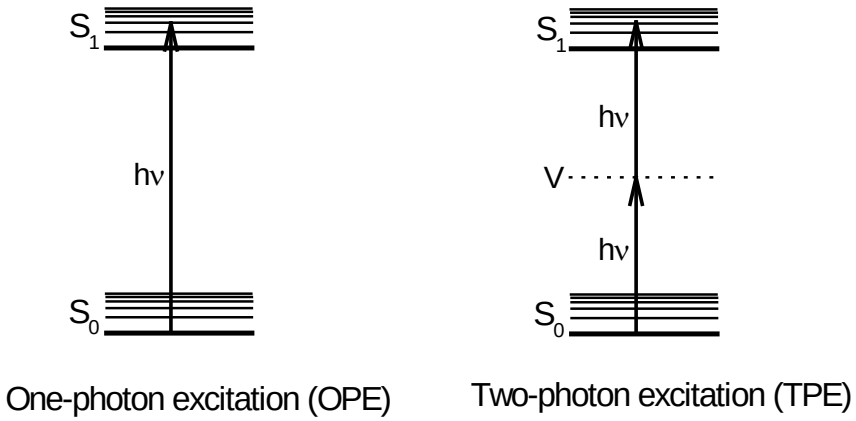

Figure 1-11: Jablonski diagram illustrating the one-photon and two-photon excitation processes. (S_0: ground state; S_1: the first excited singlet state; V: the virtual energy state.)

However, clinical applications of 2-γ PDT have been limited due to the low 2-γ absorption cross sections (σ in Goeppert-Mayer units; 1 GM = 10^{-50} cm^4 s $photon^{-1}$) of conventional PDT photosensitizers. The values of σ for the commonly used 1-γ photosensitizers, including Photofrin®, Visudyne® and protoporphyrin IX, range from 2 GM to 60 GM (144). Khurana *et al.* found that, at a peak irradiance of 1.75×10^{11} W cm^{-2}, the light doses required to kill 50% of cells (LD_{50}) through 2-γ activation of Photofrin® (σ = 10 GM at 800 nm) and Visudyne® (σ = 51 GM at 900 nm) were more than 100 times higher than those required for 1-γ PDT treatment (147). Therefore, novel photosensitizers with much higher σ values (up to about 17,000 GM) have been synthesized and their photodynamic properties have been explored (134, 148-152). For example, *in vivo* experiments performed by Collins *et al.* demonstrated that a conjugated porphyrin dimer (P_2C_2-NMeI) could induce single blood-vessel closure through a TPE mechanism when activated by a 300 femtosecond (fs)

laser beam centered at 920 nm (148). Spangler *et al.* successfully synthesized a new 2-γ PDT triad, which showed effective treatment up to about 2 cm depth in animal experiments (149, 152). These promising initial results indicate that 2-γ PDT can potentially enable minimally-invasive treatment of deeper and larger tumors than those treated with conventional 1-γ PDT.

1.7 Combination of NIR-PDT with chemotherapy

Thanks to the advances in cancer research, we are becoming more and more aware that cancer is not a single disease but a heterogeneous population of cells, which may be grouped into more than one hundred diseases. Many cancers traditionally thought as a single disease should actually be separated into several subcategories. This understanding helps explain why many of the commonly occurring cancers, including breast, lung and ovarian cancers, are initially responsive to conventional chemotherapy and radiotherapy, but become resistant to the treatment after a while. There are several mechanisms that a cancer cell may be resistance to chemotherapy (153-159), which can either be intrinsic or acquired. Intrinsic resistance involves the existence of cancer cells that are resistant before receiving the treatment, while cancer cells that are initially sensitive may develop resistance during the treatment process. At the molecular level, a variety of mechanisms have been proposed to be responsible for drug resistance (159). For example, the multi-drug resistance proteins (MRP), which belong to the family of ATP-binding cassette (ABC) transporters, can bind to a wide range of chemotherapeutic drugs and transport the drug molecules outside the cell leading to a decreased intracellular concentration of the drug. Of relevance to this project, CDDP is a

substrate for the multi-drug resistance protein 2 (MRP2), also known as ATP-binding cassette sub-family C member 2 (ABCC2), while VP-16 has been found to be a substrate for multidrug resistance protein 1 (MDR1) or ATP-binding cassette sub-family B member 1 (ABCB1), MRP1/ABCC1 and MRP2/ABCC2 (151). Some drugs rely on specific transporters to enter the cells. Mutations in these receptors may reduce the cellular uptake of those drugs. Many other factors, such as decreased drug activation, increased DNA damage repair, and increased inactivation of the drug or its toxic intermediates, may also increase the resistance to the treatment. Therefore, a permanent cure for many cancers would require a combination of two or more cancer therapies (8, 160).

Photodynamic therapy is a novel clinical approach, which uses the combination of light and light-activatable drugs to treat various types of tumors and some other non-malignant conditions (28-37). A few PDT drugs have been approved for clinical use (Table 1-1). However, these drugs are activated by visible light (630-690 nm), where light has a tissue penetration depth of only 2-4 millimeters (mm) (96, 161) and the resulting effective treatment depth is very limited. As have been discussed in Section 1.5.4, using NIR light for photosensitizer activation has the potential of treating deep-seated or large tumors. In addition, conventional PDT requires the presence of oxygen (Section 1.5), which makes PDT ineffective for the treatment of hypoxic solid tumors. Therefore, the combination of PDT, especially NIR-light activated PDT, with conventional chemotherapy may have the following properties and thus, overcome the limitations of the single therapies:

- **Minimizing the side effects of chemotherapy:** First, the combination treatment may produce an additive or even synergistic effect, so that the dose of the most toxic component may be reduced and therefore, lessening the severe side effects normally associated with the administration of chemotherapeutic drugs. Second, the use of light to activate the PDT drug allows local targeting of the treatment site and leads to reduced toxic effects on the surrounding normal tissues.
- **Having the potential of overcoming chemotherapy resistance:** In general, cancer cells resistant to chemotherapy do not show cross-resistance to PDT treatment (162). In other words, cancer cells resistant to chemotherapeutic drugs may be sensitive to PDT treatment. Moreover, the combination treatment may produce synergistic effects, which have the potential of removing resistance to the drugs (9).
- **Having the potential of treating hypoxic solid tumors:** The chemotherapeutic drugs may replace the requirement of oxygen in conventional PDT. Therefore, the combination therapy may be effective in treating hypoxic tumors.
- **Having the potential of treating tumor metastasis:** While PDT alone is a local treatment, its combination with a systemically administered chemotherapeutic drug may be used to treat the primary and metastatic tumors at the same time.

1.7.1 Combination of PDT with CDDP

The combination effects of PDT with CDDP, one of the most widely used chemotherapeutic cancer drugs, has been studied by several research groups (163-167). In 1998, Canti *et al.* investigated the combination effects of CDDP with PDT, mediated by aluminium disulfonated phthalocyanine ($AlPcS_2$), in murine tumor bearing mice and observed an additive effect (163). One year later, Duska *et al.* demonstrated that the combination of CDDP with photoimmunotherapy, using chlorin e6 conjugated to the murine monoclonal antibody OC-125 as the photosensitizer, enhanced the cytotoxicity of CDDP in a synergistic

manner in cisplatin-resistant ovarian cancer cells *ex vivo* (164). The combination of CDDP with Photofrin®-mediated PDT has been found to induce synergistic enhancement of cytotoxicity in mouse lymphoma L5178Y (LY) cells (168) and human non-small cell lung cancer H1299 cells (166). Interestingly, Crescenzi *et al.* found that the combination effect of low-dose CDDP with ICG-mediated PDT in MCF-7 breast cancer cells was synergistic according to the MTT assay results, but additive based on the data from the trypan blue assay (165). More recently, Compagnin *et al.* reported that they did not observe additive/synergistic effect in the oesophageal squamous carcinoma cells (KYSE-510) treated with the combination of low dose CDDP and Photofrin®-mediated PDT (167). Those results suggest that the combination effects may be dependent on many factors such as the drug/light dose, type of the photosensitizer, cell type, assay used to evaluate the cytotoxicity, etc.

Another approach, in which the photosensitizers are covalently linked with CDDP, has been explored by some research groups (169-173). Lottner *et al.* synthesized 35 new compounds, in which CDDP was combined with HpDs in the same molecule, and found that some of them showed enhanced cytotoxicity against the bladder cancer cell lines TCC-SUP and J82 (169). Mao *et al.* conjugated CDDP with the photosensitizer silicon(IV) phthalocyanine (SiPc) and evaluated the photocytotoxicity against human cervical cancer HeLa cells (170). This combination was shown to be able to maintain the intrinsic functions of each unit and serve as agents for both DNA-targeting PDT and red light activated photochemotherapy. Bulgakov *et al.* recently synthesized covalently linked CDDP and octacarboxy substituted zinc phthalocyanine conjugates, which were found to be very

efficient in generating singlet oxygen with yields ~0.47-0.60 and showed higher activity against human laryngeal cancer (HEp2) and lung adenocarcinoma (A549) cells than the parent octacarboxy-substituted PcZn (171). The conjugates of hydroxy aluminium octacarboxy phthalocyanine and CDDP were found to have higher triplet and singlet oxygen quantum yields than the parent phthalocyanine, although their cytotoxicity was not studied (172). This approach of combining CDDP and a photosensitizer within the same molecule has the advantages of maintaining the functions of the single units and increasing the quantum yield of $^1O_2$ due to the heavy atom effect and thus, may be more effective in killing cancer cells than the single treatments.

1.7.2 Combination of PDT with other chemotherapeutic drugs

The combination effects of PDT with conventional chemotherapeutic drugs other than CDDP, including VP-16, doxorubicin (Adriamycin), 5-fluoro-2'-deoxyuridine (5FdUr) and gemcitabine, have also been investigated extensively (174-179). Gantchev *et al.* investigated the interactions between VP-16 and PDT with aluminium tetrasulfonated phthalocyanine ($AlPcS_4$) as the photosensitizer in human leukaemic K562 cells and observed synergistic enhancement of drug cytotoxicity (174). The combination effects of 5-fluoro-2'-deoxyuridine (5FdUr) and mTHPC-mediated PDT were studied in human breast (MCF-7) and human prostate (LNCaP) cancer cells by Zimmermann *et al.* (176). Depending on the protocol and concentration of 5FdUr, the combination treatment resulted in an additive/antagonistic effect in LNCaP cells but an additive/synergistic was observed in MCF-7 cells. The authors found

that the combination treatment induced much stronger effects than expected in one patient with multiple basal cell carcinomas. In another study, Kirveliene *et al.* found that the degree of cytotoxicity enhancement induced by the combination treatment depends on whether the chemotherapeutic drug doxorubicin (Dox) was administrated 24 h prior to or immediately after light exposure of mTHPC-sensitized murine hepatoma MH-22A cells (177). Animal experiments have been performed by Xie *et al.*, who observed significant enhancement of the antitumor activity of Photosan®-mediated PDT by low dose gemcitabine in human pancreatic cancer cell (SW1990) bearing mice (178). More recently, Diez *et al.* showed that the administration of low dose DOX or vincristine (VCR) increased the anticancer effect ALA-mediated PDT in a sensitive murine leukemic cell line (LBR) but didn't affect the cytotoxicity of ALA-PDT in the two resistant cell lines LBR-D160 and LBR-V160 (179). Again, those studies have demonstrated that the combination effects of PDT and conventional chemotherapy may be antagonistic, additive or synergistic depends on many factors.

In summary, numerous studies have reported the use of PDT in combination with conventional chemotherapy aiming to enhance the antitumor activity of single therapies. Additive/synergistic enhancement of cytotoxicity has been reported in some studies (163-166, 168, 174, 176-179), but antagonistic effect has also been observed (167, 176, 179). Clearly, the combination effect has a strong dependence upon many factors, including the cell type, type of the PDT and chemotherapeutic drug, light dose, and treatment schedule, and a molecular mechanism underlying the observed synergistic enhancement of cytotoxicity

is still lacking. Therefore, a better understanding of drug interactions in the combination therapy is expected to be beneficial to the development of more effective treatment approaches. In the case of CDDP, its cytotoxicity is generally accepted to arise from the drug's ability to bind with cellular DNA and induce DNA damages. Hydrolysis is the conventional mechanism of the initial action of CDDP (155, 156, 180, 181). Recently, our group has obtained the precise molecular mechanism of CDDP action by using femtosecond time resolved laser spectroscopy (fs-TRLS) (182, 183). It was found that the dissociative electron-transfer (DET) of CDDP with the guanine base, which is most likely to donate an electron among the four DNA bases, is responsible for the activation of CDDP. This DET mechanism of CDDP has been confirmed both experimentally by Kopyra et al. (184) in studying dissociative attachments of nearly zero eV (electron volt) electrons to gas-phase CDDP and theoretically by Kuduk-Jaworska et al. (185) in their quantum chemical studies of the reaction of e_{pre}^- with aqueous CDDP. This new mechanistic insight has the potential to improve existing therapies using CDDP and enable the development of novel combination treatments for challenging cancers. Based on this mechanism, we have developed a novel combination therapy, in which a biological electron donor (TMPD; N,N,N′,N′-tetramethyl-p-phenylenediamine) has been demonstrated to enhance the cytotoxicity of CDDP in a synergistic manner and overcome cisplatin-resistance in the human lung A549 and ovarian NIH:OVCAR-3 cancer cells (9). These studies show the promise of applying the molecular mechanistic understanding of action of drugs to develop novel combination therapies and improve the therapeutic efficacy.

1.7.3 Indocyanine green as a potential NIR photosensitizer

Indocyanine green (ICG) is a NIR dye that was approved by FDA in 1956. It has been successfully used in various medical applications such as blood volume determination (186), cardiac output measurement (187), fluorescence probing of proteins (188), and pharmacokinetic analysis (189). The UV-Vis absorption spectrum of ICG in plasma has a maximum near 800 nm (Figure 1-10), which falls right into the tissue "optical window" for PDT. Therefore, this dye has been considered to be a potential sensitizer for PDT applications and its photodynamic efficacy has also been explored (108, 165, 190-201). The involvement of $^1O_2$ has been suggested based on the observation that the cell killing effect could be inhibited by the $^1O_2$ quencher sodium azide (190, 192), although direct detection of $^1O_2$ luminescence at 1270 nm was not successful. However, ICG has several intrinsic properties, including short blood half-life (2 to 4 minutes (202)), poor photo- and thermal-stability, non-specific binding with proteins, and vulnerablility to aggregation (203), which have limited its application as a photosensitizer and medical imaging probe. One potential way of increasing the effectiveness of ICG as a PDT agent is to combine this treatment with conventional chemotherapy. Indeed, the combination of ICG-mediated PDT with low-dose CDDP induced a synergistic effect in MCF-7 cells, although the combination effect was found to be additive according to the trypan blue assay results (165). As has been discussed in Sections 1.7.1 and 1.7.2, the combination effect is dependent on a variety of factors. Investigation of the combination effects of ICG-mediated PDT with other chemotherapy drugs may provide us with a better understanding of the mechanism of drug interactions

during the treatment process and thus, helps the development of more effective combinations of PDT and chemotherapy.

Encapsulation of ICG within micelles and nanoparticles has also been explored extensively over the past decade to overcome the above mentioned limitations of ICG (102, 106, 107, 109, 111-113, 115-118, 201). These encapsulating approaches were demonstrated to be able to improve various properties of ICG such as photo- and thermal-stability, fluorescence quantum yield, and blood half-life. By using tumor-targeting ligands, these systems could further improve the tumor-specificity of the dye (112, 113, 115, 117). However, only two of those systems were investigated for photodynamic killing of cancer cells. ICG-conjugated gold nanorods were found to be able to increase the yield of $^1O_2$ and serve simultaneously as PDT and photothermal therapy (PTT) agents (111). The ICG-ormosil nanoparticles showed a similar level of cytotoxicity as that induced by free ICG, while having improved aqueous stability (201). Therefore, further experiments will be necessary to assess the PDT efficacy of those novel drug systems. Considering the improved stability and tumor-specificity of those systems, combination treatments of chemotherapy and PDT using those novel systems as the photosensitizers may offer great therapeutic potentials.

1.8 Bioluminescence-activated PDT

Bioluminescence is a type of chemiluminescence that takes place inside a living organism where the energy of a chemical reaction is released in the form of light emission. Fireflies are one of the most famous examples of bioluminescent organisms. Bioluminescence has been

widely used in detection and imaging applications (204-208). The fact that no external excitation source is required offers the advantage of eliminating any possible background noise associated with scattered light and autofluorescent light. The idea of using bioluminescence as an internal light source for PDT has been tested by several research groups over the past two decades (104, 209-212). It has the potential of overcoming the limitation of tissue penetration depth of external light. There are three bioluminescent systems that have been investigated for PDT applications:

- Coelenterazine-luciferase: Coelenterazine is the substrate for many luciferases and the light-emitting molecule in many marine invertebrates such as the luminescent Aequorea jellyfish. It can emit blue light with a maximum around 458 nm in the presence of luciferase, oxygen and calcium.

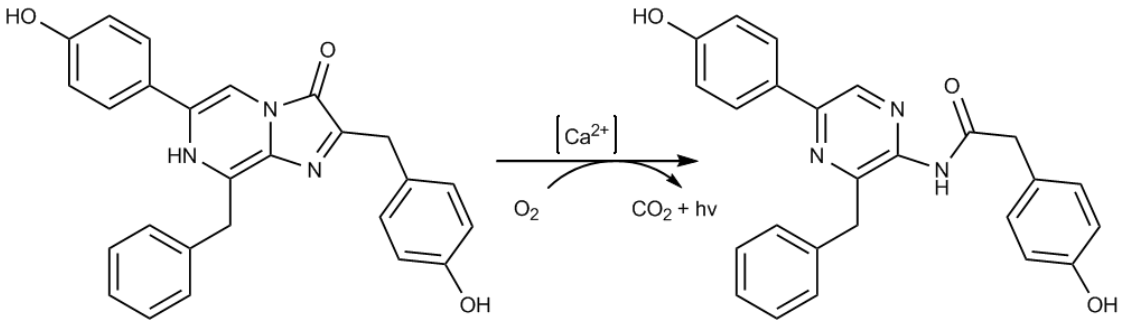

Figure 1-12: Mechanism of light generation by coelenterazine.

- Luminol: Luminol can undergo a blue light-emitting process (λ_{max} = 425 nm (213)) when mixed with an oxidizing agent such as hydrogen peroxide (H_2O_2). The reaction can be catalyzed by enzymes such as horseradish peroxidase and metal ions (e.g. cations of iron and copper).

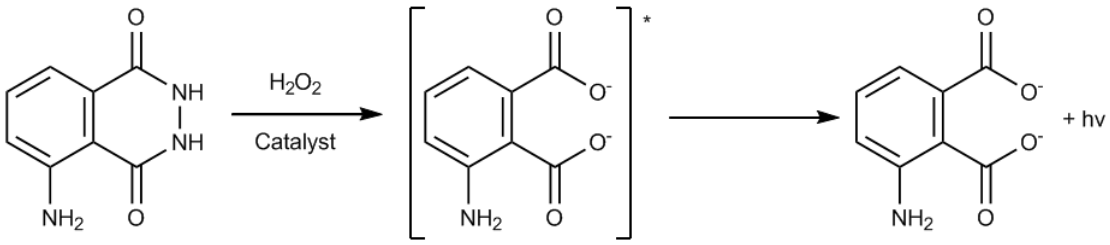

Figure 1-13: Mechanism of light generation by luminol.

- Firefly luciferin-luciferase: Firefly luciferin is the light-emitting compound present in many firefly species. It can emit yellow light catalyzed by luciferase (EC 1.13.12.7) in the presence of Mg^{2+}.

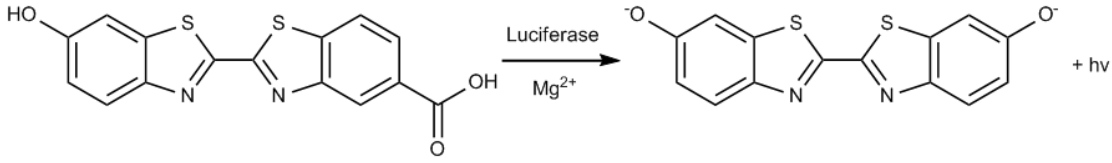

Figure 1-14: Mechanism of light generation by firefly luciferin.

In 1994, Carpenter *et al.* studied the antiviral activity of hypericin activated by the bioluminescence of luciferin (209). Almost ten years later, Theodossiou *et al.* studied the *in vitro* photodynamic activity of Rose Bengal activated by firefly luciferin in luciferase-transfected mouse embryonic fibroblast (NIH 3T3) cells (210). In contrast, Schipper *et al.* evaluated the photodynamic cytotoxicity of firefly luciferase bioluminescence in several malignant and nonmalignant cell lines, including MCF-7, NIH 3T3, 3T3L1 (derived from mouse 3T3 cells), CHO (Chinese hamster ovary cells), 293T (a highly transfectable derivative of human embryonic kidney 293 cells), and A375M (human melanoma cells) (211). They concluded that bioluminescence of firefly luciferase didn't generate enough light to induce hypericin or Rose Bengal photocytotoxicity. However, the study performed by

Laptev *et al.* demonstrated that bioluminescence of luminol could activate bioconjugates composed of transferrin (Tf) and Hp and induce significant cell killing in leukaemia K562 and U-76 cells (104). Recently, Chen *et al.* found that bioluminescence of luminol could effectively activate 5-ALA-mediated PDT in a human epithelial colorectal adenocarcinoma cell line (Caco-2) (214). In the same year, Yuan *et al.* reported their studies of the anticancer and antimicrobial activity of a new bioluminescence system consists of luminol and a cationic oligo(p-phenylene vinylene) as the photosensitizer (215). Positive results were obtained by Hsu *et al.*, who developed a system containing luciferase-immobilized quantum dots for bioluminescent activation of Foscan®-loaded micelles and this system was found to be sufficient to induce tumor cell killing *in vitro* and delay tumor growth *in vivo* (212). These results suggest the potential of using bioluminescence as the internal light source for photodynamic treatment of human cancers, with an increased treatment depth compared with conventional PDT.

1.9 PDT dosimetry

Fluence or radiant exposure represents the amount of energy measured in *Joules (J)* per unit area (i.e. $J\ cm^{-2}$). The typical values in conventional PDT are 25-500 $J\ cm^{-2}$ for surface treatment and 100-400 $J\ cm^{-2}$ for interstitial applications (52).

Penetration depth (δ) refers to the depth at which the light intensity has dropped to *1/e* (=0.37) of the initial intensity. The penetration depth is not the same as the depth of PDT treatment (d_t), which depends on a number of factors including the type of the photosensitizer

and its mechanism of action, the level of tissue oxygenation, and light dose. Most clinically approved photosensitizers have d_t values in the range 3-5δ (34).

Power (P) represents the amount of energy delivered per unit time measured in *Watts* (*W*): 1 $W = 1\ J\ s^{-1}$.

Power density or irradiance is the power of electromagnetic radiation per unit area incident on a surface measured in $W\ cm^{-2}$. The maximum allowed values in conventional PDT are 200 and 400 $mW\ cm^{-2}$ for surface and interstitial treatments, respectively (52).

1.10 Scope of the thesis

In Chapter 2, we describe the experimental techniques, namely femtosecond (fs) time-resolved laser spectroscopy (fs-TRLS) and steady-state spectroscopy, which have been applied to characterize the photophysical properties of the potential anticancer drugs investigated in the present work. In Chapter 3, we present the results of *in vitro* cytotoxicity studies of a 2nd-generation photosensitizer pyropheophorbide *a* methyl ester (MPPa) activated through one- and two-photon excitation in human cervical (HeLa), lung (A549) and ovarian (NIH:OVCAR-3) cancer cell lines. Photophysical properties of MPPa have also been investigated by using fs-TRLS and steady-state spectroscopy. The results of the combination therapy of PDT mediated by the near-infrared (NIR) dye, indocyanine green (ICG), with two types of chemotherapy drugs, namely the type II topoisomerase (TOPII) inhibitors VP-16 and VM-26, and the platinum-based drugs cisplatin (CDDP) and oxaliplatin (OXP), are

presented in Chapter 4 and 5, respectively. The possibility of using bioluminescence of luminol as an internal light source for PDT has also been explored and the results are presented in Chapter 6. Chapter 7 is a summary of all the key results of this project and discussion of future works.

2 Experimental Techniques and Theory

In this project, we have applied both femtosecond time-resolved laser spectroscopy (fs-TRLS) pioneered by the Nobel Laureate Prof. Ahmed H. Zewail (216) at the California Institute of Technology and steady-state spectroscopy to characterize the photophysical properties of the compounds used in this study. In our group, the fs-TRLS techniques have been successfully applied to study the ultrafast dynamics of a variety of systems. Those studies have greatly deepened our understanding of the molecular mechanisms of action of drugs used in chemo-, radio- and photodynamic therapy of cancers (19, 20, 182, 183, 217-221).

2.1 Femtosecond time-resolved pump-probe transient absorption spectroscopy

The standard methodology for fs time-resolved pump-probe transient absorption spectroscopy has been applied (182, 183, 217, 219-223). Figure 2-1 shows a schematic representation of the experimental setup and the basic principle of fs time-resolved pump-probe transient absorption spectroscopy.

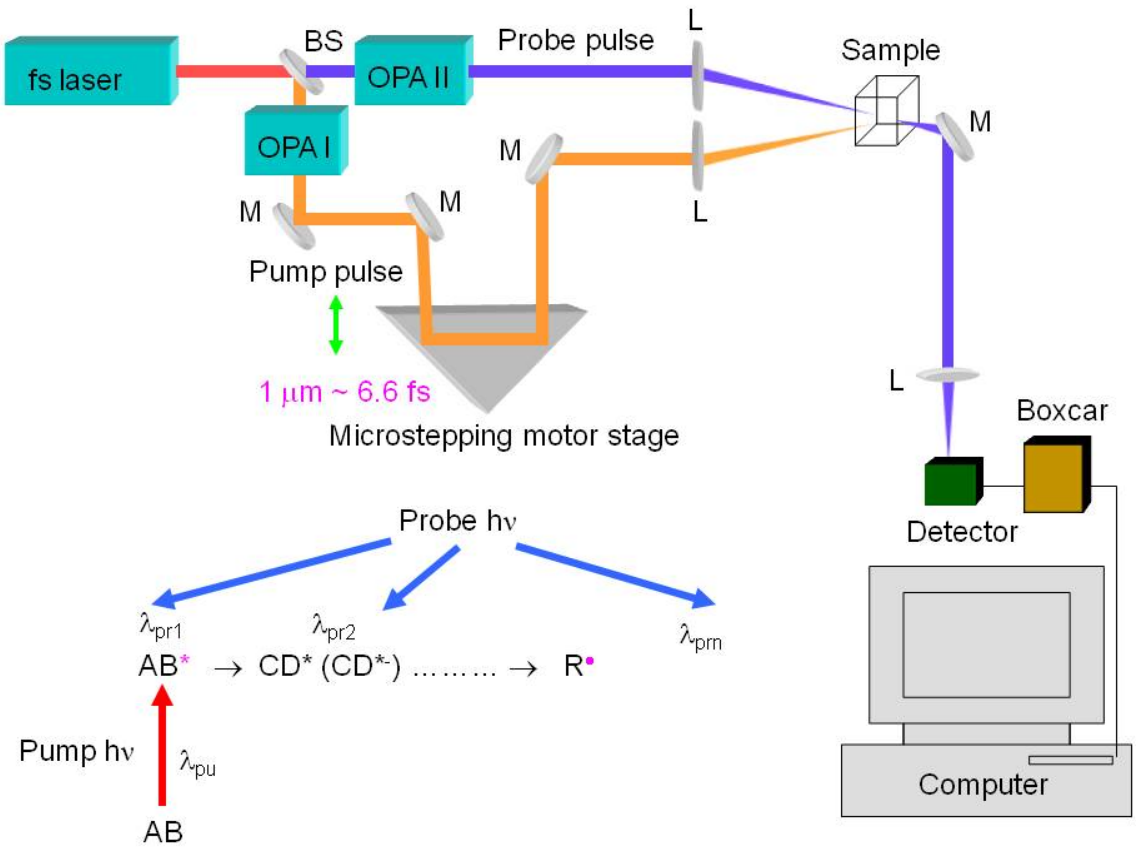

Figure 2-1: Schematic diagram of the experimental setup for femtosecond time-resolved pump-probe transient absorption spectroscopy. (BS: beam splitter; fs: femtosecond; L: lens; M: mirror; OPA: optical parametric amplifier).

We use a Spectra-Physics Ti:sapphire laser system producing 800 nm laser pulses with duration of 100-120 fs, an average energy of 1 mJ, and a repetition rate of 1 kHz. In order to achieve a fs time-resolution, two fs laser pulses are required: one, the “pump” pulse, is applied to initiate a reaction, for example, to promote a sample molecule to an excited state or to generate a reacting species, while the “probe” pulse is used to monitor the evolution and decay of a specific reaction intermediate, such as an excited-state molecule. We used two

optical parametric amplifiers (OPA), which can produce laser pulses with wavelengths from ~266 nm to a few micrometers, to generate the pump and probe pulses, respectively. To avoid polarization anisotropy, the polarization of the pump pulse is set to be at the magic angle of 54.7˚ with respect to the probe pulse.

Correct measurement of intensity requires the measured intensity ($I = I_{\parallel} \cos^2\theta + I_{\perp} \sin^2\theta$, where $I_{\parallel}$ and $I_{\perp}$ are the intensities parallel and perpendicular to the polarization of the pump pulse, respectively, and θ is the angle between the polarization of the pump and probe pulses) to be proportional to the total intensity ($I_{total} = I_{\parallel} + 2I_{\perp}$), regardless of the polarization degree of the sample (224). Therefore, the value of θ should satisfy the equation $3 \cos^2\theta = 1$ yielding $\theta = 54.7^{\circ}$. The use of the magic angle condition is especially important for measuring decay kinetic traces due to the fact that $I_{\parallel}$ and $I_{\perp}$ usually have distinctly different kinetics (224). The time delay between the pump pulse and the probe pulse is varied by moving a microstepping motor stage, which can change the optical path difference (OPD) between these two pulses. For example, an OPD of 1 μm corresponds to a time difference of 3.3 fs. Therefore, a fs time resolution can be achieved. If the reaction intermediates have distinctly different absorption spectra, the behavior of each reaction intermediate may be monitored by choosing a probe wavelength that matches the absorption spectrum of each species. Labview (**Lab**oratory **V**irtual **I**nstrument **E**ngineering **W**orkbench; National Instruments, Austin, TX, USA) programs are used to control the motion of the microstepping motor stage and collection of data from a gated integrator and Boxcar averager system.

2.2 Femtosecond time-resolved pump-probe transient fluorescence spectroscopy

In fluorescence spectroscopy, a fs time resolution can be achieved by using the sum frequency generation (SFG) technique (225), which is also known as fluorescence upconversion. Figure 2-2 shows schematically the experimental setup. The same laser system as that described in Section 2.1 is used. The pump pulse is used to excite the molecules to an excited state and thus, generate fluorescence emission. The fluorescent light is then collected by using two parabolic mirrors and focused onto a BBO (barium borate) crystal. The probe pulse is focused on to the same BBO crystal to mix with the fluorescent light. Sum frequency generation at the BBO crystal obeys the energy and momentum conservation laws:

Energy Conservation: $$h\nu_1 + h\nu_2 = h\nu_3; \quad (2\text{-}1)$$

Momentum Conservation: $$\hbar\overrightarrow{k_1} + \hbar\overrightarrow{k_2} = \hbar\overrightarrow{k_3}, \quad (2\text{-}2)$$

where h is the Planck's constant, ν is the frequency of the photon, $\hbar$ is the reduced Planck constant, and $\vec{k}$ is the wave vector.

According to Equation (2-1), the up-converted photon has an energy that equals the sum of the energies of the two incident photons. In other words, the up-converted fluorescence light is at a shorter wavelength than the fluorescence of the sample. The momentum conservation law requires the BBO crystal to be set at a specific angle and orientation in order to obtain the maximum un-converted fluorescence signal. This is also known as the phase matching condition. The up-converted fluorescence light is then focused

into the entrance slit of a CM112 Compact 1/8 Meter Double Monochromator (Spectral Products, Connecticut, USA) coupled with an AD111 Photobyte-P™ Photomultiplier Detection System (Spectral Products, Connecticut, USA). Wavelength selection, pump-probe time delay and data acquisition are controlled by Labview programs.

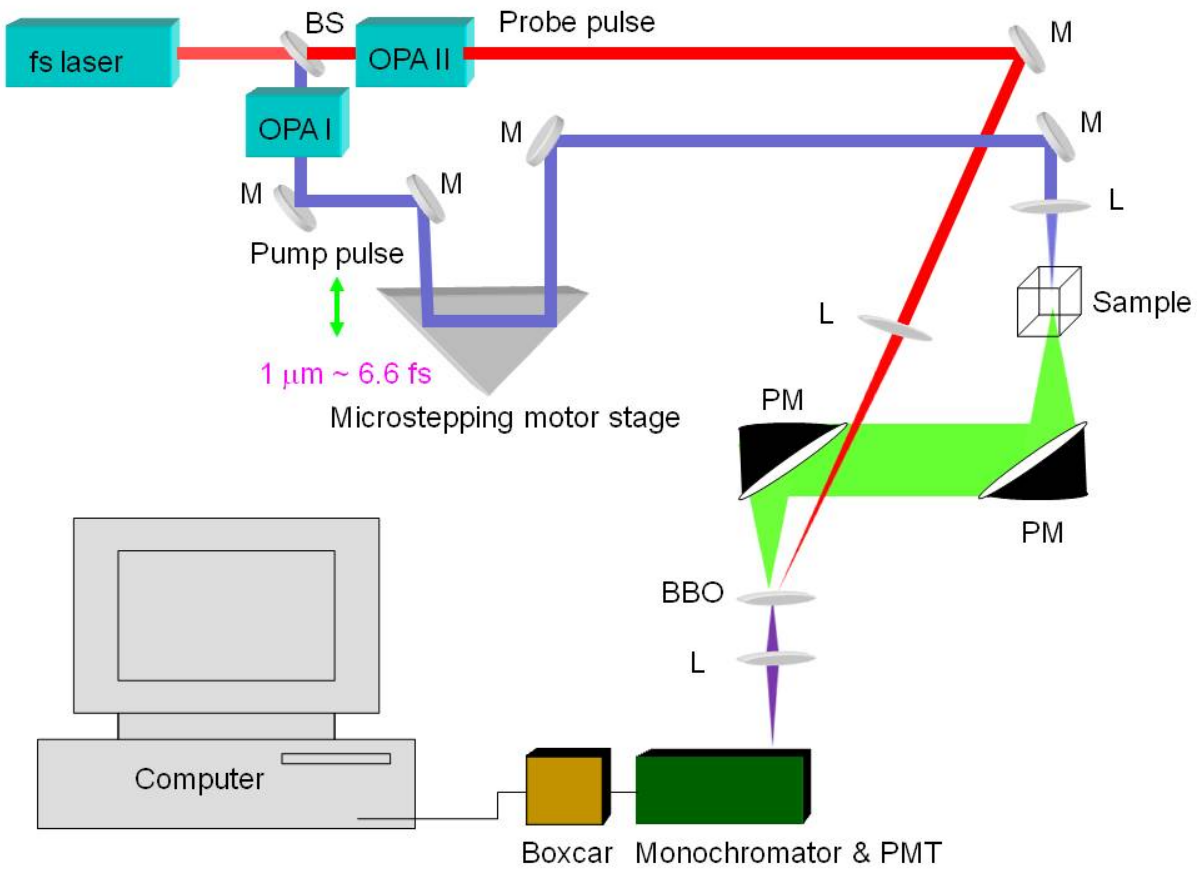

Figure 2-2: Schematic diagram of the experimental setup for femtosecond time-resolved pump-probe transient fluorescence spectroscopy. (BBO: barium borate; BS: beam splitter; fs: femtosecond; L: lens; M: mirror; OPA: optical parametric amplifier; PM: parabolic mirror; PMT: photomultiplier tube).

2.3 Steady-state fluorescence spectroscopy

Figure 2-3 is a schematic representation of the experimental setup for one- and two-photon induced steady-state fluorescence spectroscopy. The same laser system as that used in fs time-resolved absorption and fluorescence spectroscopy is used as the excitation source. The excitation wavelength can be tuned by an OPA coupled with a series of colored filters. The excitation power can be adjusted by a series of neutral density filters. The laser beam is focused vertically into a 5 mm quartz cuvette using a biconvex lens with a focal length of 75.6 mm. The fluorescence signal that transmitted through the side of the cuvette is focused by two parabolic mirrors into the entrance slit of the monochromator. The monochromator and photomultiplier tube (PMT) are controlled by Labview programs. A gated integrator and Boxcar averager system is used to obtain the fluorescence intensity.

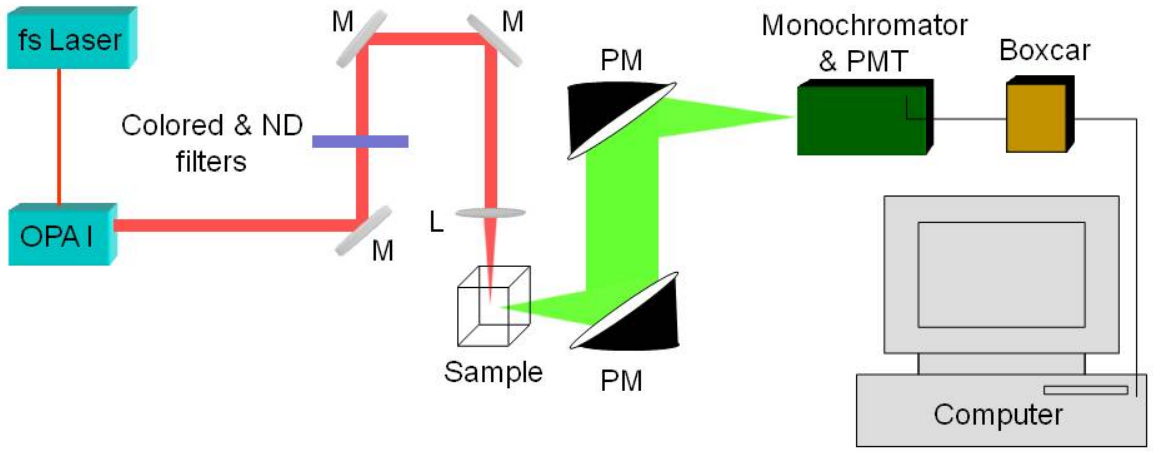

Figure 2-3: Schematic diagram of the experimental setup for steady-state fluorescence spectroscopy. (fs: femtosecond; L: lens; M: mirror; ND: neutral density; OPA: optical parametric amplifier; PM: parabolic mirror; PMT: photon multiplier tube).

The fluorescence spectra obtained with this homemade fluorescence spectrophotometer have been corrected for collection efficiency of the detection system, which can be calculated by using the efficiency data of the gratings inside the monochromator and the PMT provided by the manufacturer. In order to determine the accuracy of this correction, we have compared the corrected one-photon induced fluorescence spectrum of 5 μM $ZnPcS_4$ in methanol with that measured on a commercial fluorescence spectrophotometer (Varian Cary Eclipse, Palo Alto, CA, USA) (Figure 2-4). The two fluorescence spectra overlap with each other. Therefore, all the fluorescence spectra obtained from our homemade fluorescence spectrophotometer have been corrected using the same collection efficiency as used here.

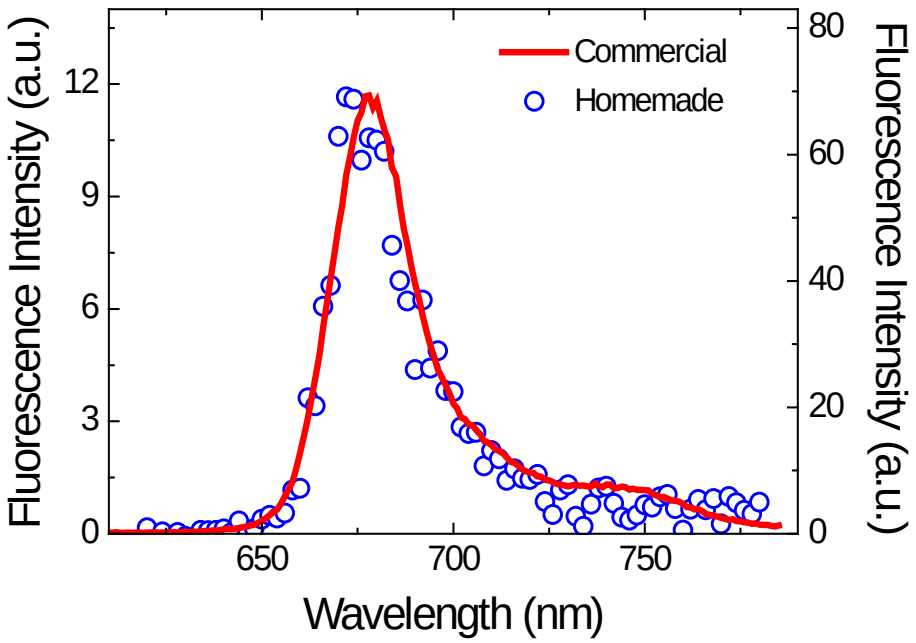

Figure 2-4: One-photon induced fluorescence spectra of 5 μM $ZnPcS_4$ in methanol measured on a commercial (red solid line) and a homemade (blue open circles) fluorescence spectrophotometer. The excitation wavelength was 400 nm.

2.4 One-photon and two-photon excitation induced fluorescence

One-photon excitation (OPE) is a linear process in which light attenuation is defined by Beer Lambert's law:

$$\frac{dI}{dx} = -\alpha c I, \tag{2-3}$$

$$I(x) = I_0 e^{-\alpha c x}, \tag{2-4}$$

where I_0 and I are the incident and transmitted light intensity, respectively, x is the light path length, c is the concentration of the sample, and α is the one-photon absorption cross section.

Two-photon excitation (TPE) is a non-linear optical process that involves simultaneous absorption of two photons by the same molecule (137). The attenuation of light by two-photon absorption can be calculated using the following equations:

$$\frac{dI}{dx} = -\sigma c I^2, \tag{2-5}$$

$$I(x) = \frac{I_0}{1+\sigma c I_0 x}, \tag{2-6}$$

where I_0 and I are the incident and transmitted light intensity, respectively, x is the light path length, c is the concentration of the sample, and σ is the two-photon absorption cross section in *Goeppert-Mayer (GM) units* (1 GM = 10^{-50} cm^4 s photon^{-1}).

2.4.1 Measurement of two-photon absorption cross section

The two-photon absorption cross section (σ) of a molecule can be determined by using the following equation (226):

$$\sigma_s = \frac{\Sigma_F(s)\cdot\Phi_F(r)}{\Sigma_F(r)\cdot\Phi_F(s)} \cdot \sigma_r, \qquad (2\text{-}7)$$

where the subscripts *r* and *s* denote the reference and the sample, respectively, Σ_F is the integrated intensity of the two-photon induced fluorescence, and Φ_F is the fluorescence quantum yield, which is assumed to be the same under one- and two-photon excitation. To test this assumption, we have measured the one- and two-photon induced fluorescence spectra of the two photosensitizers pyropheophorbide a methyl ester (MPPa) and Zn(II) phthalocyanine tetrasulfonic acid ($ZnPcS_4$) using our homemade fluorometer. The spectra of 50 μM MPPa and $ZnPcS_4$ in methanol have been measured with excitation wavelengths of 400 and 800 nm (Figure 2-5). For both compounds, the one- and two-photon induced fluorescence spectra overlap with each other. Therefore, two-photon absorption cross section of MPPa can be determined by using Equation (2-7) and $ZnPcS_4$ as the standard.

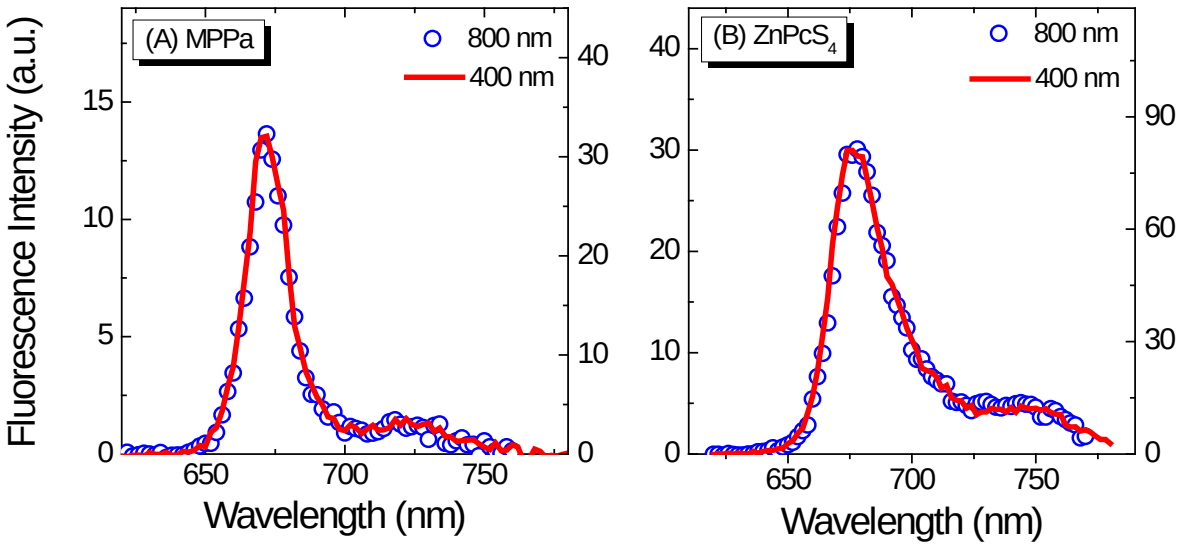

Figure 2-5: One- and two-photon induced fluorescence spectra of (A) 50 μM MPPa and (B) 50 μM $ZnPcS_4$ in methanol measured on a homemade fluorescence spectrophotometer. The excitation wavelength was 400 nm (red solid line) and 800 nm (blue open circle), respectively.

2.4.2 Measurement of fluorescence quantum yield

The fluorescence quantum yield Φ_F can be determined by using a standard reference with a known Φ_F following the equation below (52):

$$\Phi_F(s) = \Phi_F(r) \cdot \frac{Grad_s}{Grad_r} \cdot \frac{n_s^2}{n_r^2}, \quad (2\text{-}8)$$

where the subscripts *r* and *s* denote the reference and the sample, respectively, Φ_F is the fluorescence quantum yield, *Grad* is the gradient from the plot of integrated fluorescence intensity versus absorbance, and *n* is the refractive index of the solvent.

3 *In vitro* Cytotoxicity Studies and Photophysical Characterization of Pyropheophorbide-a Methyl Ester under One- and Two-Photon Excitation

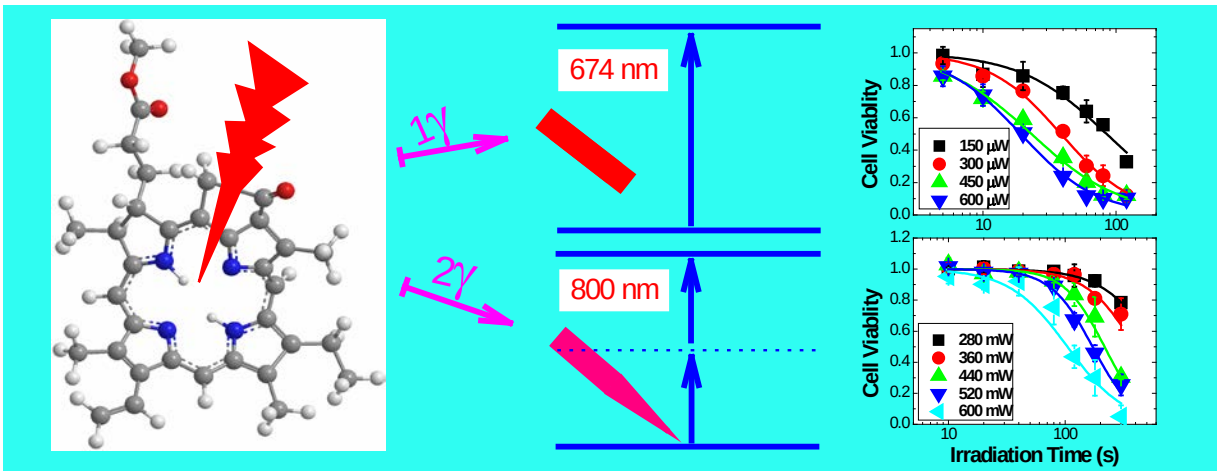

3.1 Background

Photodynamic therapy (PDT) has emerged as a novel clinical approach that involves the administration of a photo-activatable compound (photosensitizer) and subsequent exposure of the target diseased tissue to light (including laser sources) for the treatment of various tumors and other non-malignant conditions (28-37). PDT has potential advantages over surgery and other therapies of being minimally invasive, with local targeting, and having few systemic side effects. The therapeutic effects of PDT are believed to be caused by cytotoxic reactive oxygen species (ROS), including singlet oxygen ($^1O_2$), superoxide anion radical ($O_2^{\cdot-}$), hydroxyl radical ($OH^{\cdot}$) and hydrogen peroxide (H_2O_2), generated from reactions between the excited triplet state photosensitizer and biological molecules such as O_2 and water (H_2O).

Over the past decades, a few photosensitizers have been approved for clinical use (Table 1-1) (28-37). Among these, Photofrin® is the first one approved by the U.S. Food and Drug Administration (FDA) and continues to be the most widely used PDT drug. However, it has several drawbacks. First, Photofrin® is not a pure compound but a mixture of several monomeric and oligomeric non-metallic porphyrins. Second, it's absorption in the optical window for PDT is very low leading to a limited effective treatment depth of this drug. The penetration depth of light into tissue depends strongly on the wavelength. In particular, there is an "optical window" for PDT between 700 and 950 nm, where the absorbance of light by biological molecules is relatively low (96). Below about 700 nm endogenous chromophores, particularly haemoglobin/oxyhaemoglobin and melanin, are highly absorbing, while above

about 900 nm absorption by water becomes dominant (96, 131). The use of near-infrared (NIR) light, which can penetrate deeper into tissues, to activate the photosensitizers has the potential of improving the treatment efficiency of PDT (52, 134, 135). Moreover, Photofrin® accumulates in the skin and remains there for up to six weeks (99) leaving the patients very sensitive to sun light and strong room light after the treatment. Several second-generation photosensitizers, including δ-aminolevulinic acid, also known as 5-aminolevulinic acid (ALA; Levulan®), the methyl ester of ALA (Metvix®), a benzoporphyrin derivative Visudyne (Verteporfin®), tetra(m-hydroxyphenyl)chlorin (mTHPC; temoporfin; Foscan®), and a chlorophyll derivative mono-(L)-aspartylchlorin-e6 (MACE, LS11, NPe6, Talaporfin; Aptocine™) have been approved either worldwide or in some countries for treating cancers. Compared with the first-generation photosensitizers, these second-generation photosensitizers are chemically pure, highly efficient, and cause much less skin photosensitivity.

Pyropheophorbide-a methyl ester (MPPa, also known as PPME), a semi-synthetic molecule derived from chlorophyll *a*, is one of a number of emerging second-generation PDT agents (129, 227-234). Compared with the FDA-approved photosensitizer Photofrin®, MPPa has a much stronger absorption in the red part of the visible spectrum: its molar extinction coefficient ε = 47,500 M^{-1} cm^{-1} at λ = 667 nm (229) is about 15 times that of Photofrin® with ε = 3,200 M^{-1} cm^{-1} at λ = 630 nm (144). Of particular relevance here, MPPa has a very strong absorption peak around 400 nm, nearly double that at 667 nm, as shown in Figure 3-7. However, no previous studies have examined the effectiveness of PDT with MPPa via two-

photon (2-γ) excitation at 800 nm, although its one-photon (1-γ) PDT efficacy has been studied in a number of cancer cell lines *in vitro* (129, 227-234). Two-photon excitation (TPE), originally predicted by the Nobel Laureate Maria Goeppert-Mayer in the 1930s (137), is a non-linear optical process in which a molecule is promoted to an excited state by simultaneous absorption of two photons. This concept has been successfully applied in confocal fluorescence microcopy for more than two decades (138-140). Two-photon activated photodynamic therapy, denoted here as 2-γ PDT, has also been explored since 1990 (141, 142, 144-148, 151, 152) and has several potential advantages over conventional 1-γ PDT using (quasi) continuous-wave (CW) illumination. First, there is experimental evidence *in vivo* that 2-γ PDT can treat to greater depths in tissue (152) by using NIR light, although a rigorous quantitative understanding of this has not been reported. Second, reduced interaction of NIR light with tissues leads to higher differential excitation of the photosensitizer and so, in principle, minimizes the side effects and allows higher light doses to be administered. Third, due to the non-linear nature of 2-γ excitation, activation of the photosensitizer is confined to the region of highest light intensity (the basis of 2-γ confocal fluorescence microscopy), which further improves 3D control of the spatial localization of treatment. This has been demonstrated in the use of 2-γ PDT to target single blood vessels in preclinical models (148). However, the utility of 2-γ PDT has been limited by the low 2-γ absorption cross section (σ) of currently used photosensitizers. For example, at a peak irradiance of 1.75×10^{11} W cm^{-2}, the light doses required to kill 50% of cells (LD_{50}) of two clinically-approved photosensitizers, Photofrin® with a 2-γ absorption cross section $\sigma = 10$ in Goeppert-

Mayer (GM) units (1 GM = 10^{-50} cm^4 s $photon^{-1}$) at 800 nm and Visudyne® with σ = 51 GM at 900 nm, have been found to be 11,300 J cm^{-2} and 1,700 J cm^{-2}, respectively (147), which are about 2 orders of magnitude higher than those required for 1-γ PDT of the same compounds. Several novel photosensitizers designed explicitly to have much higher σ values (up to about 17,000 GM) have been synthesized (134, 146, 148, 150-152, 235-242) and some of them have been explored for PDT applications, with promising initial results. For example, *in vivo* experiments by Collins *et al.* have demonstrated single blood-vessel closure by 2-γ PDT using a conjugated porphyrin dimer activated by a 300 femtosecond (fs) laser beam at 920 nm (148), while Spangler *et al.* have showed effective treatment up to about 2 cm depth in tumor tissue *in vivo* using a new 2-γ PDT triad (149, 152, 237). These positive initial findings have inspired further investigation of 2-γ PDT, including the present work.

In the present study, we have evaluated the 1-γ and 2-γ PDT efficacy of MPPa in cisplatin-sensitive human cervical (HeLa) and cisplatin-resistant lung (A549) and ovarian (NIH:OVCAR-3) cancer cells *in vitro*. While 1-γ PDT experiments were performed by using a 674 nm laser, 2-γ PDT cytotoxicity of MPPa was activated at the optimal tissue-penetrating NIR wavelength of 800 nm. We have also measured the steady-state fluorescence spectra of MPPa under both 1-γ and 2-γ excitation and determined its fluorescence quantum yield and 2-γ absorption cross section. Finally, we have measured the excited singlet state lifetime of MPPa by performing femtosecond (fs) time-resolved transient absorption spectroscopic measurements.

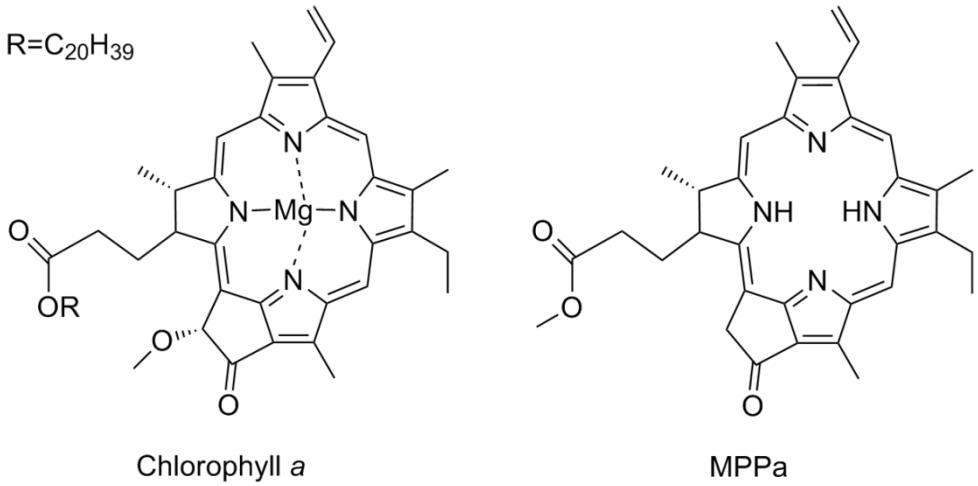

Figure 3-1: Chemical structures of chlorophyll *a* and pyropheophorbide a methyl ester (MPPa).

3.2 Materials and methods

3.2.1 Chemicals and cell lines

Pyropheophorbide-a methyl ester (MPPa; $C_{34}H_{36}N_4O_3$; MW = 548.7 g mol^{-1}; 95% of purity) and Zn(II) phthalocyanine tetrasulfonic acid ($ZnPcS_4$; $C_{32}H_{16}N_8O_{12}S_4Zn$; MW = 898.19 g mol^{-1}) purchased from Frontier Scientific Inc. (Logan, UT, USA) were used without any further purification. A stock solution of 2.5 millimolar (mM) MPPa was made in acetone and then stored in the dark at -20˚C. A stock solution of 5 mM ZnPcS4 was made in ultrapure water with a resistivity of >18 MΩ/cm obtained from a Barnstead Nanopure (Thermo Scientific, Dubuque, IA, USA) water system and stored in the dark at 4˚C. Penicillin-streptomycin antibiotics (PS), minimum essential medium Eagle (MEM), nutrient

mixture F12 Ham Kaighn's modification (F12K), RPMI-1640 Medium, and trypsin-EDTA (0.5 g L^{-1} porcine trypsin and 0.2 g L^{-1} EDTA·4Na in Hank's Balanced Salt Solution with phenol red) were purchased from Sigma-Aldrich (Sigma-Aldrich Canada Ltd., Oakville, ON, Canada) and fetal bovine serum (FBS) from Hyclone Laboratories (Logan, UT, USA). The HeLa (ATCC#: CCL-2™), A549 (ATCC#: CCL-185™) and NIH:OVCAR-3 (ATCC#: HTB-161™) cell lines were obtained from the American Type Culture Collection (ATCC, Manassas, VA, USA). HeLa cells were cultivated in MEM supplemented with 10% FBS, 100 units mL^{-1} penicillin G and 100 μg mL^{-1} streptomycin. A549 cells were cultivated in F12K supplemented with 10% FBS, 100 units mL^{-1} penicillin G and 100 μg mL^{-1} streptomycin. The complete growth medium for NIH:OVCAR-3 cells was RPMI-1640 medium supplemented with 20% FBS, 100 units mL^{-1} penicillin G, 100 μg mL^{-1} streptomycin and 0.01 mg mL^{-1} bovine insulin. The cell culture was kept at 37˚C in a humidified atmosphere containing 5% CO_2.

3.2.2 Subcellular localization

Exponentially growing HeLa, A549 and NIH:OVCAR-3 cells were seeded in 96-well microplates at densities of 3×10^3, 3×10^3 and 4×10^3 cells/well, respectively. After overnight incubation, the cells were incubated with 5 μM MPPa for 24 h in the dark. For the last 30 min of incubation, Hoechst 33342 was added for nuclear staining at a final concentration of 1 μg mL^{-1}. After incubation, the cells were washed twice with phosphate-buffered saline (PBS) and fixed with 4% paraformaldehyde. The images were taken on a Nikon Eclipse

TS100/TS100-F microscope with filter sets of Ex/Em of BP510-560/LP590 nm and BP330-380/LP420 nm for MPPa and Hoechst 33342, respectively.

3.2.3 Laser treatment conditions

One-photon laser irradiation was carried out by using a 674 nm laser with a pulse duration of 120 fs and a pulse repetition rate of 500 Hz. The average irradiance and corresponding peak irradiance were 1 mW cm^{-2} and 1.57×10^{7} W cm^{-2}, respectively. Cells were exposed for different times to vary the total light dose (J cm^{-2}).

Two-photon laser irradiation was carried out by using an 800 nm laser with a pulse duration of 120 fs and a pulse repetition rate of 1 kHz. The peak irradiance was 3.9×10^{10} W cm^{-2}. The laser spot size was ~0.12 cm^2, which illuminated the entire cell monolayer in each of the 384 microplate wells uniformly. Cells were exposed for different periods of time (0 - 5 min) to achieve different light doses (J cm^{-2}).

3.2.4 One-photon PDT treatment

Exponentially growing HeLa, A549 and NIH:OVCAR-3 cells were seeded in 96-well microplates at densities of 5×10^{3}, 5×10^{3} and 7×10^{3} cells/well, respectively. After overnight incubation, cells were incubated with various concentrations of MPPa for 18 h in the dark. Cells were then washed twice with PBS and fresh complete culture medium was added before irradiation. The irradiated cells were then kept in the incubator for 48 h and cell

viability was evaluated by the MTT assay, a widely used colorimetric technique that measures cell viability (see below).

Apoptosis was assessed by Hoechst 33342 staining, for which HeLa cells were seeded in 96-well microplates at a density of 3×10^3 cells/well. After overnight incubation, the cells were incubated with 10 μM MPPa, light-irradiated at 0.04 J cm^{-2} and incubated for 24 h. For the final 30 min of incubation, Hoechst 33342 was added for nuclear staining at a final concentration of 1 μg mL^{-1}. After incubation, the cells were washed twice with PBS and fixed with 4% paraformaldehyde. Images were taken on a Nikon Eclipse TS100/TS100-F microscope with a filter set of Ex/Em of BP330-380/LP420 nm.

3.2.5 Two-photon PDT treatment

Cells were grown and incubated in MPPa as for the 1-γ treatments. Photocytotoxicity was measured by using the MTT assay at 48 or 72 h post treatment.

The cellular morphology changes were observed by a light microscope. HeLa cells were incubated with 20 μM MPPa for 18 h in the dark, then washed twice with PBS and irradiated with 800 nm, 120 fs laser at a peak irradiance of 3.9×10^{10} W cm^{-2}. The images were taken 24 h later on a Nikon Eclipse TS100 microscope.

3.2.6 MTT cell viability assay

Cell viability was evaluated by the standard MTT assay using a commercial kit (V-13154, Invitrogen, Life Technologies Inc., Burlington, ON, CA). The stock solution of 12 mM MTT (3-(4,5-dimethylthiazol-2-yl)-2,5-diphenyltetrazolium bromide; MW = 414 g mol^{-1}) was prepared by adding 1 mL of sterile PBS to one 5 mg vial of MTT. The SDS-HCl solution was prepared by adding 10 mL of 0.01 M HCl to 1 mg of SDS (sodium dodecyl sulfate; MW = 288 g mol^{-1}).

At the end of incubation period, the medium was replaced with 100 (96-well plates) or 30 (384-well plates) μL of fresh phenol red-free complete culture medium and 10 (96-well plates) or 3 (384-well plates) μL of the MTT solution (5 mg mL^{-1}). After 2-4 h incubation, 100 (96-well plates) or 30 (384-well plates) μL of SDS-HCl was added to each well. After 4-18 h incubation, the absorbance at 570 nm was measured with a Multiskan GO microplate spectrophotometer (Thermo Scientific, Mississauga, ON, Canada). Cell viability was expressed as the percentage of the control cells, and the data are presented as means of at least three wells ± S.D (standard deviation).

3.2.7 Steady-state absorption and fluorescence spectroscopic measurements

Steady-state absorption spectra of MPPa were measured on a DU 530 UV/Vis spectrophotometer (Beckman Coulter, Fullerton, CA, USA). Samples were prepared in 5 mm

quartz cuvettes. One-photon induced steady-state fluorescence spectra of MPPa and ZnPcS4 were measured on a fluorescence spectrophotometer (Varian Cary Eclipse, Palo Alto, CA, USA). Two-photon induced steady-state fluorescence spectra were measured on a homemade fluorescence spectrophotometer (see Chapter 2). Samples were prepared in 5 mm quartz cuvettes. All measurements were performed at room temperature.

3.2.7.1 Fluorescence quantum yield

The fluorescence quantum yield of MPPa (Φ_F) can be determined using Equation (2-8). The 1-γ absorbance was measured at 400 nm. The 1-γ fluorescence was excited at 400 nm and measured on a fluorescence spectrophotometer. The fluorescence quantum yield of the reference (Zn(II) phthalocyanine tetrasulfonic acid; $ZnPcS_4$) is $\Phi_F = 0.104$ in methanol at 400 nm (243).□

3.2.7.2 Two-photon excitation cross section

The 2-γ excitation cross section (σ) of MPPa can be determined using Equation (2-7). The 2-γ induced fluorescence emissions of MPPa and the reference ($ZnPcS_4$) were excited at 800 nm and measured with a homemade fluorescence spectrophotometer (see Chapter 2) at various excitation powers. The concentration of both MPPa and $ZnPcS_4$ was fixed at 50 μM. For $ZnPcS_4$ in methanol, the fluorescence quantum yield is $\Phi_F = 0.104$ and the 2-γ absorption cross section is $\sigma = 28.6$ GM at 800 nm (243).

3.2.8 Femtosecond time-resolved transient absorption spectroscopic measurements

The experimental setup for femtosecond time-resolved transient absorption spectroscopy has been described in Chapter 2. The pump and probe wavelengths were fixed at 667 and 475 nm, respectively. Samples were prepared in 5 mm quartz cuvettes. All measurements were performed at room temperature.

3.2.9 Data analysis

3.2.9.1 Dose-response curve analysis

The drug- and light-dose response curves were fitted with a sigmoidal logistic function ($y = \frac{A_1 - A_2}{1+(\frac{x}{x_0})^p} + A_2$, where A_1 is the top asymptote, A_2 is the bottom asymptote, x_0 is the point of inflection, and p can be loosely described as the parameter that affects the slope of the area about the inflection point) by using Origin software (OriginLab, Northampton, MA, USA). The drug concentration (IC_{50}) or light dose (LD_{50}) required to produce a 50% cell killing effect were determined on the basis of the fitted data.

3.2.9.2 Transient absorption and fluorescence decay kinetics analysis

In order to determine the lifetimes from the transient absorption decay kinetic traces, we fitted the curves with multi-exponential functions using the Scientist software (MicroMath Inc., Saint Louis, MO, USA).

3.3 Results and discussion

3.3.1 Subcellular localization of MPPa

Understanding of the intracellular uptake and subcellular distribution of a photosensitizer is an important step for evaluating the therapeutic efficacy. Figure 3-2 shows the subcellular localization of MPPa in the 3 tumor cell lines. The cells were incubated with 5 μM MPPa for 24 h and the nuclei were stained with Hoechst 33342. Marked differences were observed in the subcellular localization of MPPa between the cell lines. Thus, strong red MPPa fluorescence was observed throughout the cytoplasm in HeLa and A549 cells (Figure 3-2, upper and middle panels), while bright red spots suggestive of spherical structures such as lysosomes were observed in the NIH:OVCAR-3 cells (Figure 3-2, lower panel).

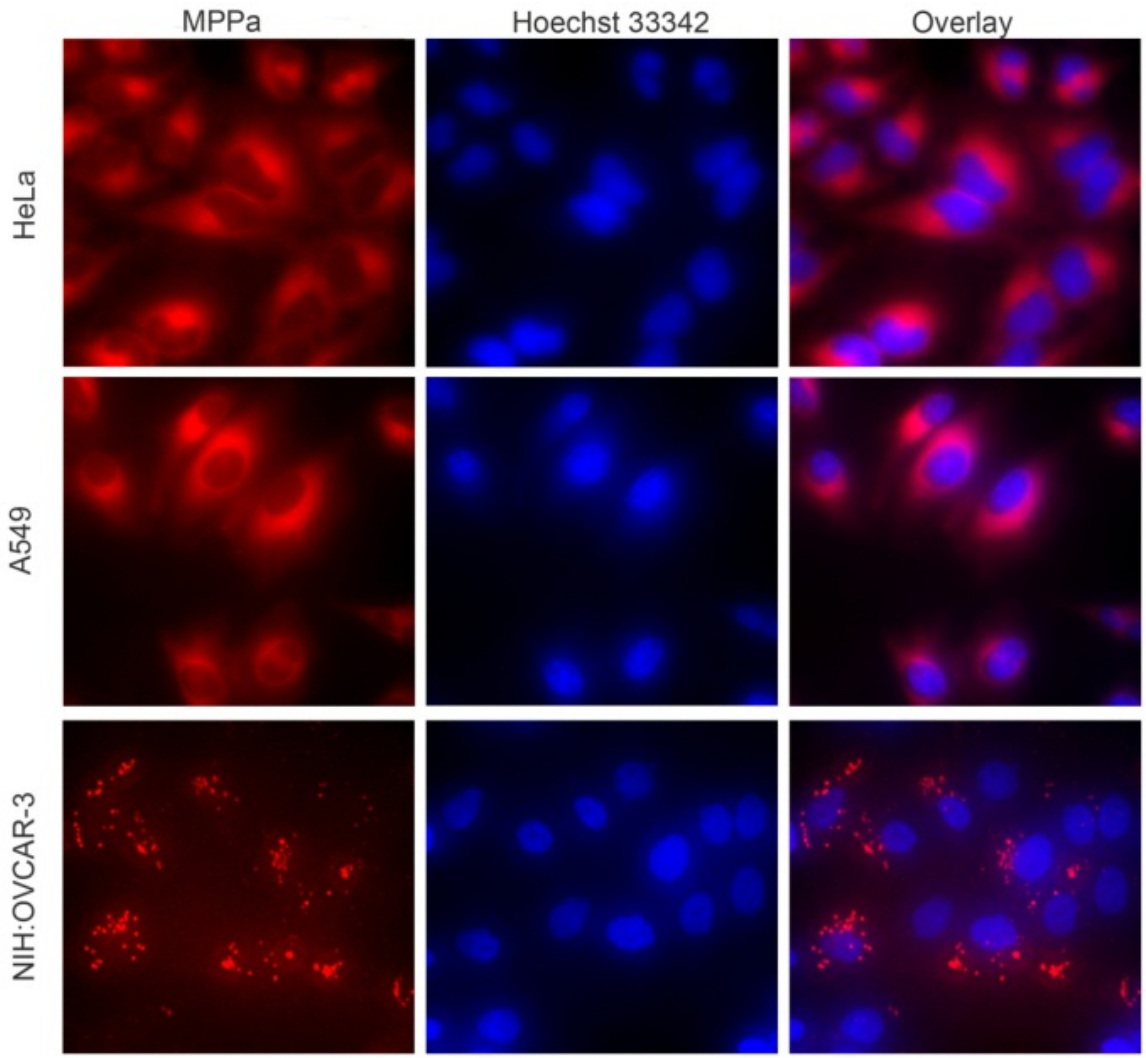

Figure 3-2: Subcellular localization of MPPa in HeLa, A549 and NIH:OVCAR-3 cells. The cells were incubated with 5 μM MPPa for 24 h. For the final 30 min of incubation, Hoechst 33342 was added for nuclear staining. After incubation, the cells were washed twice with PBS and fixed with 4% paraformaldehyde. The images were taken on a Nikon Eclipse TS100/TS100-F microscope. MPPa is shown in red (λ_{ex} = 510-560 nm; λ_{em} > 590 nm). Hoechst 33342 is shown in blue (λ_{ex} = 330-380 nm; λ_{em} > 420 nm).

The subcellular localization of MPPa in other cell types has been reported by other groups. Matroule *et al.* (227) found that MPPa mainly accumulated at the cytoplasmic membrane, in lysosomes and in the endoplasmic reticulum in HCT-116 colon cancer cells. A different distribution was observed in nasopharyngeal (HONE-1), lung (NCI-h446) and ovarian (COC1/DDP) carcinoma cells, with co-localization of MPPa with a mitochondria-specific probe (Mitotracker) (229, 230, 233). Recently, Guelluy *et al.* (129) demonstrated that the co-localization of MPPa with the mitochondria in HCT-116 cells could only be observed when its concentration in the culture medium was ≥ 4 μM, which was much higher than 0.25 μM used by Matroule *et al.* (227). In the present study, the three cell lines were treated identically (with 5 μM MPPa), and markedly different MPPa distributions were observed, supporting the general conclusion that the subcellular localization of MPPa is unusually dependent on cell type. The reasons for this behavior have not been determined. However, since the PDT sensitivity is known to depend strongly on the subcellular localization of the photosensitizer, due to the fact that the light-generated cytotoxic singlet oxygen ($^1O_2$) generated during PDT has a very short lifetime (<~ μs) and hence diffusion length (<~100 nm) (68), this cell-type dependence clearly merits further investigation.

3.3.2 One-photon activated photocytotoxicity of MPPa

The MTT cell viability assay has been performed to evaluate the 1-γ activated PDT efficacy of MPPa at 674 nm and the results are shown in Figure 3-3. The dark control without irradiation showed that MPPa had slight dark cytotoxicity at high concentration. The

photocytotoxicity of MPPa was light dose dependent, as expected. Thus, at a very low light dose (LD) of 0.03 J cm^{-2}, the IC_{50} was 7.2 ± 0.4, 6.5 ± 0.7 and 6.8 ± 0.6 μM in HeLa, A549 and NIH:OVCAR-3 cells, respectively (Table 3-1). At 0.06 J cm^{-2}, the corresponding values were 5.3 ± 0.3, 3.4 ± 0.3 and 3.6 ± 0.4 μM. Thus, the IC_{50} values in cisplatin-resistant A549 and NIH:OVCAR-3 cells were comparable with those in cisplatin-sensitive HeLa cells. In general, cancer cells resistant to chemotherapy do not show cross-resistance to PDT treatment (162). Our observation of high sensitivity of cisplatin-resistant lung and ovarian cancer cells to MPPa-mediated PDT is therefore likely due to different mechanisms of action between these two modalities (159, 162). The present results suggest that MPPa-mediated PDT may be developed as an effective treatment for cancers that are resistant to this widely used chemotherapeutic drug. Interestingly, the photocytotoxicity was not significantly altered by the more localized distribution of MPPa in NIH:OVCAR-3 cells than in HeLa and A549 cells. This indicates that the photocytotoxicity (IC_{50}) is not only dependent on the localization of MPPa but also on the light dose and whether the drug is activated through one- or two-photon excitation (see further results in Section 3.3.3).

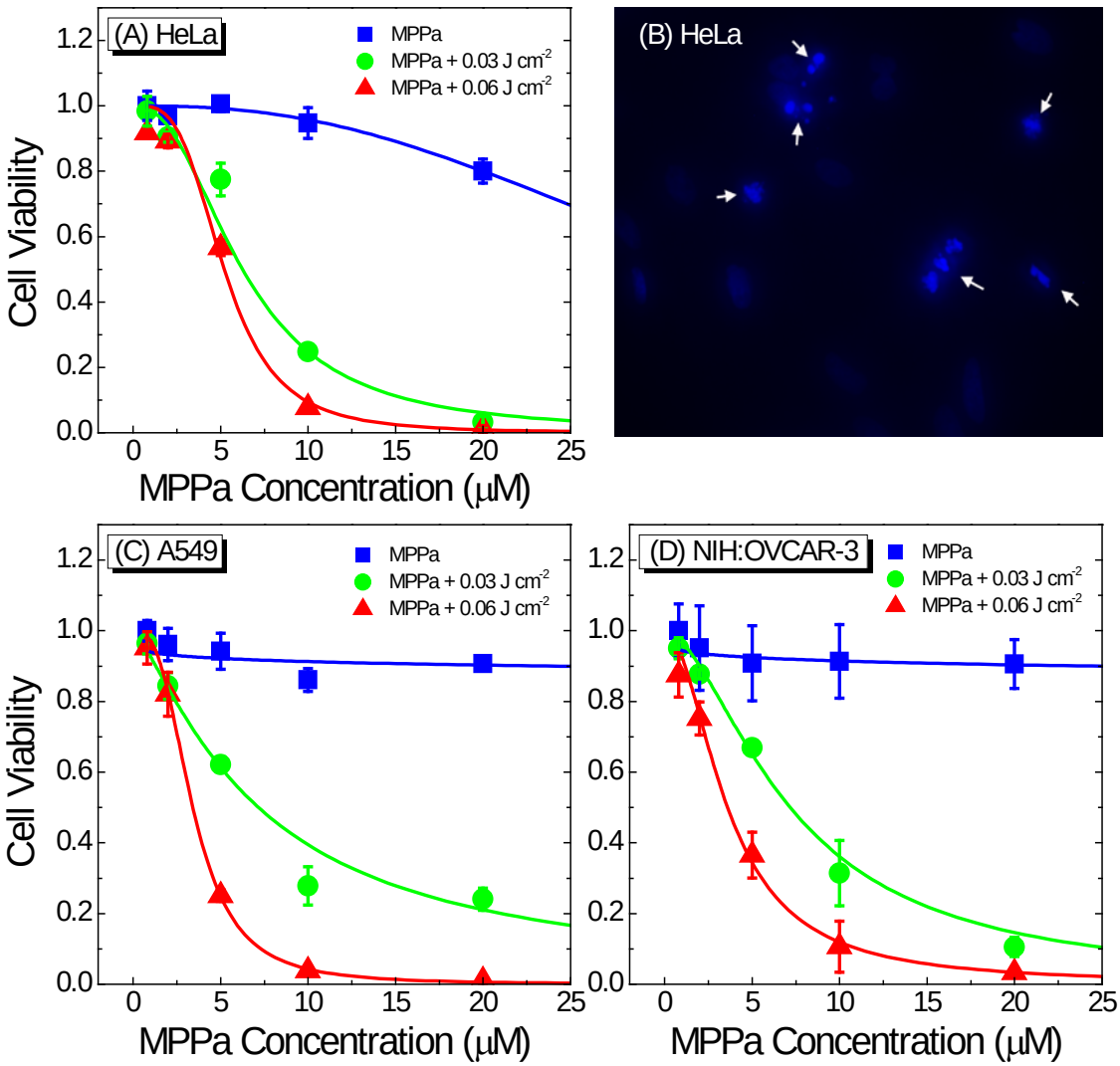

Figure 3-3: Drug-dose response curves for cell viability of (A) HeLa, (C) A549 and (D) NIH:OVCAR-3 cells treated by 1-γ activated PDT of MPPa. Cells were incubated with various concentrations of MPPa for 18 h and then irradiated at 674 nm. Cell viability was evaluated by using the standard MTT assay 48 h after laser irradiation. The solid lines are best fits to the experimental data using a logistic function in Origin software. (B) Apoptosis analyzed by Hoechst 33342 staining. HeLa cells were incubated with 10 μM MPPa, light-irradiated at 0.04 Jcm^{-2} and incubated for 24 h. Arrows indicate apoptotic cells.

Table 3-1: *In vitro* 1-γ IC_{50}, 2-γ IC_{50} and 2-γ LD_{50} of MPPa calculated from Figure 3-3(A, C and D) and Figure 3-4.

Cell line		HeLa			A549			NIH:OVCAR-3		
1-γ Excitation	Light Dose (J cm^{-2})	0	0.03	0.06	0	0.03	0.06	0	0.03	0.06
	IC_{50} (μM)	> 20	7.2 ± 0.4	5.3 ± 0.3	> 50	6.5 ± 0.7	3.4 ± 0.3	> 30	6.8 ± 0.6	3.6 ± 0.4
2-γ Excitation	Light Dose (J cm^{-2})	0	886		0	886		0	886	
	IC_{50} (μM)	> 20	4.1 ± 0.3		> 50	9.6 ± 1.0		> 30	1.6 ± 0.3	
	MPPa Con. (μM)	0	10		0	10		0	10	
	LD_{50}* (J cm^{-2})	-	576 ± 13		-	478 ± 18		-	360 ± 26	

* Normalized to the group treated with 10 μM MPPa alone.

The 1-γ photocytotoxicity of MPPa has previously been studied in a number of cell lines, including colon (HCT-116), lung (NCI-h446), nasopharyngeal (HONE-1), prostate (PC-3M), ovarian (COC1/DDP) and breast carcinomas (MDA-MB-231, MDA-MB-435, and MCF-7) (129, 227-234), and has been shown to induce apoptotic cell death. In order to determine the mode of cell death in the present study, HeLa cells were incubated with 10 μM

MPPa, irradiated at a light dose of 0.04 J cm^{-2} and stained with Hoechst 33342 at 24 h after laser irradiation. Typical characteristics of apoptotic cells, including nuclear condensation and fragmentation, were clearly seen (Figure 3-3B).

Table 3-2: Comparison of 1-γ PD_{50} (light-drug product required to produce a 50% cell killing effect) of MPPa with values calculated from the literature.

Cell line	**MPPa Con. (μM)**	**Light Dose (J cm^{-2})**	**PD_{50} (μM J cm^{-2})**	**Reference**
A549	0 - 20	0 - 0.06	0.20 ± 0.01	This work
COC1/DDP	0 - 4	0 - 8	0.5 - 0.8	(227)
HCT-116	6	0-9.6	15	(222)
	0 - 5	6.6	26	(123)
HeLa	0 - 20	0 - 0.06	0.27 ± 0.07	This work
HONE-1	0 - 2	0 - 1	0.2 - 0.25	(224)
MDA-MB-231	0 - 4	0 - 8	14 - 20	(228)
MDA-MB-435			28	
MCF-7			32	
NCI-h446	0 - 6	0 - 6	1.9 - 5.6	(223)
NIH:OVCAR-3	0 - 20	0 - 0.06	0.21 ± 0.01	This work
PC-3M	0 - 4	0 - 8	3.2 - 7.0	(225)
	2	0 - 6	12	(226)

We note that the light doses of 0.03-0.06 J cm^{-2} used here are much lower than the range ~0.1-10 J cm^{-2} used in previous studies (129, 227-234). It is known that the light-drug product required to produce a 50% cell killing effect (PD_{50}) can be reduced by increasing the

extracellular concentration of MPPa (229). Table 3-2 compares the 1-γ PD_{50} of MPPa in different cancer cell lines. In the present study, the PD_{50} values are 0.27 ± 0.07, 0.20 ± 0.01 and 0.21 ± 0.01 in HeLa, A549 and NIH:OVCAR-3 cancer cells, respectively. These are much lower than the range of 1.9-32 reported for HCT-116 colon, MDA-MB-231, MDA-MB-435 and MCF-7 breast, NCI-h446 lung and PC-3M prostate cancer cells (129, 229-232, 234), but comparable to the results of Tan *et al.* in COC1/DDP ovarian (233) and Li *et al.* in HONE-1 nasopharyngeal cancer cells (230), confirming that the MPPa-mediated PDT sensitivity varies greatly among cancer cell lines. More critically, we have used monochromatic 674 nm light, which matches an absorption peak of MPPa (insert in Figure 3-7). This contrasts with previous studies (129, 227, 229, 230) that used conventional broad-band light sources, so that there was only partial overlap with the MPPa absorption spectrum. The LED (light-emitting diode) used by Tan *et al.* emitted at 630 nm (233), far from the MPPa absorption maximum. Although Tian *et al.* (231, 232, 234) used 670 ± 11 nm light, their PD_{50} values were much higher than our results. As shown in the insert in Figure 3-7, the absorption spectrum of MPPa in the cell culture medium has a high degree of overlap with the Gaussian (FWHM = 11 nm) emission profiles of red light centered at both 670 and 674 nm. The difference between the PD_{50} values obtained here with those of Tian *et al*. is likely due to the different cell lines used. The fs pulsed laser used in the present study might also play an important role in reducing the PD_{50}. Grecco *et al.* compared the *in vitro* and *in vivo* photodynamic response to a fs pulsed laser with a CW laser under the same average power and light dose conditions and found that the fs laser was about twice as effective as the CW laser (244). Therefore, our observations of low PD_{50} values suggest that 1-γ PDT of

MPPa activated by a fs laser could be developed as an effective treatment for selected cancers.

3.3.3 Two-photon activated photocytotoxicity of MPPa

We also investigated the photodynamic activity of MPPa under 2-γ excitation with ~120 fs pulse of 800 nm light at a repetition rate of 1 kHz. Tightly focused laser beams are commonly used in 2-γ studies, due to the requirement of extremely high peak irradiances for excitation, so that it has been found to be difficult to quantify the photocytotoxic effect by the same colorimetric assays normally used for 1-γ PDT experiments, because of the need to irradiate the cells uniformly while using a diffraction-limited focal spot. The first quantitative *in vitro* evaluation of 2-γ PDT was performed by Khurana *et al.* (147), who developed a confocal laser scanning microscope-based technique for both light delivery and response measurements. In the present study, we have used a 2.54 cm diameter biconvex lens (f = 125 mm) to focus the laser beam and placed an aperture above the microplate to produce a quasi-uniform distribution at the cell plane. In order to evaluate the cell response using the standard MTT assay, we have replaced the 96-well microplates with 384-well microplates, which have a well area (0.11 cm^2) that is slightly smaller than the area of the laser spot at the cell plane (0.12 cm^2).

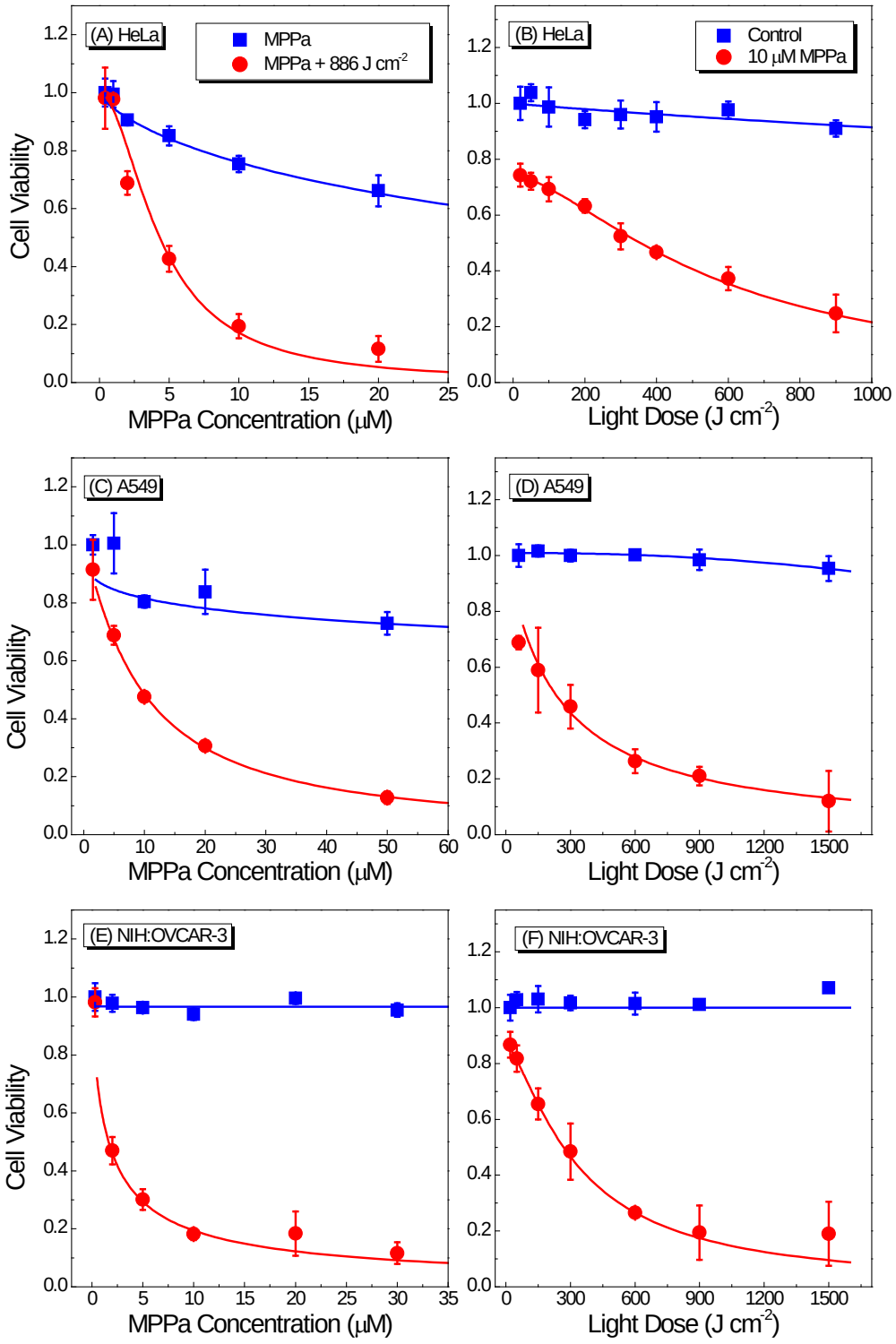
(A) HeLa
MPPa
MPPa + 886 J cm-2
Cell Viability
MPPa Concentration (μM)
(B) HeLa
Control
10 μM MPPa
Light Dose (J cm-2)
(C) A549
MPPa Concentration (μM)
(D) A549
Light Dose (J cm-2)
(E) NIH:OVCAR-3
MPPa Concentration (μM)
(F) NIH:OVCAR-3
Light Dose (J cm-2)

Figure 3-4: Drug- and light-dose response curves for cell viability of (A and B) HeLa, (C and D) A549 and (E and F) NIH:OVCAR-3 cells treated by 2-γ activated PDT of MPPa. Cells were incubated with various concentrations of MPPa for 18 h and then irradiated with 800 nm 120 fs laser at an average power of 600 mW and a peak irradiance of 3.9×10^{10} W cm^{-2}. Cell viability was evaluated by using the standard MTT assay 48 h after laser irradiation. The solid lines are best fits to the experimental data using a logistic function in Origin software.

As shown in Figure 3-4 and Figure 3-5, MPPa can be effectively activated under these conditions. Figure 3-4 shows the drug- and light-dose response of 2-γ activated photocytotoxicity of MPPa, and the IC_{50} and LD_{50} values are summarized in Table 3-1. At a light dose of 886 J cm^{-2}, the IC_{50} values of MPPa were measured to be 4.1 ± 0.3, 9.6 ± 1.0 and 1.6 ± 0.3 μM in HeLa, A549 and NIH:OVCAR-3 cells, respectively. The corresponding LD_{50} for 10 μM MPPa were 576 ± 13, 478 ± 18 and 360 ± 16 J cm^{-2}, i.e., approximately 3~5 times lower than the published value of 1,700 J cm^{-2} for Visudyne® and 20-30 times lower than that of Photofrin® (11,300 J cm^{-2}) (147). These LD_{50} values of MPPa were about half of the LD_{50} of the conjugated porphyrin dimer (σ = 16,000 GM at 920 nm) used by Collins *et al.* for *in vivo* blood vessel closure (148), which was ~1,020 J cm^{-2} (i.e., ~60% of the LD_{50} of Visudyne® under identical experiment conditions) (150).

Since the light dose required for significant photodynamic killing by 2-γ excitation is much higher than that normally used in 1-γ PDT, it is very important to investigate whether any direct photodamage has been caused by laser irradiation in the absence of the photosensitizer. It was shown by Karotki *et al.* (144), for example, in vascular endothelial cells that the threshold peak irradiance for direct photomechanical damage from fs laser

irradiation is about 8×10^{11} W cm^{-2}, while Samkoe *et al.* (146) showed that a 780 nm, 100 fs laser beam with a peak irradiance of 3.7×10^{11} W cm^{-2} and a fluence of 1.1×10^{8} J cm^{-2} caused no significant photomechanical damage to the chicken chorioallantoic membrane. The peak irradiance (I_{peak}) can be calculated by:

$$I_{average} = \frac{P_{average}}{A}, \tag{3-1}$$

$$I_{peak} = \sqrt{\frac{ln2}{\pi}} \cdot \frac{2}{\tau f} \cdot I_{average}, \tag{3-2}$$

where $P_{average}$ is the average laser power, A is the area of the laser spot at the cell plane, τ is the pulse duration (FWHM; full width at half maximum) and f is the pulse repetition rate. The highest average laser power of 600 mW used in the present study corresponds to I_{peak} = 3.9×10^{10} W cm^{-2}, which is about one order of magnitude smaller than the published threshold value (144), although this may be somewhat cell-type dependent. The corresponding average irradiance is 5 W cm^{-2}, about six orders of magnitude lower than those (~10^{6} W cm^{-2}) used by Karotki *et al.* (144) and Khurana *et al.* (147). As shown in Figure 3-4, laser irradiation alone caused no measurable cell death in the absence of MPPa. The light microscope images also confirmed the absence of observable direct damage at a light dose of 886 J cm^{-2} in the absence of MPPa (Figure 3-5B). In contrast, morphological changes typical of apoptotic cell death were observed at light doses of 222 and 443 J cm^{-2} in the presence of MPPa (Figure 3-5E and F).

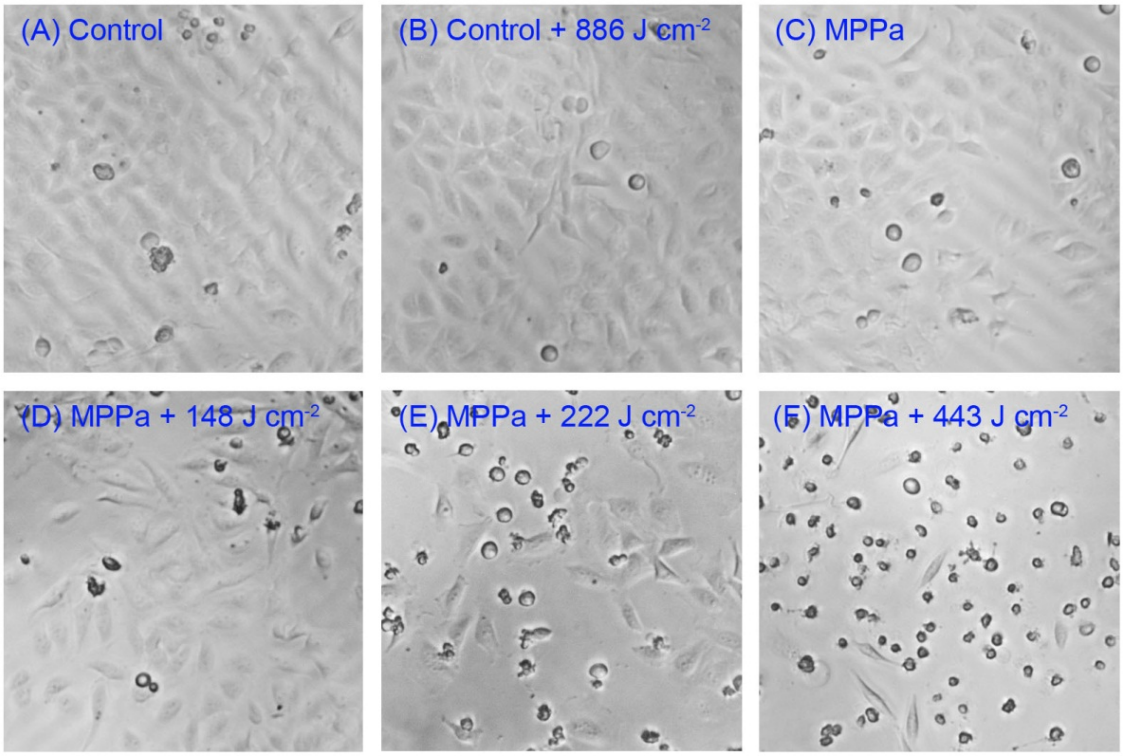

Figure 3-5: 2-γ PDT of MPPa induced changes in HeLa cell morphology. Cells were incubated with 20 μM MPPa for 18 h and then irradiated by 800 nm, 120 fs laser with a peak irradiance of 3.9×10^{10} W cm^{-2} and light doses in the range 0-886 J cm^{-2}. The images were taken on a Nikon Eclipse TS100 microscope 24 h after treatment.

3.3.4 Power dependence of one- and two-photon PDT

It has been pointed out by Karotki *et al.* (144) that 1-γ excitation could also contribute to the photocytotoxicity observed in 2-γ PDT treatments, due to the long-wavelength "tail" of the 1-γ absorption spectrum. As shown in Figure 3-7, however, MPPa has no detectable absorption at 800 nm (within the noise level), so there should be minimal cell killing as a result of 1-γ activation of MPPa at this wavelength. Moreover, we have investigated the

power dependence of the PDT efficiency of MPPa activated at 674 and 800 nm: 1-γ absorption should have a linear dependence on light intensity, while 2-γ absorption has a quadratic dependence. According to Khurana *et al.* (141), for an *n*-photon process, the irradiation time required to kill 50% of the cells (t_{50}) and the laser power (P) should satisfy the following equations:

$$t_{50} \propto {I_{peak}}^{-n} = (\sqrt{\frac{ln2}{\pi}} \cdot \frac{2}{\tau f} \cdot \frac{P}{A})^{-n}, \quad (3\text{-}3)$$

i.e.

$$\log(t_{50}) = n \cdot \log(P^{-1}) + constant, \quad (3\text{-}4)$$

In order to determine $\log(t_{50})$, the cell viability was plotted as a function of the laser irradiation time (Figure 3-6A and C) at various laser powers and fitted by non-linear regression with variable Hill slope using Origin software. The resultant $\log(t_{50})$ values were then plotted against $\log(P^{-1})$ and fitted to Equation (3-4), as shown in Figure 3-6B and D. The gradient of the linear fit (Figure 3-6B) was 1.10 ± 0.06, confirming 1-γ activation of MPPa at 674 nm excitation. The corresponding gradient for 800 nm fs-pulsed laser PDT treatment (Figure 3-6D) was 2.04 ± 0.17, confirming 2-γ activation.

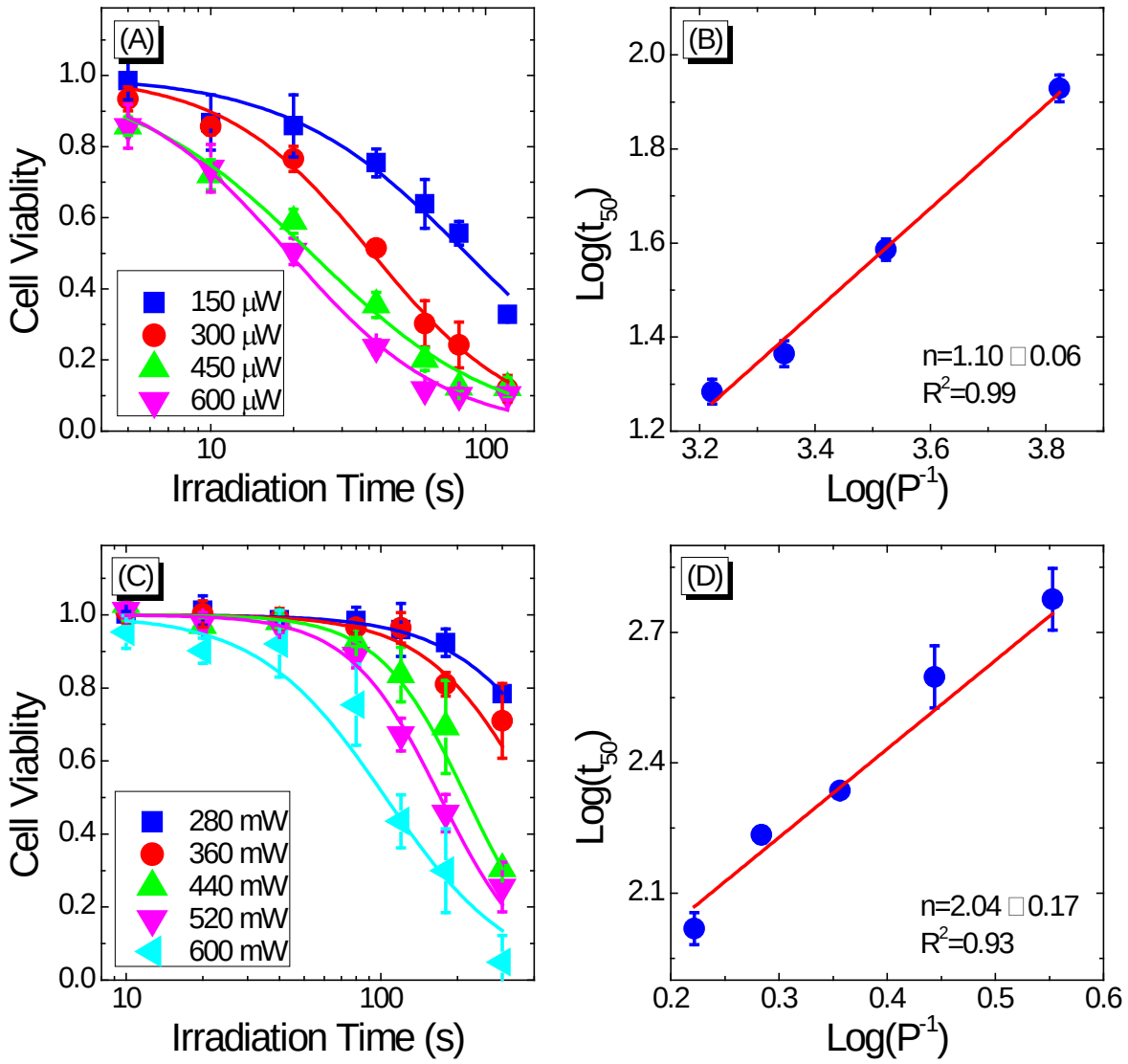

Figure 3-6: Power dependence of 1- and 2-γ PDT efficiency of MPPa. (A and B) 1- γ PDT in NIH:OVCAR-3 cells: 5μM MPPa for 18 h, 674 nm, 120 fs laser at various powers. MTT assay at 48 h after treatment: means ± S.D. of 3 replicates. The irradiation time required to kill 50% of the cells (t_{50}) was determined for each laser power (150, 300, 450 and 600 μW) and log(t_{50}) was plotted against log(P^{-1}). The slope, n = 1.10 ± 0.06, confirming 1-γ activation (141). (C and D) 2- γ PDT efficiency of MPPa in HeLa cells: 10 μM MPPa for 18 h, 800 nm 120 fs laser at various powers. MTT at 72 h after treatment: means ± S.D. of 3 replicates. The t_{50} was determined for each laser power (280, 360, 440, 520 and 600 mW) and log(t_{50}) was plotted against log(P^{-1}). The gradient of the linear fit to these points is 2.04 ± 0.17, confirming 2-γ activation as described in Ref. (141).

3.3.5 Steady-state absorption spectra of MPPa

We have measured the UV-Vis absorption spectra of MPPa in acetone and the cell culture medium (phenol-red free minimum essential medium (MEM)) (Figure 3-7). MPPa has two absorption peaks at 408 and 667 nm in acetone consistent with the values reported in the literature (229, 245). In MEM, the peaks are shifted slightly to 400 and 672 nm.

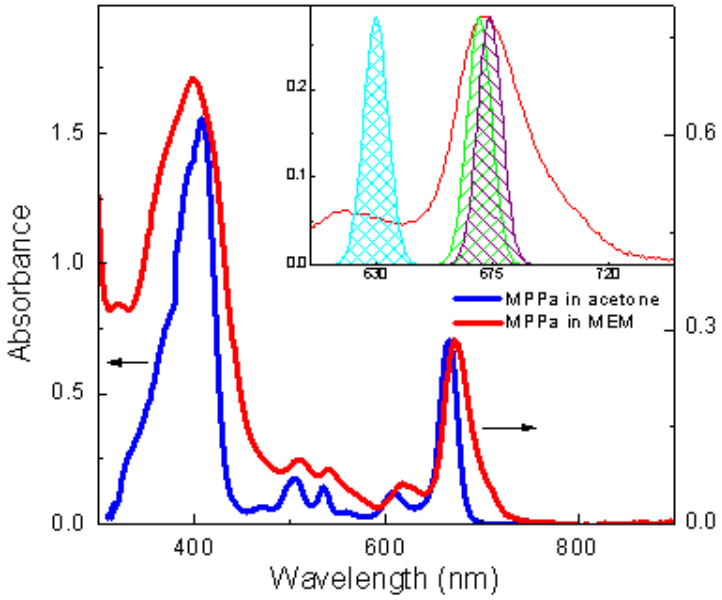

Figure 3-7: UV-Vis absorption spectra of 25 μM MPPa in acetone (blue line) and phenol-red free minimum essential medium (MEM: red line). The insert compares the absorption spectrum in MEM with the Gaussian (FWHM = 11 nm) emission profiles of red light centered at 630, 670 and 674 nm, respectively.

3.3.6 Fluorescence quantum yield of MPPa in methanol

We have determined the fluorescence quantum yield (Φ_F) of MPPa in methanol, using Zn(II) phthalocyanine tetrasulfonic acid ($ZnPcS_4$) as a reference. Figure 3-8A and C show the

fluorescence spectra of various concentrations of MPPa and $ZnPcS_4$ in methanol. MPPa has an emission maximum of 672 nm and a small shoulder peak around 718 nm. The fluorescence peaks of $ZnPcS_4$ are at 678 and 742 nm. Figure 3-8B and D show the integrated fluorescence intensities of MPPa and $ZnPcS_4$ as a function of absorbance at 400 nm. The R^2 coefficients of linear fits to the data are 0.987 and 0.996 for MPPa and $ZnPcS_4$, respectively. Using Equation (2-8), the Φ_F value of MPPa has been determined to be 0.23 ± 0.02, which is very close to the published value of 0.21 in dimethylformamide (246).

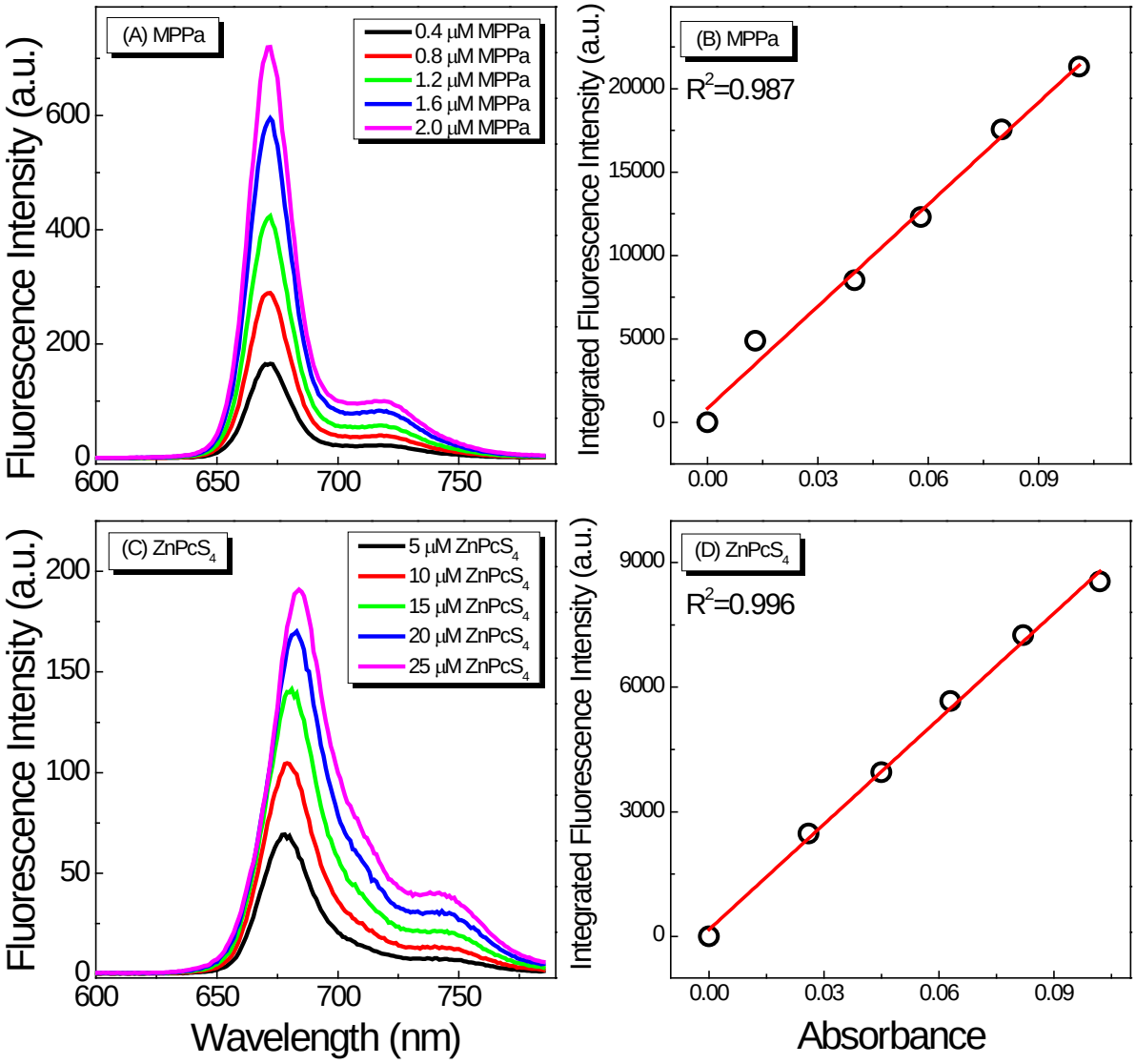

Figure 3-8: 1-γ Fluorescence spectra of (A) MPPa and (C) $ZnPcS_4$ at various concentrations excited at 400 nm. (B) and (D) The integrated fluorescence intensities of MPPa and ZnPcS4 in methanol as a function of optical absorbance at 400 nm. The R^2 coefficient of the linear fits was 0.987 and 0.996 for MPPa and ZnPcS4, respectively.

3.3.7 Two-photon absorption cross section of MPPa in methanol at 800 nm

Figure 3-9 shows the 2-γ induced fluorescence spectra of MPPa and $ZnPcS_4$ in methanol at various excitation powers at 800 nm. As shown in Chapter 2, the 2-γ induced fluorescence spectra of both MPPa and $ZnPcS_4$ are identical to those induced by 1-γ excitation. Therefore, the two-photon absorption cross section of MPPa can be determined by using Equation (2-7). The inserts show $\log(F_{max})$ *versus* log(Power), where F_{max} is the 2-γ induced fluorescence intensity at 672 nm for MPPa and at 684 nm for $ZnPcS_4$. The linear fits yield slopes of 2.06 ± 0.06 and 1.82 ± 0.03 for MPPa and $ZnPcS_4$, respectively, confirming 2-γ excitation. Using Equation (2-7), we obtain $\sigma = 3.5 \pm 0.3$ GM for MPPa in methanol at 800 nm, which is consistent with the value of 3.1 GM for Photofrin® in methanol (243). Although the value of σ for MPPa is lower by a factor of about 5,000 than the reported $\sigma = 16{,}000$ GM for the conjugated porphyrin dimer (148), our measured 2-γ LD_{50} of 10 μM MPPa is about half of the 2-γ LD_{50} of the dimer in SK-OV-3 cells (150). In fact, the 2-γ LD_{50} of the dimer has been found to be ~60% of that of another currently used 1-γ photosensitizer Visudyne® ($\sigma = 51$ GM) under identical experiment conditions, in spite of the 300-fold large difference in σ (150). This confirms the importance of other factors such as the intracellular concentration/localization of the photosensitizer and the mechanisms of action (types of the ROS and their yields), in determining the overall photodynamic efficiency (52).

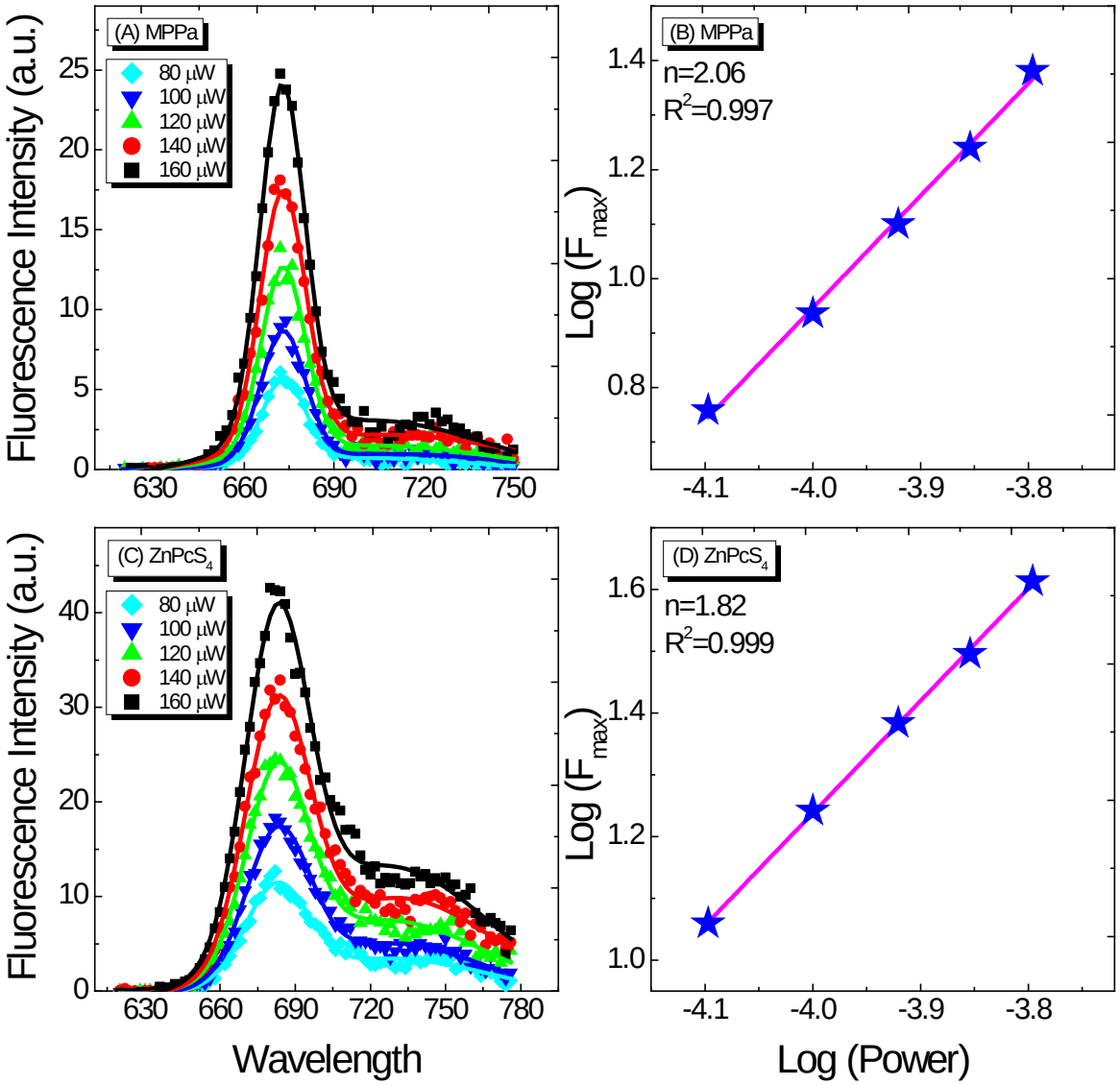

Figure 3-9: 2-γ Induced fluorescence spectra of (A) MPPa and (C) $ZnPcS_4$ in methanol at various excitation powers, for 800 nm excitation. The solid lines are the best Gaussian fits. (B) and (D) Show plots of log(F_{max}) versus log(Power), where F_{max} is the 2-γ induced fluorescence intensity at 672 nm for MPPa and at 684 nm for $ZnPcS_4$. The solid lines are the best linear fits, yielding slopes of 2.06 ± 0.06 and 1.82 ± 0.03 for MPPa and $ZnPcS_4$, respectively, confirming two-photon excitation.

3.3.8 Femtosecond time-resolved transient absorption spectroscopic results

We have obtained fs time-resolved transient absorption decay kinetics of MPPa in water and ethanol (Figure 3-10). The excitation and probe wavelengths were 667 and 475 nm, respectively. The decay kinetics in water could be fitted adequately with a multi-exponential function yielding two short decaying lifetimes of 0.31 ± 0.04 and 11.4 ± 1.2 ps and a much longer one on the scale of nanoseconds. In ethanol, the signal was found to be much stronger than that observed in water at the same probe wavelength. The transient absorption intensity decreased slowly with increasing pump-probe delay time. The decaying lifetime was found to be 12.0 ± 0.6 ns. It is known that pheophorbides aggregate in aqueous solutions (245). Therefore, the shorter lifetimes of 0.31 and 11.4 ps observed in water are likely the excited-state lifetimes of the aggregates while the longer lifetime corresponds to the monomeric form of MPPa. In ethanol, MPPa has been found to be monomeric up to 50 μM (245). The lifetime of 12.0 ns observed in ethanol, which is in good agreement with the fluorescence lifetime of 6.0 ns inside HCT-116 cells (129), can thus be assigned to the excited singlet state lifetime of MPPa monomers.

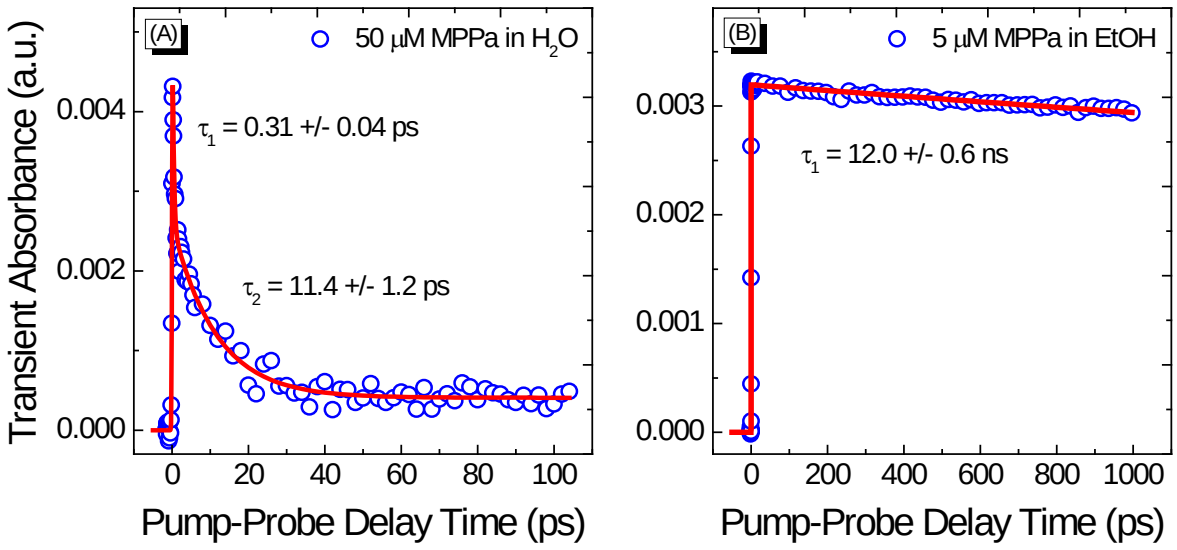

Figure 3-10: Femtosecond time-resolved pump-probe transient absorption decay kinetics of (A) 50 μM MPPa in water and (B) 5 μM MPPa in ethanol. The blue open circles are the experimental data and the red solid lines are best fits to the experimental data. The pump and probe wavelengths were 667 and 475 nm, respectively. The pump powers were 50 and 5 μW for MPPa in water and ethanol, respectively.

It has been suggested that singlet oxygen ($^1O_2$) is not the only ROS responsible for cell killing following MPPa-mediated PDT treatment (129, 228). Generation of ROS by MPPa has previously been measured indirectly by using electron spin resonance (ESR) (129, 245). The involvement of hydroxyl radical ($^{\cdot}OH$) has been confirmed in those studies, although there are some discrepancies with regard to the relative contribution of each species. Those findings suggest that MPPa can act as both a Type I and Type II photosensitizer. While a Type II reaction mainly takes place in the excited triplet state of a photosensitizer ($^3PS^*$) due to spin selection rules, a Type I reaction may occur in the excited singlet state of the photosensitizer ($^1PS^*$) as well as $^3PS^*$. In the case of MPPa, $^{\cdot}OH$ has been suggested to be a secondary product of superoxide anion radicals ($O_2^{\cdot-}$) generated from one-electron reduction

of molecular oxygen by the excited singlet state of MPPa (^{1}MPPa*) (129, 245). However, to the best of our knowledge, no direct transient absorption spectroscopic detection of $O_2^{-\cdot}$ has been reported. Although $O_2^{-\cdot}$ has an absorption band in the UV range (247), most photosensitizers also have very strong absorption in this wavelength range making direct spectroscopic detection of $O_2^{-\cdot}$ extremely difficult. In the present study, we have obtained for the first time the fs time-resolved transient absorption decay kinetic traces of MPPa in water and ethanol. Our observation of an excited singlet state lifetime of 12.0 ns for MPPa in ethanol indicates that fs time-resolved laser spectroscopy (fs-TRLS) may be an useful tool to study the initial reactions leading to the generation of $O_2^{-\cdot}$ by the excited singlet state of MPPa (^{1}MPPa*). Furthermore, Delanaye *et al.* have shown that a $^{\cdot}$OH scavenger reduced the ESR signal of light irradiated MPPa in liposomes by ~74% (245). This result suggests that the yield of $O_2^{-\cdot}$ might be high in MPPa-mediated PDT. Therefore, MPPa may be a good model compound for studying the Type I reaction pathway of PDT.

3.4 Summary

Photodynamic therapy (PDT) is a novel cancer therapy that has been successfully used in treating various cancers. However, more widespread application of PDT has been hindered due to the limited treatment depth of currently approved photosensitizers. The present study demonstrates that the 2nd-generation PDT sensitizer MPPa can be effectively activated not only by 1-γ excitation at 674 nm but also by 2-γ excitation at 800 nm using a fs laser. These

treatments caused effective cell killing in both cisplatin-sensitive human cervical (HeLa) and cisplatin-resistant human lung (A549) and ovarian (NIH:OVCAR-3) cancer cells *in vitro*.

MPPa has a 1-γ absorption maximum at 674 nm in cell culture medium (Figure 3-7), which locates at a much longer wavelength than that of Photofrin®, and its molar extinction coefficient at 667 nm in acetone is about 15 times that of Photofrin® at 630 nm (144, 229). Previously, a number of groups have reported the *in vitro* 1-γ PDT efficacy of MPPa and the cancer cell lines studied have showed different sensitivity to MPPa-mediated PDT treatment (Table 3-2) (129, 229-232, 234). In the present study, we have found that both cisplatin-sensitive HeLa and cisplatin-resistant A549 and NIH:OVCAR-3 cancer cell lines are sensitive to MPPa-mediated PDT treatment. Moreover, we note that our values of PD_{50} in all the three cancer cell lines are about 10 times lower than that in lung cancer (NCI-h446) cells reported by Sun *et al.* (229), who have found that MPPa is as effective as 5,10,15,20-tetrakis(meta-hydroxyphenyl)chlorine (mTHPC), a 2nd-generation photosensitizer approved by European Medicines Evaluation Agency for the palliative treatment of patients suffering from advanced head and neck squamous cell carcinoma. Therefore, our results suggest that MPPa may be developed as an effective 1-γ PDT agent for selected cancers.

Recently, 2-γ excitation has been explored as a potential approach to increase the treatment depth of PDT (141, 142, 144-148, 151, 152). For example, photosensitizers that normally absorbs at 400 nm could be activated by absorbing two photons at 800 nm, which can penetrate much deeper into tissues. We note that although the 1-γ PDT efficacy of MPPa has been evaluated in a number of cell lines, 2-γ PDT effects of this photosensitizer have not

been reported previously. Here, we have determined the value of σ to be 3.5 GM for MPPa in methanol at 800 nm. We have also evaluated the 2-γ photocytotoxicity of MPPa in three human cancer cell lines, namely the cancers of human cervix (HeLa), lung (A549) and ovary (NIH:OVCAR-3). With a peak irradiance of 3.9×10^{10} W cm^{-2}, which is more than one order of magnitude lower than the threshold value for direct photomechanical damage (144), we have obtained LD_{50} values of 576 ± 13, 478 ± 18 and 360 ± 16 J cm^{-2} in HeLa, A549 and NIH:OVCAR-3 cells, respectively. It's worth pointing out that, our measured σ = 3.5 GM for MPPa is lower by a factor of about 5,000 than that of 16,000 GM for the conjugated porphyrin dimer (148), but the 2-γ LD_{50} of MPPa is ~50% of that of the later in SK-OV-3 cells (150). This observation suggests that although σ is an important factor in determining the 2-γ PDT efficacy of a photosensitizer, other factors such as the intracellular concentration/localization and the mechanisms of action of the photosensitizer should also be considered when developing novel 2-γ PDT agents.

Cisplatin is the most widely used chemotherapeutic drug and the cornerstone in treating ovarian, testicular, cervical, bladder, lung, head and neck, lymphomas and brain cancers. Cancer cells often have a positive initial response but become refractory over time and 70–90% of patients die of progressive chemo-resistant disease, so that it remains a major challenge to cure these cancers, especially ovarian and lung cancers (9, 248-250). The present observation of effective killing of cisplatin-resistant lung and ovarian cancer cells by either 1- or 2-γ PDT of MPPa may provide new strategies for treatment of these challenging cancers.

Moreover, we have for the first time obtained the fs time-resolved transient absorption decay kinetic traces of MPPa in water and ethanol. Two short lifetimes of 0.31 and 11.4 ps have been obtained from the kinetics of MPPa in water, which have been assigned to be the excited state lifetime of MPPa aggregates. In ethanol, the excited singlet state lifetime of MPPa is determined to be on the nanosecond time scale (12.0 ns). Previous studies have demonstrated the involvement of ROS other than $^1O_2$ in MPPa-mediated PDT treatment (129, 228, 245) suggesting the importance and effectiveness of the Type I reactions in inducing cytotoxicity. Therefore, further fs time-resolved laser spectroscopic studies of MPPa may improve our understanding of the initial reactions that lead to the generation of $O_2^{-\cdot}$ in PDT and help develop novel PDT treatment approaches for cancers.

4 Combination of Near Infrared Light-Activated Photodynamic Therapy Mediated by Indocyanine Green with Etoposide or Teniposide Chemotherapy

4.1 Background

Indocyanine green (ICG) is a near-infrared fluorescent dye approved by the U.S. Food and Drug Administration (FDA) for various clinical applications (186-189). As shown in Figure 1-10, ICG has an absorption maximum near 800 nm. It can be activated by near-infrared (NIR) light that penetrates relatively deep into tissues and therefore, has been considered to be a potential NIR photosensitizer for photodynamic therapy (PDT). The antitumor activity of ICG has been reported by several research groups (190-196, 199, 200). It has been suggested that the photocytotoxicity of ICG involves the generation of singlet oxygen ($^1O_2$) (190, 192). However, the yield of $^1O_2$ has been found to be extremely low due to a low yield of excited triplet states (~10^{-5}) (251), which are believed to be responsible for the generation of $^1O_2$. Moreover, this dye has a short blood half-life of 2 to 4 minutes (202), poor photo- and thermal-stability, non-specific binding with proteins, and is vulnerable to aggregation (203). These properties of ICG have greatly limited the application of this dye as a PDT agent.

Etoposide (VP-16) and teniposide (VM-26) are two semisynthetic podophyllotoxin derivatives that are currently in clinical use for the treatment of various cancers (15, 16). Etoposide has been approved for treating acute myeloid leukemia, choriocarcinoma, small and non-small cell lung carcinoma, lymphoma, advanced ovarian carcinoma, and testicular cancers. Teniposide has been approved for the treatment of bladder cancer, malignant lymphoma, and central nervous system tumors. Both drugs are believed to act on type II topoisomerases (TOPII), which can bind covalently with the 5' ends of DNA resulting in the formation of transient double strand breaks (DSBs). Binding of VP-16/VM-26 with TOPII can create permanent DNA DSBs that may activate cellular pathways leading to cancer cell death. Although these two drugs are efficient, they have severe side effects such as alopecia, gastrointestinal toxicities, leucopoenia, myelosuppression, and development of secondary leukemia (16, 252-255). In fact, in preclinical and clinical studies, etoposide is normally given in combination with other chemotherapeutic drugs such as cisplatin (CDDP) and carboplatin (255-260), which may lower the effective dose of VP-16 leading to reduced side effects associated with VP-16. For example, the combination of VP-16 and CDDP was reported to produce a strong synergistic effect in P 388 leukemia cells both *in vitro* and *in vivo* (256) and to be more effective than the single drugs in treating xenografts of small cell lung carcinoma (259). The combination of VP-16 with carboplatin was found to be as effective as VP-16-CDDP combination in terms of response and survival but showed less toxicity in treating small-cell lung cancers (257). While a number of these combinations have been demonstrated to be effective in treating some tumors, toxic side effects associated with the chemotherapeutic drugs other than VP-16, such as cisplatin and carboplatin, should also

be considered. Moreover, the development of drug-resistance remains a big problem in chemotherapy of cancers.

PDT has several advantages over conventional radio- and chemotherapy, including fewer side effects, local targeting, and less acquired resistance to the treatment. Combination of PDT with conventional chemotherapy has been explored as a promising approach for enhancing the antitumor activity of single therapies and reducing side effects associated with the administration of chemotherapeutic drugs. Additive to synergistic enhancement of cytotoxicity by the combination treatment has been reported in some studies (163-166, 174, 176, 178, 179), but antagonistic effects have also been reported (167, 176, 179). Using aluminium phthalocyanine ($AlPcS_4$) as the photosensitizer, Gantchev *et al.* studied the combination effects of VP-16 with PDT and observed synergistic enhancement of cytotoxicity in human leukaemic cells K562 (174). The combination effects were found to be dependent upon treatment protocol and cell type by Zimmermann *et al.*, who observed additive/synergistic effects in human breast (MCF-7) cells but antagonistic effects in human prostate (LNCaP) cancer cells treated by the combination of PDT mediated by 5,10,15,20-tetra(m-hydroxyphenyl)chlorin (mTHPC) and chemotherapy mediated by 5-fluoro-2'-deoxyuridine (5FdUr) (176). Later, Crescenzi *et al.* studied the combination effects of low-dose CDDP with ICG-mediated PDT in MCF-7 breast cancer cells and observed synergistic enhancement according to MTT assay data (165). However, their data from trypan blue assay showed an additive effect. Those results suggest that the combination effects have strong dependence upon a variety of factors, including cell type, the

photosensitizer and chemotherapeutic drug under investigation, and the treatment schedule. Moreover, a molecular mechanism for synergistic enhancement of cytotoxicity is still not available. Therefore, the development of novel treatment approaches may improve our understanding of the molecular mechanism underlying synergism induced by the combination of PDT and chemotherapy.

In the present study, we have investigated the combination effects of ICG-mediated PDT and chemotherapy mediated by etoposide (VP-16) in human lung (A549), cervical (HeLa) and ovarian (NIH:OVCAR-3) cancer cells as well as in a human normal fibroblast cell line (GM05757). Cytotoxicity has been evaluated by using the standard MTT cell viability assay. We have also examined the cytotoxicity of the laser-irradiated mixtures of ICG and VP-16 and altered the sequence of drug addition to see if the combination effects are dependent upon the schedule of treatment. Moreover, we have used commercial fluorescence kits to detect the generation of DNA DSBs and $^1O_2$. Cytotoxicity of the combination of ICG-PDT and VM-26, which is an analog of VP-16, has also been evaluated in A549 cells. Finally, we have determined the fluorescence lifetime of VP-16 and studied the reaction between ICG and VP-16 by performing steady-state and femtosecond (fs) time-resolved laser spectroscopic measurements.

4.2 Materials and methods

4.2.1 Chemicals and cell lines

4,5-Benzoindotricarbocyanine (indocyanine green; ICG; $C_{43}H_{47}N_2NaO_6S_2$; MW = 775 g mol^{-1}), 4'-demethylepipodophyllotoxin-9-(4,6-o-ethylidene-b-d-glucopyranoside) (etoposide; VP-16; $C_{29}H_{32}O_{13}$; MW = 588.6 g mol^{-1}) and 4'-dimethyl-9-(4,6-O-2-thenyid)-epipodophyllotoxin (teniposide; VM-26; $C_{32}H_{32}O_{13}S$; MW = 656.65 g mol^{-1}) were purchased from Sigma-Aldrich (Sigma-Aldrich Canada Ltd., Oakville, Ontario, Canada) and used without any further purification. A stock solution of 5 mM ICG was prepared weekly in ultrapure water (Barnstead Nanopure, Thermo Scientific, Dubuque, IA, USA) with a resistivity of > 18 MΩ cm^{-1} and stored in the dark at -20˚C. Stock solutions of 50 mM VP-16 and 10 mM VM-26 were made in dimethyl sulfoxide (DMSO) and stored at -20˚C.

The culture conditions for the human lung (A549), cervical (HeLa) and ovarian (NIH:OVCAR-3) cancer cells were the same as those described in Chapter 3. The human normal fibroblast cell line GM05757 was obtained from the Coriell Institute, Human Genetic Mutant Cell Repository (Camden, NJ, USA) and grew in minimum essential medium Eagle (MEM) supplemented with 10% fetal bovine serum (FBS), 100 units mL^{-1} penicillin G and 100 μg mL^{-1} streptomycin. The cell culture was kept at 37˚C in a humidified atmosphere containing 5% CO_2.

4.2.2 Laser treatment conditions

Irradiation was carried out by using an 800 nm laser with a pulse duration of 120 fs and a pulse repetition rate of 1 kHz. The average power was 360 mW and the corresponding average irradiance was 81 mW cm^{-2}. Duration of exposure was varied to get different light doses (J cm^{-2}).

4.2.3 Photocytotoxicity of ICG

Exponentially growing A549 cells were seeded into 96-well microplates at a density of 5×10^3 cells/well. After overnight incubation, the cells were incubated with ICG for 5 h in the dark. The cells were then washed twice with phosphate-buffered saline (PBS) and fresh culture medium was added for irradiation. Cells were placed back into an incubator after laser irradiation and cells viability was evaluated 20 h later by using the standard MTT assay as described in Chapter 3.

4.2.4 Cytotoxicity of the combination treatment of ICG-PDT and VP-16/VM-26 chemotherapy *in vitro*

Exponentially growing A549, HeLa, NIH:OVCAR-3 and GM05757 cells were seeded into 384-well microplates at densities of 3×10^3, 3×10^3, 4×10^3 and 3×10^3 cells/well, respectively. After overnight incubation, the cells were incubated with various concentrations of ICG, VP-16 or VM-26 for 4 h in the dark. Cells were then washed twice with PBS and fresh

complete culture medium was added before irradiation. The irradiated cells were then kept in an incubator for 45 h and cell viability was evaluated by the standard MTT cell viability assay as described in Chapter 3.

4.2.5 Effects of treatment sequence on cytotoxicity induced by the combination of ICG-PDT and VP-16 in A549 and HeLa cells

Exponentially growing A549 and HeLa cells were seeded into 384-well microplates at a density of 3×10^3 cells/well. Cells were incubated with 50 μM of ICG for 4 h, washed twice with PBS, and fresh complete culture medium was added for irradiation. After laser irradiation, various concentrations of VP-16 were added. After 4 h incubation, cells were washed twice with PBS, fresh complete medium was added, and cells were then put back into an incubator. Cell viability was evaluated by the standard MTT cell viability assay 45 h later as described in Chapter 3.

4.2.6 Cytotoxicity of the laser-irradiated mixtures of ICG and VP-16 in A549 cells

Exponentially growing A549 cells were seeded into 384-well microplates at a density of 3×10^3 cells/well. Mixtures of various concentrations of ICG and VP-16 were made in complete F12K medium and then exposed to laser irradiation. The drug mixtures were then added to the corresponding wells in 384-well microplates. After 4 h incubation, cells were washed twice with PBS and fresh complete culture medium was added. The cells were then

put back into an incubator and cell viability was evaluated 45 h later by the standard MTT cell viability assay as described in Chapter 3.

4.2.7 Detection of DNA double-strand breaks by using HCS DNA damage kit

Many chemotherapeutic drugs, including VP-16 and VM-26, produce multiple forms of DNA damages. Among them, DNA double-strand breaks (DSBs) are more difficult to repair than other forms of damages such as single-strand breaks (SSBs) (19). Failure to reseal the DSBs may lead to cell death. Recently, phosphorylation of histone 2AX (H2AX), a member of the histone 2A family, has been identified as a sensitive marker of DNA DSBs: this process can take place within a few minutes in response to DSBs (261). Therefore, we have used the HCS DNA damage kit (Invitrogen, Life Technologies Inc., Burlington, ON, Canada) to measure the yield of DNA DSBs induced by the combination treatment of ICG-PDT and VP-16 following the manufacturer's protocol. Briefly, cells were seeded and treated with drugs and laser irradiation as described in Section 4.2.4. At the end of the incubation period (18 h), cells were fixed using 4% paraformaldehyde (PF) in PBS and permeabilized with 0.25% Triton® X-100 in PBS. The cells were then stained with Alexa Fluor® 555, which detects phosphorylated H2AX (γH2AX), and Hoechst 33342 for nuclear morphology evaluation. The images were taken on a Nikon Eclipse TS100/TS100-F microscope with filter sets of Ex/Em of BP510-560/LP590 nm and BP330-380/LP420 nm for Alexa Fluor® 555 and Hoechst 33342, respectively. All the images were taken with an

exposure time of 6 s. Background images were taken for each channel under the same experimental conditions. The final images presented in Section 4.3.8 are corrected images obtained after subtracting the background images using Photoshop software (Adobe Systems Inc., San Jose, CA, USA).

It has been reported by Kim *et al.* that the total area of γH2AX foci is a more sensitive parameter than the total number of the foci for measuring the amount of DNA DSBs (262). Therefore, in order to quantify the yield of DNA DSBs, we have calculated the average of integrated fluorescence intensity from the Alexa Fluor® 555 channel and plotted the results as a function of VP-16 concentration. Each data point represents the mean ± S.D. of three to five images.

4.2.8 Detection of singlet oxygen by using singlet oxygen sensor green

Singlet oxygen is believed to be the major ROS that is responsible for the cytotoxic effects generated during PDT treatment. In order to determine whether $^1O_2$ is involved in this study, we have used a commercial fluorescence probe for $^1O_2$ detection (Singlet Oxygen Sensor Green (SOSG)) (Invitrogen, Life Technologies Inc., Burlington, ON, Canada) to measure the relative yields of $^1O_2$ under different treatment conditions. Figure 4-1 shows the chemical structures of SOSG and SOSG endoperoxide (SOSG-EP). In the parent compound SOSG, fluorescence is quenched by an intra-molecular electron transfer reaction. Upon reaction with $^1O_2$, SOSG is converted to SOSG-EP, in which electron transfer is blocked and fluorescence

emission is restored (263). A stock solution of 5 mM SOSG was prepared in methanol and stored at -20˚C in the dark. The work solution of 20 μM SOSG was prepared in PBS immediately before use.

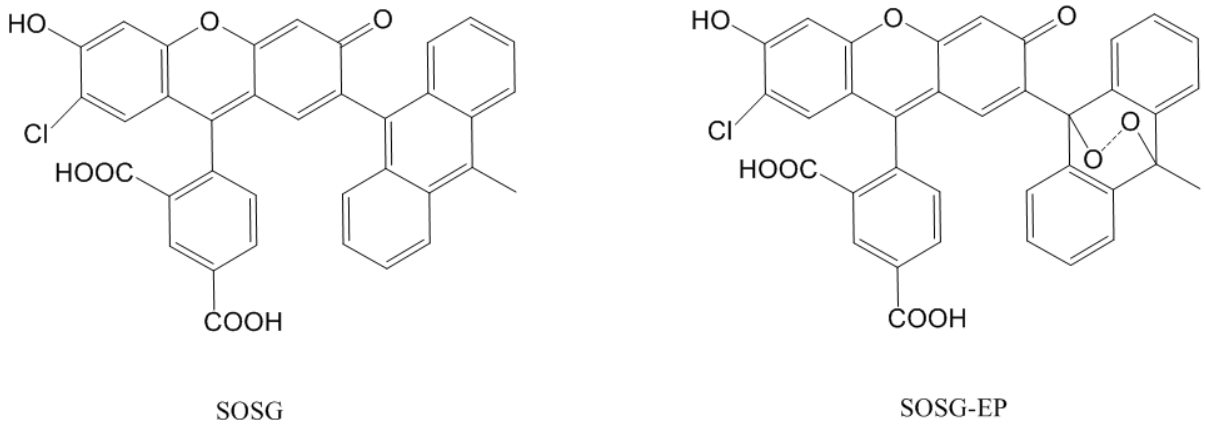

Figure 4-1: Chemical structures of singlet oxygen sensor green (SOSG) and SOSG endoperoxide (SOSG-EP). In SOSG, the fluorescence is quenched by an intra-molecular electron transfer reaction. Reaction of SOSG with singlet oxygen ($^1O_2$) leads to the formation of SOSG-EP, which can emit strong green fluorescence with a maximum of 536 nm (263).

A549 cells were seeded and incubated with ICG and VP-16 as described in Section 4.2.4. After incubation, drug containing medium was removed and cells were washed twice with PBS. Irradiation was done in the presence of PBS, 20 μM SOSG, 50% D_2O or 20 μM + 50% D_2O. Immediately after laser irradiation, cells were washed three times with PBS and fresh culture medium was added. Images were then taken on a Nikon Eclipse TS100/TS100-F microscope with a filter set of Ex/Em of BP450-490/LP520 nm. All the images were taken with an exposure time of 7 s. A background image was taken under the same experimental conditions. The final images presented in Section 4.3.9 were corrected

images obtained by subtracting the background image using Photoshop software (Adobe Systems Inc., San Jose, CA, USA). In order to quantify the yields of singlet oxygen, we calculated the average of integrated fluorescence intensity of SOSG-EP. Each data point represents the mean ± S.D. of three images.

4.2.9 Steady-state absorption and fluorescence spectroscopic measurements

Steady-state absorption spectra of mixtures of ICG and VP-16 were measured on a Multiskan GO microplate spectrophotometer (Thermo Scientific, Mississauga, ON, Canada). Samples were prepared in complete F12K medium in 96-well microplates. Steady-state absorption spectra of VP-16 were measured on a DU 530 UV/Vis spectrophotometer (Beckman Coulter, Fullerton, CA, USA). Samples were prepared in 5 mm quartz cuvettes using ultrapure water. Steady-state fluorescence spectra were measured on a homemade fluorescence spectrophotometer (see Chapter 2). Samples were prepared in 5 mm quartz cuvettes using ultrapure water. All measurements were performed at room temperature.

4.2.10 Femtosecond time-resolved transient absorption and fluorescence spectroscopic measurements

The experimental setups for femtosecond time-resolved transient absorption and fluorescence spectroscopy have been described in Chapter 2. In the transient absorption experiment, the pump wavelength was fixed at 266 nm while two probe wavelengths (299 and 570 nm) were

chosen in order to distinguish between different intermediate species. Power dependence of transient absorption intensity of water and VP-16 samples was also measured to determine whether one- or two-photon excitation process was involved. For transient fluorescence measurements, the excitation and detection wavelengths were 266 and 353 nm, respectively. Samples were prepared in 5 mm quartz cuvettes using ultrapure water. All measurements were performed at room temperature.

4.2.11 Data analysis

4.2.11.1 Dose-response curve analysis

The drug- and light-dose response curves were fitted with a sigmoidal logistic function by using Origin software (OriginLab, Northampton, MA, USA). The drug concentration (IC_{50}) or light dose (LD_{50}) required to produce a 50% cell killing effect was determined on the basis of the fitted data.

4.2.11.2 Modified fractional effect analysis

Fractional effect analysis is the most straight forward method for the evaluation of combination effects (9, 264). In this study, we have observed that addition of ICG at non-cytotoxic concentrations can enhance the cytotoxicity of the chemotherapeutic drugs VP-16 and VM-26 slightly even when cells are not exposed to laser irradiation. Considering this "dark effect" of the combination treatment, we have modified the fractional effect analysis for calculating the expected additive effects by using the following equation, in which the

effect induced by the chemotherapeutic drug has been replaced by the dark effect of ICG and the chemotherapeutic drug:

$$f_{com.} = f_{dark} \times f_{PDT}, \quad (4\text{-}1)$$

where $f_{com.}$, f_{dark} and f_{PDT} denote the fraction of survived cell with the combination (ICG-PDT + VP-16/VM-26), dark (ICG + VP-16/VM-26) and PDT (ICG + laser irradiation) treatments, respectively. The observed effects of the combination treatment are then compared with the expected additive effects: the effect is synergistic if the observed cell viability is lower than the expected additive effect and antagonistic if it is higher than the calculated value.

4.2.11.3 Transient absorption and fluorescence decay kinetics analysis

In order to determine the lifetimes from the transient absorption and fluorescence decay kinetic traces, we have fitted the curves with multi-exponential functions using the Scientist software (MicroMath Inc., Saint Louis, MO, USA).

4.3 Results and discussion

4.3.1 Drug- and light-dose responses of A549 cells to ICG-PDT treatment

We have evaluated the photodynamic efficacy of ICG activated by an 800 nm laser. In this experiment, the cells were incubated with various concentrations of ICG for 5 h and then exposed to laser light irradiation. Cell viability was determined by using the standard MTT

assay. The results are shown in Figure 4-2. Photocytotoxicity of ICG increased in a drug- and light-dose dependent manner. At a light dose of 100 J cm^{-2}, the IC_{50} of ICG was calculated to be 68.5 ± 1.7 μM. The LD_{50} values were found to be 28.8 ± 1.9 and 14.1 ± 1.2 J cm^{-2} for 100 and 200 μM ICG, respectively.

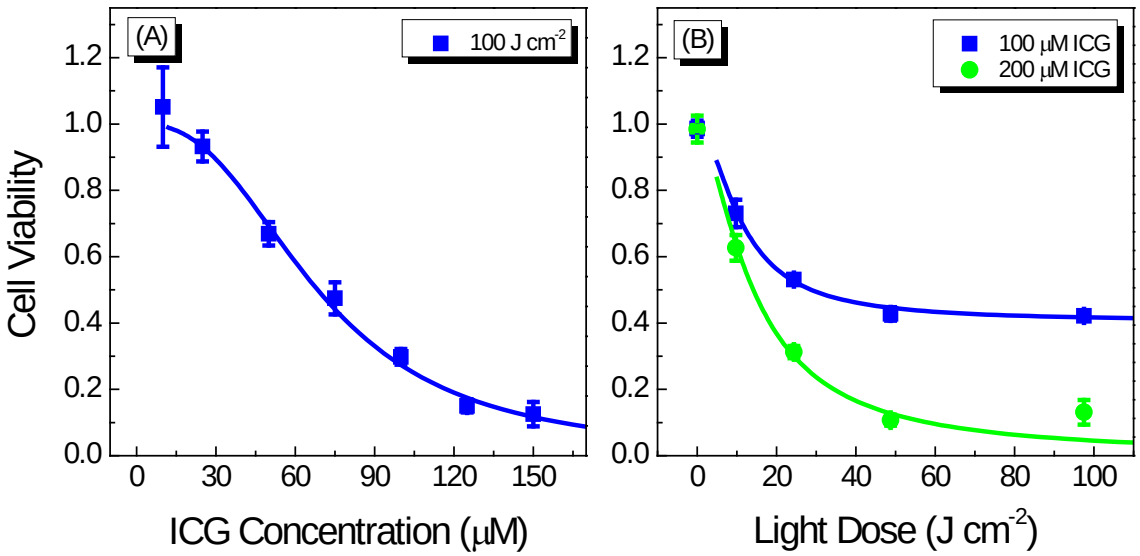

Figure 4-2: (A) Drug-dose and (B) light-dose response curves for cell viability of A549 cells treated with ICG-mediated PDT. The cells were incubated with ICG for 5 h and then irradiated at 800 nm. Cell viability was evaluated by using the standard MTT assay 20 h after laser irradiation. The solid lines are best fits to the experimental data using a logistic function in Origin software.

Anticancer activity of ICG has previously been studied by several research groups in a number of cell lines, including HeCaT keratinocytes, HT-29 human colon cancer, SCL1 and SCL2 squamous cell carcinoma, N1 fibroblasts, human SKMEL 188 melanoma, mouse S91 melanoma, human skin Sk-Mel-28 melanoma, and MDA-MB231 breast cancer cells (190-192, 195, 199, 200, 265). For example, with 24 h drug-incubation and a light dose of

24 J cm^{-2}, the IC_{50} of ICG was reported to be 20.1, 43.9, 61.8, and 62.3 μM in HaCaT, SCL1, SCL2, and N1 cells, respectively (265). The photodynamic efficacy of ICG in A549 cells observed in the present study is consistent with what have been reported in other cell lines. However, ICG is much less efficient in killing cancer cells than Photofrin®, the first clinically approved and currently the most widely used photosensitizer, which has an IC_{50} value of only 0.5 μM in A549 cells at a lower light dose (266). Moreover, the blood half-life of ICG has been reported to be only 2-4 minutes (202). It will be very difficult to achieve an ICG concentration high enough to have significant antitumor effects under *in vivo* conditions. Therefore, we have explored the combination of ICG-PDT with conventional chemotherapy as a potential way of enhancing the effectiveness of ICG as a promising NIR agent for PDT.

4.3.2 Drug- and light-dose responses induced by the combination treatment of ICG-PDT and VP-16 in A549 cells

We have measured drug- and light-dose responses of A549 cells to the combination treatment of ICG-PDT and VP-16 (Figure 4-3 and Figure 4-4). As shown in Figure 4-3, with a drug incubation time of 4 h, IC_{50} of VP-16 was determined to be 41.7 ± 7.7 μM in A549 cells. When combining VP-16 with 20 μM ICG, cytotoxicity was not affected significantly (IC_{50} = 37.4 ± 8.7 μM). Laser irradiation, at a light dose of 100 J cm^{-2}, reduced the IC_{50} dramatically to be 18.8 ± 1.6 μM, which was ~45% of that of VP-16. With higher ICG concentrations of 30 and 50 μM, a slight increase in cytotoxicity was observed even without laser irradiation. However, with the range of drug concentration in Figure 4-3B and C, the

IC_{50} values could not be determined accurately. At a light dose of 100 J cm^{-2}, the values of IC_{50} were calculated to be 10.9 ± 0.7 and 1.77 ± 0.17 μM, which were 26% and 4% of the IC_{50} of VP-16, for 30 and 50 μM ICG, respectively. We have also investigated the dependence of cytotoxicity of the combination treatment on ICG concentration. ICG was found to be only slightly cytotoxic in A549 cells with less than 7% of cells killed up to a concentration of 80 μM. VP-16 alone at a concentration of 2 μM was found to be not cytotoxic. Combination of 2 μM VP-16 with ICG at concentrations of 10 and 20 μM didn't show enhanced cytotoxicity, while at higher ICG concentrations of 60 and 80 μM, cytotoxicity was increased from 4.1 ± 7.0% to 14.3 ± 4.7% and from 6.7 ± 2.9% to 20.7 ± 2.6%, respectively. With laser irradiation, the IC_{50} of ICG was found to be 155.7 ± 15.3 μM. In the presence of 2 μM VP-16, the IC_{50} was reduced by more than 73% (41.8 ± 1.8 μM). Moreover, we performed fractional effect analysis to evaluate the combination effects as described in Section 3.2.9. Considering the dark cytotoxicity of ICG + VP-16, we compared the combination effects with the cytotoxicity of ICG + VP-16 instead of that of VP-16 alone. As shown in Figure 4-3, the dashed line and solid stars represent the predicated additive effects calculated using Equation (4-1). The observed effects were found to be the equal to or lower than the predicated additive effects indicating additive to synergistic enhancement of cytotoxicity induced by the combination treatment.

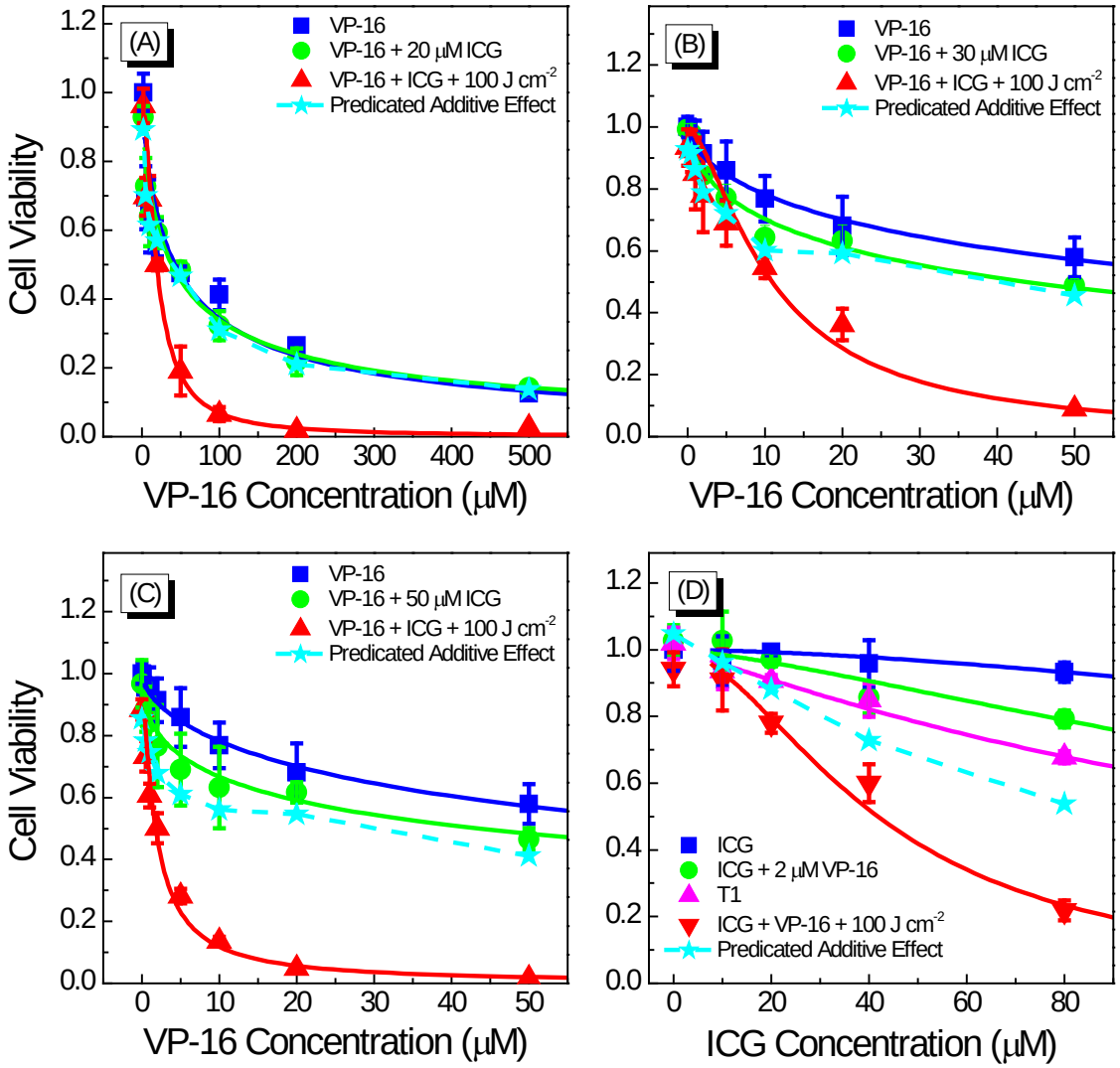

Figure 4-3: Drug-dose response curves for cell viability of A549 cells treated with the combination of ICG-PDT and VP-16. Cells were treated with ICG and VP-16 for 4 h after overnight incubation and then irradiated with 800 nm laser at a light dose of 100 J cm^{-2}. Cell viability was evaluated by MTT cell viability assay 45 h after laser irradiation. The solid lines are best fits to the experimental data using a logistic function in Origin software. The dashed line and solid stars represent the calculated additive effect.

We have observed a wide range of synergistic enhancement of cytotoxicity by the combination treatment of ICG-PDT and VP-16 and the degree of synergy has a strong

dependence upon the concentration of both ICG and VP-16. Although we have also observed slight increases in cytotoxicity in cells treated with ICG and VP-16 but without laser irradiation, this effect requires relative high concentrations of ICG and VP-16. It is well known that the blood half-life of ICG is about 2-4 min (202) resulting in limited accumulation of ICG in tissues and organs. Therefore, the dark effect is not likely to be significant under *in vivo* conditions. Moreover, one objective of this study is to overcome the severe side effects of chemotherapeutic drugs. Thus, it is considered to be desirable to lower the concentration of VP-16, which is also expected to help reduce dark cytotoxicity of the combination treatment.

We have performed further experiments to study the light-dose dependence of cytotoxicity produced by the combination treatment of ICG-PDT and VP-16. The results are shown in Figure 4-4. As discussed above, low concentrations of both ICG and VP-16 should be used to minimize the dark cytotoxicity induced by the combination of ICG and VP-16. In this experiment, we varied the irradiation time to achieve various light doses between 0 and 100 J cm^{-2} and evaluated the cytotoxicity of several combinations of ICG and VP-16. As shown in Figure 4-4, laser irradiation in the absence of both drugs was not cytotoxic up to a light dose of 100 J cm^{-2}. Cytotoxicity of the group treated with VP-16 alone didn't change significantly with increasing light dose. At a concentration of 30 μM, ICG didn't show significant photo-cytotoxicity. When cells were incubated with 50 μM ICG, percentages of cell killed were increased from 2.1 ± 1.6% to 14.7 ± 5.1% and from 5.1 ± 3.4% to 26.1 ± 2.9% at light doses of 50 and 100 J cm^{-2}, respectively. The LD_{50} of ICG was much

higher than 100 J cm^{-2} and couldn't be determined accurately from this experiment. Without laser irradiation, we observed a 10% increase in cytotoxicity of ICG + VP-16 compared with an expected additive effect. With laser irradiation, cell viability of the groups incubated with both ICG and VP-16 decreased dramatically with increasing light dose and the LD_{50} values were determined to be 28.0 ± 9.3, 14.4 ± 10.4, 6.55 ± 2.79 and 6.84 ± 6.06 J cm^{-2}. We have also performed fractional effect analysis using Equation (4-1) and the expected additive effects have been plotted as dashed line and filled stars in Figure 4-4. With laser irradiation, the observed combination effects are found to lie below the additive effect curves for all the concentrations of ICG and VP-16 evaluated in this experiment confirming synergistic enhancement of cytotoxicity by the combination treatment of ICG-PDT and VP-16 in a wide range of drug concentration and light dose.

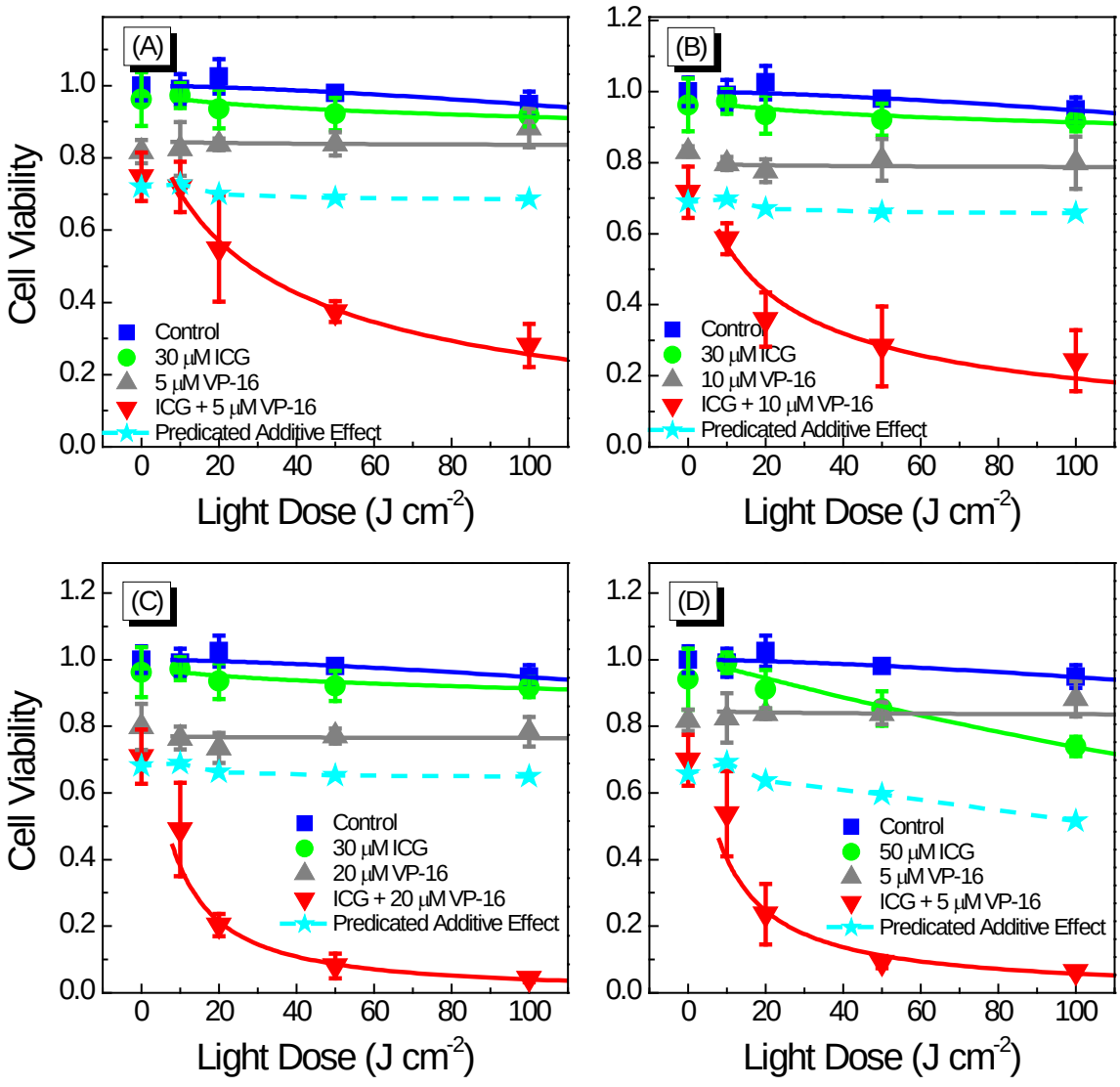

Figure 4-4: Light-dose response curves for cell viability of A549 cells treated with the combination of ICG-PDT and VP-16. Cells were treated with ICG and VP-16 for 4 h after overnight incubation and then irradiated with an 800 nm laser at a light dose of 100 J cm^{-2}. Cell viability was evaluated by MTT cell viability assay 45 h after laser irradiation. The solid lines are best fits to the experimental data using a logistic function in Origin software. The dashed line and filled stars represent the calculated additive effect.

The application of ICG as a PDT agent has been limited by the short blood half-life of 2-4 min (202), which lowers the accumulation of this drug into tissues and organs. In this study, we have found that at a light dose of 100 J cm^{-2} (the typical light dose range for clinic applications of conventional PDT: 25-500 J cm^{-2} (52)), IC_{50} of ICG is much larger than 80 μM in A549 cells. In cells treated with 50 μM ICG and laser irradiation, LD_{50} is much higher than 100 J cm^{-2}. These results indicate that relative high drug- and light-doses are required for effective killing of cancer cells by ICG. Here, we have demonstrated that co-incubation of the human lung cancer A549 cells with ICG and low dose VP-16 can increase the cytotoxicity in a synergistic manner leading to reduced effective doses of both drugs as well as light doses. A more than 20 times reduction in IC_{50} of VP-16, from > 40 μM to 1.77 μM, has been observed in the cells treated with VP-16 and 50 μM ICG. Moreover, we have found that the degree of enhancement is light-dose dependent. These observations indicate that combining PDT mediated by ICG and VP-16 chemotherapy is a promising approach for improving the therapeutic effectiveness of ICG-PDT and reducing the side effects of VP-16 chemotherapy at the same time.

ICG has been chosen in this study for several reasons. First, ICG has already been approved by the US FDA for clinical applications other than PDT. Second, ICG-PDT is activated by NIR light that can penetrate deeper into tissues. Therefore, the combination of ICG-PDT with VP-16 has the potential of treating larger tumor volumes. Combination of PDT with VP-16 has been reported by Gantchev *et al.* (174, 175). However, the photosensitizers used in those studies are metallic phthalocyanine ($AlPcS_4$/$ZnPcS_4$), which

requires red light for activation (λ_{max} ~ 670 nm (267)). Stolik *et al.* have reported that the penetration depths of 780 and 835 nm light are ~10-130% larger than that of 674 nm light depending on tissue type (161). In lung carcinoma, for example, the values were determined to be 2.01, 2.82 and 3.89 mm for 674, 780 and 835 nm light, respectively. Therefore, ICG-mediated PDT has the potential of treating deeper tumors than those can be treated by $AlPcS_4$/$ZnPcS_4$-mediated PDT. Third, there have been tremendous efforts on improving the tumor specificity of ICG as well as increasing accumulation of the drug into tumors and some of these systems have been shown to be superior to free ICG as imaging and photothermal therapy agents (109, 112, 115-118, 268). It would be of great interest to explore the PDT effectiveness of those systems either alone or in combination with other treatment modalities such as VP-16-mediated chemotherapy.

4.3.3 Cytotoxicity of the combination treatment of ICG-PDT and VP-16 in HeLa and NIH:OVCAR-3 cells

We have evaluated the cytotoxicity of the combination treatment of ICG-PDT and VP-16 in two more cancer cell lines: the human cervical cancer HeLa and ovarian cancer NIH:OVCAR-3 cells. The treatment procedure was the same as that applied in A549 cells. Figure 4-5A and B show the drug-dose response of HeLa cells to the combination treatment. The IC_{50} of VP-16 was determined to be 22.6 ± 6.0 μM. The combination of 20 μM ICG with VP-16 didn't change the cytotoxicity significantly. Laser irradiation, at a light dose of 100 J cm^{-2}, reduced the IC_{50} by ~50% (11.3 ± 2.1 μM). ICG treatment alone was found to be

not toxic up to the highest concentration of 80 μM. At a light dose of 100 J cm^{-2}, the IC_{50} of ICG was determined to be 37.9 ± 1.8 μM. When cells were treated with mixtures of ICG and 50 μM VP-16, cell viability decreased from 51.7% ± 3.6% to 35.2% ± 2.6% with increasing ICG concentration. The combination effects were found to fall below the calculated additive effects suggesting synergistic enhancement of cytotoxicity by the combination treatment. Figure 4-5C and D show the results obtained in NIH:OVCAR-3 cells. The IC_{50} of VP-16 was determined to be 209.4 ± 19.4 μM, which was about 5 and 9 times those in A549 and HeLa cells, respectively. The IC_{50} of ICG at a light dose of 100 J cm^{-2}, was determined to be 188.0 ± 36.0 μM, slightly higher than that in A549 cells and 5 times that in HeLa cells. These results show that sensitivity to both VP-16 and ICG-PDT treatment decreased in the order of HeLa > A549 > NIH:OVCAR-3. At a light dose of 100 J cm^{-2}, the IC_{50} values of VP-16 and ICG were measured to be 81.9 ± 6.4 μM and 73.9 ± 6.1 μM, which were ~40% of those without laser irradiation. The results of fractional effect analysis showed that combination treatment of ICG-PDT and VP-16 enhanced cytotoxicity of the single treatments in a synergistic manner.

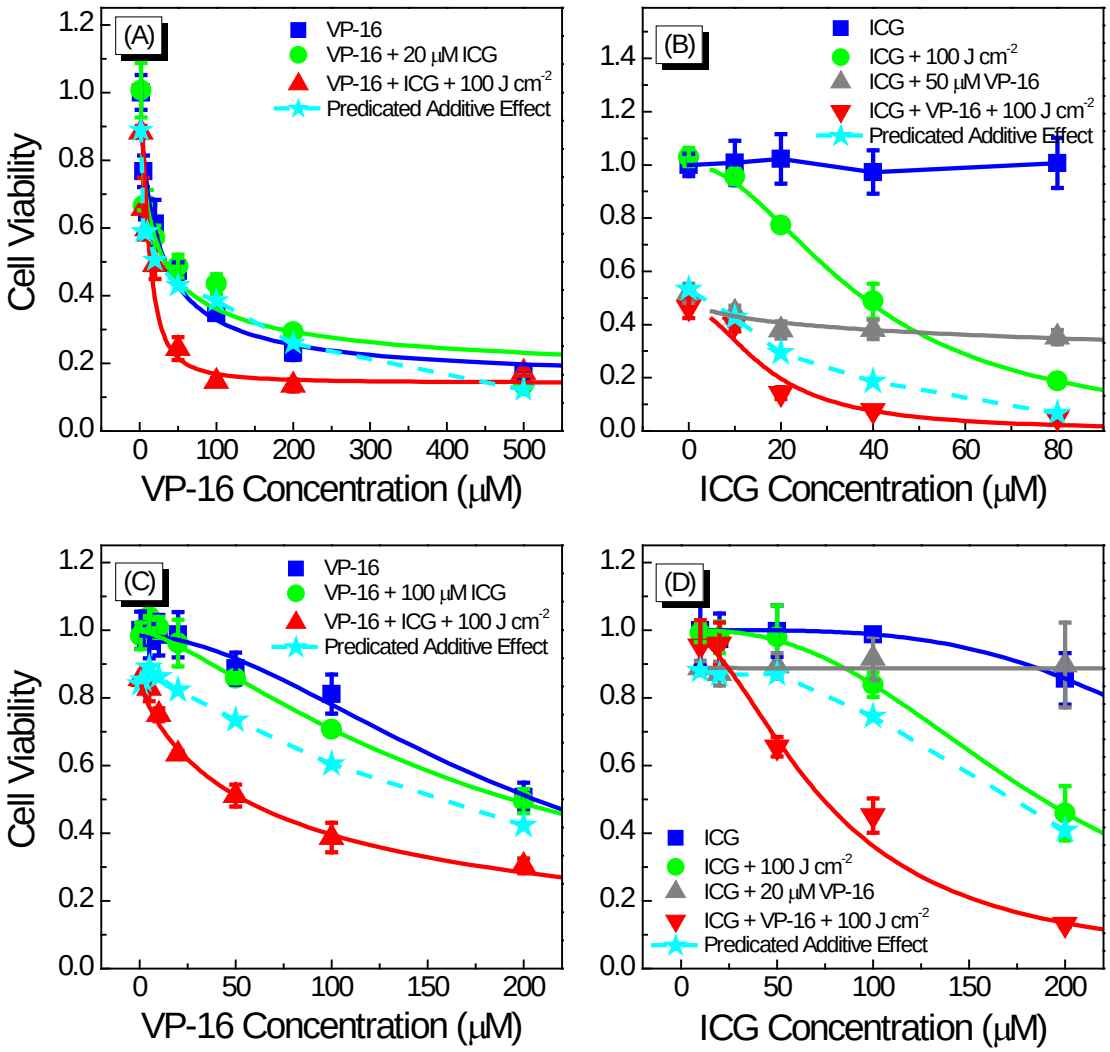

Figure 4-5: Drug-dose response curves for cell viability of (A) and (B) HeLa and (C) and (D) NIH:OVCAR-3 cells treated with the combination of ICG-PDT and VP-16. Cells were treated with ICG and VP-16 for 4 h after overnight incubation and then irradiated with an 800 nm laser at a light dose of 100 J cm^{-2}. Cell viability was evaluated by MTT assay 45 h after laser irradiation. The solid lines are best fits to the experimental data using a logistic function in Origin software. The dashed line and filled stars represent the calculated additive effect.

Table 4-1 is a summary of IC_{50} values obtained from Figure 4-3 and Figure 4-5. HeLa cells have been shown to be most sensitive to both ICG-PDT and VP-16 among the three cell

lines studied here. The combination treatment of ICG-PDT and VP-16 has been shown to induce a moderate synergistic effect of ~50% reduction in IC_{50} of both VP-16 and ICG. A549 cells are less sensitive to the single treatments than HeLa cells. However, strong synergy has been observed with the combination treatment of ICG-PDT and VP-16. We have obtained a more than 95% reduction in IC_{50} of VP-16 in cells treated with 50 μM ICG + 100 J cm^{-2}.

Table 4-1: A summary of the values of IC_{50} calculated from Figure 4-3 and Figure 4-5.

Treatment	ICG/VP-16 Con. (μM) / Cell Line	IC_{50} (μM)		
		A549	**HeLa**	**NIH:OVCAR-3**
VP-16	0	41.7 ± 7.7	22.6 ± 6.0	209.4 ± 19.4
VP-16 + ICG + 100 J cm^{-2}	20	18.8 ± 1.6	11.3 ± 2.1	--
	30	10.9 ± 0.7	--	--
	50	1.77 ± 0.17	--	--
	100	--	--	81.9 ± 6.4
ICG + 100 J cm^{-2}	0	155.7 ± 15.3	37.9 ± 1.8	188.0 ± 36.0
ICG + VP-16 + 100 J cm^{-2}	2	41.8 ± 1.8	--	--
	20	--	--	73.9 ± 6.1

Compared with HeLa and A549 cells, NIH:OVCAR-3 cells are more resistant to the single treatments as well as the combination treatment. Cell viability of ~30% has been observed following 100 μM ICG + 200 μM VP-16 + 100 J cm^{-2} treatment. Therefore, effective killing of NIH:OVCAR-3 cells will require relatively high concentrations of both drugs and light doses, which may be difficult to achieve in *in vivo* experiments.

4.3.4 Photocytotoxicity of the combination treatment of ICG-PDT and VP-16 in GM05757 cells

We have tested the cytotoxicity of the combination treatment of ICG-PDT and VP-16 chemotherapy in a human normal fibroblast cell line GM05757. The results are shown in Figure 4-6. Sensitivity to VP-16 chemotherapy treatment was found to be similar in GM05757 normal fibroblast and A549 lung cancer cells with a ~40% cell killing effect observed at a VP-16 concentration of 50 μM in both cell lines. No significant difference was observed between the groups treated with VP-16 alone or VP-16 + 50 μM ICG. At an ICG concentration of 50 μM and a light dose of 50 J cm^{-2}, cell viability was 60.0 ± 3.5% and 85.3 ± 5.1% in GM05757 and A549 cells, respectively. This result suggests that GM05757 cells are more sensitive than A549 cells to ICG-PDT treatment. When treated with 50 μM ICG and irradiated at 50 J cm^{-2}, there were still 29.5 ± 2.6 % of the cells survived at a VP-16 concentration of 50 μM in GM05757 cells. In contrast, cell viability was found to be 9.2 ± 1.8% at a much lower VP-16 concentration of 5 μM in A549 cells. Moreover, although

the combination effects have been found to be lower than the expected additive effects, the degree of synergy is much lower in GM05757 cells than that observed in A549 cells.

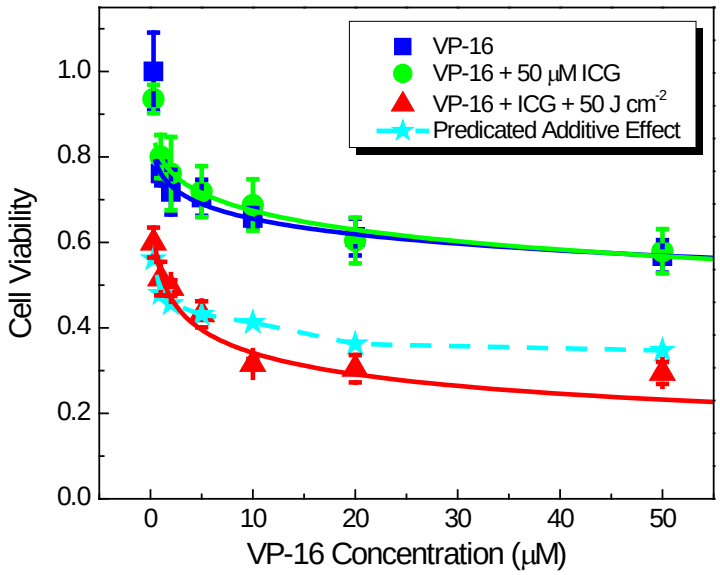

Figure 4-6: Drug-dose response curves for cell viability of human normal fibroblast cells (GM05757) treated with the combination of ICG-PDT and VP-16. Cells were treated with ICG and VP-16 for 4 h after overnight incubation and then irradiated with an 800 nm laser at a light dose of 100 J cm^{-2}. Cell viability was evaluated by MTT assay 45 h after laser irradiation. The solid lines are best fits to the experimental data using a logistic function in Origin software. The dashed line and filled stars represent the calculated additive effect.

The results in this experiment show that, the normal cells may have similar levels of sensitivity to PDT treatment as those of cancer cells. Fortunately, in PDT, local targeting of the diseased tissue can be achieved by selective delivery of laser beams. Sensitivity to VP-16 treatment has been found to be similar in GM05757 and A549 cells. However, the combination treatment can induce a much stronger synergistic effect in A549 cells than in GM05757 cell and is more effective in killing A549 cells than GM05757 cells.

We have evaluated the cytotoxicity of the combination treatment of ICG-PDT and VP-16 in three human cancer cell lines and one human normal fibroblast cell line. Our results show that among all four cell lines studied, HeLa and GM05757 cells are more sensitive to ICG-PDT treatment than the other two cell lines. Similar levels of sensitivity to VP-16 chemotherapeutic treatment have been observed among HeLa, GM05757 and A549 cells, while NIH:OVCAR-3 cell are much more resistant to VP-16 as well as ICG-PDT. When ICG-PDT is combined with VP-16 chemotherapy, slight synergy is produced in GM05757 cells. Synergism is most significant in A549 cells. Moderate synergy has also been observed in HeLa and NIH:OVCAR-3 cells. However, much higher drug and light doses are required to induce significant killing of NIH:OVCAR-3 cells. These findings suggest that the combination of ICG-PDT and VP-16 chemotherapy may be developed as an effective treatment approach for selected cancers such as lung cancers.

4.3.5 The effects of treatment sequence on the cytotoxicity of the combination of ICG-PDT and VP-16 in A549 and HeLa cells

We have tested whether the presence of VP-16 at the time of laser irradiation is required for synergistic enhancement of cytotoxicity. In this experiment, cells were incubated with ICG for 4 h and then irradiated at 800 nm. After laser irradiation, cells were incubated with VP-16 for 4 h. MTT assay was performed 45 h after the removal of VP-16. The results are shown in Figure 4-7.

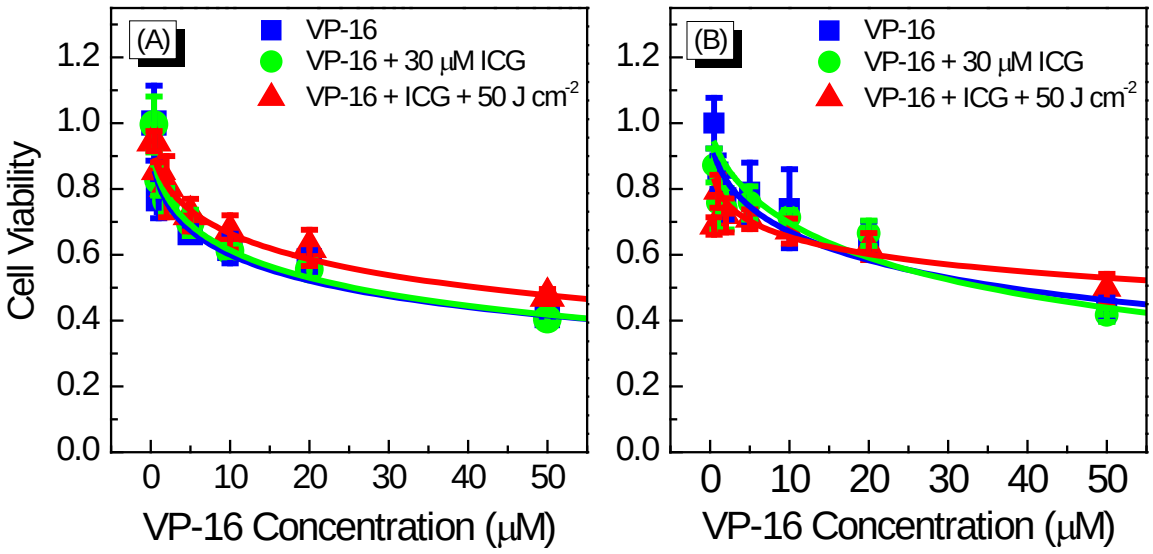

Figure 4-7: Sequence-dependent cytotoxicity of the combination treatment of ICG-PDT and VP-16 in (A) A549 and (B) HeLa cells. The cells were incubated with ICG for 4 h and then irradiated at 800 nm. VP-16 was added after laser irradiation. Cell viability was evaluated 45 h after laser irradiation by using the standard MTT assay. The solid lines are best fits to the experimental data using a logistic function in Origin software.

At the highest VP-16 concentration of 50 μM tested, we observed a cell viability of ~50% in both A549 and HeLa cells similar to the level of cytotoxicity observed in Sections 4.3.2 and 4.3.3, where cells were treated with VP-16 before laser irradiation. No significant difference in cell viability was observed among the groups treated with VP-16, VP-16 + ICG and VP-16 + ICG + 50 J cm^{-2} in either A549 or HeLa cells. This is in contrast to the strong synergistic effects observed in cells co-incubated with ICG and VP-16 before laser irradiation. This observation suggests that the presence of VP-16 at the time of laser irradiation is essential for synergistic enhancement of cytotoxicity induced by the combination treatment of ICG-PDT and VP-16.

4.3.6 Cytotoxicity of the laser-irradiated mixture of ICG and VP-16 in A549 cells

We performed another experiment in which we made several mixtures of ICG and VP-16 in the complete cell culture medium and irradiated them with various light doses. Cells were incubated with the laser-irradiated mixtures of drugs for 4 h and then incubated with drug-free medium for 45 h before adding MTT. The results are shown in Figure 4-8. Cytotoxicity of the cell culture medium and VP-16 at all three concentrations evaluated in this experiment didn't show significant dependence on light dose (Figure 4-8A). In cells treated with the mixtures of 50 μM ICG and VP-16, cytotoxicity didn't change significantly with increasing light dose (Figure 4-8B). When ICG was combined with VP-16, we noted that the cell viability decreased slightly compared with the groups treated with VP-16 alone. This has been attributed to be the dark effect discussed in Section 4.3.2. These results show that the cytotoxicity of the combination treatment of ICG-PDT and VP-16 differs dramatically from that of the laser irradiated mixtures of the two drugs. Therefore, it is likely that the observed synergistic effects induced by the combination treatment involve certain intracellular components such as enzymes.

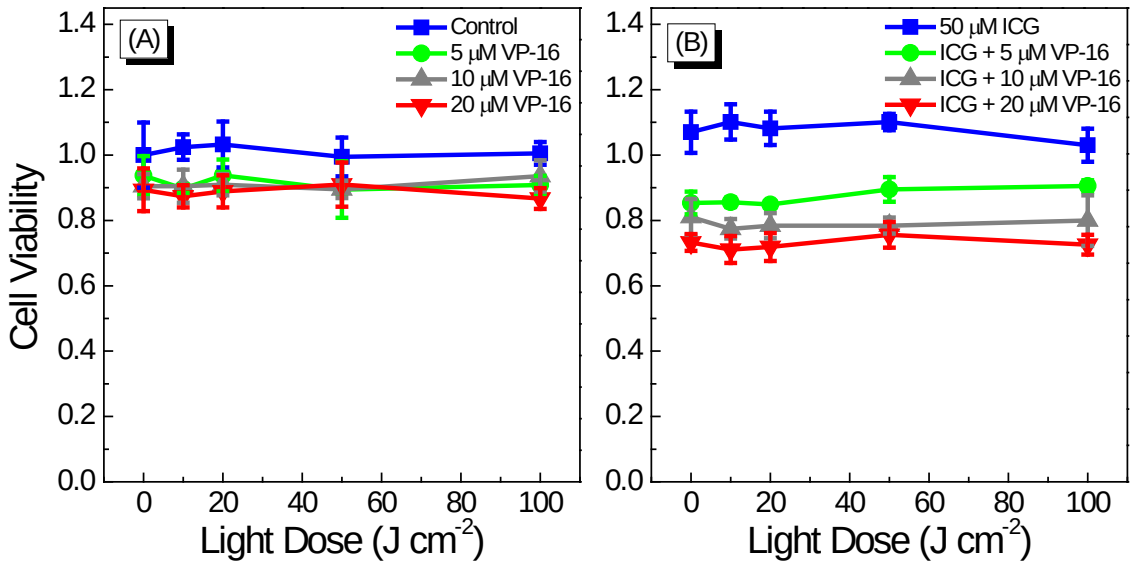

Figure 4-8: Cytotoxicity of laser-irradiated mixtures of ICG and VP-16 in A549 cells. Cells were treated with the photo-irradiated mixtures of ICG and VP-16 for 4 h. Cell viability was evaluated by using the standard MTT assay 45 h after the removal of the drugs.

The steady-state absorption spectra of 30 μM ICG and 30 μM ICG + 20 μM VP-16 were also recorded at all five light doses to see whether the presence of VP-16 affected the photo-degradation rate of ICG (Figure 4-9). We have calculated the differences in maximum absorbance between the laser-irradiated samples and dark controls and plotted the normalized values as a function of light dose in Figure 4-9C. Photo-degradation of ICG alone or in the presence of 20 μM VP-16 showed a linear dependence on irradiation dose. We didn't observe significant difference between the degradation rate of ICG in the absence and in the presence of VP-16. This finding indicates that there is no direct interaction between ICG and VP-16 in the complete cell culture medium under laser irradiation at 800 nm up to a light dose of 100 J cm^{-2}.

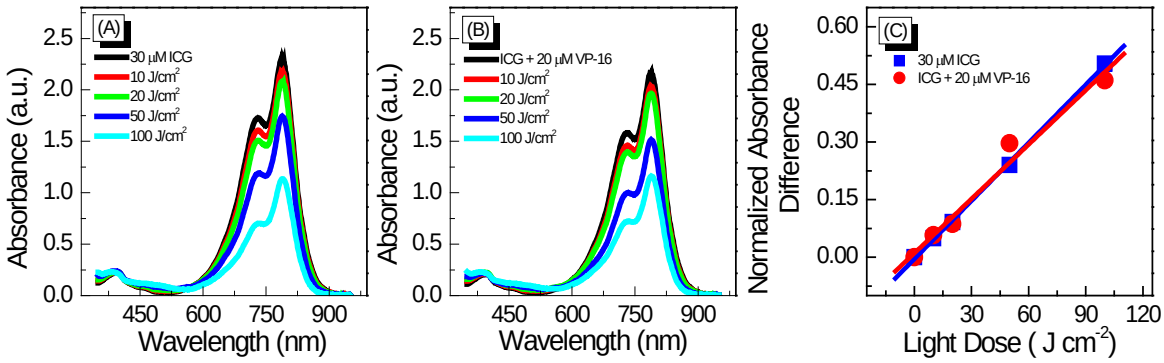

Figure 4-9: Spectral changes of 30 μM ICG in complete F12K cell culture medium with increasing light dose (A) in the absence and (B) presence of 20 μM VP-16. (C) Shows the absorbance difference between the laser irradiated samples and the dark controls as a function of light dose normalized to the absorbance of the dark controls. The solid lines are the best linear fits to the data.

Fluorescence measurements have been widely applied in physical, chemical and biological studies due to the extreme sensitivity of fluorescence to local environment. In this experiment, we measured the steady-state fluorescence spectra of 10 μM ICG in the presence of 0, 0.5 and 1 mM VP-16 (Figure 4-10A) to see whether there was direct interactions between ICG and VP-16 under laser irradiation. An excitation wavelength of 720 nm instead of 800 nm was chosen in order to minimize contribution from scattered light to the fluorescence intensity of the samples. Since the stock solution of VP-16 was made in DMSO, the fluorescence spectra of ICG in the presence of the same amounts of DMSO as that added in Figure 4-10A were also recorded and shown in Figure 4-10B.

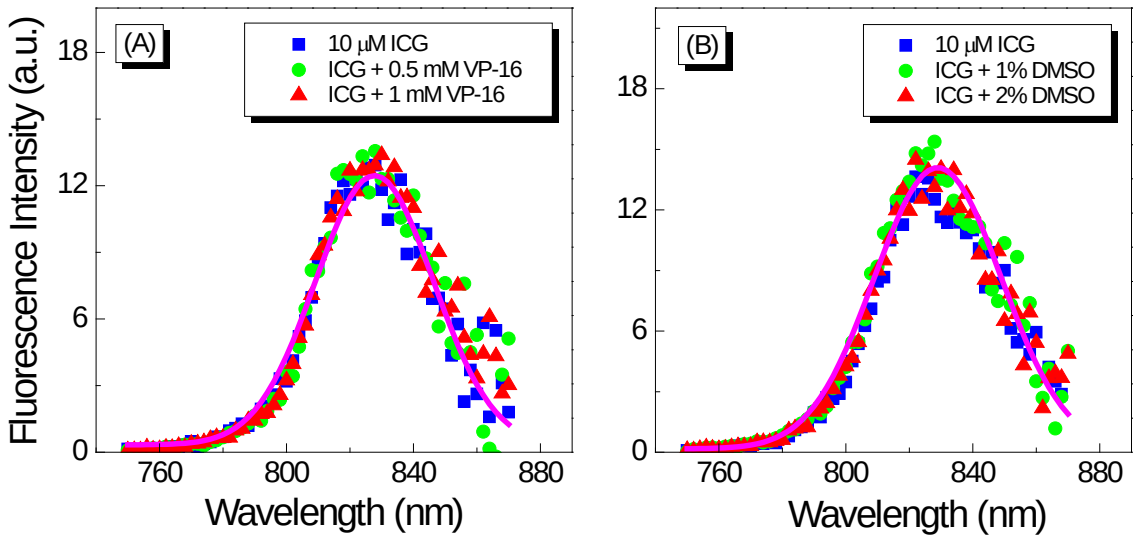

Figure 4-10: (A) Fluorescence spectra of 10 μM ICG in the presence of 0, 0.5, or 1 mM of VP-16. The excitation wavelength was 720 nm. The emission maximum is 829 nm. (B) The same amount of DMSO as in (A) was added to ICG in order to account for any effect due to the addition of the solvent of VP-16. The solid lines are the best Gaussian fits to the spectra of 10 μM ICG.

The fluorescence of ICG has a maximum at 829 nm consistent with the fluorescence maximum of ICG in water reported by Gerega *et al.* (269). With the addition of VP-16 or DMSO, no significant change in the fluorescence spectrum of ICG was observed. This observation is in agreement with what has been observed in the steady-state absorption experiment confirming the absence of direct interaction between the excited singlet state of ICG ($^1ICG^*$) and VP-16.

4.3.7 Electron-transfer-induced synergistic enhancement of cytotoxicity by the combination treatment of ICG-PDT and VP-16

Previously, Gantchev *et al.* have suggested that the mechanism for synergistic enhancement of cytotoxicity produced by combination of metallic phthalocyanine-mediated PDT and VP-16 is PDT-induced depletion of intracellular glutathione (GSH), an antioxidant that is believed to be able to reduce the highly cytotoxic radicals of VP-16 (175). In order to see whether this mechanism is responsible for the synergism observed in the present study, we have performed an experiment in which the cells were treated with VP-16 immediately after laser irradiation (see Section 4.3.5). We should have observed synergistic enhancement of cytotoxicity, if the ICG-PDT treatment induced cellular damages, which were expected to last for hours following laser irradiation (200), had potentiated the cytotoxicity of VP-16. Therefore, the strong synergy induced by the combination of ICG-PDT and VP-16 is not likely due to ICG-PDT produced cellular damages but involves direct or indirect interaction between ICG and VP-16 during the course of laser irradiation.

In our group, we have identified an electron-transfer reaction between a biological electron donor (TMPD; N,N,N′,N′-tetramethyl-p-phenylenediamine) and cisplatin (CDDP) responsible for synergistic enhancement to cytotoxicity in selected cancer cell lines (9). Based on the following considerations, we have proposed a similar mechanism in the present study: the enzyme-mediated electron-transfer reaction from VP-16 to ^{1}ICG* could induce synergistic enhancement of cytotoxicity *in vitro*. First, we have calculated the free energy

change of the electron-transfer reactions between ICG/^{1}ICG* and VP-16 by using the following Rehm-Weller equation (270):

$$\Delta G\ (eV) = nF(E_{ox} - E_{red}) - w_p - E_{00}, \quad (4\text{-}2)$$

where n is the number of electrons transferred, F is the Faraday's constant, E_{ox} and E_{red} are the oxidation potential of the donor and reduction potential of the acceptor, respectively, w_p describes the Coulombic attraction between ions generated by electron transfer reactions, and E_{00} is the energy of excitation. For most electron transfer reactions, nF is approximately equal to one and can be disregarded in the calculations. The work term, w_p, can also be disregarded due to the lack of electrostatic attraction between a charged species (ICG) and a neutral species (VP-16). The oxidation potential of VP-16 is 0.51 eV vs. SHE at pH 7 (271). The reduction potentials of ICG in acetonitrile have been reported to be -0.59 eV vs. SHE (272). Therefore, the free energy change of one-electron transfer from ICG to VP-16 can be estimated to be 1.1 eV suggesting that this reaction is thermodynamically unfavorable. When ICG is excited to ^{1}ICG*, the free energy change can be estimated to be -0.45 eV. A negative free energy change indicates that one-electron transfer from VP-16 to ^{1}ICG* is thermodynamically favorable. Second, we have demonstrated that incubating the cells with VP-16 immediately after ICG-PDT treatment didn't show any synergistic effect. This observation cannot be explained by independent action of ICG-PDT and VP-16 to activate different cellular pathways. Third, although our steady-state absorption and fluorescence spectroscopic results indicate the absence of direct reaction between ^{1}ICG* and VP-16, binding of VP-16 with intracellular enzymes such as oxidases may lower the activation

energy and increase the reaction rate. In humans, VP-16 can be oxidized by oxidases to phenoxy radicals (273), which may be further converted to metabolites that have been shown to be more activate than the parent compound VP-16 in inducing DNA DSBs (12-14, 274). Therefore, $^{1}ICG^{*}$ may act as an electron acceptor in those systems and facilitate the generation of VP-16 radicals.

4.3.8 Combination treatment of ICG-PDT and VP-16 increased the yield of DNA double strand breaks

To further investigate the mechanism underlying the synergistic effects observed in MTT assay results, we measured the yield of DNA DSBs. For this, the commercial HCS DNA damage kit was used. Representative images are shown in Figure 4-11, Figure 4-12 and Figure 4-13 for A549, HeLa and NIH:OVCAR-3 cells, respectively. VP-16 is known to cause DNA DSBs and γH2AX has been shown to be a sensitive marker of DNA DSBs induced by a variety of DNA damaging agents including VP-16 (262, 275-277). In the present study, γH2AX foci (red channel) were indeed observed when cells were treated with VP-16 (row #2). While the brightness of red fluorescence didn't change significantly when cells were treated with VP-16 and ICG (row #3), laser irradiation produced significantly more γH2AX foci as shown in the last row.

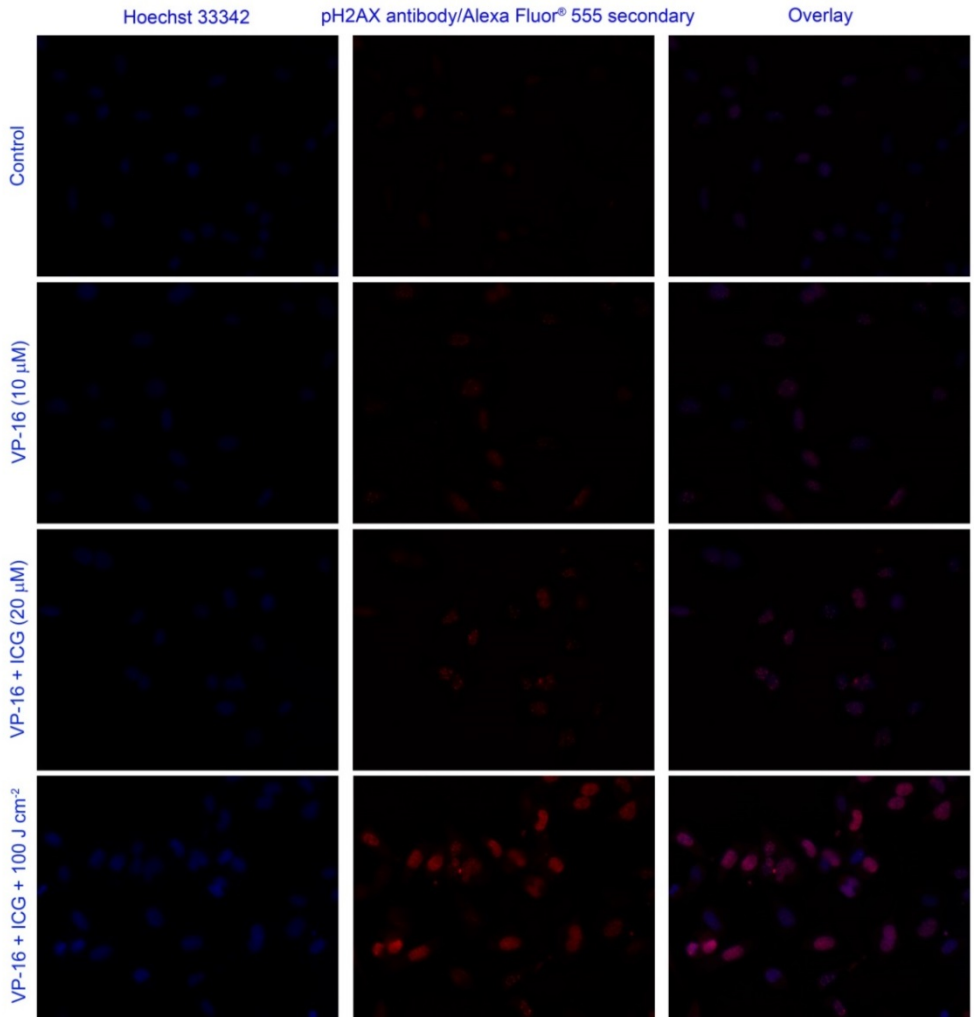

Figure 4-11: Representative images of the combination treatment of ICG-PDT and VP-16 in A549 cells using the HCS DNA damage kit. The cells were treated with VP-16 and ICG after overnight incubation. After 4 h incubation, the cells were washed twice with PBS and irradiated at 800 nm. DNA damages were measured using the HCS DNA damage kit 18h after laser irradiation. The images were taken on a Nikon Eclipse TS100/TS100-F microscope. Alexa Fluor® 555 is shown in red (λ_{ex} = 510-560 nm; λ_{em} > 590 nm). Hoechst 33342 is shown in blue (λ_{ex} = 330-380 nm; λ_{em} > 420 nm). The exposure time was 6 s. Background images were taken under the same experimental conditions and subtracted using Photoshop software.

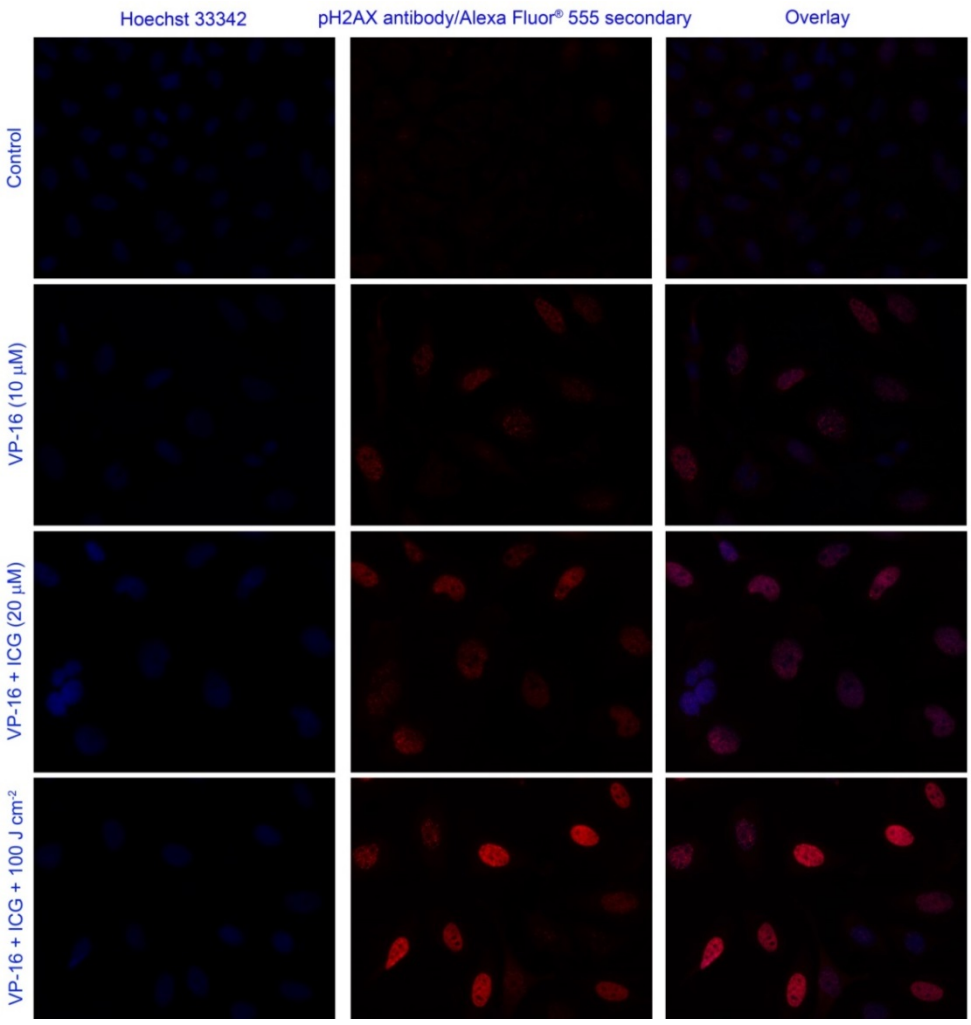

Figure 4-12: Representative images of cytotoxicity of the combination treatment of ICG-PDT and VP-16 in HeLa cells using the HCS DNA damage kit. The experimental conditions were identical to those in A549 cells.

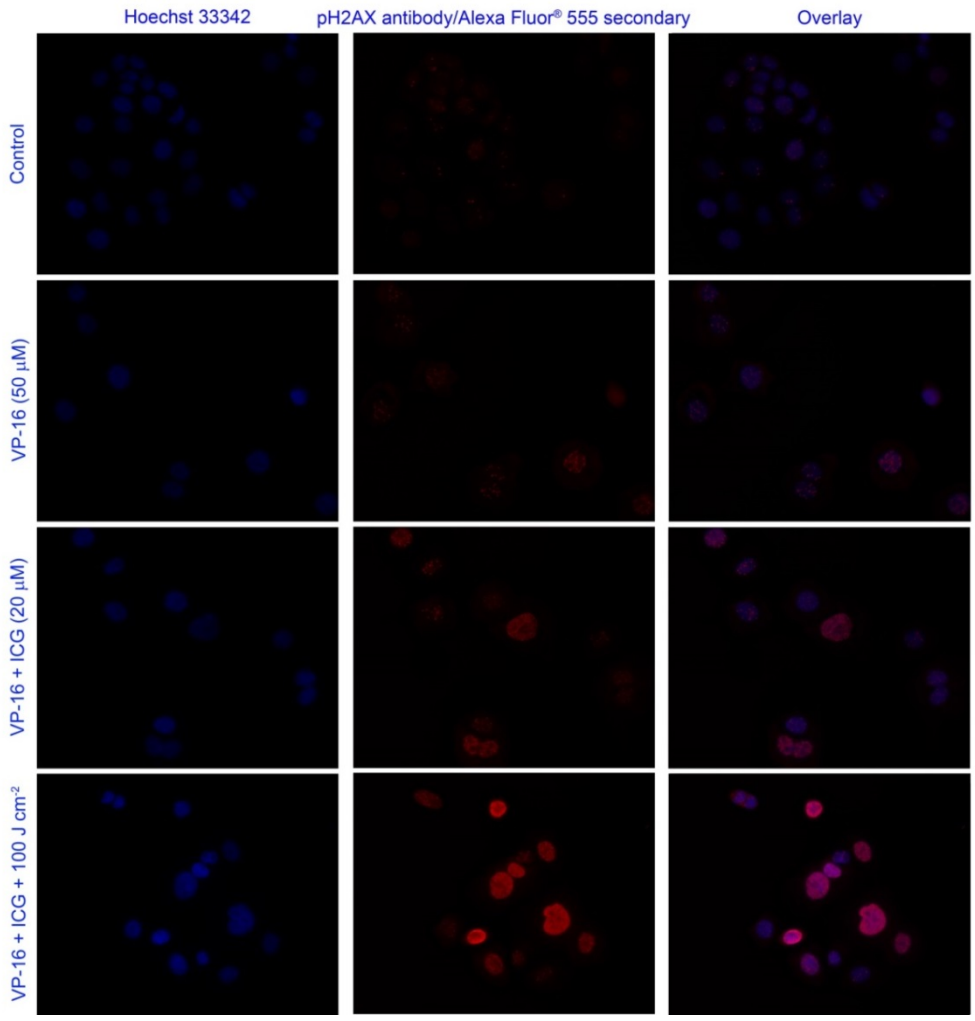

Figure 4-13: Representative images of cytotoxicity of the combination treatment of ICG-PDT and VP-16 in NIH:OVCAR-3 cells using the HCS DNA damage kit. The experimental conditions were identical to those in A549 cells.

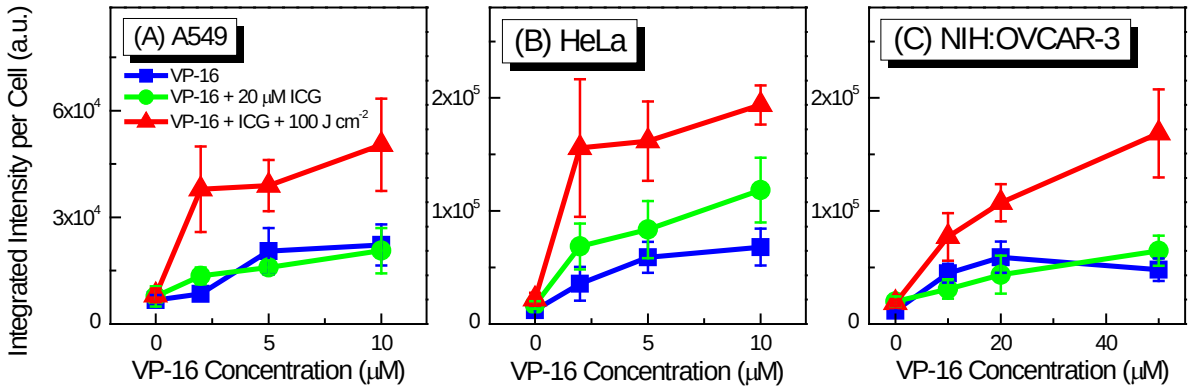

Figure 4-14: Integrated Alexa Fluor® 555 fluorescence intensity per cell as a function of VP-16 concentration in (A) A549, (B) HeLa and (C) NIH:OVCAR-3 cells using the HCS DNA damage kit. The integrated fluorescence intensity was calculated and the number of cells was counted using the Photoshop software. Results represent mean ± S.D. of at least three images.

It has been suggested that the relative yield of DNA DSBs could be measured more accurately by using the total area of γH2AX foci than the total number of the foci (262). Therefore, we plotted the average of integrated fluorescence intensity of the red channel as a function of VP-16 in Figure 4-14. Intensity of γH2AX foci increased with increasing VP-16 concentration in all three cancer cell lines. When cells were treated with ICG and VP-16, the intensity of γH2AX foci was not changed significantly in A549 and NIH:OVCAR-3 cells. A slightly higher intensity was obtained in HeLa cells. With a light dose of 100 J cm^{-2}, the fluorescence intensity was increased by ~2 fold suggesting increased yields of DNA DSBs. These results indicate that increased generation of DNA DSBs by the combination treatment of ICG-PDT and VP-16 is at least partially responsible for the synergistic enhancement of cytotoxicity observed in MTT experiments.

4.3.9 Detection of singlet oxygen induced by the combination treatment of ICG-PDT and VP-16 in A549 cells

In PDT, tumor destruction is believed to be achieved through the generation of cytotoxic ROS especially $^1O_2$. Therefore, we detected the intracellular generation of $^1O_2$ following laser irradiation by using a fluorescence probe for $^1O_2$ known as the singlet oxygen sensor green (SOSG). Representative images are shown in Figure 4-15. The first column shows the images from the control group and the groups treated with 50 μM ICG, 100 μM VP-16 and ICG + VP-16. No detectible fluorescence was observed. The second column shows the images from the same drug treatment groups with the addition of 20 μM SOSG. Weak green fluorescence can be seen. The third column shows the results of the groups treated with the drugs and laser irradiation at a light dose of 50 J cm^{-2}. The fluorescence of the group treated with ICG + VP-16 + 50 J cm^{-2} was found to be brighter than that of the other groups in the same column. In the last column, cells were irradiated in the presence of 20 μM SOSG + 50% D_2O. Again, the group treated with both drugs and laser irradiation showed brighter fluorescence than the other three images. We also noted that the fluorescence intensity of images in the last column was stronger than the corresponding ones in the other three columns.

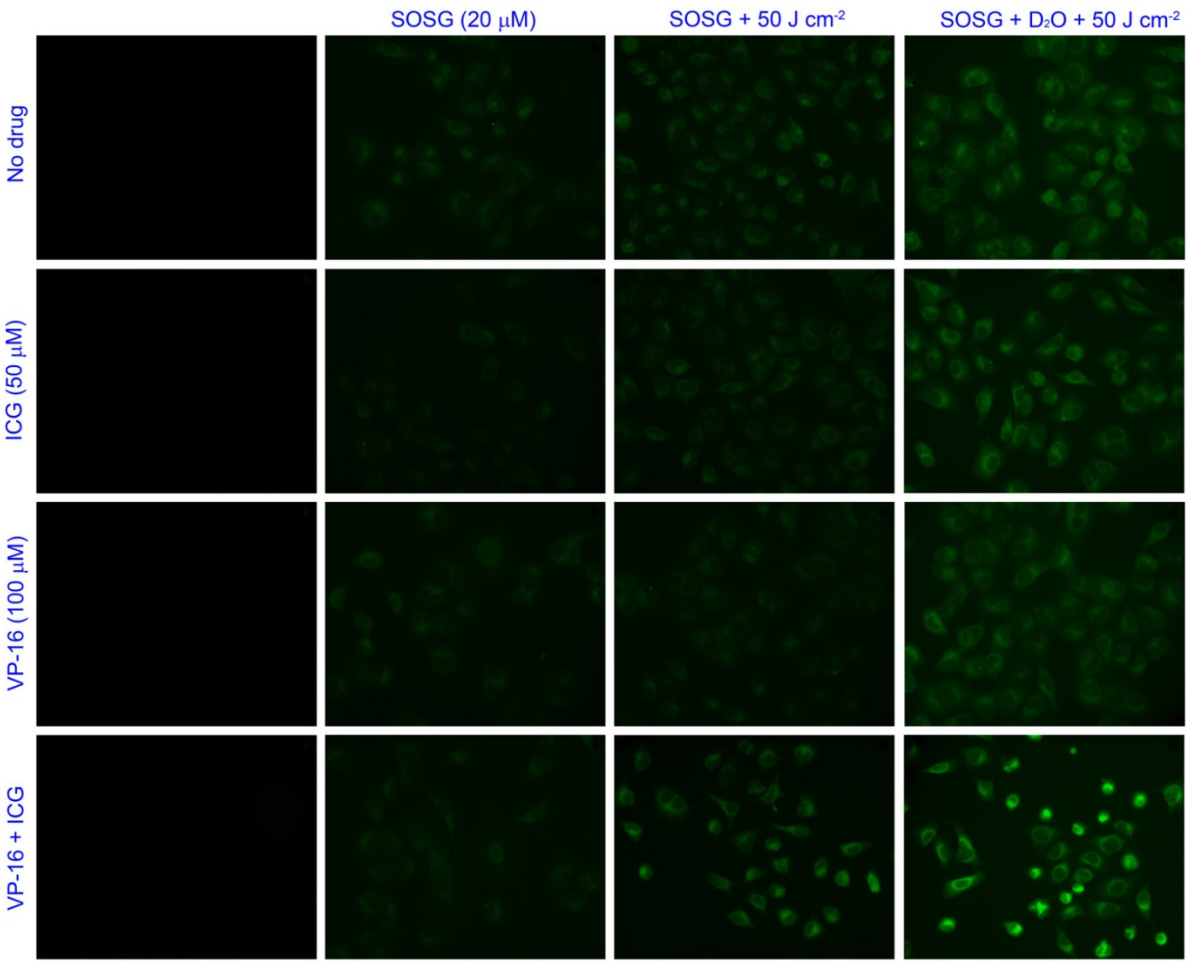

Figure 4-15: Fluorescence detection of intracellular singlet oxygen generation using Singlet Oxygen Sensor Green (SOSG) in A549 cells. The cells were incubated with 50 μM ICG, 100 μM VP-16 or the combination of the two drugs for 4 h. After incubation, the cells were irradiated at 800 nm in the absence or presence of 20 μM SOSG. The enhanced fluorescence intensity in the presence of 50% D_2O confirms the involvement of $^1O_2$. The images were taken on a Nikon Eclipse TS100/TS100-F microscope after irradiation. The filter set with λ_{ex} = 450-490 nm and λ_{em} > 520 nm was used. All images were taken with an exposure time of 6 s. A background image was taken under the same experimental conditions and subtracted using Photoshop software.

To quantify the relative yield of $^1O_2$, we calculated the average fluorescence intensity per cell by using Photoshop software. The results are plotted in Figure 4-16.

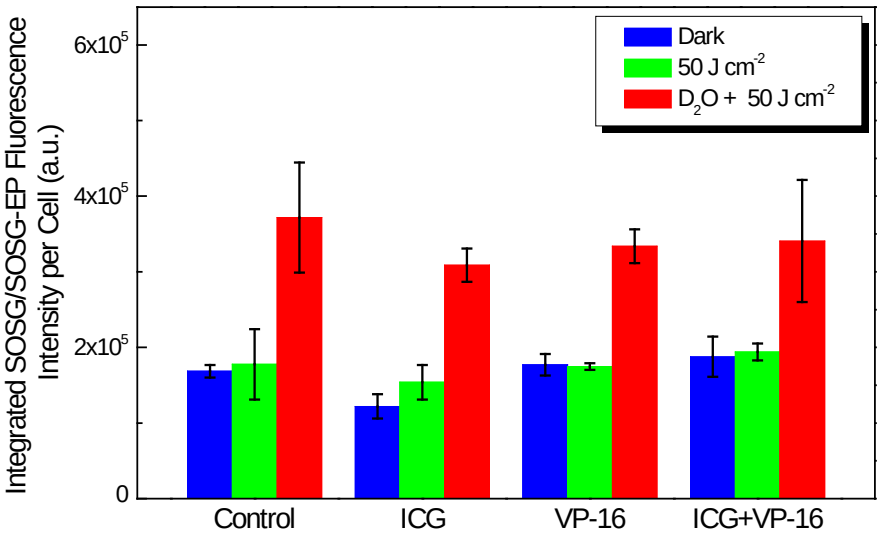

Figure 4-16: Integrated SOSG/SOSG-EP fluorescence intensity per cell in A549 cells. The integrated fluorescence intensity was calculated and the number of cells was counted using the Photoshop Software. Results represent mean ± S.D. of at three images.

Without laser irradiation, no significant difference was observed among the groups not treated with drug, treated with ICG only, VP-16 only and ICG + VP-16. The difference between the groups treated with or without laser irradiation was found to be not significant. In the presence of 50% D_2O, we observed a ~2-fold increase in the average fluorescence intensity compared with the group irradiated in the absence of D_2O. It's worth noting that the average fluorescence of SOSG-EP of the samples treated with both ICG and VP-16 didn't differ significantly from those treated with either ICG or VP-16, while the fluorescence images from the samples treated with ICG + VP-16 looked brighter than those from the other treatment groups (Figure 4-15). We noted that, with laser irradiation, cells in the ICG + VP-16 treatment groups appeared to be smaller and more rounded while those in the ICG or VP-16 treatment groups were more extended. This is reasonable because cell

shrinkage and rounding are morphology characteristics of cell undergoing apoptosis. Therefore, the brighter fluorescence observed in Figure 4-15 is likely due to the reduced volume of the cells instead of increased yields of SOSG-EP. This is not surprising considering the extremely low $^1O_2$ yield of ICG (218, 251). The observation of a 2-fold increase in the intensity of the green fluorescence in the presence of D_2O suggested involvement of $^1O_2$, which was generated probably by cellular metabolism instead of ICG-PDT treatment.

4.3.10 Drug-dose response of the combination treatment of ICG-PDT and VM-26 in A549 cells

We also evaluated the cytotoxicity of ICG-PDT in combination with another podophyllotoxin derivative VM-26. The treatment procedure was the same as that applied in combination treatment of ICG-PDT and VP-16. The results are shown in Figure 4-17. The IC_{50} of VM-26 was determined to be 3.31 ± 0.54 μM, which was ~8% of that of VP-16. When cells were incubated with VM-26 and 50 μM ICG, the IC_{50} was reduced slightly to 1.85 ± 0.28 μM, which could be attributed to the dark effects discussed in Section 4.3.2. With laser irradiation, further reduction of more than 90% (IC_{50} = 0.27 ± 0.07 μM) was observed at a light dose of 100 J cm^{-2}.

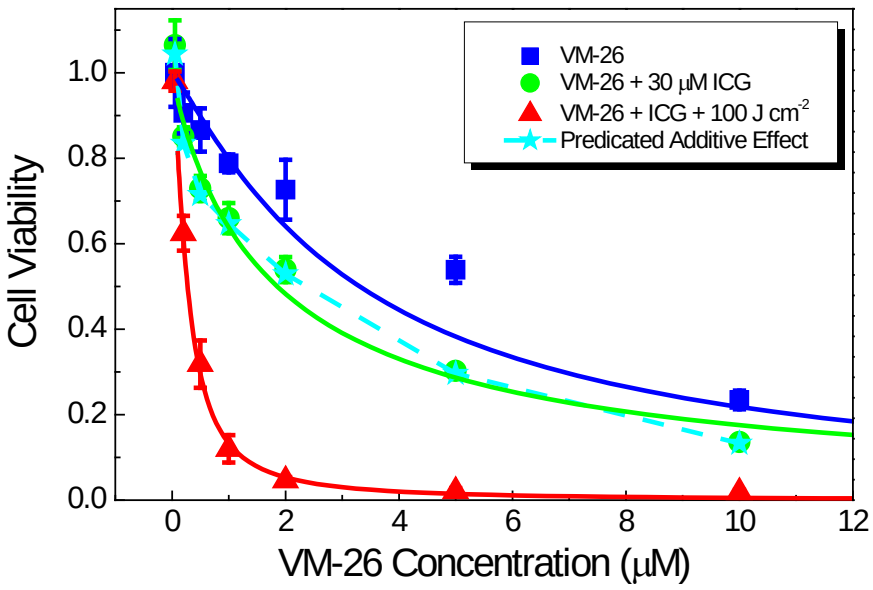

Figure 4-17: Drug-dose response curves for cell viability of A549 cells treated with the combination of ICG-PDT and VM-26. Cells were treated with ICG and VM-26 for 4 h after overnight incubation and then irradiated with an 800 nm laser at a light dose of 100 J cm^{-2}. Cell viability was evaluated by MTT cell viability assay 45 h after laser irradiation. The solid lines are best fits to the experimental data using a logistic function in Origin software. The dashed line and solid stars represent the calculated additive effect.

Both VP-16 and VM-26 are derivatives of podophyllotoxin and their antitumor activities have been studied in a number of cell lines (278-281). It has been found that VM-26 is about 10 times more effective than VP-16 in a human lymphoblastic leukemia cell line (CCRF-CEM (278)) and several human small cell and non-small cell lung carcinoma cell lines (NCI-H69, NCI-N592, OC-TOL, OC-ROL, OC-NYH (279), NCI-H460, NCI-H187, NCI-H209, NCI-h522, NCI-H1284, NCI-H322, and NCI-H69 (280)). In the present study, we have obtained an IC_{50} of VM-26 that is ~8% of the IC_{50} of VP-16 consistent with the higher potency of VM-26 than VP-16 reported by other research groups. The lower IC_{50} of VM-26 has been attributed to be a higher uptake of VM-26 than VP-16

(282). In cells treated with VM-26 and ICG-PDT at an ICG concentration of 30 μM, the degree of reduction in IC_{50} has been found to be ~15% higher than that observed with VP-16 under the same ICG-PDT treatment conditions. A similar level of synergy observed when combining ICG-PDT with VP-16 and VM-26 suggests the involvement of the same mechanism, which has been proposed in Section 4.3.7. The oxidation potential of VM-26 has been reported to be 0.56 eV vs. SHE at pH 7 (283), which is 0.05 eV higher than that of VP-16 (271). The free energy change of one-electron transfer from VM-26 to $^1ICG^*$ can be estimated to be -0.4 eV by using Equation (4-2) indicating that this reaction is also energy favorable. The close oxidation potentials of VP-16 and VM-26 are expected to lead to a similar level of synergy, which has been confirmed by the MTT cytotoxicity results. This finding is in agreement with our proposal of an electron-transfer-based mechanism for synergistic enhancement of cytotoxicity. These results also show that synergistic enhancement of cytotoxicity is not limited to the combination of ICG-PDT with VP-16. It has also been achieved with VM-26. Therefore, studies of the combination effects of ICG-PDT with other chemotherapeutic drugs would be of great help in the development of clinically effective treatment strategies.

4.3.11 Steady-state absorption and fluorescence spectra of VP-16

We have measured the steady-state absorption and fluorescence spectra of VP-16 in water (Figure 4-18). VP-16 has an absorption maximum at 283 nm, which is the same as that observed in absolute methanol (284). The fluorescence spectrum has been recorded with our

homemade fluorometer and corrected by using the collection efficiency of the system as described in Chapter 2. When excited at 266 nm, the fluorescence spectrum of 100 μM VP-16 has a maximum at 350 nm. Holthuis *et al.* have reported that the fluorescence maximum of VP-16 is ~320 nm in absolute methanol (284). It is well known that solvent polarity can have a dramatic effect on fluorescence spectra: a spectral shift may be produced as a result of decreased excited-state energy with increasing solvent polarity (224). The red-shifted fluorescence spectrum obtained in this study is likely due to an increase in solvent polarity from methanol to water.

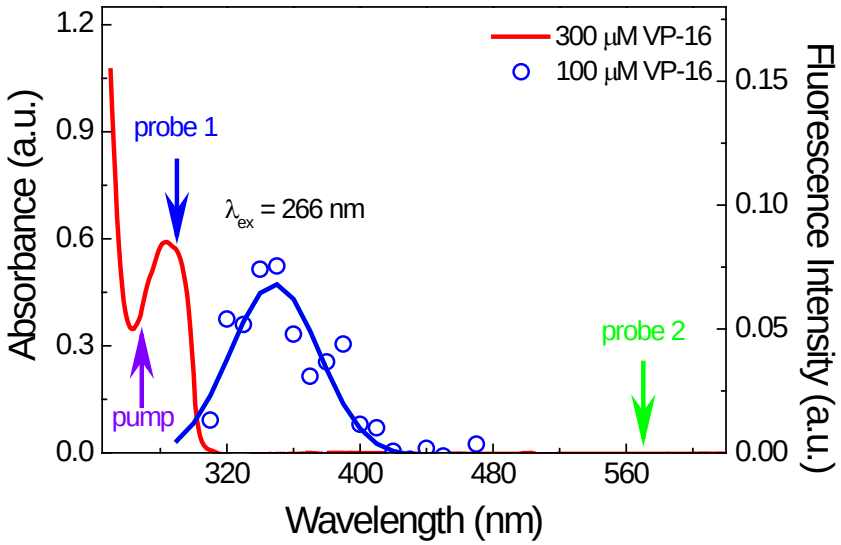

Figure 4-18: UV-visible absorption spectrum of 300 μM VP-16 and steady-state fluorescence spectrum of 100 μM VP-16 in water. The arrows indicate the pump and probe wavelengths in the transient absorption experiment. The excitation wavelength for the fluorescence spectrum was 266 nm. The blue solid line is the best Gaussian fit to the experimental data.

4.3.12 Femtosecond time-resolved transient absorption spectroscopic results

We have obtained the femtosecond time-resolved transient absorption decay kinetic profiles of various concentrations of VP-16 in water (Figure 4-19B and Figure 4-20). The pump wavelength was 266 nm, where VP-16 had significant absorbance (Figure 4-18). Previously, Lu *et al.* have demonstrated that, in aqueous solution, VP-16 can be ionized by 248 nm laser to generate VP-16 cation radicals ($VP\text{-}16^{+\cdot}$), which have an absorption maximum at 290 nm (285). Since the pump wavelength of 266 nm used in this study was very close to 248 nm used by Lu *et al.*, our first experiment was conducted with a probe wavelength of 290 nm to see whether $VP\text{-}16^{+\cdot}$ were generated under our experimental conditions. Figure 4-19 shows the transient absorption kinetics of the solvent water and 200 μM VP-16 at various pump powers. With a pump wavelength of 266 nm, solvated electrons can be generated through two-photon excitation of water (222). Indeed, we observed positive signals in pure water at all the pump powers used in this experiment (Figure 4-19A). The strong signal at delay time zero is the coherent spike produced from the interaction between the ultra-short pump and probe pulses (219). The curves can be fitted with a bi-exponential function yielding a short lifetime of 34.3 ± 18.8 ps and a much longer one, which is beyond the detection limit of our fs-TRLS system. The pre-exponential factor of the short-lived component has been plotted as a function of pump power in Figure 4-19D. The linear fit to the data points on a log-log plot yields a slope of 2.2 ± 0.3 ps confirming a quadratic dependence of the signal on laser power. Therefore, the species detected in pure water can be assigned to be solvated electrons

generated from two-photon excitation of water. Figure 4-19B show the transient absorption kinetics of VP-16. In Figure 4-19C, the contribution from the solvated electrons has been removed by subtracting the signal of pure water from that of VP-16. Fitting of the data with a bi-exponential function gives a short lifetime of 74.0 ± 3.8 ps and a longer one of on the scale of nanosecond. The lifetime of the short-lived component is much longer than that observed in pure water indicating that this species is not solvated electron generated from photoionization of VP-16. We have tentatively assigned this short-lived species to be the excited singlet state of VP-16 (^{1}VP-16*). The long-lived component, as shown in Figure 4-19D, has a linear dependence on laser power suggesting that a one-photon process is responsible the generation of this species. Previously, Sun *et al.* reported that VP-16 could capture the solvated electrons to produce the anion radicals of VP-16 (VP-16$^{-\cdot}$) (286), which had absorption at the currently probe wavelength of 290 nm (285). If the VP-16$^{-\cdot}$ was produced from the reaction of VP-16 with the solvated electron, the absorbance should show a quadratic dependence on pump power. Therefore, our observation of a linear dependence of the contribution from the long-lived species on pump power ruled out the possibility that this component was the VP-16$^{-\cdot}$. Moreover, we noted that Lu *et al.* had obtained the transient absorption spectrum of VP-16 from 248 nm laser photolysis and assigned the species having an absorption maximum at 290 nm to be VP-16$^{+\cdot}$ generated from one-photon ionization of VP-16 (285). Accompanying the generation of VP-16$^{+\cdot}$, solvated electrons, which have a broad absorption band extending from the near-ultraviolet range to the near-infrared range, should have also been produced. Therefore, the slow decaying component could be a mixture

of solvated electrons, VP-16$^{+\cdot}$ and VP-16*. In order to determine the identity of this long-lived species, we performed more experiments by changing the probe wavelength to 570 nm, where absorption by VP-16$^{+\cdot}$ was negligible (285).

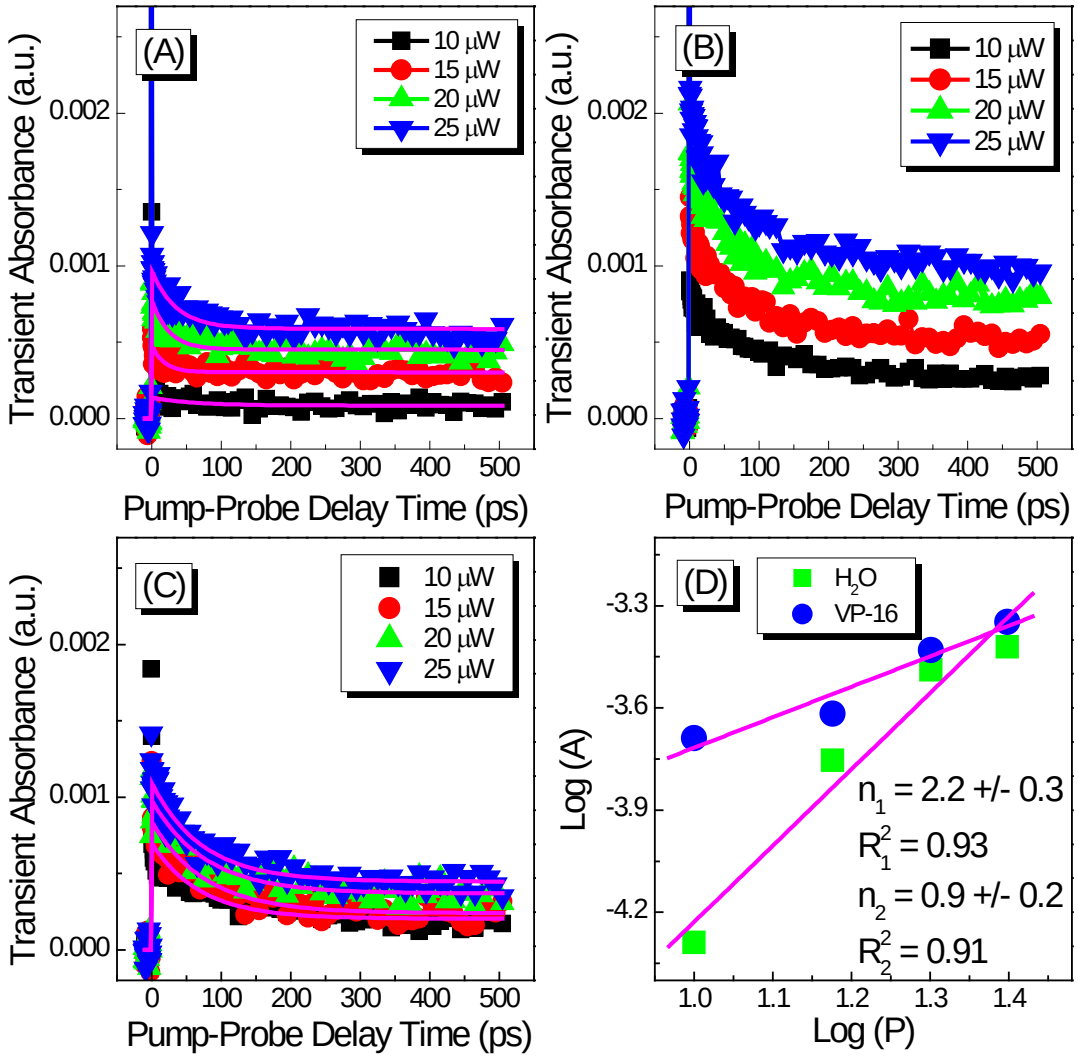

Figure 4-19: Power-dependence of the transient absorption decay kinetics of (A) water and (B) 200 μM VP-16. (C) The transient absorption curves for VP-16 after removing the contribution from the solvent water. The pump and probe wavelengths were 266 and 290 nm, respectively. The pink solid lines represent the best fits to the experimental data with a

multi-exponential function using Scientist software. (D) The log-log plot of the pre-exponential factors against pump power. Linear fits to the data yield slopes of 2.2 ± 0.3 and 0.9 ± 0.2 for water and VP-16, respectively, confirming two-photon generation of solvated electrons in water and one-photon excitation of VP-16.

Figure 4-20 shows the transient absorption kinetics of various concentration of VP-16 in water. The pump and probe wavelength were 266 and 570 nm, respectively. As shown in Figure 4-20A, pure water has very strong signal at this probe wavelength at a pump power of only 6 μW. The intensity of the short-lived component increased with increasing concentration of VP-16 without affecting the intensity of the long-lived component. Considering that the stock solution of VP-16 was made in DMSO, a pre-solvated electron scavenger (19), the kinetic trace of 2% DMSO in water was also recorded to see whether the addition of DMSO had any effect on the signal of the solvated electrons. The kinetic trace of 2% DMSO overlapped with that of pure water indicating that the contribution from DMSO was negligible. We further removed the contribution of water to kinetic traces by subtracting the signal of pure water from that of VP-16 solutions and the results are shown in Figure 4-20B. The data can be adequately fitted with a single-exponential function to produce a decaying lifetime of 90.0 ± 3.8 ps, which is very close to the lifetime of 74.0 ± 3.8 ps observed at 290 nm suggesting that the same species has been detected. However, the long-lived component observed at 290 nm was not observed at 570 nm. This finding suggests that no detectable amount of solvated electrons has been generated from VP-16 under our experimental conditions and the long-lived species detected at 290 nm is not the cation radical of VP-16. Therefore, the long-lived component is most likely the excited triplet state of VP-16 (^{3}VP-16*). However, further investigation is required to confirm the identity of this

species, which is beyond the scope of this study. The transient absorption results show that under our experimental conditions, VP-16 is not ionized by the laser pulses. The excited singlet state of VP-16 has been detected at both 290 and 570 nm and the lifetime has been determined to be in the range 70-90 ps.

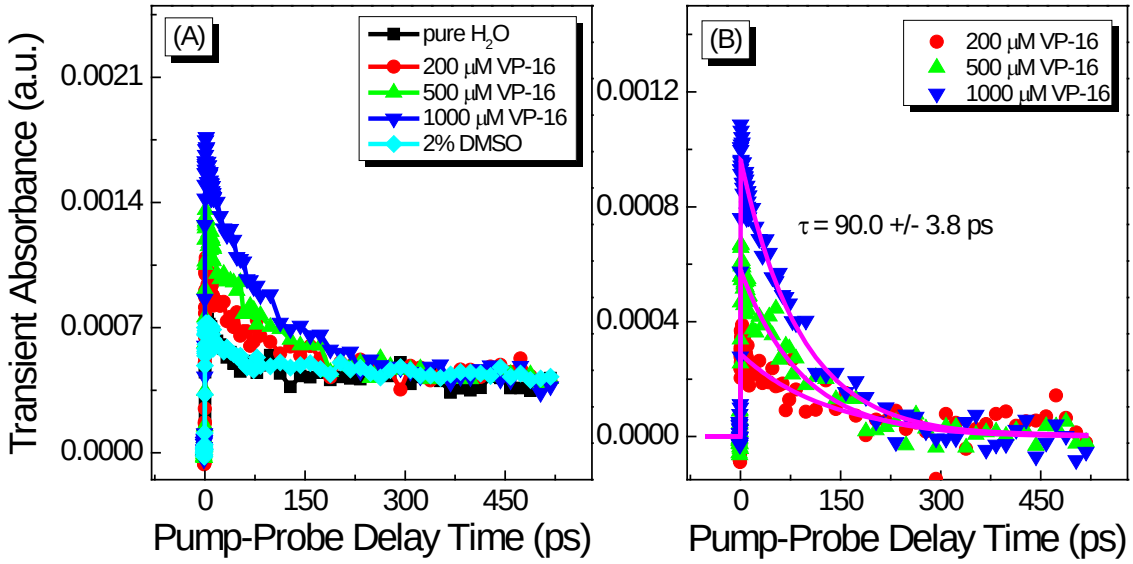

Figure 4-20: Pump-probe transient absorption decay kinetics of 200, 500 and 1000 μM VP-16 in water. The pump and probe wavelengths were 266 and 570 nm, respectively. The pump power was 6 μW. (A) The experimental data. (B) The decay kinetics of VP-16 after removing the contribution from the solvated electrons generated from the solvent. The solid lines represent the best fits to the experimental data yielding a decaying lifetime of 90.0 ± 3.8 ps.

4.3.13 Femtosecond time-resolved fluorescence spectroscopic results

To further confirm that the short-lived species detected by the transient absorption measurements is ^{1}VP-16*, we have performed transient fluorescence spectroscopic

experiments. Figure 4-21 shows the transient fluorescence decay kinetics of 500 μM VP-16 in water excited at 266 nm. The detection wavelength was 353 nm.

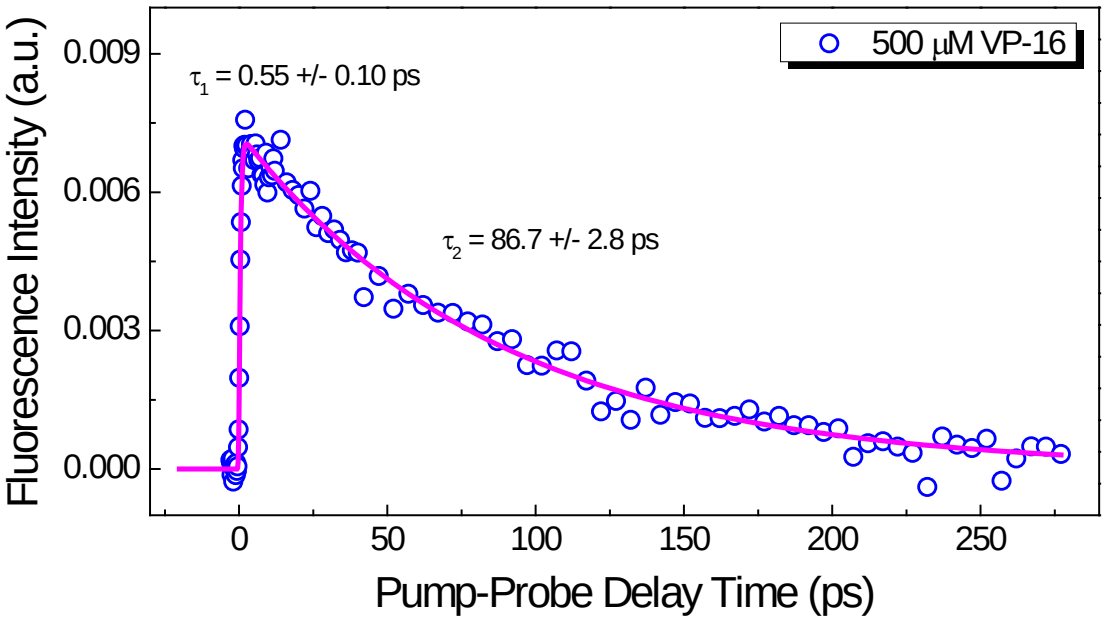

Figure 4-21: Pump-probe fluorescence decay kinetics of 500 μM VP-16 in water. The excitation and emission wavelengths were 266 and 353 nm, respectively. The open blue circles are the experimental data. The solid red line represents the best fits to the experimental data yielding a rising lifetime of 0.55 ± 0.10 ps and a decaying lifetime of 86.7 ± 2.8 ps.

The kinetic trace can be fitted with a single-exponential function yielding a fluorescence lifetime of 86.7 ± 2.8 ps, which is consistent with the excited singlet state lifetime of VP-16 determined by transient absorption spectroscopy.

The fs time-resolved laser spectroscopy (fs-TRLS) has been demonstrated to be a powerful tool in studying the ultrafast dynamics of molecules and unraveling the molecular mechanism of action of anticancer drugs (19, 20, 182, 183, 217-221). In the present study,

we have performed fs time-resolved transient absorption and fluorescence spectroscopic studies on VP-16. The fluorescence lifetime of VP-16 in water has been determined to be 86.7 ± 2.8 ps. To the best of our knowledge, this has not been reported before. We have also obtained the transient absorption kinetic traces of ^{1}VP-16* at 290 and 570 nm. Although the pump wavelength of 266 nm is closed to 248 nm used by Lu *et al.* (285), no significant contribution from VP-16$^{+\cdot}$ has been observed in the present study. The long-lived species detected at 290 nm has been assigned to ^{3}VP-16*. These results suggest that the fs-TRLS may be applied in studying the mechanism of anticancer activity of VP-16.

4.4 Summary

We have performed *in vitro* cytotoxicity studies on the combination effects of ICG-PDT with VP-16 or VM-26 in three human cancer (A549, HeLa and NIH:OVCAR-3) cell lines and one human normal fibroblast (GM05757) cell line. Sensitivity to VP-16 treatment has been found to be similar among A549, HeLa and GM05757 cells. HeLa and GM05757 cells have been shown to be much more sensitive to ICG-PDT treatment than the other two cell lines. Among all four cell lines studied, NIH:OVCAR-3 cells are most resistant to both VP-16 and ICG-PDT treatments. With combination treatment of ICG-PDT and VP-16/VM-26, strong synergistic enhancement of cytotoxicity has been observed in A549 cells in wide ranges of drug concentrations and light doses. A more than 95% reduction in IC_{50} has been obtained in cells co-treated with VP-16 and 50 μM ICG + 100 J cm^{-2}. The degree of enhancement has been found to be moderate in HeLa and NIH:OVCAR-3 cells and lowest in GM05757 cells.

We have measured the relative yields of DNA DSBs by using the commercial HCS DNA damage kit and found that the combination treatment can increase the yields of DSBs by ~2-fold in the three cancer cell lines. These findings suggest that ICG-mediated PDT may be combined with VP-16/VM-26 in treating selected cancers such as lung cancers. Synergistic enhancement of cytotoxicity has the potential of increasing the effectiveness of treatment and more importantly, reducing toxic side effects of the chemotherapeutic drugs. Furthermore, the observation of a strong dependence of the degree of synergy on light dose suggests that the reaction can be controlled by light. Targeted delivery of laser beams may further reduce the overall toxicity of the treatment.

The synergism has been demonstrated to depend on the sequence of treatment. Synergistic effects were not observed when VP-16 was added after laser irradiation. This finding indicates the involvement of direct or indirect interaction between ICG and VP-16 during the course of laser irradiation. We have also evaluated the cytotoxicity of the laser-irradiated mixtures of the drugs and found that intracellular components, probably enzymes, might be required for the activation of the drugs. Based on these results, we have proposed an electron-transfer-based mechanism for synergistic effects observed in cytotoxicity studies. The electron-transfer reaction from VP-16/VM-26 to $^{1}ICG^{*}$ has been found to be thermodynamically favorable with negative free energy changes of -0.45 and -0.4 eV for VP-16 and VM-26, respectively. The small difference between the free energy changes of the two drugs implies a similar level of cytotoxicity associated with the reactions, which has indeed been observed: reductions of 74% and 95% in IC_{50} have been observed for VP-16 and

VM-26, respectively. This result is also in agreement with our proposed mechanism for synergism.

In summary, these studies may help improve our understanding of the molecular mechanisms underlying the synergistic enhancement of ICG-PDT with chemotherapeutic drugs and thus, facilitate the development of more effective treatment approaches for cancers.

5 Combination of Near Infrared Light-Activated Photodynamic Therapy Mediated by Indocyanine Green with Cisplatin/Oxaliplatin Chemotherapy

5.1 Background

Cisplatin (CDDP) is one of the most widely used chemotherapeutic drugs currently available for treating cancers of various organs such as bladder, blood vessel, bone, brain, cervix, lymphoma, lung, and ovary (7-9). The major cellular target of CDDP is believed to be nuclear DNA. Several forms of damages, including single strand breaks (SSBs), double strand breaks (DSBs), and intrastrand or interstrand crosslinks, can be formed upon reaction of CDDP with DNA (7, 287, 288). These DNA damages may be repaired through a number of DNA repair pathways. However, failure to repair these damages may trigger apoptosis that finally leads to cancer cell death. The great success of CDDP as an anticancer drug has stimulated the development of many platinum-based anticancer drugs. Among them, carboplatin and oxaliplatin (OXP) have been approved by the U.S. Food and Drug Administration (FDA) for clinic use (7, 287, 288). Carboplatin is less toxic than CDDP and thus, produces fewer side effects. However, its spectrum of activity is identical to that of

CDDP making it not effective against CDDP-resistant cancers. Oxaliplatin is currently being used in combination with 5-fluorouracil (5FdUr) for the treatment of metastatic colorectal cancers. It has also been found to be effective in treating cancers that are resistant to CDDP and carboplatin.

Despite the wide use of platinum-based anticancer drugs, especially cisplatin, their administration is often associated with severe side effects and many cancers acquire resistance to the drugs overtime (153, 156, 158, 249, 250). One of the approaches to overcome these limitations of platinum-based drugs is to combine conventional chemotherapy with photodynamic therapy (PDT). In PDT, both the photosensitizing agents and light are not toxic by themselves. It is the combination of these two components that produces antitumor effects. Combination of chemotherapy with PDT may produce synergistic effects that can reduce the toxic side effects of the chemotherapeutic drugs. Moreover, the combination treatment has the potential of overcoming drug resistance. Therefore, many research groups have investigated the combination effects of PDT with chemotherapy that involves CDDP, 5FdUr, etoposide (VP-16), and a number of other chemotherapeutic drugs (163-167, 169, 170, 174, 176-179, 289). Some of these combinations have been demonstrated to produce synergistic enhancement of cytotoxicity. However, a mechanistic understanding of synergy induced by the combination treatment is still lacking. Recently, we have obtained the precise molecular mechanism of action for the chemotherapeutic drug CDDP and proposed that the dissociative electron-transfer (DET) reactions between CDDP and the guanine base in DNA, which is most likely to donate an

electron among the four DNA bases, are responsible for the activation of CDDP (182). In another paper, Dr. Lu has demonstrated that one-electron transfer from the excited singlet state of indocyanine green (^{1}ICG*) to CDDP can increase the yield of DNA DSBs in plasmid DNA and suggested that the combination of these two drugs may produce enhanced cytotoxicity against cancer cells (183). Based on this electron-transfer mechanism, we have developed a combination therapy of CDDP with a biological electron donor (TMPD; N,N,N′,N′-tetramethyl-p-phenylenediamine), which can enhance the cytotoxicity of CDDP in a synergistic manner and lead to complete removal of cisplatin-resistance in the human lung A549 and ovarian NIH:OVCAR-3 cancer cells (9). These findings suggest that the electron-transfer reaction between ^{1}ICG* and CDDP may have application in cancer treatment as well. More importantly, since ICG is activated by light, selective initiation of the electron-transfer reaction may be achieved by controlled delivery of light and thus, lead to further reduction in toxic side effects of CDDP.

In the present study, we have evaluated the *in vitro* cytotoxicity of the combination of ICG-PDT and CDDP or its analog OXP in the human cervical (HeLa and HeLa S3) and lung (A549) cancer cells. We have also investigated the dependence of the combination effects on treatment sequence. Steady-state absorption spectroscopic experiments have been performed to study the electron-transfer reaction between ICG and CDDP or OXP.

5.2 Materials and methods

5.2.1 Chemicals and cell culture

cis-Diammineplatinum(II) dichloride (cisplatin; CDDP; $Pt(NH_3)_2Cl_2$; MW = 300 g mol^{-1}), [SP-4-2-(1R-trans)]-(1,2-cyclohexanediamine-N,N′)[ethanedioata(2--)-O,O’]platinum (oxaliplatin; OXP; $C_8H_{14}N_2O_4Pt$; MW = 397.29 g mol^{-1}), and 4,5-benzoindotricarbocyanine (indocyanine green; ICG; $C_{43}H_{47}N_2NaO_6S_2$; MW = 775 g mol^{-1}) were purchased from Sigma-Aldrich (Sigma-Aldrich Canada Ltd., Oakville, ON, Canada) and used without any further purification. Stock solutions of 3 mM CDDP and 5 mM OXP were made in ultrapure water with a resistivity of >18 MΩ cm^{-1} obtained from a Barnstead Nanopure water system (Thermo Scientific, Dubuque, IA, USA) and stored at 4˚C. A stock solution of 5 mM ICG was made weekly in ultrapure water and stored in the dark at -20˚C.

The culture conditions for the human lung (A549) and cervical (HeLa) cancer cells were the same as those described in the previous Chapter 3. Human cervical cancer HeLa S3 cells (ATCC#: CCL-2.2™; a clonal derivative of the parent HeLa cell line) were cultured in minimum essential medium Eagle (MEM) medium supplemented with 10% fetal bovine serum (FBS), 100 units mL^{-1} penicillin G and 100 μg mL^{-1} streptomycin. The cell culture was kept at 37˚C in a humidified atmosphere containing 5% CO_2.

5.2.2 Laser treatment conditions

Irradiation was carried out by using an 800 nm laser with a pulse duration of 120 fs and a pulse repetition rate of 1 kHz. The average laser power was 360 mW corresponding to an average irradiance of 81 mW cm^{-2}. Duration of exposure was varied to get different light doses (J cm^{-2}).

5.2.3 Dark cytotoxicity of the combination of ICG and CDDP in A549 and HeLa cells

Exponentially growing A549 and HeLa cells were seeded into 96-well microplates at a density of 5×10^3 cells/well. After overnight incubation, the cells were incubated with ICG and CDDP for 24 h (HeLa) or 48 h (A549) in the dark. At the end of incubation period, cells were washed once with phosphate-buffered saline (PBS) and cell viability was evaluated by using the standard MTT assay as described in Chapter 3.

5.2.4 Cytotoxicity of the combination treatment of ICG-PDT and CDDP in A549 and HeLa cells

Exponentially growing A549 and HeLa cells were seeded into 96-well microplates at a density of 5×10^3 cells/well or 384-well microplates at a density of 3×10^3 cells/well. After overnight incubation, cells were incubated with ICG and CDDP for 5 h in the dark. Cells were then washed twice with PBS and fresh complete culture medium was added before laser

irradiation. The irradiated cells were then kept in an incubator for 20 h and cell viability was evaluated by the MTT assay as described in Chapter 3.

5.2.5 Effects of treatment sequence on the cytotoxicity of the combination treatment of ICG-PDT and CDDP in A549 cells

Exponentially growing A549 cells were seeded into 96-well microplates at a density of 5×10^3 cells/well. After overnight incubation, cells were incubated with various concentrations of CDDP for 24 h in the dark. Drug-containing medium was then replaced with fresh culture medium and ICG was added at a final concentration of 100 μM. At the end of the 5 h incubation period, cells were washed twice with PBS and fresh complete culture medium was added for laser irradiation. The irradiated cells were then kept in an incubator for 20 h and cell viability was evaluated by the MTT assay as described in Chapter 3.

5.2.6 Steady-state absorption spectroscopic measurements

Steady-state absorption spectroscopic results were measured using a DU-530 UV-Vis spectrophotometer (Beckman Coulter, Fullerton, CA, USA). Samples were prepared in ultrapure water and the absorbance at the peak wavelength of 778 nm was measured immediately after sample preparation and recorded again at 18 and 48 h.

5.2.7 Dark cytotoxicity of the combination of ICG and oxaliplatin in HeLa and HeLa S3 cells

Exponentially growing HeLa and HeLa S3 cells were seeded into 96-well microplates at a density of 5×10^3 cells/well. After overnight incubation, the cells were incubated with ICG and OXP for 24 h in the dark. Cells were washed twice with PBS and fresh culture medium was added. Plates were then kept in an incubator for another 24 h. Cell viability was evaluated by using the MTT assay as described in Chapter 3.

5.2.8 Cytotoxicity of the combination treatment of ICG-PDT and oxaliplatin in HeLa and HeLa S3 cells

Exponentially growing HeLa and HeLa S3 cells were seeded into 96-well microplates at a density of 5×10^3 cells/well. After overnight incubation, cells were incubated with ICG and OXP for 24 h in the dark. Cells were then washed twice with PBS and fresh complete culture medium was added before laser irradiation. The irradiated cells were then kept in an incubator for 24 h and cell viability was evaluated by the MTT assay as described in Chapter 3.

5.2.9 Data analysis

The drug- and light-dose response curves were fitted with a sigmoidal logistic function by using Origin software (OriginLab, Northampton, MA, USA). The corresponding half-

maximal inhibitory concentration (IC_{50}) or light dose (LD_{50}) values were determined on the basis of the fitted data. Fractional effect analysis was performed as described in Chapter 4.

5.3 Results and discussion

5.3.1 Dark cytotoxicity of the combination of ICG and CDDP in A549 and HeLa cells

As shown in Ref. (183), electron-transfer reactions can take place both in the ground-state and excited singlet state of the photosensitizer ICG. In order to see whether the ground-state reactions had any effect on cell viability, we first assessed the dark cytotoxicity of the combination of ICG and CDDP in cisplatin-resistant A549 and cisplatin-sensitive HeLa cells. Cells were separated into two treatment groups: one group of cells were treated with various concentration of CDDP and in the second group, cells were co-incubated with ICG and CDDP.

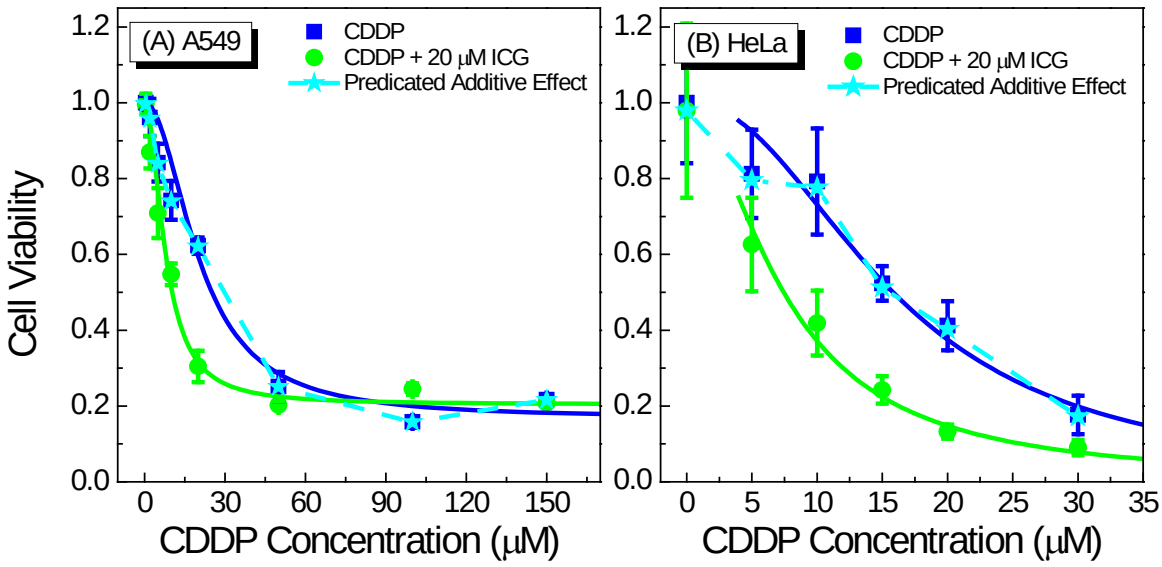

Figure 5-1: Drug-dose response curves for cell viability of (A) A549 and (B) HeLa cells treated with the combination of ICG and CDDP. The cells were incubated with various concentrations of ICG and CDDP for 24 h (HeLa) or 48 h (A549). Cell viability was evaluated by using MTT cytotoxicity assay at the end of the incubation period. The solid lines are best fits to the experimental data using a logistic function in Origin software. The dashed line and solid stars represent the calculated additive effect.

As shown in Figure 5-1, cell viability in the group treated with both drugs was lower than that in the group treated with CDDP only. This result indicates an enhanced cytotoxicity induced by the combination of ICG and CDDP. Without ICG, the IC_{50} of CDDP was determined to be 25.2 ± 2.4 and 15.8 ± 0.7 μM in A549 and HeLa cells, respectively. It is worth pointing out that drug incubation time for A549 cells is 48 h while that for HeLa is 24 h. When the two cell lines are treated identically, A549 cells are much more resistant to CDDP than HeLa cells. In A549 cells, we observed that ~20% of cells survived at a CDDP concentration of 50 μM and further increasing CDDP concentration up to 150 μM didn't affect cell viability significantly. This observation confirms the resistance of A549 cells to

CDDP treatment. When CDDP was given in combination with ICG, the IC_{50} values were determined to be 10.3 ± 1.2 and 7.4 ± 0.7 μM in A549 and HeLa cells, respectively, approximately 50% of the corresponding ones in the absence of ICG. This result indicates that the combination of ICG and CDDP produced a similar level of enhancement of cytotoxicity in the two cell lines studied. However, while we were able to decrease HeLa cell viability to below 10% with the combination treatment, viability of A549 cells was ~20% over a CDDP concentration range of 50-150 μM for both CDDP and ICG + CDDP treatment groups. This observation suggests that A549 cells are resistant to the combination treatment of ICG and CDDP. We further performed fractional effect analysis as described in Chapter 4. In the group treated with both ICG and CDDP, values of cell viability were found to be equal to or lower than the predicated additive effects suggesting an additive to synergistic enhancement of cytotoxicity by the combination of ICG and CDDP in A549 and HeLa cells.

Combination effects of ICG-PDT and CDDP have been studied by Crescenzi *et al.* (165). They found that the combination of low-dose CDDP and ICG-PDT produced a synergistic effect in MCF-7 breast cancer cells based on the MTT assay data but an additive effect when cell viability was evaluated by the trypan blue assay. They suggested that this observation was due to the differences in the mechanisms of these two assays. We noted that cytotoxicity data for the combination of ICG and CDDP without laser irradiation were not presented in their report. Our studies on the combination effects of ICG and CDDP, VP-16, or VM-26 have confirmed that synergistic enhancement of cytotoxicity could be observed in the absence of laser irradiation. This finding suggests that it is very important to consider

dark cytotoxicity induced by the drugs when evaluating combination effects of PDT and other treatment approaches. Failure to do this may lead to an overestimation of combination effects. Therefore, in the present study, calculation of additive effects has been based on data from ICG + CDDP treatment group instead of those from CDDP treatment group. This approach is expected to provide a better way of estimating the contribution from light irradiation treatment that can be controlled by targeted delivery of laser beams, while enhancement of cytotoxicity in the absence of light irradiation might lead to increased overall toxicity *in vivo*.

In 2012, we reported our observations of a highly effective electron-transfer reaction between CDDP and a biological electron donor TMPD and demonstrated that this combination could dramatically reduce viability of cisplatin-sensitive human cervical (HeLa) and highly cisplatin-resistant human lung (A549) and ovarian (NIH:OVCAR-3) cancer cells *in vitro* (9). Moreover, the combination treatment removed resistance to CDDP in A549 and NIH:OVCAR-3 cells. Those findings suggest that one-electron reduction of CDDP could be an effective way of increasing the anticancer activity of CDDP and even has the potential of overcoming resistance to CDDP. ICG, both in its ground state and excited singlet state, has been found to be able to donate one electron to CDDP (183). Therefore, our observation of synergistic enhancement of cytotoxicity induced by the combination of ICG and CDDP is likely a result of electron-transfer reactions between ICG and CDDP. However, unlike what have been observed in combination of CDDP and TMPD, A549 cells have been found to be resistant to both CDDP and ICG + CDDP treatments in the present study. The season for this

observation is not clear. One possible explanation is that the redox potential of ICG (0.96 eV *vs* NHE (290)) is more positive than that of TMPD (0.29 eV *vs* NHE (291)) making it less likely to donate an electron to CDDP. Therefore, it is expected that promoting ICG to an excited state may make the electron-transfer reaction more thermodynamically favorable. In fact, Dr. Lu has demonstrated that electron-transfer reactions between $^{1}ICG^{*}$ and CDDP can increase the yield of DNA DSBs in plasmid DNA and suggested that this reaction may enhance cytotoxicity as well (183). Moreover, although we have observed synergistic enhancement of cytotoxicity by the combination of ICG and CDDP *in vitro*, a 50% in IC_{50} is achieved with a relatively high ICG concentration and a long drug incubation time. As mentioned earlier, the blood half-life of ICG is only 2-4 minutes (202). It is difficult to maintain an ICG concentration high enough to cause significant damage to tumors *in vivo*. Therefore, we further evaluated the photocytotoxicity of the combination of ICG and CDDP to see whether we could achieve more significant synergistic enhancement of cytotoxicity and overcome drug-resistant to CDDP by exciting ICG to a higher energy state.

5.3.2 Photocytotoxicity of the combination treatment of ICG and CDDP in A549 cells

Considering the short blood half-life of IG and strong dark cytotoxicity of the ground-state reactions, we shortened the drug incubation time to 5 h. Figure 5-2 shows the drug-dose response curves of A549 cells to the combination treatment of ICG-PDT and CDDP. As shown in Figure 5-2A, cell viability decreased gradually with increasing CDDP

concentration. The IC_{50} was found to be higher than 100 μM. With the addition of 200 μM ICG, cell viability decreased slightly compared with that of CDDP only group in the CDDP concentration range ~0-100 μM. At CDDP concentrations higher than 100 μM, cell viability curve of ICG + CDDP treatment group overlapped with that of CDDP treatment group. This result indicates that dark cytotoxicity of ICG and CDDP may be reduced by shortening the drug incubation time. With a light dose of 24.4 J cm^{-2}, cell viability was 69.1 ± 8.7% in the absence of CDDP. Fractional effect analysis results showed that the combination effect was slightly synergistic at low CDDP concentrations and additive or slightly antagonistic at high CDDP concentrations.

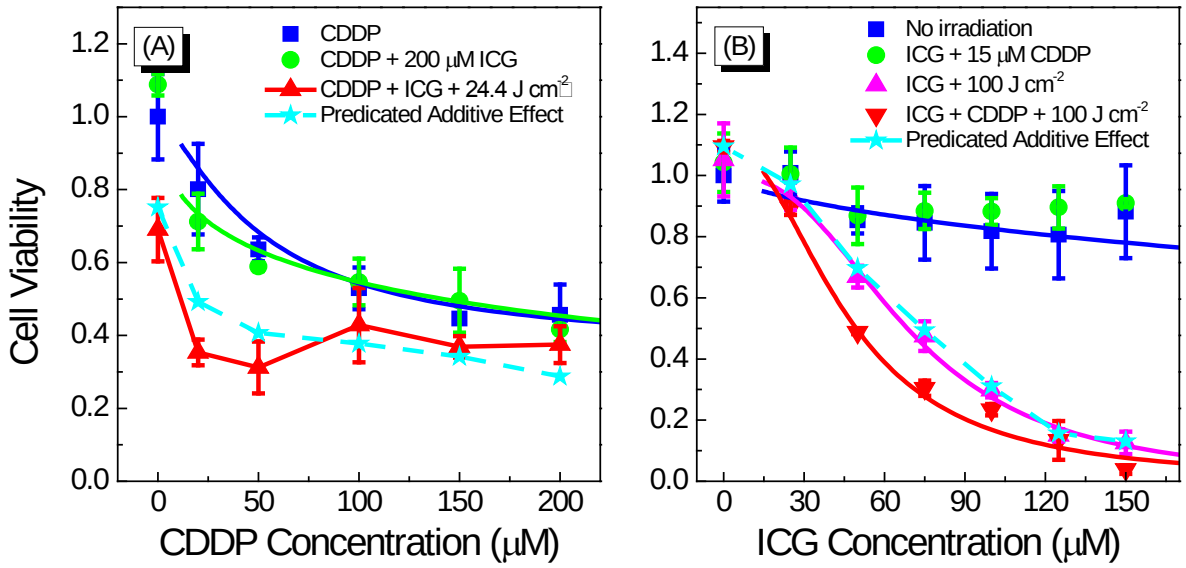

Figure 5-2: Drug-dose response curves for cell viability of A549 cells treated with the combination of ICG-PDT and CDDP by using the standard MTT cell viability assay. The drug incubation time was 5 h and MTT was performed 20 h after laser irradiation. The solid lines are best fits to the experimental data using a logistic function in Origin software. The dashed line and solid stars represent the calculated additive effect. (Note: the dose-response

curve of CDDP + ICG + 24.4 J cm^{-2} treatment group in (A) could not be fitted with a logistic function.)

As discussed in Section 5.3.1, both ICG and $^1ICG^*$ can donate electrons to CDDP and induce cytotoxicity. At low CDDP concentrations, the rate of ground-state reactions is relatively low. When ICG is promoted to its excited singlet state $^1ICG^*$, which has a redox potential of -0.6 eV vs. NHE (290), the electron transfer reaction rate may be increased and thus produce a synergistic effect. At high CDDP concentrations, reactions in the ground-state of ICG become dominant. However, ground-state reactions have been shown in Section 5.3.1 to be not effective in overcoming resistance to CDDP. Therefore, additive or slightly antagonistic effect was observed. These findings suggest that it is desirable to lower the concentration of CDDP in the combination treatment of ICG-PDT and CDDP in order to achieve synergistic enhancement of cytotoxicity.

We have further studied the dependence of combination effects on ICG concentration by fixing CDDP concentration at 15 μM while varying ICG concentration from 0 to 150 μM (Figure 5-2B). Without laser irradiation, ICG and ICG + 15 μM CDDP were found to be only slightly cytotoxic killing less than 20% of the cells. With a light dose of 100 J cm^{-2}, the IC_{50} values were determined to be 68.7 ± 6.9 and 45.4 ± 1.2 μM for ICG and ICG + CDDP treatment groups, respectively. Results of fractional effect analysis showed that additive to synergistic effects were produced by the combination treatment.

Figure 5-3 shows the light-dose response of A549 cells to ICG-PDT and ICG-PDT + CDDP treatment. In the absence of CDDP, the LD_{50} of 100 μM ICG was found

to be > 100 J cm^{-2}. Without laser irradiation, cell viability was 86.8 ± 3.2% and 76.0 ± 0.8% for ICG in combination with 20 and 30 μM CDDP, respectively. With laser irradiation, cell viability decreased in a light-dose dependent manner. The values of LD_{50} were determined to be 25.1 ± 5.9 and 14.6 ± 21.8 J cm^{-2} for groups treated with 20 and 30 μM CDDP, respectively. Fractional effect analysis results showed that the observed effects were equal to or lower than the calculated additive effects indicating additive/synergistic enhancement of cytotoxicity induced by the combination treatment. However, in the presence of CDDP, there were still ~30% of the cells survived at a light dose of 50 J cm^{-2} and further increasing the light dose to 100 J cm^{-2} didn't reduce cell viability significantly. This is probably due to a limited accumulation of ICG inside the cells with a relatively short drug incubation time of 5 h and quick consumption of ICG by laser irradiation.

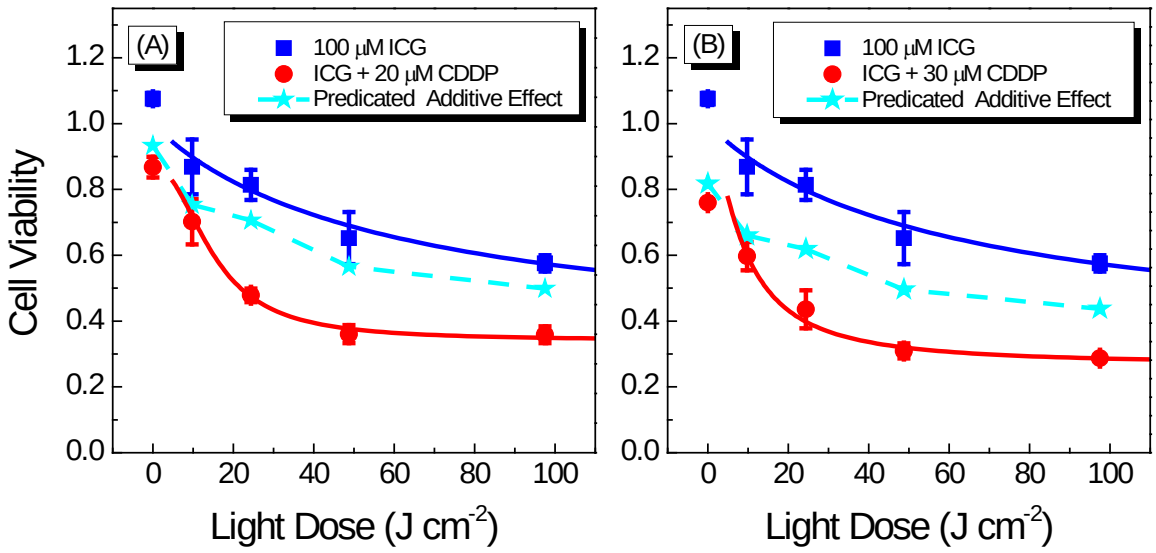

Figure 5-3: Light-dose response curves for cell viability of A549 cells treated with ICG-PDT alone or in combination with CDDP by using the standard MTT cell viability assay. The drug incubation time was 5 h and MTT was performed 20 h after laser irradiation. The solid lines

are best fits to the experimental data using a logistic function in Origin software. The dashed line and solid stars represent the calculated additive effect.

We have observed synergistic enhancement of cytotoxicity induced by combing ICG-PDT with CDDP and found that the degree of synergy is dependent on light dose and the concentration of both drugs. These findings are consistent with the proposed mechanism that electron-transfer reactions between ICG/^{1}ICG* and CDDP are responsible for the enhanced cytotoxicity. Indeed, we have observed synergistic enhancement of cytotoxicity under specific treatment conditions. The results of our *in vitro* cytotoxicity studies suggest that synergistic effects are more likely to be induced with lower CDDP and ICG concentrations, a shorter time interval between drug administration and laser irradiation, and higher light doses. Moreover, our observations of electron-transfer-induced synergistic enhancement of cytotoxicity in combination therapies of low-dose CDDP and ICG-PDT or other treatment approaches may be further explored to develop more effective combinations for the treatment of cancers.

5.3.3 Sequence dependence of the combination effect in A549 and HeLa cells

In order to see whether the combination effect was dependent on the sequence of treatment, we treated the cells with various concentrations of CDDP for 24 h and then with ICG for 5 h before laser irradiation. Cell viability was determined 20 h after laser irradiation. Figure 5-4A shows drug-dose dependence of cell viability in A549 cells. The IC_{50} of CDDP was found to be 16.4 ± 0.7 μM, slightly lower than the value of 25.2 ± 2.4 μM with a drug incubation time

of 48 h (Figure 5-1A). This was probably because exposing the cells to ambient air during laser irradiation made them more sensitive to CDDP treatment. The combination of CDDP with 100 μM ICG didn't alter the cytotoxicity significantly having an IC_{50} of 17.9 ± 1.6 μM. Laser irradiation reduced cell viability to 67.2 ± 7.5% in the absence of CDDP. In the presence of CDDP, the observed effect was found to be close to the predicated additive effect at low CDDP concentrations. At CDDP concentrations higher than 20 μM, slight synergy was produced by the combination treatment.

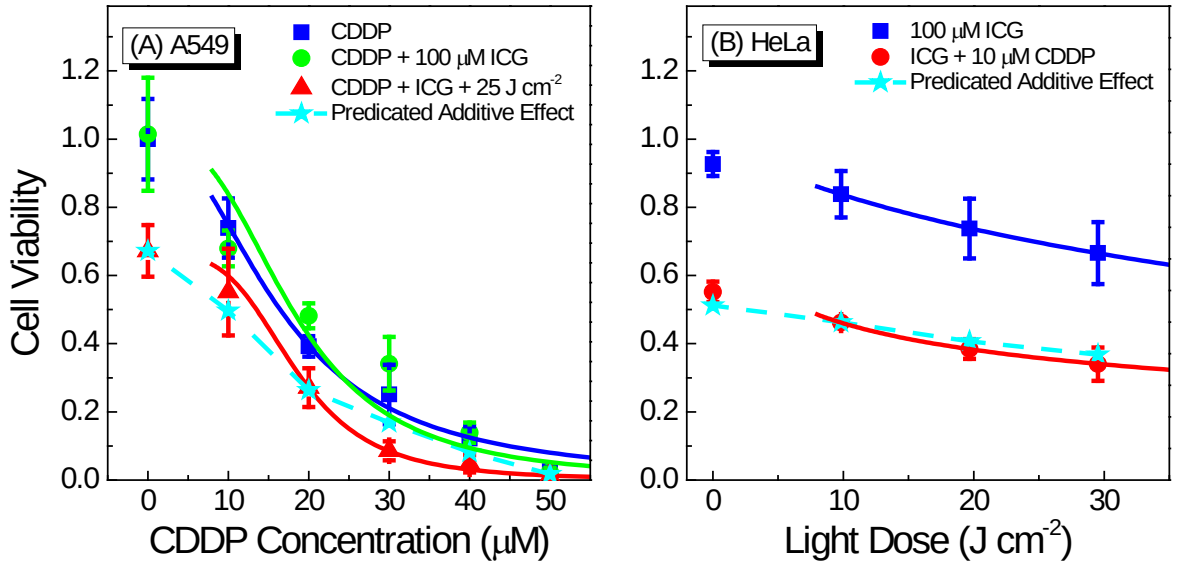

Figure 5-4: Effect of treatment sequence on cell viability of (A) A549 and (B) HeLa cells treated with the combination of ICG-PDT and CDDP. The cells were incubated with various concentrations of CDDP for 24 hours and then with 100 μM ICG for 5 hours followed by laser irradiation at 800 nm. Cell viability was evaluated by using MTT assay 20 hours after laser irradiation. The solid lines are best fits to the experimental data using a logistic function in Origin software. The dashed line and solid stars represent the calculated additive effect.

In HeLa cells, LD_{50} of 100 μM ICG was found to be higher than 30 J cm^{-2} (Figure 5-4B). Combing ICG with 10 μM CDDP reduced the cell viability to 55.2 ± 3.0%. No significant difference was observed between the combination effect and predicated additive effect curves indicating an additive effect was produced by the combination treatment.

By treating the cells with CDDP and ICG separately, we have successfully lowered the dark cytotoxicity compared with that observed in cells co-incubated with ICG and CDDP. We have also shown that the combination effect of ICG-PDT and CDDP is additive to slightly synergistic under the conditions of this experiment. This is reasonable since the majority of intracellular CDDP should have been converted to other forms that may not be able to react with ICG/^{1}ICG* at the end of 24 h incubation so that the ICG-PDT and CDDP treatment can act independently. The lower degree of synergy observed in this experiment than that in Sections 5.3.1 and 5.3.2 is consistent with the proposal that synergistic enhancement of cytotoxicity produced by the combination treatment involves electron-transfer reactions between ICG/^{1}ICG* and CDDP.

5.3.4 Steady-state absorption spectra change of ICG induced by CDDP and oxaliplatin

It has been shown by Dr. Lu that the electron transfer reaction between ICG and CDDP can be observed by measuring steady-state absorption spectra changes of the samples (183). In this experiment, we studied the reaction between ICG and CDDP or OXP by measuring the

steady-state absorbance of the mixtures of ICG and various concentrations of CDDP or OXP at 778 nm ($A_{778\ nm}$) 0, 18 and 48 h after sample preparation. The results are plotted in Figure 5-5.

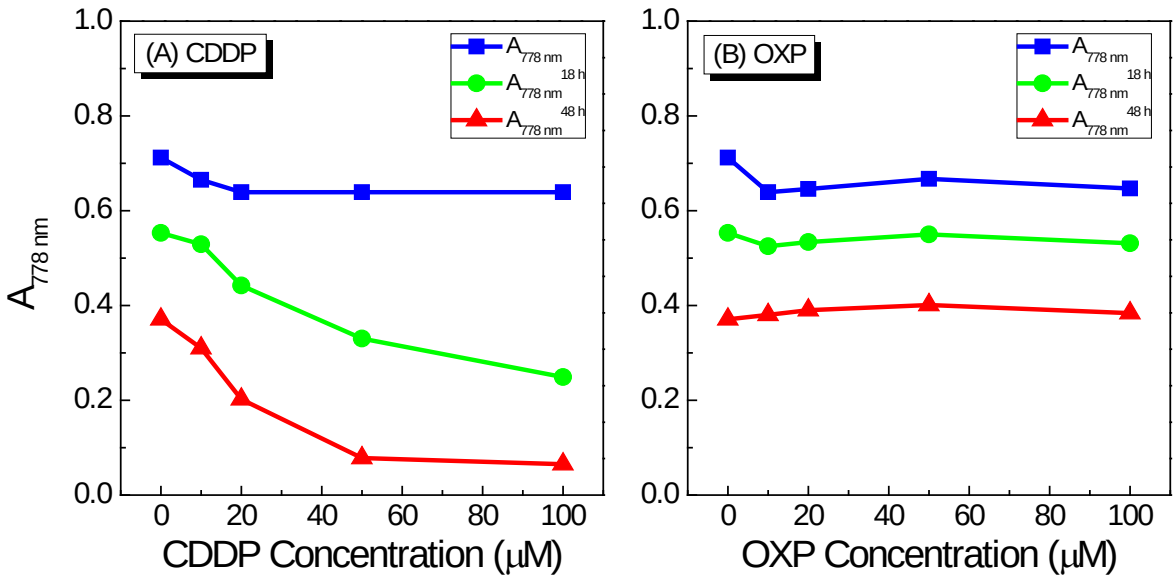

Figure 5-5: Steady-state absorbance change of ICG at the absorption peak of 778 nm in the presence of various concentrations of (A) CDDP and (B) OXP. The values of absorbance were recorded immediately after sample preparation and then recorded 18 and 48 h later.

Without CDDP or OXP, the absorbance of ICG decreased by 22.3% and 47.9% at 18 and 48 h, respectively. At 0 h, $A_{778\ nm}$ of ICG decreased slightly with increasing concentration of CDDP and OXP. At 18 and 48 h, $A_{778\ nm}$ decreased more quickly with increasing CDDP concentration than at 0 h. Absorbance decreased by more than 85% at a CDDP concentration of 50 μM 48 h after sample preparation, which was 39.4% more than that in the absence of CDDP. These results are consistent with the spectra change of ICG due to electron transfer reaction with CDDP (183). In contrast, $A_{778\ nm}$ in the presence of various

concentrations of OXP were found to be very close to those of ICG only sample at all three time points. This observation suggests that electron transfer reactions between ICG and OXP are absent or at least much weaker than that between ICG and CDDP. Therefore, dark cytotoxicity by the combination of ICG and OXP is expected to be less significant than that observed with the combination of ICG and CDDP.

5.3.5 Dark cytotoxicity of the combination of ICG and oxaliplatin in HeLa and HeLa S3 cells

We investigated the cytotoxicity of ICG in combination with OXP in HeLa and HeLa S3 cells by incubating the cells with various concentrations of OXP in the absence or presence of 100 μM ICG for 24 h. The cells were then washed and incubated with drug-free medium. Cell viability was determined by MTT assay 24 h after the removal of drugs. The results are shown in Figure 5-6. Cytotoxicity of OXP increased in a dose-dependent manner in both cell lines. In the absence of ICG, IC_{50} of OXP was determined to be 121.0 ± 5.9 and 2.52 ± 2.45 μM in HeLa and HeLa S3 cells, respectively. This result shows that HeLa S3 cells are about 50 times more sensitive to OXP than HeLa cells. At a concentration of 100 μM, ICG was found to be slightly cytotoxic to both HeLa and HeLa S3 cells, with ~20% of the cells killed by ICG treatment. We performed fractional effect analysis on the combination effect of ICG and OXP. As shown in Figure 5-6A, the combination effect curve overlaps with the calculated additive effect curve at low OXP concentrations suggesting an additive effect induced by the combination treatment. A slightly antagonistic effect was

observed at OXP concentrations higher than ~120 μM, which was roughly the IC_{50} of OXP in HeLa cells. In HeLa S3 cells, the observed effect curve was found to be higher than the additive effect curve indicating an antagonistic effect at all the OXP concentrations tested in this experiment. We noted that the lowest OXP concentration of 2 μM tested was close to the IC_{50} of OXP in HeLa S3 cells and data for lower concentrations of OXP was not measured. Therefore, the combination effect could not be determined in the OXP concentration range 0-2 μM.

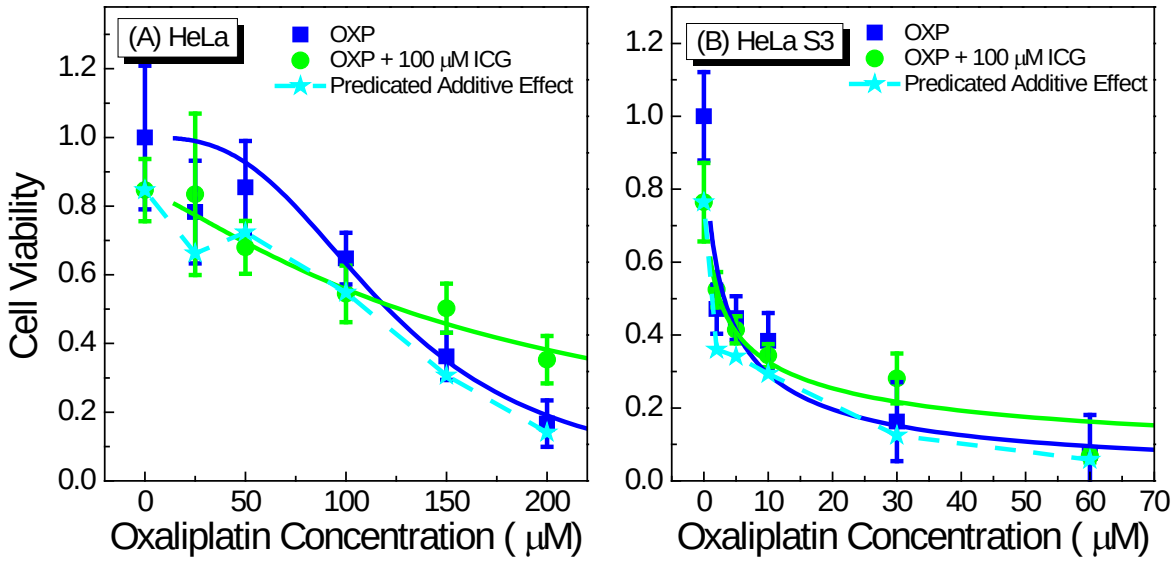

Figure 5-6: Drug-dose response curves for cell viability of (A) HeLa and (B) HeLa S3 cells treated with the combination of ICG and OXP. The cells were treated with ICG and OXP for 24 h and incubated with drug-free medium for another 24 h. Cell viability was evaluated by using MTT cytotoxicity assay at the end of the incubation period. The solid lines are best fits to the experimental data using a logistic function in Origin software. The dashed line and solid stars represent the calculated additive effect.

The absence of a synergistic effect by the combination treatment of ICG and OXP in HeLa and HeLa S3 cells is consistent with our steady-state absorption spectroscopic results and suggests that OXP is much less reactive than CDDP towards ICG. The season for the slightly antagonistic effect observed at high OXP concentrations is not clear. Considering that ICG has a broad absorption spectrum in the visible range, it is possible that ICG has some absorbance at the detection wavelength of 570 nm for MTT assay and thus, has contributed the antagonistic effect observed. However, contribution from free ICG is not likely, since we have washed the cells with PBS before performing MTT assay. The observation that the combination effect is dependent upon OXP concentration suggests the existence of direct/indirect interaction between these two drugs. Determination of the mechanism for the observed antagonistic effect will require further experiments that are beyond the scope of this thesis.

5.3.6 Cytotoxicity of the combination treatment of ICG-PDT and oxaliplatin in HeLa and HeLa S3 cells

We evaluated the photocytotoxicity of the combination of ICG and OXP in HeLa and HeLa S3 cells. Cells were incubated with various concentrations of ICG and OXP for 24 h and then exposed to laser irradiation at 800 nm. Cell viability was determined by MTT assay 24 h after laser irradiation. Figure 5-7 shows that photocytotoxicity of ICG in HeLa cells increased with increasing total light dose. The LD_{50} of 200 μM ICG was determined to be 37.6 ± 2.7 J cm^{-2}. Cell viability was decreased to be 74.4 ± 5.4% and 48.8 ± 3.0%, when the

cells were treated with ICG in combination with 10 and 40 μM OXP, respectively. Fractional effect analysis results showed that the combination of ICG-PDT and OXP produced an additive effect at 10 μM OXP and a slightly antagonistic effect at 40 μM OXP in HeLa cells. We noted that the combination of ICG and 40 μM OXP produced an antagonistic effect without laser irradiation and the degree of antagonism didn't change significantly with increasing light dose.

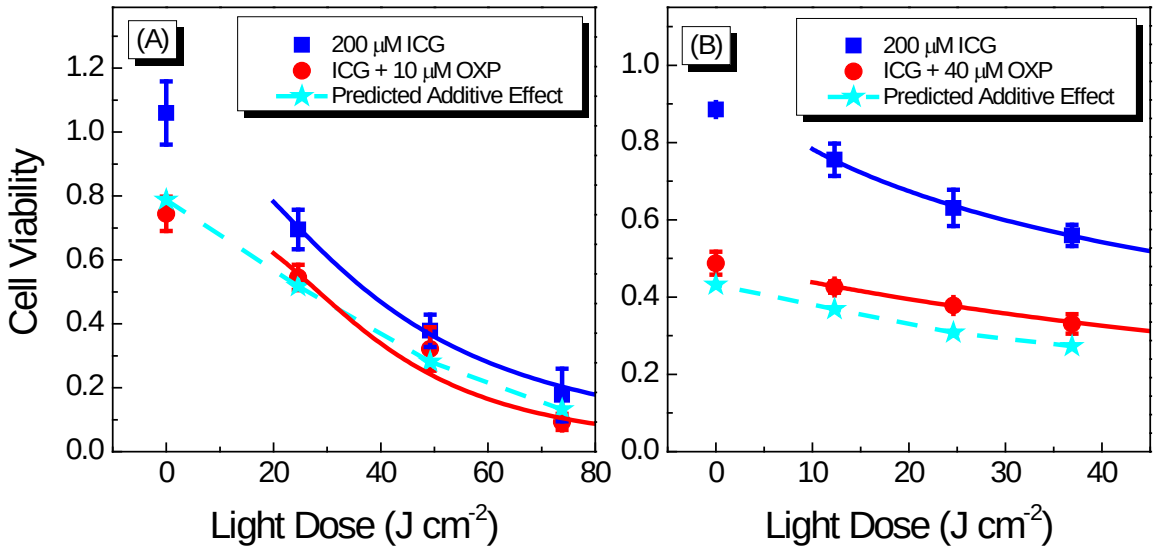

Figure 5-7: Light-dose response curves for cell viability of HeLa cells treated with ICG-PDT alone or in combination with OXP by using the standard MTT cell viability assay. The cells were incubated with the drugs for 24 hours before exposing to laser irradiation. Cell viability was evaluated 24 hours after laser irradiation. The solid lines are best fits to the experimental data using a logistic function in Origin software. The dashed line and solid stars represent the calculated additive effect.

The combination effect of ICG-PDT and OXP was also evaluated in HeLa S3 cells. Figure 5-8A compares the light-dose response curves for cell viability to ICG-PDT treatment

in HeLa and HeLa S3 cells. At an ICG concentration of 200 μM, the LD_{50} values were calculated to be 37.8 ± 1.9 and 58.9 ± 7.3 J cm^{-2} in HeLa and HeLa S3 cells, respectively. This result shows that HeLa S3 cells are slightly more resistant to ICG-PDT treatment than HeLa cells. Figure 5-8B shows the cytotoxicity of the combination treatment of ICG-PDT and OXP in HeLa S3 cells. At an ICG concentration of 50 μM, cell viability was found to be 71.9 ± 10.4%. With a light dose of 25 J cm^{-2}, cell viability was decreased to be 41.6 ± 11.9%. The observed effect curve overlapped with the calculated additive effect curve indicating that an additive effect was produced by the combination treatment of ICG-PDT and OXP.

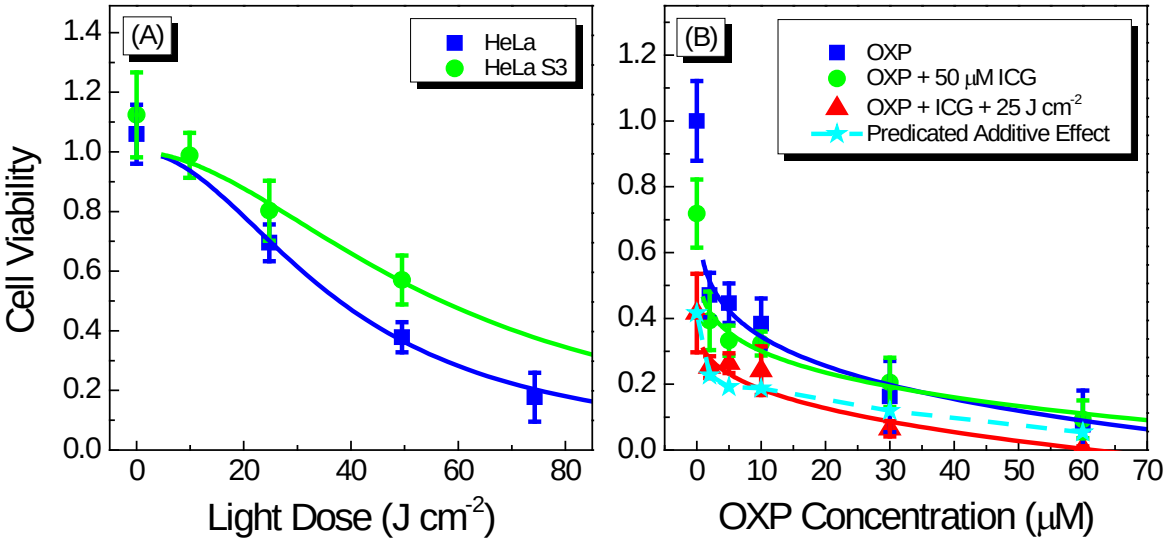

Figure 5-8: (A) Light-dose response curves for cell viability of HeLa and HeLa S3 cells treated with ICG-PDT. (B) Drug-dose response curves for cell viability of HeLa S3 cells treated with OXP, OXP + 50 μM ICG, and OXP + ICG + 25 J cm^{-2} by using the standard MTT cell viability assay. The cells were incubated with the drugs for 24 hours before expose to laser irradiation. Cell viability was evaluated 24 hours after laser irradiation. The solid lines are best fits to the experimental data using a logistic function in Origin software. The dashed line and solid stars represent the calculated additive effect.

The combination of ICG and OXP has been demonstrated to produce an additive to slightly antagonistic effect in HeLa and HeLa S3 cancer cells both without and with laser irradiation. Antagonistic effect has been found to be significant at relatively high OXP concentrations and not dependent on light dose. The observation of an additive effect is consistent with the lower activity of OXP towards ICG than that of CDDP in aqueous solutions (Section 5.3.4). Unfortunately, we haven't observed any synergistic enhancement of cytotoxicity with laser treatment. The finding that the degree of antagonism doesn't depend on light dose implies the absence of direct interaction between $^{1}ICG^{*}$ and OXP. Although synergistic effects are absent, the combination of ICG-PDT with low dose OXP is expected to produce an additive effect and thus, has the potential of lowering the effective dose of oxaliplatin and reducing the toxic side effects.

5.4 Summary

In this chapter, we have evaluated the dark and photocytotoxicity of the combination of ICG and CDDP in cisplatin-resistant human lung cancer (A549) and cisplatin-sensitive human cervical cancer (HeLa) cells. We have demonstrated that ICG, both in the ground- and excited-state, can enhance the cytotoxicity of CDDP in a synergistic manner. The degree of synergy has a strong dependence upon treatment conditions. Lower concentrations of CDDP and ICG, a shorter time interval between drug and light treatment, and a higher light dose have been found to favor the observation of synergistic enhancement of cytotoxicity. We have also found that co-incubation of cells with ICG and CDDP can produce a higher level of

synergy than pre-treating cells with CDDP for 24 h. However, the combination of ICG or ICG-PDT with CDDP cannot overcome CDDP resistance in A549 cells, in contrast with what has been observed in the combination therapy of CDDP and the biological electron donor TMPD (9). This difference has been attributed to ICG being a thermodynamically less favorable electron donor than TMPD. Laser irradiation may provide enough energy to increase the reaction rate. However, when high concentrations of CDDP are used, ground-state reactions may compete with excited-state reactions making it very difficult to selectively activate the excited-state reaction pathway.

We have also evaluated the dark and photo-cytotoxicity of the combination of ICG and OXP in human cervical cancer HeLa and HeLa S3 cell lines. Combination of ICG and OXP has been found to produce an additive to slightly antagonistic effect without or with laser irradiation. The absence of synergistic effects is consistent with the steady-state absorption spectroscopic results, which suggest that OXP is much less reactive than CDDP towards ICG in aqueous solutions. The finding that the antagonistic effect is not dependent on light dose implies that no direct interaction between $^{1}ICG^{*}$ and OXP is involved.

The observation of additive to synergistic effects induced by combing ICG-PDT with low dose CDDP/OXP suggests that ICG-PDT may be applied in combination with chemotherapy mediated by CDDP or OXP. These combination treatment approaches has the potential of reducing the effective dose of the chemotherapeutic drugs and thus, lowering the toxic side effects commonly associated with chemotherapy. All these findings strongly support the proposal that electron-transfer from $ICG/^{1}ICG^{*}$ to CDDP is responsible for the

synergy induced by the combination of ICG or ICG-PDT with CDDP. Therefore, this electron-transfer-based combination therapy of PDT and chemotherapy should be further explored in order to develop more effective treatment approaches.

6 Bioluminescence of Luminol Activated Photodynamic Killing of Human Cervical Cancer Cells *in vitro*

6.1 Background

Luminol (5-amino-2,3-dihydro-1,4-phthalazine-dione) is a light-emitting chemical that can produce blue light at a maximum of 425 nm in the presence of a variety of oxidizing agents such as horseradish peroxide and metal cations including iron, cobalt, and copper (213, 292-295). It has been widely used for the detection of oxidizing radicals in forensic science, biochemistry, and clinical diagnostics (205, 296-299). Recently, the therapeutic potential of luminol has been demonstrated in several studies, in which the light generated from chemical reactions of luminol can serve as an internal light source to initiate photodynamic killing of cancer cells through a bioluminescence resonant energy transfer (BRET) mechanism (104, 214, 215). Compared with conventional photodynamic therapy (PDT), bioluminescence-activated PDT is, in principle, not limited by the tissue penetration depth of light, which has greatly hindered the more widespread application of conventional PDT. In 2006, Laptev *et al.* reported that bioluminescence of luminol could activate bioconjugates composed of transferrin (Tf) and Hp and induce significant cell killing in leukaemia K562 and U-76 cells (104). More recently, Yuan *et al.* developed a new bioluminescence system consists of

luminol and a cationic oligo(p-phenylene vinylene), which showed significant anticancer activity both *in vitro* and *in vivo* (215). Using 5-aminolaevulinic acid (5-ALA) as the photosensitizer, Chen *et al.* found that bioluminescence of luminol could effectively activate photodynamic killing of human epithelial colorectal adenocarcinoma (Caco-2) cells (214).

In the past two decades, not only luminol but also other bioluminescence systems including firefly luciferin-luciferase and coelenterazine-luciferase have been evaluated for PDT applications (209-212). In 1994, Carpenter *et al.* studied the antiviral activity of hypericin activated by the bioluminescence of luciferin (209). Later, Theodossiou *et al.* assessed the *in vitro* photodynamic activity of Rose Bengal activated by firefly luciferin in luciferase-transfected mouse embryonic fibroblast cell line NIH 3T3 (210). Three years later, Schipper *et al.* evaluated the photodynamic cytotoxicity induced by the bioluminescence of firefly luciferase in several malignant and nonmalignant cell lines including MCF7 (human breast adenocarcinoma), NIH 3T3, 3T3L1 (a continuous substrain of 3T3), CHO (Chinese hamster ovary), 293T (a highly transfectable derivative of human embryonic kidney 293 cells), and A375M (melanoma) and concluded that the bioluminescence system didn't generate sufficient light to induce Rose Bengal or hypericin photocytotoxicity (211). They raised an important question of whether bioluminescence could produce enough photons for the activation of the photosensitizers. However, a more recent study performed by Hsu *et al.* showed that a luciferase-immobilized quantum dots system could activate Foscan®-loaded micelles and induce tumor cell killing *in vitro* as well as delay tumor growth *in vivo* (212). The results of that study, together with those reported by Yuan *et al.* and Chen *et al.* (214,

215), suggest that it is possible to develop bioluminescence-activated PDT approaches for effective destruction of cancers.

In the present study, we have evaluated the cytotoxicity of two porphyrin photosensitizers meso-tetra(4-sulfonatophenyl)porphine dihydrochloride ($TPPS_4$) and Fe(III) meso-tetra(4-sulfonatophenyl)porphine chloride (FeTPPS) activated by the bioluminescence of luminol in a human cervical carcinoma cell line (HeLa) and two normal human fibroblast cell lines (GM05757 and MRC-5). We have also compared the cytotoxicity of the photosensitizers induced by the bioluminescence of luminol and 400 nm light produced by a femtosecond (fs) laser.

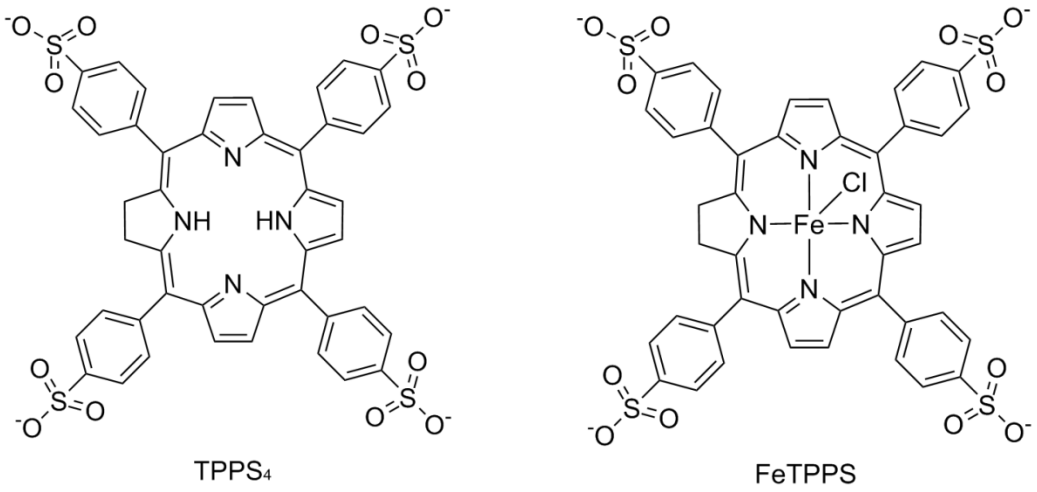

Figure 6-1: Chemical structures of $TPPS_4$ and FeTPPS.

6.2 Materials and methods

6.2.1 Chemicals and cell lines

Meso-tetra(4-sulfonatophenyl)porphine dihydrochloride ($TPPS_4$; $C_{44}H_{32}Cl_2N_4O_{12}S_4$; MW = 1007.91 g mol^{-1}) and Fe(III) meso-tetra(4-sulfonatophenyl)porphine chloride (FeTPPS; $C_{44}H_{28}ClFeN_4O_{12}S_4$; MW = 1024.27 g mol^{-1}) purchased from Frontier Scientific Inc. (Logan, UT, USA) and 5-amino-2,3-dihydro-1,4-phthalazinedione (luminol; $C_8H_7N_3O_2$; MW = 177.2 g mol^{-1}) from Sigma-Aldrich (Sigma-Aldrich Canada Ltd., Oakville, ON, Canada) were used without any further purification. Stock solutions of 5 mM $TPPS_4$ and FeTPPS were made in ultrapure water with a resistivity of >18 MΩ/cm obtained from a Barnstead Nanopure (Thermo Scientific, Dubuque, IA, USA) water system and then stored in the dark at -20˚C. Stock solutions of luminol (500 mM) were made in 1 M NaOH immediately before the experiments.

The culture conditions for the human cervical cancer (HeLa) and normal human skin fibroblast (GM05757) cells were the same as those described in Chapters 3 and 4. The normal human lung fibroblast (MRC-5) cells were obtained from the Coriell Institute, Human Genetic Mutant Cell Repository (Camden, NJ, USA) and grew in minimum essential medium Eagle (MEM) supplemented with 10% fetal bovine serum (FBS), 100 units mL^{-1} penicillin G and 100 μg mL^{-1} streptomycin. The cell culture was kept at 37˚C in a humidified atmosphere containing 5% CO_2.

6.2.2 Steady-state absorption spectra

Steady-state absorption spectra of $TPPS_4$ and FeTPPS were measured on a DU 530 UV/Vis spectrophotometer (Beckman Coulter, Fullerton, CA, USA). Samples were prepared in 5 mm quartz cuvettes using phosphate-buffered saline (PBS).

6.2.3 Cytotoxicity of the combination of luminol and $TPPS_4$ in HeLa cells by MTT assay

Exponentially growing HeLa cells were plated at a density of 5×10^3 cells/well in 96-well microplates. Following overnight incubation, cells were treated with different concentrations of luminol and $TPPS_4$ in phenol red-free medium containing 1% fetal bovine serum (FBS). After 24 or 48 h incubation in a humidified incubator, cells were washed twice with PBS. Cell viability was determined by the standard MTT assay as described in Chapter 3.

6.2.4 Cytotoxicity of the combination of luminol and $TPPS_4$ in HeLa cells by clonogenic assay

Exponentially growing HeLa cells were plated in six-well plates at densities of 100, 150 and 200 cells/well using phenol red-free medium containing 1% FBS. The cells were allowed to attach for 4 h prior to the addition of drugs. After 24 h incubation with various concentrations of luminol and $TPPS_4$, cells were washed twice with PBS and fresh culture medium containing 10% FBS was added. Plates were then put back into an incubator to allow the

formation of clearly visible clones (10 days). Cells were fixed with glutaraldehyde (6.0% v/v in water), stained with crystal violet (0.5% w/v in water), and counted manually. Survival fraction was expressed as the percentage of the control wells. The resulting data are based on the mean value of three wells and the error bars represent the standard error of mean (S.E.M).

6.2.5 Cytotoxicity of the combination of luminol and FeTPPS in HeLa cells by MTT assay

Exponentially growing HeLa cells were plated at a density of 5×10^3 cells/well in 96-well microplates. Following overnight incubation, cells were treated with different concentrations of luminol and FeTPPS in phenol red-free medium containing 1% FBS. After 48 h incubation in a humidified incubator, cells were washed twice with PBS. Cell viability was determined by the standard MTT assay as described in Chapter 3.

6.2.6 Cytotoxicity of $TPPS_4$- and FeTPPS-mediated PDT activated by 400 nm laser light in HeLa cells

Exponentially growing HeLa cells were plated at a density of 5×10^3 cells/well in 96-well microplates. Following overnight incubation, cells were treated with different concentrations of $TPPS_4$ or FeTPPS in phenol red-free medium containing 1% FBS. After 24 h incubation in a humidified incubator, cells were washed twice with PBS and irradiated by a 400 nm fs laser with a repetition rate of 500 Hz. The average power was 3 mW corresponding to a power

density of 4.23 mW cm^{-2}. Twenty four hours after laser irradiation, cell viability was determined by the standard MTT assay as described in Chapter 3.

6.2.7 Cytotoxicity of the combination of luminol and $TPPS_4$ or FeTPPS in GM05757 and MRC-5 cells by MTT assay

Exponentially growing GM05757 and MRC-5 cells were plated at a density of 5×10^3 cells/well in 96-well microplates. Following overnight incubation, cells were treated with different concentrations of luminol and $TPPS_4$ or FeTPPS in phenol red-free medium containing 1% FBS. After 48 h incubation in a humidified incubator, cells were washed twice with PBS. Cell viability was determined by the standard MTT assay as described in Chapter 3.

6.2.8 Data analysis

The drug-dose response curves were fitted with a sigmoidal logistic function by using Origin software (OriginLab, Northampton, MA, USA). The corresponding half-maximal inhibitory concentration (IC_{50}) values were determined on the basis of the fitted data. Fractional effect analysis was performed as described in Chapter 4.

6.3 Results and discussion

6.3.1 Steady-state absorption spectra of $TPPS_4$ and FeTPPS

We first measured the steady-state absorption spectra of $TPPS_4$ and FeTPPS in PBS. As shown in Figure 6-2, $TPPS_4$ has a major absorption peak at 412 nm. The absorption band of FeTPPS is much broader than that of $TPPS_4$ with a tail extending beyond 500 nm. It is well known that luminol can emit strong blue light in the wavelength range of ~350-550 nm (215). The solid blue line in Figure 6-2 indicates the position of the bioluminescence maximum of luminol at 425 nm. The absorption spectra of both $TPPS_4$ and FeTPPS overlap significantly with the bioluminescence spectrum of luminol. Therefore, energy transfer from luminol to $TPPS_4$ or FeTPPS is possible through a fluorescence resonance energy transfer (FRET) mechanism, which requires spectral overlap between the donor emission spectrum and the acceptor absorption spectrum.

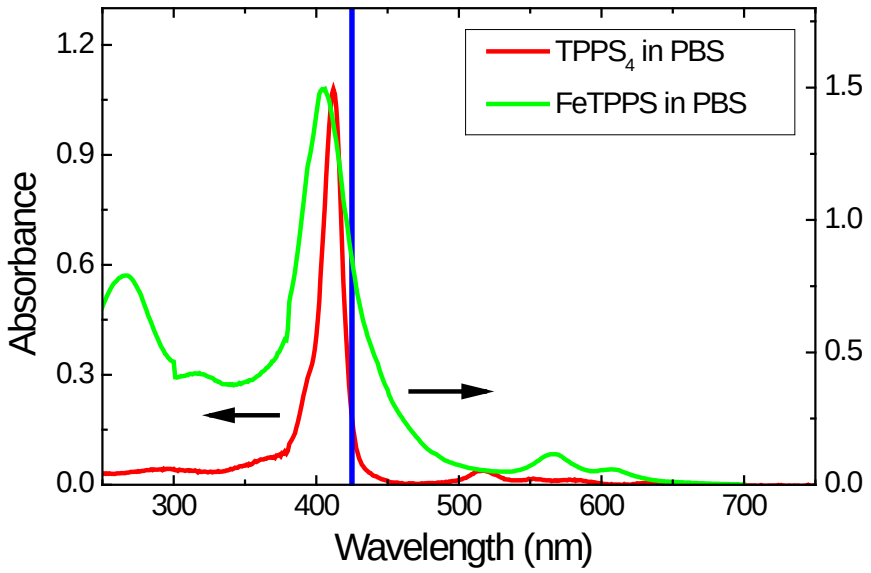

Figure 6-2: UV-Vis absorption spectra of $TPPS_4$ and FeTPPS in PBS. The solid blue line indicates the position of the emission peak of luminol at 425 nm.

6.3.2 Cytotoxicity of the combination of luminol and $TPPS_4$ in human cervical cancer HeLa cells

We have evaluated the cytotoxicity of the combination of luminol and $TPPS_4$ in HeLa cells by performing the standard MTT cell viability assay and clonogenic assay. Figure 6-3 shows the data obtained from the MTT assay. With 24 h drug incubation, the IC_{50} of $TPPS_4$ was determined to be > 500 μM, which was reduced to be 190.2 ± 32.9 μM by increasing the drug incubation time to 48 h. Luminol at a concentration of 2 mM was found to be slightly cytotoxic producing a cell killing effect of ~34% after 24 h drug incubation. Considering the cytotoxicity of luminol, we calculated the relative IC_{50} instead of the absolute values. In Figure 6-3A, the value was found to be 361.1 ± 53.0 μM for the group treated with the

combination of $TPPS_4$ and 2 mM luminol. Luminol at a lower concentration of 1 mM was found to be less cytotoxic even with a longer drug incubation time of 48 h. From Figure 6-3B, we obtained an IC_{50} of 53.2 ± 5.0 μM in the presence of luminol, which was ~28% of the value in the absence of luminol. The combination effect of luminol and $TPPS_4$ was estimated by comparing the observed effect to the additive effect calculated by using Equation (4-1) described in Chapter 4. The observed effect curves were found to lie below the predicated additive effect curves indicating that the combination treatment induced a synergistic effect. For example, at a $TPPS_4$ concentration of 400 μM, more than 90% of the cells were killed by the combination treatment, while a predicated additive response yielded 64.2% cell killing.

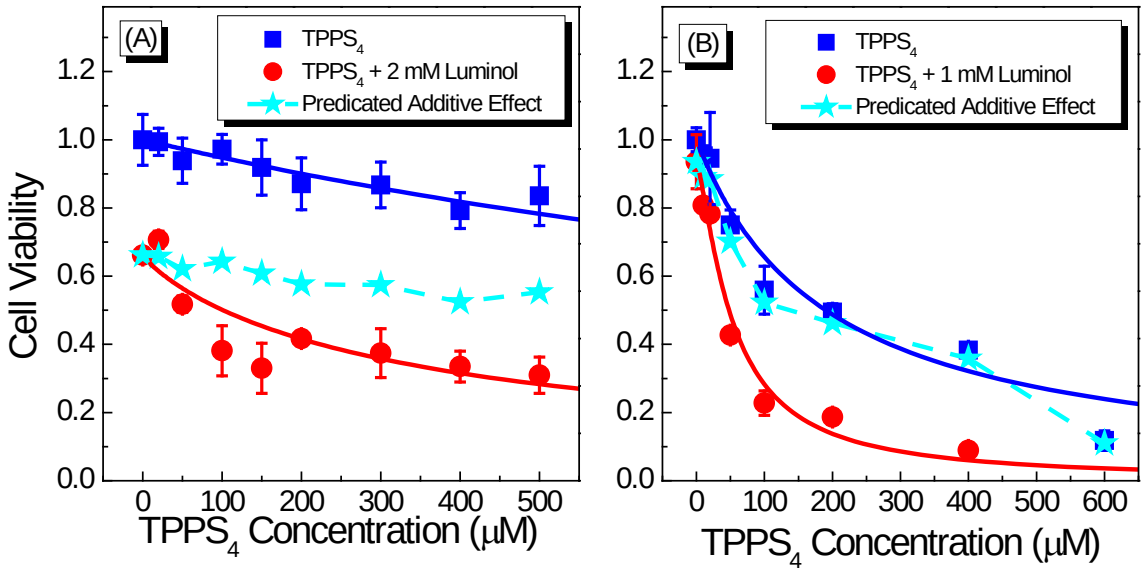

Figure 6-3: Cytotoxicity of the combination of luminol and $TPPS_4$ in human cervical cancer HeLa cells. Cells were incubated with various concentrations of luminol and $TPPS_4$ in cell culture medium containing 1% FBS for (A) 24 h or (B) 48 h. At the end of incubation period, cell viability was assessed by MTT cell viability assay. The solid lines are best fits to the

experimental data using a logistic function in Origin software. The dashed line and solid stars represent the calculated additive effect.

We have further evaluated the long-term proliferation rate of HeLa cells treated with the combination of luminol and $TPPS_4$ by performing clonogenic assay. The results are shown in Figure 6-4. In the absence of luminol, the IC_{50} of $TPPS_4$ was found to be larger than 400 μM. The survival fraction was approximately 70% at the highest $TPPS_4$ concentration of 400 μM tested in this experiment. Luminol at concentrations of 1 and 1.5 mM was found to be slightly cytotoxic and the corresponding values of survival fraction were 96.5 ± 7.8% and 83.0 ± 10.0%, respectively. The combination effect of luminol and $TPPS_4$ was assessed by performing fractional effect analysis as described in Chapter 4. The observed effects were found to be lower than the corresponding predicated additive effects suggesting the induction of synergistic effects by the combination treatment. This observation is consistent with what have been obtained from the MTT cell viability assay. We found that the relative IC_{50} values were 164.5 ± 49.9 and 68.4 ± 30.9 μM when cells were co-incubated with 1 and 1.5 mM luminol, respectively. This result indicates that the degree of synergism is also dependent on the dose of luminol.

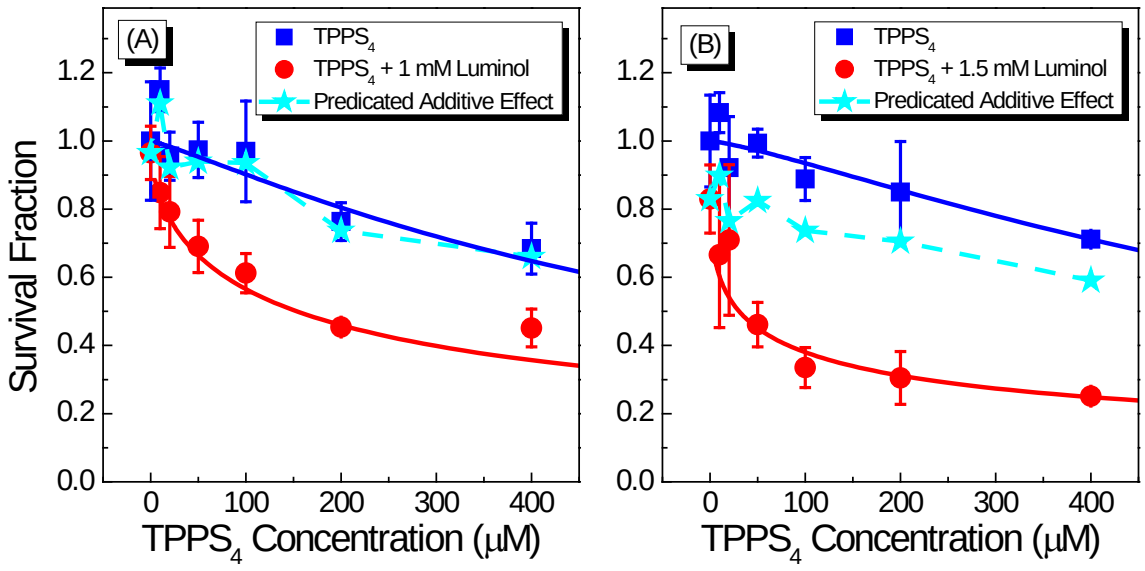

Figure 6-4: Clonogenic survival of HeLa cells treated with the combination of luminol and $TPPS_4$. Cells were incubated with various concentrations of luminol and $TPPS_4$ in cell culture medium containing 1% FBS for 24 h. At the end of incubation period, cells were washed twice with PBS and fresh medium containing 10% FBS was added. After 10 days, the resulting colonies were fixed, stained with crystal violet, and counted manually. The solid lines are best fits to the experimental data using a logistic function in Origin software. The dashed line and solid stars represent the calculated additive effect.

We note that the concentrations of luminol used in the present study are relatively high. Luminol has been reported to be relatively nontoxic. The oral drug dose lethal for 50% of a test population is > 500 mg kg^{-1} in rats (300). A luminol dose of 200 mg kg^{-1} has been used in a recently study performed by Gross *et al.*, who have applied the bioluminescence of luminol to monitor myeloperoxidase (MPO) activity in mice (205). Assuming that 70% of body weight is water, the molar concentration can be calculated by using the following equation:

$$C = \frac{D\rho}{0.7MW} \times 10^{-3}, \qquad (6\text{-}1)$$

where C is the molar concentration in mol L^{-1}, D is the dose in mg kg^{-1}, ρ is water density in g L^{-1}, and MW is the molecular weight in g mol^{-1}. Luminol has a molecular weight of 177.2 g mol^{-1}. Therefore, a luminol dose of 200 mg kg^{-1} corresponds to a molar concentration of 1.6 mM. In another study, Yuan *et al.* have used luminol concentrations of 0.5 and 2 mM in *in vitro* and *in vivo* experiments, respectively (215). The results of those studies suggest that millimolar (mM) concentrations of luminol can be used in animal studies.

6.3.3 Cytotoxicity of the combination of luminol and FeTPPS in HeLa cells

It is well known that iron both as free ions and in complexes can greatly enhance the bioluminescence intensity of luminol (213, 294, 296, 298, 301-303). Therefore, we have evaluated the cytotoxicity of the combination of luminol and FeTPPS, in which an iron atom is added to the center of the porphyrin ring of $TPPS_4$ (Figure 6-1), to see whether we can observe synergistic enhancement of cytotoxicity as obtained with $TPPS_4$. As shown in Figure 6-5A, in the absence of luminol, cytotoxicity of FeTPPS increased with increasing FeTPPS concentration. The IC_{50} was determined to be 48.8 ± 2.6 μM, which was approximately 26% of that of $TPPS_4$ under the same treatment conditions. In the presence of 1 mM luminol, the IC_{50} was reduced to 10.3 ± 0.5 μM. To assess the effects of luminol concentration on the cytotoxicity of the combination treatment, we performed one more experiment with a fixed FeTPPS concentration of 20 μM and varying concentrations of luminol. As shown in Figure 6-5B, luminol alone was only slightly cytotoxic up to a

concentration of 1 mM, at which less than 15% of the cells was killed. An IC_{50} of 1.98 ± 0.14 mM was obtained. When cells were co-incubated with luminol and 20 μM FeTPPS, the relative IC_{50} was determined to be 0.42 ± 0.08 mM. The results of fractional effect analysis showed that the combination of luminol and FeTPPS produced a synergistic effect and the degree of synergism was dependent upon the concentrations of both FeTPPS and luminol.

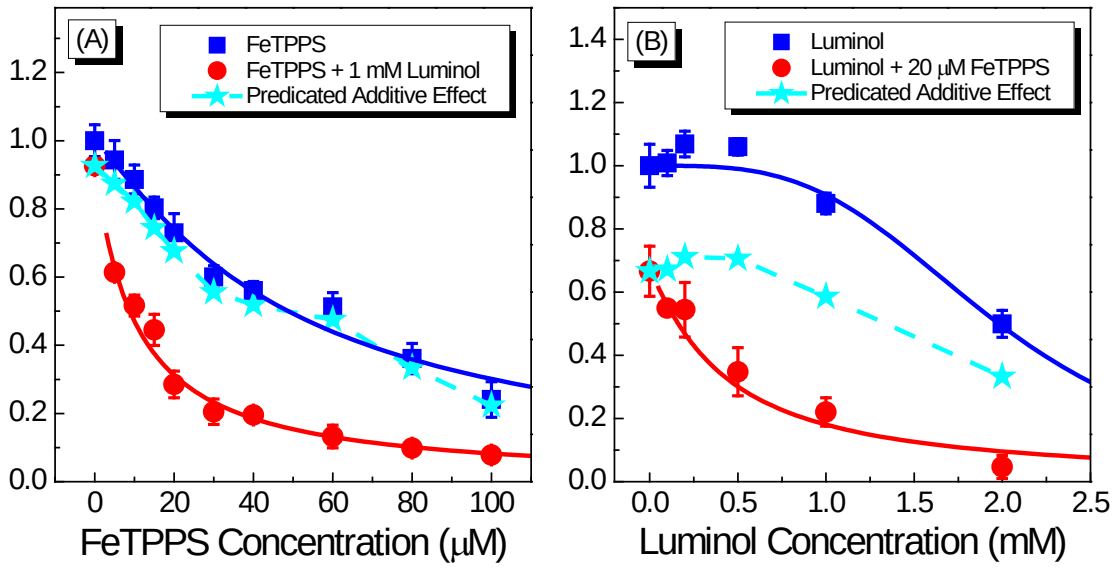

Figure 6-5: Cytotoxicity of the combination of luminol and FeTPPS in HeLa cells by MTT cell viability assay. Cells were incubated with various concentrations of luminol and FeTPPS in cell culture medium containing 1% FBS for 48 h. The solid lines are best fits to the experimental data using a logistic function in Origin software. The dashed line and solid stars represent the calculated additive effect.

6.3.4 Cytotoxicity of $TPPS_4$ and FeTPPS-mediated PDT activated by 400 nm laser light in HeLa cells

Cytotoxicity of $TPPS_4$ and FeTPPS activated by an external light source has also been evaluated in HeLa cells. Cells were treated with various concentrations of $TPPS_4$ and FeTPPS in 1% FBS for 24 h and then irradiated by a 400 nm laser at a light dose of 0.25 J cm^{-2}. The results are shown in Figure 6-6. Without laser irradiation, the IC_{50} of $TPPS_4$ was found to be higher than 400 μM similar to the results obtained in Section 6.3.2. With laser irradiation, an IC_{50} of 161.2 ± 171.6 μM was observed, which was ~45% of the value obtained when cells were co-incubated with $TPPS_4$ and 2 mM luminol for 24 h. Therefore, the level of cytotoxicity induced by incubating the cells with the mixtures of $TPPS_4$ and 2 mM luminol was comparable to that achieved when $TPPS_4$ was activated by a 400 nm laser at a light dose of 0.25 J cm^{-2}. Figure 6-6B shows the drug-dose response curves for cells treated with FeTPPS. The IC_{50} of FeTPPS was found to be 45.6 ± 3.9 μM, which was not affected significantly by laser irradiation at a light dose of 0.25 J cm^{-2}.

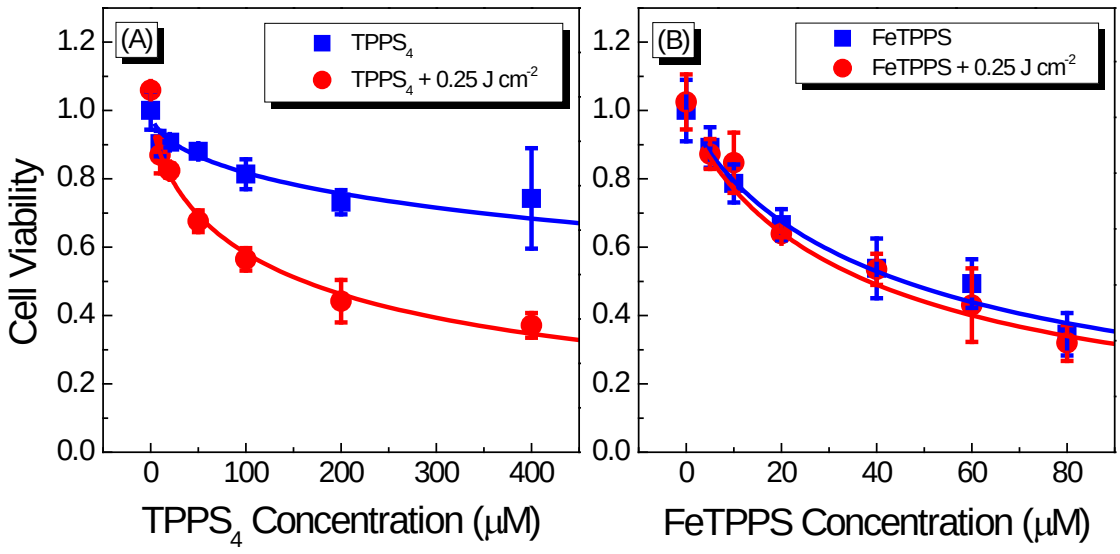

Figure 6-6: Drug-dose response curves for cell viability of HeLa cells treated with (A) $TPPS_4$- and (B) FeTPPS-mediated PDT by using the standard MTT cell viability assay. Cells were incubated with various concentrations of $TPPS_4$ and FeTPPS in cell culture medium containing 1% FBS for 24 h and then irradiated by a 400 nm fs laser at a light dose of 0.25 J cm^{-2}. Cell viability was determined 24 h after laser irradiation. The solid lines are best fits to the experimental data using a logistic function in Origin software.

Previously, Schipper *et al.* have raised an important question of whether the bioluminescence system can generate enough light to induce significant photodynamic killing of cancer cells (211). They have performed a series of experiments to determine whether bioluminescence of firefly luciferase (fLuc) can produce sufficient photons to activate photocytotoxicity of two photosensitizers (hypericin and Rose Bengal) in a number of nonmalignant and malignant cell lines. In contrast to the results reported by Theodossiou *et al.* (210), Schipper *et al.* didn't observe significant photodynamic effects under the same experimental conditions as those used in Ref. (210) and suggested that the cell line used by Theodossiou *et al.* contained an unknown contamination making the cells extremely sensitive to PDT. However, two novel bioluminescence systems have recently been developed and

demonstrated to be efficient in activating photodynamic killing of cancer cells both *in vitro* and *in vivo* (212, 215). In the present study, we have compared the cytotoxicity of $TPPS_4$ induced by luminol and an external laser source. We have found that under the same drug incubation conditions, laser irradiation at a wavelength of 400 nm and a light dose of 0.25 J cm^{-2} produced a similar level of cytotoxicity as that produced by co-incubation of the cells with $TPPS_4$ and 2 mM luminol. These promising initial results indicate that bioluminescence may be utilized as an internal light source for PDT and has the potential of extending the application of PDT to the treatment of deep tumor masses.

We didn't observe significant photocytotoxicity of FeTPPS under the same laser irradiation conditions as those applied to $TPPS_4$. In fact, FeTPPS is not considered to be an efficient PDT agent probably due to its low yield of cytotoxic ROS. Photocytotoxicity of FeTPPS may become significant at higher light doses. However, this was not tested due to the limited power of our laser system at 400 nm. Higher light doses will require prolonged irradiation of the cells. When FeTPPS was combined with luminol, we did observe a synergistic enhancement of cytotoxicity (Figure 6-5). We have further estimated the degree of synergism by calculating the ratios between the IC_{50} values of the photosensitizer in the absence and presence of luminol. The value for FeTPPS have been found to be 4.74, which is slightly higher than that of 3.58 for $TPPS_4$ suggesting that FeTPPS is more efficient than $TPPS_4$ in luminol-activated killing of HeLa cells. This observation is in contrast to the much lower activity of FeTPPS than $TPPS_4$ when the photosensitizers are activated by a 400 nm laser. One possible explanation is that the presence of iron in FeTPPS can greatly enhance

the bioluminescence of luminol and lead to increased cytotoxicity. Indeed, Motsenbocker *et al.* have shown that the relative luminescence intensity of luminol in 0.2 M NaOH is 305 a. u. (arbitrary unit) in the presence of FeTPPS, while the value in the presence of $TPPS_4$ is 0 a. u. (304). Therefore, the observation of a synergistic effect induced by the combination of luminol and FeTPPS supports the assumption that the photosensitizers can be activated by the bioluminescence of luminol.

6.3.5 Cytotoxicity of the combination of luminol and $TPPS_4$ and/or FeTPPS in two normal human fibroblast cell lines

One potential drawback of bioluminescence-activated PDT is a lack of tumor selectivity. Although most of the PDT sensitizers have been shown to have a higher affinity towards cancer cells than normal cells, selective destruction of tumors by PDT treatment still relies strongly on targeted delivery of light. Therefore, we have also evaluated the cytotoxicity of luminol and its combination with $TPPS_4$ and FeTPPS in two normal human fibroblast cell lines GM05757 and MRC-5. As shown in Figure 6-7A, luminol is slight cytotoxic in GM05757 cells. At the highest concentration of 8 mM, less than 40% of the cells were killed following 48 h drug incubation. Cytotoxicity of $TPPS_4$ and FeTPPS was also found to be lower than that observed in HeLa cells. More importantly, when GM05757 cells were co-incubated with the photosensitizers and 1 mM luminol, the values of cell viability did not differ significantly from those in the absence of luminol. This observation indicates that a

synergistic effect is absent under the same treatment conditions as those which induced a synergistic enhancement of cytotoxicity in HeLa cells.

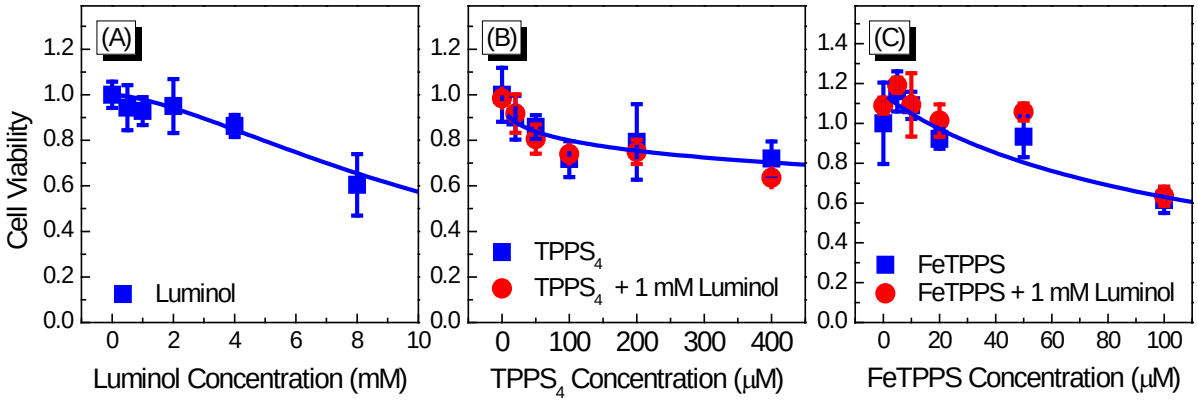

Figure 6-7: Cytotoxicity of luminol, $TPPS_4$, FeTPPS and the combination of luminol and $TPPS_4$/FeTPPS in normal human skin fibroblast GM05757 cells. Cells were incubated with various concentrations of luminol, $TPPS_4$ and FeTPPS in cell culture medium containing 1% FBS for 48 h. At the end of incubation period, cell viability was assessed by MTT cell viability assay. The solid lines are best fits to the experimental data using a logistic function in Origin software.

In the normal human lung fibroblast MRC-5 cells, luminol showed a low level of cytotoxicity with less than 20% of the cells killed up to 2 mM (Figure 6-8A). The IC_{50} of FeTPPS was determined to be 19.4 ± 2.3 μM, which was lower than that in HeLa cells indicating higher cytotoxicity of FeTPPS in this cell line. However, when cells were co-incubated with the photosensitizers and 1 mM luminol, no synergistic enhancement of cytotoxicity was observed in MRC-5 cells, while the relative IC_{50} was found to be reduced by nearly 80% in HeLa cells.

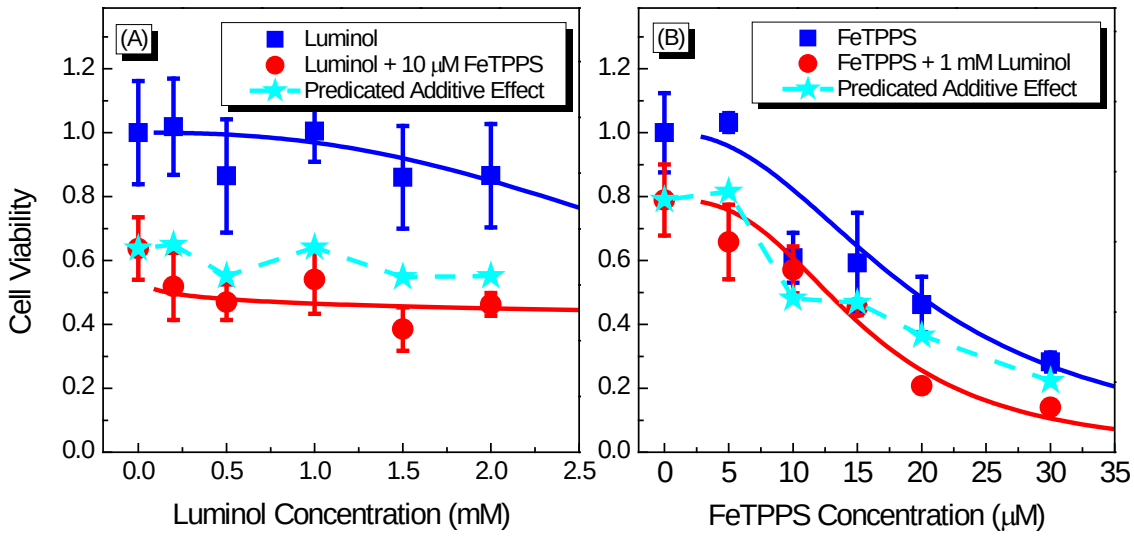

Figure 6-8: Cytotoxicity of the combination of luminol and FeTPPS in normal human lung fibroblast MRC-5 cells. Cells were incubated with various concentrations of luminol and FeTPPS in cell culture medium containing 1% FBS for 48 h. At the end of incubation period, cell viability was assessed by MTT cell viability assay. The solid lines are best fits to the experimental data using a logistic function in Origin software.

The absence of synergistic effects in the two normal human fibroblast cell lines treated by the combination of luminol and $TPPS_4$ or FeTPPS suggests that the combination treatment has the potential of treating selected cancers while causing minimal damages to healthy cells. Although the molecular mechanism underlying the observed difference between the HeLa cancer cell line and the two normal cell lines has not been investigated in the present study, it may be associated with the difference in the level of oxidative stress between the cancer and normal cell lines. Chemiluminescence of luminol has been proven to be a powerful tool for the detection of various oxidizing agents that can cause light emission from luminol (205, 213, 294, 296-299, 301, 304, 305). For example, Gross *et al.* have demonstrated that bioluminescence of luminol can be used to MPO activity, whose activation is associated with

pathogenesis of inflammatory disease states (e.g. cancer) in animal models (205). Good co-localization of luminol bioluminescence with tumor sites has been achieved and the signal-to-background ratio has been found to exceed 3,000. Therefore, bioluminescence of luminol may have intrinsic selectivity towards cancerous tissues and thus, may be developed as an internal light source for non-invasion PDT treatment of deep tumors that cannot be easily reached by conventional PDT.

6.4 Summary

Photodynamic therapy (PDT) has been proven to be an effective treatment approach for various human diseases including cancer. However, treatment of deep tumors remains a major challenge in PDT research due to the limited tissue penetration depth of external light (38, 306-308). In the present study, we have employed a novel approach in which bioluminescent light generated from luminol serves as an internal light source for the activation of the photosensitizers. Synergistic enhancement of cytotoxicity induced by the combination treatment of luminol and $TPPS_4$ has been observed in the human cervical cancer HeLa cells by performing the MTT cell viability assay and clonogenic assay. Similar effects have been observed when luminol is combined with FeTPPS, which is much less active than $TPPS_4$ when excited by a 400 nm fs laser. This observation supports the assumption that the synergistically enhanced cytotoxicity induced by the combination treatment of luminol and $TPPS_4$ or FeTPPS is a result of photodynamic activation of the photosensitizers by the bioluminescent light emitted from luminol. More importantly, we have demonstrated that the

same combination treatment produce an additive effect in two human normal fibroblast cell lines (GM05757 and MRC-5). These results suggest that the bioluminescence of luminol activated PDT of $TPPS_4$ or FeTPPS may favor the destruction of diseased tissues that have a higher than normal level of oxidative stress and thus, has the potential of treating deep-seated tumors in a non-invasive manner.

7 Conclusions and Future Research

The objective of this project has been to develop more effective treatment approaches that have the potential of increasing the penetration depth of photodynamic therapy (PDT) for the treatment of deeper and thicker tumor masses. In this chapter, we summarize the major results presented in the present thesis and discuss possible future research.

Two-photon activated PDT

In Chapter 3, we have demonstrated that the second-generation photosensitizer pyropheophorbide a methyl ester (MPPa; also known as PPME) can induce effective killing of cancer cells of human cervix (HeLa), lung (A549) and ovary (NIH:OVCAR-3) through both one-photon (1-γ; at 674 nm) and two-photon (2-γ; at 800 nm) excitation. Our finding that the photocytotoxicity induced in cisplatin-sensitive HeLa cells is comparable to that observed in cisplatin-resistant A549 and NIH:OVCAR-3 cells indicates that PDT mediated by MPPa has the potential of treating cisplatin-resistant cancers. More significantly, effective 2-γ activation of the drug at the optimal wavelength for tissue penetration offers the opportunity of increasing the treatment depth and improving tumor targeting.

Recent 2-γ PDT studies have been mainly focused on the development of photosensitizers that have high 2-γ absorption cross section (σ) values (134, 146, 148, 150-

152, 235-242). Our observation that MPPa with a low σ = 3.5 GM can be effectively activated at a peak irradiance of 3.9×10^{10} W cm^{-2}, which is about 10 times lower than the published threshold value (144), suggests the importance of factors other than σ in determining the effectiveness of the treatment and thus, should also be considered when developing novel treatment approaches.

Combination of NIR-PDT and chemotherapy

In Chapter 4, we have described synergistic enhancement of cytotoxicity in HeLa, A549 and NIH:OVCAR-3 cells treated with the combination of PDT mediated by the near infrared (NIR) dye indocyanine green (ICG) and etoposide (VP-16) chemotherapy as well as in A549 cells treated with ICG-PDT and teniposide (VM-26). The presence of VP-16 at the time of laser irradiation has been found to be critical for the observation of synergistic effects. We have further investigated the mechanism underlying the observed synergistic effects by performing steady-state and femtosecond time-resolved spectroscopic studies. An electron-transfer-based mechanism, in which ICG can act as an oxidizing agent to increase the yield of VP-16 metabolites that have been suggested to be more cytotoxic than VP-16 (13, 14, 274, 309), has been proposed, although direct spectroscopic detection of the reaction products has been found to be challenging.

In Chapter 5, we have presented the results of the combination of ICG-PDT and the platinum-based chemotherapeutic drugs cisplatin (CDDP) and oxaliplatin (OXP). Low dose CDDP/OXP in combination with ICG-PDT has been found to produce additive or slight

synergistic effects. An electron-transfer reaction between ICG and CDDP has been observed by performing steady-state absorption spectroscopic studies. This observation supports the proposal that this electron-transfer reaction is responsible for synergistic enhancement of cytotoxicity induced by the combination treatment.

The positive initial results obtained in the present study suggest that the combination of ICG-PDT with conventional chemotherapy mediated by VP-16/VM-26 or CDDP/OXP may increase the therapeutic effectiveness of ICG-PDT and lower the toxic side effects of the chemotherapeutic drugs at the same time.

Bioluminescence-activated PDT

In Chapter 6, synergistic enhancement of cytotoxicity has been observed in HeLa cells treated with the combination of luminol and $TPPS_4$/FeTPPS while an additive effect has been observed in the human normal fibroblast GM05757 and MRC-5 cells. Effective activation of $TPPS_4$/FeTPPS by the bioluminescence of luminol suggests that this system may be developed as a novel treatment option that is not limited by the tissue penetration depth of external light and thus, has the potential of treating deep-seated tumors.

All the three approaches explored in the present study have been shown to be able to induce significant killing in selected cancer cell lines. Further evaluation using other cell types and in animal models are expected to deepen our understanding of the mechanisms underlying the observed high effectiveness of the treatment and help the design of more effective modalities.

In recent year, drug-delivery systems such as micelles and various types of nanoparticles have been studied extensively (102, 106, 107, 109, 111-113, 115-118, 129, 201, 310, 311). Guelluy *et al.* have demonstrated that encapsulation of MPPa within liposomes of dimyristoyl-L-a-phosphatidylcholine (DMPC) can increase the intracellular concentration of the drug by 5 times in a human colon carcinoma (HCT-116) cell line (129). Various encapsulating approaches have also been demonstrated to improve the photophysical and photochemical properties of ICG as well as enable the use of tumor-targeting ligands, which further improves the tumor-specificity of the dye (102, 106, 107, 109, 111-113, 115-118, 201). Although we are not aware of any nanoparticle-based system for luminol delivery, nanoparticles conjugated with luciferase or D-Luciferin have been shown to improve the tumor-specificity of the drugs (310, 311). Therefore, encapsulation of the drugs studied in the present project within nanoparticles may further increase the therapeutic potential of these drugs.

References

1. Chappell H, Mery L. Canadian cancer statistics 2012. Canadian Cancer Society's Steering Committee on Cancer Statistics. 2012.
2. Siegel R, Naishadham D, Jemal A. Cancer statistics, 2013. CA-Cancer J Clin. 2013;63(1):11-30.
3. Siegel R, DeSantis C, Virgo K, Stein K, Mariotto A, Smith T, et al. Cancer treatment and survivorship statistics, 2012. CA-Cancer J Clin. 2012;62(4):220-41.
4. Döbrönte Z, Wittmann T, Karacsony G. Rapid development of malignant metastases in the abdominal wall after laparoscopy. Endoscopy. 1978;10(02):127-30.
5. Nduka C, Monson J, Menzies-Gow N, Darzi A. Abdominal wall metastases following laparoscopy. Br J Surg. 1994;81(5):648-52.
6. FY 2012 innovative drug approvals. 2012.
7. Florea A, Büsselberg D. Cisplatin as an anti-tumor drug: Cellular mechanisms of activity, drug resistance and induced side effects. Cancers. 2011;3(1):1351-7.
8. Postiglione I, Chiaviello A, Palumbo G. Enhancing photodynamic therapy efficacy by combination therapy: Dated, current and oncoming strategies. Cancers. 2011;3(2):2597-629.
9. Luo T, Yu J, Nguyen J, Wang C, Bristow RG, Jaffray DA, et al. Electron transfer-based combination therapy of cisplatin with tetramethyl-p-phenylenediamine for ovarian, cervical, and lung cancers. Proc Natl Acad Sci. 2012;109(26):10175-80.
10. Dyson PJ, Sava G. Metal-based antitumour drugs in the post genomic era. Dalton Trans. 2006(16):1929-33.
11. Lindsey RH, Bromberg KD, Felix CA, Osheroff N. 1, 4-benzoquinone is a topoisomerase II poison. Biochemistry. 2004;43(23):7563-74.
12. Bender RP, Ham AL, Osheroff N. Quinone-induced enhancement of DNA cleavage by human topoisomerase IIα: Adduction of cysteine residues 392 and 405. Biochemistry. 2007;46(10):2856-64.
13. Jacob DA, Mercer SL, Osheroff N, Deweese JE. Etoposide quinone is a redox-dependent topoisomerase II poison. Biochemistry. 2011;50(25):5660-7.

14. Jacob DA, Gibson EG, Mercer SL, Deweese JE. Etoposide catechol is an oxidizable topoisomerase II poison. Chem Res Toxicol. 2013;26(8):1156-8.
15. Hartmann JT, Lipp H. Camptothecin and podophyllotoxin derivatives. Drug Safety. 2006;29(3):209-30.
16. Bailly C. Contemporary challenges in the design of topoisomerase II inhibitors for cancer chemotherapy. Chem Rev. 2012;112(7):3611-40.
17. Delaney G, Jacob S, Featherstone C, Barton M. The role of radiotherapy in cancer treatment. Cancer. 2005;104(6):1129-37.
18. Moding EJ, Kastan MB, Kirsch DG. Strategies for optimizing the response of cancer and normal tissues to radiation. Nat Rev Drug Discov. 2013;12(7):526-42.
19. Nguyen J, Ma Y, Luo T, Bristow RG, Jaffray DA, Lu Q. Direct observation of ultrafast-electron-transfer reactions unravels high effectiveness of reductive DNA damage. Proc Natl Acad Sci. 2011;108(29):11778-83.
20. Lu Q. Effects and applications of ultrashort-lived prehydrated electrons in radiation biology and radiotherapy of cancer. Mutat Res -Rev Mutat. 2010;704(1):190-9.
21. Craft JM, Hallahan D. Towards novel radiosensitizing agents: The role of cytosolic PLA2α in combined modality cancer therapy. Future Med Chem. 2011;3(7):835-43.
22. Raab O. Ueber die wirkung fluorescirender stoffe auf infusorien. Zeitung Biol. 1900;39:524-6.
23. Von Tappeiner H, Jesionek A. Therapeutische versuche mit fluoreszierenden stoffen. Münch Med Wochenschr. 1903;47:2042-4.
24. Diamond I, Mcdonagh A, Wilson C, Granelli S, Nielsen S, Jaenicke R. Photodynamic therapy of malignant tumours. The Lancet. 1972;300(7788):1175-7.
25. Dougherty TJ, Grindey G, Fiel R, Weishaupt KR, Boyle D. Photoradiation therapy. II. cure of animal tumors with hematoporphyrin and light. JNCI. 1975;55(1):115-21.
26. Kelly J, Snell M, Berenbaum M. Photodynamic destruction of human bladder carcinoma. Br J Cancer. 1975;31(2):237-44.
27. Dougherty TJ, Kaufman JE, Goldfarb A, Weishaupt KR, Boyle D, Mittleman A. Photoradiation therapy for the treatment of malignant tumors. Cancer Res. 1978;38(8):2628-35.

28. Hua Z, Gibson SL, Foster TH, Hilf R. Effectiveness of δ-aminolevulinic acid-induced protoporphyrin as a photosensitizer for photodynamic therapy *in vivo*. Cancer Res. 1995;55(8):1723-31.

29. Dougherty TJ, Henderson BW, Gomer CJ, Jori G, Kessel D, Korbelik M, et al. Photodynamic therapy. JNCI. 1998;90(12):889-905.

30. Georgakoudi I, Foster TH. Singlet oxygen-versus nonsinglet oxygen-mediated mechanisms of sensitizer photobleaching and their effects on photodynamic dosimetry. Photochem Photobiol. 1998;67(6):612-25.

31. Chen Q, Huang Z, Luck D, Beckers J, Brun PH, Wilson BC, et al. Preclinical studies in normal canine prostate of a novel palladium-bacteriopheophorbide (WST09) photosensitizer for photodynamic therapy of prostate cancer. Photochem Photobiol. 2002;76(4):438-45.

32. Niedre M, Yu C, Patterson M, Wilson B. Singlet oxygen luminescence as an in vivo photodynamic therapy dose metric: Validation in normal mouse skin with topical amino-levulinic acid. Br J Cancer. 2005;92(2):298-304.

33. Weersink RA, Bogaards A, Gertner M, Davidson SRH, Zhang K, Netchev G, et al. Techniques for delivery and monitoring of TOOKAD (WST09)-mediated photodynamic therapy of the prostate: Clinical experience and practicalities. J Photochem Photobiol B: Biol. 2005;79(3):211-22.

34. Wilson B, Patterson M. The physics, biophysics and technology of photodynamic therapy. Phys Med Biol. 2008;53(9):R61-R109.

35. Lovell J, Chen J, Jarvi M, Cao W, Allen A, Liu Y, et al. FRET quenching of photosensitizer singlet oxygen generation. J Phys Chem B. 2009;113(10):3203-11.

36. Korbelik M. Cancer vaccines generated by photodynamic therapy. Photochem Photobiol Sci. 2011;10(5):664-9.

37. Agostinis P, Berg K, Cengel KA, Foster TH, Girotti AW, Gollnick SO, et al. Photodynamic therapy of cancer: An update. CA-Cancer J Clin. 2011;61(4).

38. Master A, Livingston M, Sen Gupta A. Photodynamic nanomedicine in the treatment of solid tumors: Perspectives and challenges. J Controlled Release. 2013;168(1):88-102.

39. Biomedical photonics handbook. Vo-Dinh T, editor. CRC Press LLc; 2003.

40. Saltiel J, Atwater BW. Spin-statistical factors in diffusion-controlled reactions. Adv Photochem. 1988;14:1-90.
41. McLean AJ, McGarvey DJ, Truscott TG, Lambert CR, Land EJ. Effect of oxygen-enhanced intersystem crossing on the observed efficiency of formation of singlet oxygen. J Chem Soc , Faraday Trans. 1990;86(18):3075-80.
42. Wilkinson F, McGarvey D, Olea A. Factors governing the efficiency of singlet oxygen production during oxygen quenching of singlet and triplet states of anthracene derivatives in cyclohexane solution. J Am Chem Soc. 1993;115(25):12144-51.
43. Wilkinson F, Helman W, Ross A. Quantum yields for the photosensitized formation of the lowest electronically excited singlet state of molecular oxygen in solution. Journal of Physical and Chemical Reference Data. 1993;22.
44. Olea A, Wilkinson F. Singlet oxygen production from excited singlet and triplet states of anthracene derivatives in acetonitrile. J Phys Chem. 1995;99(13):4518-24.
45. Abdel-Shafi AA, Worrall DR, Wilkinson F. Singlet oxygen formation efficiencies following quenching of excited singlet and triplet states of aromatic hydrocarbons by molecular oxygen. J Photochem Photobiol A: Chem. 2001;142:133-42.
46. Tanaka F, Furuta T, Okamoto M, Hirayama S. Inverse correlation between efficiency of singlet oxygen production and rate constant for oxygen quenching in the S_1 state of anthracene derivatives. Phys Chem Chem Phys. 2004;6(6).
47. Schmidt R. Photosensitized generation of singlet oxygen. Photochem Photobiol. 2006;82(5).
48. Tanaka F, Tsumura K, Furuta T, Iwamoto K, Okamoto M. Efficiencies of singlet oxygen production and rate constants for oxygen quenching in the S_1 state of dicyanonaphthalenes and related compounds. Photochem Photobiolo Sci. 2008;7(1).
49. Sharman WM, Allen CM, van Lier JE. Role of activated oxygen species in photodynamic therapy. Methods Enzymol. 1999;319:376-400.
50. Foote CS. Definition of type I and type II photosensitized oxidation. Photochem Photobiol. 1991;54(5):659-659.
51. Ochsner M. Photophysical and photobiological processes in the photodynamic therapy of tumors. J Photochem Photobiol B: Biol. 1997;39(1):1-18.

52. Prasad PN. Introduction to biophotonics. New Jersey: John Wiley & Sons, Inc.; 2003.
53. Gollnick SO, Owczarczak B, Maier P. Photodynamic therapy and anti-tumor immunity. Lasers Surg Med. 2006;38(5):509-15.
54. Kessel D, Luo Y, Deng Y, Chang CK. The role of subcellular localization in initiation of apoptosis by photodynamic therapy. Photochem Photobiol. 1997;65(3):422-6.
55. Vantieghema A, Assefaa Z, Vandenabeeled P, Declercqd W, Courtoisb S, Vandenheedea JR, et al. Hypericin-induced photosensitization of HeLa cells leads to apoptosis or necrosis. Involvement of cytochrome c and procaspase-3 activation in the mechanism of apoptosis. FEBS Letters. 1998;440(1):19-24.
56. Oleinick NL, Morris RL, Belichenko I. The role of apoptosis in response to photodynamic therapy: What, where, why, and how. Photochem Photobiol Sci. 2002;1(1):1-21.
57. Nakagawa T, Shimizu S, Watanabe T, Yamaguchi O, Otsu K, Yamagata H, et al. Cyclophilin D-dependent mitochondrial permeability transition regulates some necrotic but not apoptotic cell death. Nature. 2005;434(7033):652-8.
58. Buytaert E, Callewaert G, Hendrickx N, Scorrano L, Hartmann D, Missiaen L, et al. Role of endoplasmic reticulum depletion and multidomain proapoptotic BAX and BAK proteins in shaping cell death after hypericin-mediated photodynamic therapy. FASEB J. 2006;20(6):756-8.
59. Kessel D, Vicente MGH, Reiners Jr JJ. Initiation of apoptosis and autophagy photodynamic therapy. Lasers Surg Med. 2006;38(5):482-8.
60. Kessel D, Reiners Jr JJ. Apoptosis and autophagy after mitochondrial or endoplasmic reticulum photodamage. Photochem Photobiol. 2007;83(5):1024-8.
61. Kessel D, Arroyo AS. Apoptotic and autophagic responses to bcl-2 inhibition and photodamage. Photochem Photobiol Sci. 2007;6(12):1290-5.
62. Buytaert E, Dewaele M, Agostinis P. Molecular effectors of multiple cell death pathways initiated photodynamic therapy. Biochimica et Biophysica Acta (BBA)-Reviews on Cancer. 2007;1776(1).

63. Xue L, Chiu S, Azizuddin K, Joseph S, Oleinick NL. Protection by bcl-2 against apoptotic but not autophagic cell death after photodynamic therapy. Autophagy. 2008;4(1):125-7.

64. Sasnauskiene A, Kadziauskas J, Vezelyte N, Jonusiene V, Kirveliene V. Apoptosis, autophagy and cell cycle arrest following photodamage to mitochondrial interior. Apoptosis. 2009;14(3):276-8.

65. Reiners Jr JJ, Agostinis P, Berg K, Oleinick NL, Kessel D. Assessing autophagy in the context of photodynamic therapy. Autophagy. 2010;6(1):7-18.

66. Kamarulzaman EE, Benachour H, Barberi-Heyob M, Frochot C, Wahab HA, Guillemin F, et al. Vascular-targeted photodynamic therapy (VTP). 2011:99-122.

67. Inguscio V, Panzarini E, Dini L. Autophagy contributes to the death/survival balance in cancer photodynamic therapy. Cells. 2012;1(3):464-91.

68. Ogilby PR. Singlet oxygen: There is indeed something new under the sun. Chem Soc Rev. 2010;39(8):3181-209.

69. Holler N, Zaru R, Micheau O, Thome M, Attinger A, Valitutti S, et al. Fas triggers an alternative, caspase-8-independent cell death pathway using the kinase RIP as effector molecule. Nat Immunol. 2000;1(6):489-95.

70. Berghe TV, Kalai M, van Loo G, Declercq W, Vandenabeele P. Disruption of HSP90 function reverts tumor necrosis factor-induced necrosis to apoptosis. J Biol Chem. 2003;278(8):5622-9.

71. Xu Y, Huang S, Liu ZG, Han J. Poly(ADP-ribose) polymerase-1 signaling to mitochondria in necrotic cell death requires RIP1/TRAF2- mediated JNK1 activation. J Biol Chem. 2006;281(13):8788-95.

72. Buytaert E, Callewaert G, Vandenheede JR, Agostinis P. Addenda deficiency in apoptotic effectors bax and bak reveals an autophagic cell death pathway initiated by photodamage to the endoplasmic reticulum. Autophagy. 2006;2(3):238-40.

73. Lim HW, Hagan M, Gigli I. Phototoxicity induced by hematoporphyrin derivative in C5-deficient, mast cell-deficient and leukopenic mice. Photochem Photobiol. 1986;44(2):175-80.

74. Fingar VH, Wieman TJ, Doak KW. Changes in tumor interstitial pressure induced by photodynamic therapy. Photochem Photobiol. 1991;53(6):763-8.

75. Fingar VH, Wieman TJ, Wiehle SA, Cerrito PB. The role of microvascular damage in photodynamic therapy: The effect of treatment on vessel constriction, permeability, and leukocyte adhesion. Cancer Res. 1992;52(18):4914-21.

76. Fingar VH. Vascular effects of photodynamic therapy. J Clin Laser Med Surg. 1996;14(5):323-8.

77. Krammer B. Vascular effects of photodynamic therapy. Anticancer Res. 2001;21(6B):4271-7.

78. Ferrario A, von Tiehl K, Wong S, Luna M, Gomer CJ. CycloOxygenase-2 inhibitor treatment enhances photodynamic therapy-mediated tumour response. Cancer Res. 2002;62(14):3956-61.

79. Dolmans DE, Kadambi A, Hill JS, Waters CA, Robinson BC, Walker JP, et al. Vascular accumulation of a novel photosensitizer, MV6401, causes selective thrombosis in tumour vessels after photodynamic therapy. Cancer Res. 2002;62(7):2151-6.

80. Brandis A, Mazor O, Neumark E, Rosenbach-Belkin V, Salomon Y, Scherz A. Novel water-soluble bacteriochlorophyll derivatives for vascular-targeted photodynamic therapy: Synthesis, solubility, phototoxicity and the effect of serum proteins. Photochem Photobiol. 2005;81(4):983-92.

81. Longo JPF, Lozzi SP, Simioni AR, Morais PC, Tedesco AC, Azevedo RB. Photodynamic therapy with aluminum-chloro-phtalocyanine induces necrosis and vascular damage in mice tongue tumors. J Photochem Photobiol B: Biol. 2009;94(2):143-6.

82. Preise D, Scherz A, Salomon Y. Antitumor immunity promoted by vascular occluding therapy: Lessons from vascular-targeted photodynamic therapy (VTP). Photochem Photobiol Sci. 2011;10(5):681-8.

83. Wang W, Moriyama LT, Bagnato VS. Photodynamic therapy induced vascular damage: An overview of experimental PDT. Laser Phys Lett. 2013;10(2):023001-1,023001-8.

84. Henderson BW, Dougherty TJ. How does photodynamic therapy work? Photochem Photobiol. 1992;55(1):145-57.

85. Korbelik M, Krosl G, Krosl J, Dougherty GJ. The role of host lymphoid populations in the response of mouse EMT6 tumour to photodynamic therapy. Cancer Res. 1996;56(24):5647-52.

86. Gollnick SO, Vaughan L, Henderson BW. Generation of effective antitumour vaccines using photodynamic therapy. Cancer Res. 2002;62(6):1604-8.

87. Korbelik M, Sun J, Cecic I. Photodynamic therapy-induced cell surface expression and release of heat shock proteins: Relevance for tumour response. Cancer Res. 2005;65(3):1018-26.

88. Castano AP, Mroz P, Hamblin MR. Photodynamic therapy and antitumour immunity. Nat Rev Cancer. 2006;6(7):535-4.

89. Korbelik M, Sun J. Photodynamic therapy-generated vaccine for cancer therapy. Cancer Immunol Immunother. 2006;55:900-9.

90. Korbelik M, Stott B, Sun J. Photodynamic therapy-generated vaccines: Relevance of tumour cell death expression. Br J Cancer. 2007;97(10):1381-7.

91. Gollnick SO, Liu X, Owczarcza B, Musser DA, Henderson BW. Altered expression of interleukin 6 and interleukin 10 as a result of photodynamic therapy *in vivo*. Cancer Res. 1997;57(18):3904-9.

92. Hausmann W. Über die sensibilisierende wirkung des hämatoporphyrins. Biochem Zeitung. 1911;30:276-31.

93. Meyer-Betz F. Untersuchungen über die biologische (photodynamische) wirkung des hämatoporphyrins und anderer derivate des blut-und gallenfarbstoffs. Dtsch Arch Klin Med. 1913;112:476-503.

94. Schwartz S, Absolon K, Vermund H. Some relationships of porphyrins, X-rays and tumors. Univ Minn Med Bull. 1955;27:7-8.

95. Lipson RL, Baldes EJ, Olsen AM. Hematoporphyrin derivative: A new aid for endoscopic detection of malignant disease. J Thorac Cardiovasc Surg. 1961;42:623-9.

96. Eichler J, Knof J, Lenz H. Measurements on the depth of penetration of light (0.35–1.0 µm) in tissue. Radiat Environ Biophys. 1977;14(3):239-42.

97. Allison R, Sibata C. Oncologic photodynamic therapy photosensitizers: A clinical review. Photodiagnosis Photodyn Ther. 2010;7(2).

98. Senge MO, Brandt JC. Temoporfin (Foscan®, 5, 10, 15, 20-tetra (m-hydroxyphenyl) chlorin) — a second-generation photosensitizer. Photochem Photobiol. 2011;87(6):1240-96.

99. Senge MO. mTHPC – A drug on its way from second to third generation photosensitizer? Photodiagnosis Photodyn Ther. 2012;9(2):170-9.

100. Ormond AB, Freeman HS. Dye sensitizers for photodynamic therapy. Materials. 2013;6(3):817-40.

101. Nishiyama N, Stapert HR, Zhang G, Takasu D, Jiang D, Nagano T, et al. Light-harvesting ionic dendrimer porphyrins as new photosensitizers for photodynamic therapy. Bioconjug Chem. 2003;14(1):58-66.

102. Saxena V, Sadoqi M, Shao J. Enhanced photo-stability, thermal-stability and aqueous-stability of indocyanine green in polymeric nanoparticulate systems. J Photochem Photobiol B: Biol. 2004;74(1):29-38.

103. Sharman WM, van Lier JE, Allen CM. Targeted photodynamic therapy via receptor mediated delivery systems. Adv Drug Deliv Rev. 2004;56(1):53-76.

104. Laptev R, Nisnevitch M, Siboni G, Malik Z, Firer M. Intracellular chemiluminescence activates targeted photodynamic destruction of leukaemic cells. Br J Cancer. 2006;95(2):189-96.

105. Solban N, Rizvi I, Hasan T. Targeted photodynamic therapy. Lasers Surg Med. 2006;38(5):522-31.

106. Yu J, Yaseen MA, Anvari B, Wong MS. Synthesis of near-infrared-absorbing nanoparticle-assembled capsules. Chemistry of Materials. 2007;19(6):1277-84.

107. Altınoğlu EI, Russin TJ, Kaiser JM, Barth BM, Eklund PC, Kester M, et al. Near-infrared emitting fluorophore-doped calcium phosphate nanoparticles for in vivo imaging of human breast cancer. ACS Nano. 2008;2(10):2075-84.

108. Beom Joon K, Ho Gyun L, Seung Man W, Jai Il Y, Dae Hun S. Pilot study on photodynamic therapy for acne using indocyanine green and diode laser. The Journal of Dermatology. 2009;36(1):17-21.

109. Kirchherr A, Briel A, Mäder K. Stabilization of indocyanine green by encapsulation within micellar systems. Mol Pharm. 2009;6(2):480-91.

110. Lovell JF, Liu TW, Chen J, Zheng G. Activatable photosensitizers for imaging and therapy. Chem Rev. 2010;110(5):2839-57.
111. Kuo W, Chang C, Chang Y, Yang M, Chien Y, Chen S, et al. Gold nanorods in photodynamic therapy, as hyperthermia agents, and in near-infrared optical imaging. Angew Chem Int Ed. 2010;122(15):2771-5.
112. Yu J, Javier D, Yaseen MA, Nitin N, Richards-Kortum R, Anvari B, et al. Self-assembly synthesis, tumor cell targeting, and photothermal capabilities of antibody-coated indocyanine green nanocapsules. J Am Chem Soc. 2010;132(6):1929-38.
113. Zheng X, Xing D, Zhou F, Wu B, Chen WR. Indocyanine green-containing nanostructure as near infrared dual-functional targeting probes for optical imaging and photothermal therapy. Mol Pharm. 2011;8(2):447-56.
114. Bugaj AM. Targeted photodynamic therapy–a promising strategy of tumor treatment. Photochem Photobiol Sci. 2011;10(7):1097-109.
115. Bahmani B, Vullev V, Anvari B. Development of anti-HER2 conjugated ICG-loaded polymeric nanoparticles for targeted optical imaging of ovarian cancer. SPIE BiOS; International Society for Optics and Photonics; 2012.
116. HyunáChung B. Indocyanine green encapsulated nanogels for hyaluronidase activatable and selective near infrared imaging of tumors and lymph nodes. Chem Commun. 2012;48(69):8628-30.
117. Zheng C, Zheng M, Gong P, Jia D, Zhang P, Shi B, et al. Indocyanine green-loaded biodegradable tumor targeting nanoprobes for *in vitro* and *in vivo* imaging. Biomaterials. 2012;33(22):5603-9.
118. Jung B, Anvari B. Synthesis and characterization of bovine serum albumin-coated nanocapsules loaded with indocyanine green as potential multifunctional nanoconstructs. Biotechnol Prog. 2012;28(2):533-9.
119. Ballut S, Makky A, Chauvin B, Michel J, Kasselouri A, Maillard P, et al. Tumor targeting in photodynamic therapy. From glycoconjugated photosensitizers to glycodendrimeric one. Concept, design and properties. Org Biomol Chem. 2012;10(23):4485-9.

120. Puri A. Phototriggerable liposomes: Current research and future perspectives. Pharmaceutics. 2013;6(1):1-25.

121. Sano K, Nakajima T, Miyazaki K, Ohuchi Y, Ikegami T, Choyke PL, et al. Short PEG-linkers improve the performance of targeted, activatable monoclonal antibody-indocyanine green optical imaging probes. Bioconjug Chem. 2013;24(5):811-6.

122. Chen J, Jarvi M, Lo P, Stefflova K, Wilson BC, Zheng G. Using the singlet oxygen scavenging property of carotenoid in photodynamic molecular beacons to minimize photodamage to non-targeted cells. Photochem Photobiol Sci. 2007;6(12):1311-7.

123. Hamblin MR, Newman EL. Photosensitizer targeting in photodynamic therapy I. conjugates of haematoporphyrin with albumin and transferrin. J Photochem Photobiol B: Biol. 1994;26(1):45-56.

124. Cavanaugh PG. Synthesis of chlorin e6-transferrin and demonstration of its light-dependent in vitro breast cancer cell killing ability. Breast Cancer Res Treat. 2002;72(2):117-30.

125. Lutsenko S, Feldman N, Finakova G, Posypanova G, Severin S, Skryabin K, et al. Targeting phthalocyanines to tumor cells using epidermal growth factor conjugates. Tumor Biol. 1999;20(4):218-24.

126. Bechet D, Couleaud P, Frochot C, Viriot M, Guillemin F, Barberi-Heyob M. Nanoparticles as vehicles for delivery of photodynamic therapy agents. Trends Biotechnol. 2008;26(11):612-21.

127. Chatterjee D, Fong L, Zhang Y. Nanoparticles in photodynamic therapy: An emerging paradigm. Advanced drug delivery reviews. 2008;60(15).

128. da Silva A, Inada N, Rettori D, Baratti M, Vercesi A, Jorge R. *In vitro* photodynamic activity of chloro (5, 10, 15, 20-tetraphenylporphyrinato) indium (III) loaded-poly (lactide-co-glycolide) nanoparticles in LNCaP prostate tumour cells. Journal of Photochemistry and Photobiology B: Biology. 2009;94(2).

129. Guelluy PH, Fontaine-Aupart MP, Grammenos A, Lécart S, Piette J, Hoebeke M. Optimizing photodynamic therapy by liposomal formulation of the photosensitizer pyropheophorbide-a methyl ester: *in vitro* and *ex vivo* comparative biophysical

investigations in a colon carcinoma cell line. Photochem Photobiol Sci. 2010;9(9):1252-60.

130. Swami A, Shi J, Gadde S, Votruba AR, Kolishetti N, Farokhzad OC. Nanoparticles for targeted and temporally controlled drug delivery. In: Svenson S, Prud'homme RK, editors. Multifunctional Nanoparticles for Drug Delivery Applications. Springer; 2012. p. 9-29.
131. Taroni P, Pifferi A, Torricelli A, Comelli D, Cubeddu R. *In vivo* absorption and scattering spectroscopy of biological tissues. Photochem Photobiol Sci. 2003;2(2):124-9.
132. Mbambisa G, Nyokong T. Synthesis and electrochemical characterisation of a near infrared absorbing oxo vanadium (IV) octapentylthio-phthalocyanine. Polyhedron. 2008;27(13):2799-804.
133. Lu T, Shao P, Mathew I, Sand A, Sun W. Synthesis and photophysics of benzotexaphyrin: a near-infrared emitter and photosensitizer. J Am Chem Soc. 2008;130(47):15782-3.
134. Balaz M, Collins HA, Dahlstedt E, Anderson HL. Synthesis of hydrophilic conjugated porphyrin dimers for one-photon and two-photon photodynamic therapy at NIR wavelengths. Org Biomol Chem. 2009;7(5):874-88.
135. Huang YY, Mroz P, Zhiyentayev T, Sharma SK, Balasubramanian T, Ruzié C, et al. *In vitro* photodynamic therapy and quantitative structure-activity relationship studies with stable synthetic near-infrared-absorbing bacteriochlorin photosensitizers. J Med Chem. 2010;53(10):4018-27.
136. Muranaka A, Yonehara M, Uchiyama M. Azulenocyanine: a new family of phthalocyanines with intense near-IR absorption. J Am Chem Soc. 2010;132(23):7844-5.
137. Göppert-Mayer M. Über elementarakte mit zwei quantensprüngen. Annalen der Physik. 1931;401(3):273-94.
138. Denk W, Strickler JH, Webb WW. Two-photon laser scanning fluorescence microscopy. Science. 1990;248(4951):73-6.

139. Chen R, Huang Z, Chen G, Li Y, Chen X, Chen J, et al. Kinetics and subcellular localization of 5-ALA-induced PpIX in DHL cells via two-photon excitation fluorescence microscopy. Int J Oncol. 2008;32(4):861-8.

140. Chen J, Lee A, Zhao J, Wang H, Lui H, McLean DI, et al. Spectroscopic characterization and microscopic imaging of extracted and in situ cutaneous collagen and elastic tissue components under two-photon excitation. Skin Res Technol. 2009;15(4):418-26.

142. Lenz P. *In vivo* excitation of photosensitizers by infrared light. Photochem Photobiol. 1995;62(2):333-8.

142. Fisher WG, Partridge WP, Dees C, Wachter EA. Simultaneous two-photon activation of type-I photodynamic therapy agents. Photochem Photobiol. 1997;66(2):141-55.

143. Liu J, Zhao Y, Zhao J, Xia A, Jiang L, Wu S, et al. Two-photon excitation studies of hypocrellins for photodynamic therapy. J Photochem Photobiol B: Biol. 2002;68(2):156-64.

144. Karotki A, Khurana M, Lepock JR, Wilson BC. Simultaneous two-photon excitation of photofrin in relation to photodynamic therapy. Photochem Photobiol. 2006;82(2):443-52.

145. Mir Y, Houde D, van Lier JE. Two-photon absorption of copper tetrasulfophthalocyanine induces phototoxicity towards jurkat cells *in vitro*. Photochem Photobiol Sci. 2006;5(11):1024-30.

146. Samkoe KS, Clancy AA, Karotki A, Wilson BC, Cramb DT. Complete blood vessel occlusion in the chick chorioallantoic membrane using two-photon excitation photodynamic therapy: Implications for treatment of wet age-related macular degeneration. J Biomed Opt. 2007;12(3):034025-1,034025-14.

147. Khurana M, Collins HA, Karotki A, Anderson HL, Cramb DT, Wilson BC. Quantitative *in vitro* demonstration of two-photon photodynamic therapy using Photofrin® and Visudyne®. Photochem Photobiol. 2007;83(6):1441-8.

148. Collins HA, Khurana M, Moriyama EH, Mariampillai A, Dahlstedt E, Balaz M, et al. Blood-vessel closure using photosensitizers engineered for two-photon excitation. Nature Photon. 2008;2(7):420-4.

149. Spangler C, Starkey J, Rebane A, Drobizhev M, Meng F, Gong A. Synthesis, characterization and two-photon PDT efficacy studies of triads incorporating tumor targeting and imaging components. Biomedical optics (BiOS); International Society for Optics and Photonics; 2006.

150. Dahlstedt E, Collins HA, Balaz M, Kuimova MK, Khurana M, Wilson BC, et al. One- and two-photon activated phototoxicity of conjugated porphyrin dimers with high two-photon absorption cross sections. Org Biomol Chem. 2009;7(5):897-904.

151. Pawlicki M, Collins HA, Denning RG, Anderson HL. Two-photon absorption and the design of two-photon dyes. Angew Chem Int Ed. 2009;48(18):3244-66.

152. Spangler CW, Starkey JR, Dubinina G, Fahlstrom C, Shepard J. Optimization of targeted two-photon PDT triads for the treatment of head and neck cancers. SPIE BiOS; International Society for Optics and Photonics; 2012.

153. Godwin AK, Meister A, O'Dwyer PJ, Huang CS, Hamilton TC, Anderson ME. High resistance to cisplatin in human ovarian cancer cell lines is associated with marked increase of glutathione synthesis. Proc Natl Acad Sci. 1992;89(7):3070-4.

154. Liu R, Page C, Beidler DR, Wicha MS, Núñez G. Overexpression of bcl-x_L promotes chemotherapy resistance of mammary tumors in a syngeneic mouse model. Am J Path. 1999;155(6):1861-7.

155. Fuertes MA, Alonso C, Pérez JM. Biochemical modulation of cisplatin mechanisms of action: Enhancement of antitumor activity and circumvention of drug resistance. Chem Rev. 2003;103(3):645-62.

156. Agarwal R, Kaye SB. Ovarian cancer: Strategies for overcoming resistance to chemotherapy. Nat Rev Cancer. 2003;3(7):502-16.

157. Thomas H, Coley HM. Overcoming multidrug resistance in cancer: An update on the clinical strategy of inhibiting p-glycoprotein. Cancer Control. 2003;10(2):159-65.

158. Sakai W, Swisher EM, Karlan BY, Agarwal MK, Higgins J, Friedman C, et al. Secondary mutations as a mechanism of cisplatin resistance in BRCA2-mutated cancers. Nature. 2008;451(7182):1116-20.

159. Holohan C, Van Schaeybroeck S, Longley DB, Johnston PG. Cancer drug resistance: An evolving paradigm. Nat Rev Cancer. 2013;13(10):714-26.

160. Kaiser J. Combining targeted drugs to stop resistant tumors. Science. 2011;331(6024):1542-5.

161. Stolik S, Delgado J, Perez A, Anasagasti L. Measurement of the penetration depths of red and near infrared light in human "*ex vivo*" tissues. J Photochem Photobiol B: Biol. 2000;57(2):90-3.

162. Casas A, Di Venosa G, Hasan T, Batlle A. Mechanisms of resistance to photodynamic therapy. Curr Med Chem. 2011;18(16):2486-515.

163. Canti G, Nicolin A, Cubeddu R, Taroni P, Bandieramonte G, Valentini G. Antitumor efficacy of the combination of photodynamic therapy and chemotherapy in murine tumors. Cancer Lett. 1998;125(1):39-44.

164. Duska L, Hamblin M, Miller J, Hasan T. Combination photoimmunotherapy and cisplatin: Effects on human ovarian cancer *ex vivo*. JNCI. 1999;91(18):1557-63.

165. Crescenzi E, Varriale L, Iovino M, Chiaviello A, Veneziani BM, Palumbo G. Photodynamic therapy with indocyanine green complements and enhances low-dose cisplatin cytotoxicity in MCF-7 breast cancer cells. Mol Cancer Ther. 2004;3(5):537-44.

166. Crescenzi E, Chiaviello A, Canti G, Reddi E, Veneziani B, Palumbo G. Low doses of cisplatin or gemcitabine plus photofrin/photodynamic therapy: Disjointed cell cycle phase-related activity accounts for synergistic outcome in metastatic non--small cell lung cancer cells (H1299). Mol Cancer Ther. 2006;5(3):776-85.

167. Compagnin C, Mognato M, Celotti L, Canti G, Palumbo G, Reddi E. Cell proliferation and cell cycle alterations in oesophageal p53-mutated cancer cells treated with cisplatin in combination with photodynamic therapy. Cell Prolif. 2010;43(3):262-74.

168. Nonaka M, Ikeda H, Inokuchi T. Effect of combined photodynamic and chemotherapeutic treatment on lymphoma cells *in vitro*. Cancer Lett. 2002;184(2):171-8.

169. Lottner C, Bart K, Bernhardt G, Brunner H. Hematoporphyrin-derived soluble porphyrin-platinum conjugates with combined cytotoxic and phototoxic antitumor activity. J Med Chem. 2002;45(10):2064-78.

170. Mao J, Zhang Y, Zhu J, Zhang C, Guo Z. Molecular combo of photodynamic therapeutic agent silicon (iv) phthalocyanine and anticancer drug cisplatin. Chem Commun. 2009(8):908-10.
171. Bulgakov RA, Kuznetsova NA, Dolotova OV, Shevchenko EN, Plyutinskayab AD, Kaliyaa OL, et al. Covalent conjugates of ammine and diamine platinum (II) with zinc (II) octacarboxyphthalocyanine. Macroheterocycles. 2012;5(4-5):350-7.
172. Malinga N, Antunes E, Nyokong T. Synthesis and physicochemical behaviour of aluminium *bis* and *tris* (diammine platinum) octacarboxyphthalocyanine. Polyhedron. 2013;55:121-5.
173. Managa M, Idowu MA, Antunes E, Nyokong T. Photophysicochemical behavior and antimicrobial activity of dihydroxosilicon tris (diaquaplatinum) octacarboxyphthalocyanine. Spectrochim Acta Mol Biomol Spectros. 2014;125:147-53.
174. Gantchev T, Brasseur N, Van Lier J. Combination toxicity of etoposide (VP-16) and photosensitisation with a water-soluble aluminium phthalocyanine in K562 human leukaemic cells. Br J Cancer. 1996;74(10):1570-7.
175. Gantchev TG, Hunting DJ. Enhancement of etoposide (VP-16) cytotoxicity by enzymatic and photodynamically induced oxidative stress. Anti-Cancer Drugs. 1997;8(2):164-73.
176. Zimmermann A, Walt H, Haller U, Baas P, Klein SD. Effects of chlorin-mediated photodynamic therapy combined with fluoropyrimidines in vitro and in a patient. Cancer Chemother Pharmacol. 2003;51(2):147-54.
177. Kirveliene V, Grazeliene G, Dabkeviciene D, Micke I, Kirvelis D, Juodka B, et al. Schedule-dependent interaction between doxorubicin and mTHPC-mediated photodynamic therapy in murine hepatoma *in vitro* and *in vivo*. Cancer Chemother Pharmacol. 2006;57(1):65-72.
178. Xie Q, Jia L, Liu Y, Wei C. Synergetic anticancer effect of combined gemcitabine and photodynamic therapy on pancreatic cancer *in vivo*. World J Gastroenterol. 2009;15(6):737-41.

179. Diez B, Ernst G, Teijo MJ, Batlle A, Hajos S, Fukuda H. Combined chemotherapy and ALA-based photodynamic therapy in leukemic murine cells. Leuk Res. 2012;36(9):1179-84.
180. Reedijk J. New clues for platinum antitumor chemistry: Kinetically controlled metal binding to DNA. Proc Natl Acad Sci. 2003;100(7):3611-6.
181. Wang D, Lippard SJ. Cellular processing of platinum anticancer drugs. Nat Rev Drug Discov. 2005;4(4):307-20.
182. Lu Q, Kalantari S, Wang C. Electron transfer reaction mechanism of cisplatin with DNA at the molecular level. Mol Pharm. 2007;4(4):624-8.
183. Lu Q. Molecular reaction mechanisms of combination treatments of low-dose cisplatin with radiotherapy and photodynamic therapy. J Med Chem. 2007;50(11):2601-4.
184. Kopyra J, Koenig-Lehmann C, Bald I, Illenberger E. A single slow electron triggers the loss of both chlorine atoms from the anticancer drug cisplatin: Implications for chemoradiation therapy. Angewandte Chemie International Edition. 2009;48(42):7904-7.
185. Kuduk-Jaworska J, Chojnacki H, Jański JJ. Non-empirical quantum chemical studies on electron transfer reactions in trans- and cis-diamminedichloroplatinum (II) complexes. Journal of Molecular Modeling. 2011;17(9):2411-2.
186. Bradley EC, Barr JW. Determination of blood volume using indocyanine green (cardio-green) dye. Life Sci. 1968 Sep 1;7(17):1001-7.
187. Haneda K, Horiuchi T. A method for measurement of total circulating blood volume using indocyanine green. Tohoku J Exp Med. 1986;148(1):49-56.
188. Sauda K, Imasaka T, Ishibashi N. Determination of protein in human serum by high-performance liquid chromatography with semiconductor laser fluorometric detection. Anal Chem. 1986;58(13):2649-53.
189. Fleishaker JC, Friedman H, Pollock SR. Extent and variability of the first-pass elimination of adinazolam mesylate in healthy male volunteers. Pharm Res. 1991;8(2):162-7.

190. Fickweiler S, Szeimies R, Bäumler W, Steinbach P, Karrer S, Goetz AE, et al. Indocyanine green: Intracellular uptake and phototherapeutic effects *in vitro*. J Photochem Photobiol B: Biol. 1997;38(2):178-83.

191. Abels C, Karrer S. Indocyanine green and laser light for the treatment of AIDS-associated cutaneous kaposi's sarcoma. Br J Cancer. 1998;77(6):1021-4.

192. Bäumler W, Abels C, Karrer S, Weiss T, Messmann H, Landthaler M, et al. Photo-oxidative killing of human colonic cancer cells using indocyanine green and infrared light. Br J Cancer. 1999;80(3/4):360-3.

193. Costa R, Farah M, Freymüller, E., Morales P, Smith R, Cardillo J. Choriocapillaris photodynamic therapy using indocyanine green. Am J Ophthalmol. 2001;132(4):557-65.

194. Costa RA, Farah ME, Cardillo JA, Belfort R. Photodynamic therapy with indocyanine green for occult subfoveal choroidal neovascularization caused by age-related macular degeneration. Curr Eye Res. 2001;23(4):271-5.

195. Urbanska K, Romanowska-Dixon B, Matuszak Z, Oszajca J, Nowak-Sliwinska P, Stochel G. Indocyanine green as a prospective sensitizer for photodynamic therapy of melanomas. Acta Biochim, Pol. 2002;49(2):387-91.

196. Sawa M, Awazu K, Takahashi T, Sakaguchi H, Horiike H, Ohji M, et al. Application of femtosecond ultrashort pulse laser to photodynamic therapy mediated indocyanine green. Br J Ophthalmol. 2004;88(6):826-31.

197. Machálková K, Škorpíková J, Švihálek J, Mornstein V. The study of cytotoxicity and phototoxicity of indocyanine green *in vitro*. Scripta Medica. 2005;78(5):305-12.

198. Kawaguchi A, Nagao S, Takebayashi K, Higashiyama M, Komoto S, Hokari R, et al. Long-term outcome of endoscopic semiconductive diode laser irradiation therapy with injection of indocyanine green for early gastric cancer. J Gastroen Hepatol. 2008;23(8pt1):1193-9.

199. Mamoon A, Gamal-Eldeen A, Ruppel M, Smith R, Tsang T, Miller L. *In vitro* efficiency and mechanistic role of indocyanine green as photodynamic therapy agent for human melanoma. Photodiagnosis Photodyn Ther. 2009;6(2):105-16.

200. Bozkulak O, Yamaci R, Tabakoglu O, Gulsoy M. Photo-toxic effects of 809-nm diode laser and indocyanine green on MDA-MB231 breast cancer cells. Photodiagnosis Photodyn Ther. 2009;6(2):117-21.

201. El-Daly SM, Gamal-Eldeen AM, Abo-Zeid MA, Borai IH, Wafay HA, Abdel-Ghaffar AB. Photodynamic therapeutic activity of indocyanine green entrapped in polymeric nanoparticles. Photodiagnosis Photodyn Ther. 2013;10(2):173-85.

202. Cherrick GR, Stein SW, Leevy CM, Davidson CS. Indocyanine green: Observations on its physical properties, plasma decay, and hepatic extraction. J Clin Invest. 1960;39(4):592-600.

203. Landsman M, Kwant G, Mook G, Zijlstra W. Light-absorbing properties, stability, and spectral stabilization of indocyanine green. J Appl Physiol. 1976;40(4):575-83.

204. Dragulescu-Andrasi A, Liang G, Rao J. In vivo bioluminescence imaging of furin activity in breast cancer cells using bioluminogenic substrates. Bioconjugate Chem. 2009;20(8):1660-6.

205. Gross S, Gammon S, Moss B, Rauch D, Harding J, Heinecke J, et al. Bioluminescence imaging of myeloperoxidase activity *in vivo*. Nat Med. 2009;15(4):455-61.

206. O'Neill K, Lyons SK, Gallagher WM, Curran KM, Byrne AT. Bioluminescent imaging: A critical tool in pre-clinical oncology research. J Pathol. 2010;220(3):317-2.

207. McMillin DW, Delmore J, Weisberg E, Negri JM, Geer DC, Klippel S, et al. Tumor cell-specific bioluminescence platform to identify stroma-induced changes to anticancer drug activity. Nat Med. 2010;16(4):483-9.

208. Scott D, Dikici E, Ensor M, Daunert S. Bioluminescence and its impact on bioanalysis. Annu Rev Anal Chem. 2011;4:297-319.

209. Carpenter S, Fehr M, Kraus G, Petrich J. Chemiluminescent activation of the antiviral activity of hypericin: A molecular flashlight. Proc Natl Acad Sci. 1994;91(25):12273-7.

210. Theodossiou T, Hothersall J, Woods E, Okkenhaug K, Jacobson J, MacRobert A. Firefly luciferin-activated rose bengal: *in vitro* photodynamic therapy by intracellular chemiluminescence in transgenic NIH 3T3 cells. Cancer Res. 2003;63(8):1818-21.

211. Schipper M, Patel M, Gambhir S. Evaluation of firefly luciferase bioluminescence mediated photodynamic toxicity in cancer cells. Mol Imaging Biol. 2006;8(4):218-25.
212. Hsu C, Chen C, Yu H, Lin Y, Lai P. Bioluminescence resonance energy transfer using luciferase-immobilized quantum dots for self-illuminated photodynamic therapy. Biomaterials. 2013;34(4):1204-12.
213. Rose A, Waite T. Chemiluminescence of luminol in the presence of iron (II) and oxygen: Oxidation mechanism and implications for its analytical use. Anal Chem. 2001;73(24):5909-20.
214. Chen T, Huang L, Liu C, Chao P, Lin F. Luminol as the light source for in-situ photodynamic therapy. Proc Biochem. 2012;47(12):1903-8.
215. Yuan H, Chong H, Wang B, Zhu C, Liu L, Yang Q, et al. Chemical molecule-induced light-activated system for anticancer and antifungal activities. J Am Chem Soc. 2012;134(32):13184-7.
216. Zewail AH. Femtochemistry: Atomic-scale dynamics of the chemical bond using ultrafast lasers (Nobel Lecture). Angew Chem Int Ed. 2000;39(15):2586-631.
217. Wang C, Lu Q. Real-time observation of a molecular reaction mechanism of aqueous 5-halo-2′-deoxyuridines under UV/ionizing radiation. Angew Chem Int Ed. 2007;46(33):6316-20.
218. Luo T. Femtosecond time-resolved studies on the reaction pathways for the generation of reactive oxygen species in photodynamic therapy by indocyanine green [thesis]. Ontario: Univeristy of Waterloo; 2008.
219. Wang C, Luo T, Lu Q. On the lifetimes and physical nature of incompletely relaxed electrons in liquid water. Phys Chem Chem Phys. 2008;10(30):4463-70.
220. Wang C, Nguyen J, Lu Q. Bond breaks of nucleotides by dissociative electron transfer of nonequilibrium prehydrated electrons: a new molecular mechanism for reductive DNA damage. J Am Chem Soc. 2009;131(32):11320-2.
221. Wang C, Lu Q. Molecular mechanism of the DNA sequence selectivity of 5-halo-2′-deoxyuridines as potential radiosensitizers. J Am Chem Soc. 2010;132(42):14710-3.

222. Wang C, Hu A, Lu Q. Direct observation of the transition state of ultrafast electron transfer reaction of a radiosensitizing drug bromodeoxyuridine. J Chem Phys. 2006;124(24):241102-1,241102-4.

223. Wang C, Drew K, Luo T, Lu M, Lu Q. Resonant dissociative electron transfer of the presolvated electron to CCl_4 in liquid: Direct observation and lifetime of the CCl_4 transition state. J Chem Phys. 2008;128(4):041102-1,041102-4.

224. Lakowicz JR. Principles of fluorescence spectroscopy. New York: Springer; 2007.

225. Shah J. Ultrafast luminescence spectroscopy using sum frequency generation. Quantum Electronics, IEEE Journal of. 1988;24(2):276-88.

226. Goyan RL, Cramb DT. Near-infrared two-photon excitation of protoporphyrin IX: Photodynamics and photoproduct generation. Photochem Photobiol. 2000;72(6):821-7.

227. Matroule JY, Bonizzi G, Morlière P, Paillous N, Santus R, Bours V, et al. Pyropheophorbide-a methyl ester-mediated photosensitization activates transcription factor NF-κB through the interleukin-1 receptor-dependent signaling pathway. J Biol Chem. 1999;274(5):2988-3000.

228. Matroule JY, Carthy CM, Granville DJ, Jolois O, Hunt D, Piette J. Mechanism of colon cancer cell apoptosis mediated by pyropheophorbide-a methylester photosensitization. Oncogene. 2001;20(30):4070-84.

229. Sun X, Leung WN. Photodynamic therapy with pyropheophorbide-a methyl ester in human lung carcinoma cancer cell: Efficacy, localization and apoptosis. Photochem Photobiol. 2002;75(6):644-51.

230. Li KM, Sun X, Koon HK, Leung WN, Fung MC, Wong RNS, et al. Apoptosis and expression of cytokines triggered by pyropheophorbide-a methyl ester-mediated photodynamic therapy in nasopharyngeal carcinoma cells. Photodiagnosis Photodyn Ther. 2006;3(4):247-58.

231. Tian Y, Leung W, Yue K, Mak N. Cell death induced by MPPa-PDT in prostate carcinoma *in vitro* and *in vivo*. Biochem Biophys Res Commun. 2006;348(2):413-20.

232. Tian Y, Xu D, Tian X, Cui F, Yuan H, Leung W. Mitochondria-involved apoptosis induced by MPPa mediated photodynamic therapy. Laser Phys Lett. 2008;5(10):746-51

233. Tan Y, Xu CS, Xia XS, Yu HP, Bai DQ, He Y, et al. Photodynamic action of LED-activated pyropheophorbide-a methyl ester in cisplatin-resistant human ovarian carcinoma cells. Laser Phys Lett. 2009;6(4):321-7.

234. Tian YY, Hu XY, Leung WN, Yuan HQ, Zhang LY, Cui FA, et al. Investigation of photodynamic effect caused by MPPa-PDT on breast cancer. Laser Phys Lett. 2012;9(10):754-8.

235. Gao D, Agayan RR, Xu H, Philbert MA, Kopelman R. Nanoparticles for two-photon photodynamic therapy in living cells. Nano Letters. 2006;6(11):2383-6.

236. Skovsen E, Snyder J, Ogilby P. Two-photon singlet oxygen microscopy: The challenges of working with single cells. Photochem Photobiol. 2006;82(5).

237. Spangler C, Starkey J, Rebane A, Meng F, Gong A, Drobizhev M. Synthesis, characterization and preclinical studies of two-photon-activated targeted PDT therapeutic triads. Biomedical optics 2006; International Society for Optics and Photonics; 2006.

238. Ogawa K, Kobuke Y. Recent advances in two-photon photodynamic therapy. Anti-Cancer Agents in Medicinal Chemistry (Formerly Current Medicinal Chemistry. 2008;8(3).

239. Raymond JE, Bhaskar A, Goodson T, Makiuchi N, Ogawa K, Kobuke Y. Synthesis and two-photon absorption enhancement of porphyrin macrocycles. JACS. 2008;130(51):17212-3.

240. Odom SA, Webster S, Padilha LA, Peceli D, Hu H, Nootz G, et al. Synthesis and two-photon spectrum of a bis (porphyrin)-substituted squaraine. JACS. 2009;131(22):7510-1.

241. Poon CT, Chan PS, Man C, Jiang FL, Wong RNS, Mak NK, et al. An amphiphilic ruthenium (II)-polypyridyl appended porphyrin as potential bifunctional two-photon tumor-imaging and photodynamic therapeutic agent. Journal of Inorganic Biochemistry. 2010;104(1):62-70.

242. Ogawa K, Kobuke Y. Two-photon photodynamic therapy by water-soluble self-assembled conjugated porphyrins. BioMed Research International. 2012;2013.

243. Mir Y, Lier J, Allard J, Morris D, Houde D. Two-photon absorption cross section of excited phthalocyanines a femtosecond Ti-sapphire laser. Photochem Photobiol Sci. 2009;8(3):391-5.

244. Grecco C, Moriyama LT, Cosci A, Pratavieira S, Bagnato VS, Kurachi C. Necrosis response to photodynamic therapy using light pulses in the femtosecond regime. Lasers Med Sci. 2013;28(3):1177-82.

245. Delanaye L, Bahri M, Tfibel F, Fontaine-Aupart M, Mouithys-Mickalad A, Heine B, et al. Physical and chemical properties of pyropheophorbide-a methyl ester in ethanol, phosphate buffer and aqueous dispersion of small unilamellar dimyristoyl-L-α-phosphatidylcholine vesicles. Photochem Photobiol Sci. 2006;5(3):317-25.

246. al-Omari S. Energy transfer of pyropheophorbide a methyl ester in dimethylformamide solutions. Rom J Biophys. 2010;20(4):295-314.

247. Rabani J, Nielsen SO. Absorption spectrum and decay kinetics of O_2^- and HO_2 in aqueous solutions by pulse radiolysis. J Phys Chem. 1969;73(11):3736-44.

248. Jemal A, Siegel R, Xu J, Ward E. Cancer statistics, 2010. CA-Cancer J Clin. 2010;60(5):277-300.

249. Bell D, Berchuck A, Birrer M, Chien J, Cramer D, Dao F, et al. Integrated genomic analyses of ovarian carcinoma. Nature. 2011;474(7353):609-15.

250. Stewart JM, Shaw PA, Gedye C, Bernardini MQ, Neel BG, Ailles LE. Phenotypic heterogeneity and instability of human ovarian tumor-initiating cells. Proc Natl Acad Sci. 2011;108(16):6468-73.

251. Gratz H, Penzkofer A, Abels C, Szeimies R, Landthaler M, Bäumler W. Photo-isomerisation, triplet formation, and photo-degradation dynamics of indocyanine green solutions. J Photochem Photobiol A: Chem. 1999;128(1):101-9.

252. Ratain MJ, Kaminer LS, Bitran JD, Larson RA, Le Beau MM, Skosey C, et al. Acute nonlymphocytic leukemia following etoposide and cisplatin combination chemotherapy for advanced non-small-cell carcinoma of the lung. Blood. 1987;70(5):1412-7.

253. Pedersen-Bjergaard J, Daugaard G, Hansen S, Rørth M, Philip P, Larsen S. Increased risk of myelodysplasia and leukaemia after etoposide, cisplatin, and bleomycin for germ-cell tumours. The Lancet. 1991;338(8763):359-63.

254. Hande KR. Clinical applications of anticancer drugs targeted to topoisomerase II. BBA-Gene Struct Expr. 1998;1400(1):173-84.

255. Ezoe S. Secondary leukemia associated with the anti-cancer agent, etoposide, a topoisomerase II inhibitor. Int J Environ Res Publ Health. 2012;9(7):2444-53.

256. Nishikawa K, Kusama K, Ekimoto H, Takahashi K. Combination effects of etoposide with other antitumor drugs *in vitro* and *in vivo*. Gan to kagaku ryoho. Cancer & chemotherapy. 1989 Dec;16(12):3739-45.

257. Skarlos D, Samantas E, Kosmidis P, Fountzilas G, Angelidou M, Palamidas P, et al. Randomized comparison of etoposide-cisplatin vs. etoposide-carboplatin and irradiation in small-cell lung cancer: A hellenic co-operative oncology group study. Ann Oncol. 1994;5(7):601-7.

258. Mascaux C, Paesmans M, Berghmans T, Branle F, Lafitte J, Lemaıtre F, et al. A systematic review of the role of etoposide and cisplatin in the chemotherapy of small cell lung cancer with methodology assessment and meta-analysis. Lung Cancer. 2000;30(1):23-36.

259. Nemati F, Livartowski A, De Cremoux P, Bourgeois Y, Arvelo F, Pouillart P, et al. Distinctive potentiating effects of cisplatin and/or ifosfamide combined with etoposide in human small cell lung carcinoma xenografts. Clin Cancer Res. 2000;6(5):2075-86.

260. Stathopoulos G, Trafalis D, Dimitroulis J, Kosmas C, Stathopoulos J, Tsavdaridis D. Combination of three cytotoxic agents in small-cell lung cancer. Cancer Chemother Pharmacol. 2013;71(2):413-8.

261. Garcia-Canton C, Anadón A, Meredith C. γH2AX as a novel endpoint to detect DNA damage: Applications for the assessment of the *in vitro* genotoxicity of cigarette smoke. Toxicol In Vitro. 2012;26(7):1075-86.

262. Kim S, Jun DH, Kim HJ, Jeong K, Lee C. Development of a high-content screening method for chemicals modulating DNA damage response. J Biomol Screen. 2011;16(2):259-65.

263. Gollmer A, Arnbjerg J, Blaikie FH, Pedersen BW, Breitenbach T, Daasbjerg K, et al. Singlet oxygen sensor Green®: Photochemical behavior in solution and in a mammalian cell. Photochem Photobiol. 2011;87(3):671-9.

264. Peters G, Van der Wilt C, Van Moorsel C, Kroep J, Bergman A, Ackland S. Basis for effective combination cancer chemotherapy with antimetabolites. Pharmacol Ther. 2000;87(2):227-53.

265. Abels C, Fickweiler S, Weiderer P, Bäumler W, Hofstädter F, Landthaler M, et al. Indocyanine green (ICG) and laser irradiation induce photooxidation. Arch Dermatol Res. 2000;292(8):404-11.

266. Wu L, Yang L, Huang J, Zhang L, Weng X, Zhang X, et al. Cationic ester porphyrins cause high levels of phototoxicity in tumor cells and induction of apoptosis in HeLa cells. Chem Biodivers. 2009;6(7):1066-7.

267. Gantchev TG, Lier JE. Catalase inactivation following photosensitization with tetrasulfonated metallophthalocyanines. Photochem Photobiol. 1995;62(1):123-34.

268. Yaseen MA, Yu J, Wong MS, Anvari B. *In-vivo* fluorescence imaging of mammalian organs using charge-assembled mesocapsule constructs containing indocyanine green. Opt Express. 2008;16(25):20577-8.

269. Gerega A, Zolek N, Soltysinski T, Milej D, Sawosz P, Toczylowska B, et al. Wavelength-resolved measurements of fluorescence lifetime of indocyanine green. J Biomed Opt. 2011;16(6):067010-1,067010-9.

270. Rehm D, Weller A. Kinetics of fluorescence quenching by electron transfer and H-atom transfer. Is J Chem. 1970;8(2):259-71.

271. Holthuis J, Van Oort W, Römkens F, Renema J, Zuman P. Electrochemistry of podophyllotoxin derivatives: Part I. oxidation mechanism of etoposide (VP 16–213). J Electroanal Chem Interfacial Electrochem. 1985;184(2):317-29.

272. Barros TC, Toma SH, Toma HE, Bastos EL, Baptista MS. Polymethine cyanine dyes in β-cyclodextrin solution: Multiple equilibria and chemical oxidation. J Phys Org Chem. 2010;23(10):893-90.

273. Haim N, Roman J, Nemec J, Sinha BK. Peroxidative free radical formation and O-demethylation of etoposide (VP-16) and teniposide (VM-26). Biochem Biophys Res Commun. 1986;135(1):215-20.

274. Gantchev TG, Hunting DJ. The ortho-quinone metabolite of the anticancer drug etoposide (VP-16) is a potent inhibitor of the topoisomerase II/DNA cleavable complex. Mol Pharmacol. 1998;53(3):422-8.

275. Smart DJ, Halicka HD, Schmuck G, Traganos F, Darzynkiewicz Z, Williams GM. Assessment of DNA double-strand breaks and γH2AX induced by the topoisomerase II poisons etoposide and mitoxantrone. Mutat Res /Fund Mol M. 2008;641(1):43-7.

276. Watters GP, Smart DJ, Harvey JS, Austin CA. H2AX phosphorylation as a genotoxicity endpoint. Mutat Res /Genet Toxicol Environ Mutagen. 2009;679(1):50-8.

277. Matsuzaki K, Harada A, Takeiri A, Tanaka K, Mishima M. Whole cell-ELISA to measure the γH2AX response of six aneugens and eight DNA-damaging chemicals. Mutat Res /Genet Toxicol Environ Mutagen. 2010;700(1):71-9.

278. Dow LW, Sinkule JA, Look AT, Horvath A, Evans WE. Comparative cytotoxic and cytokinetic effects of the epipodophyllotoxins 4′-demethylepipodophyllotoxin-9-(4, 6-O-2-ethylidene-β-d-glucopyranoside) and 4′-demethylepipodophyllotoxin-9-(4,6-O-2-thenylidene-β-d-glucopyranoside) and their metabolites on human leukemic lymphoblasts. Cancer Res. 1983;43(12 Part 1):5699-706.

279. Roed H, Vindelov LL, Christensen IJ, Spang-Thomsen M, Hansen HH. The effect of the two epipodophyllotoxin derivatives etoposide (VP-16) and teniposide (VM-26) on cell lines established from patients with small cell carcinoma of the lung. Cancer Chemother Pharmacol. 1987;19(1):16-20.

280. Giaccone G, Gazdar AF, Beck H, Zunino F, Capranico G. Multidrug sensitivity phenotype of human lung cancer cells associated with topoisomerase II expression. Cancer Res. 1992;52(7):1666-74.

281. Bram EE, Ifergan I, Grimberg M, Lemke K, Skladanowski A, Assaraf YG. C421 allele-specific ABCG2 gene amplification confers resistance to the antitumor triazoloacridone C-1305 in human lung cancer cells. Biochem Pharmacol. 2007;74(1):41-53.

282. Holthuis J. Etoposide and teniposide. Pharm Weekbl. 1988;10(3):101-16.

283. Holthuis J, Vendrig D, Van Oort W, Zuman P. Electrochemistry of podophyllotoxin derivatives: Part II. oxidation of teniposide and some epipodophyllotoxin derivatives. J Electroanal Chem Interfacial Electrochem. 1987;220(1):101-24.

284. Kettenes-Van Den Bosch, J Jantina, Holthuis JJ, Bult A. Teniposide. Analytical Profiles of Drug Substances. 1990;19:575-600.

285. Lu C, Wang W, Lin W, Han Z, Pan J, Yao S, et al. Monophotonic ionization of etoposide in aqueous solution by 248 nm laser light: Identification of transient intermediates. J Photochem Photobiol B: Biol. 1999;49(1):61-4.

286. Sun X, Zhang C, Wang M, Wang S, Ni Y, Yao S. Laser flash photolysis and pulse radiolysis study on chemical activity of VP-16 and podophyllotoxin. Sci China Ser B. 2002;45(2):191-9.

287. Boulikas T, Vougiouka M. Cisplatin and platinum drugs at the molecular level (review). Oncol Rep. 2003;10(6):1663-82.

288. Wexselblatt E, Gibson D. What do we know about the reduction of pt (IV) pro-drugs? J Inorg Biochem. 2012;117:220-9.

289. Peng C, Lai P, Lin F, Yueh-Hsiu Wu S, Shieh M. Dual chemotherapy and photodynamic therapy in an HT-29 human colon cancer xenograft model using SN-38-loaded chlorin-core star block copolymer micelles. Biomaterials. 2009;30(21):3614-25.

290. Lee S, Bard A. Near-ir electrogenerated chemiluminescence of tricarbocyanine dyes in micellar systems. Analytical Letters. 1998;31(13):2209-2.

291. Davila J, Harriman A. Photosensitized oxidation of biomaterials and related model compounds. Photochem Photobiol. 1989;50(1):29-35.

292. Henley R, Worwood M. Luminol peroxidation catalyzed human isoferritins. Arch Biochem Biophys. 1991;286(1):238-43.

293. Henley R, Worwood M. The enhancement of iron-dependent luminol peroxidation 2, 2'-dipyridyl and nitrilotriacetate. J Biolum Chemilum. 1994;9(4):245-50.

294. Yıldız G, Demiryürek A. Ferrous iron-induced luminol chemiluminescence: A method for hydroxyl radical study. J Pharmacol Toxicol Methods. 1998;39(3):179-84.

295. Merényi G, Lind J, Eriksen TE. Luminol chemiluminescence: Chemistry, excitation, emitter. J Biolumin Chemilumin. 2005;5(1):53-6.

296. Dodeigne C, Thunus L, Lejeune R. Chemiluminescence as diagnostic tool. A review. Talanta. 2000;51(3):415-39.

297. Chen W, Tung C, Weissleder R. Imaging reactive oxygen species in arthritis. Molecular Imaging. 2004;3(3):159-62.

298. Barni F, Lewis S, Berti A, Miskelly G, Lago G. Forensic application of the luminol reaction as a presumptive test for latent blood detection. Talanta. 2007;72(3):896-913.

299. Dikalov S, Griendling K, Harrison D. Measurement of reactive oxygen species in cardiovascular studies. Hypertension. 2007;49(4):717-2.

300. Sanders J, Chen L, Burka L, Matthews H. Metabolism and disposition of luminol in the rat. Xenobiotica. 2000;30(3):263-72.

301. Seitz WR, Hercules DM. Determination of trace amounts of iron (II) using chemiluminescence analysis. Anal Chem. 1972;44(13):2143-9.

302. Klopf LL, Nieman TA. Effect of iron (II), cobalt (II), copper (II), and manganese (II) on the chemiluminescence of luminol in the absence of hydrogen peroxide. Anal Chem. 1983;55(7):1080-3.

303. Vladimirov Y, Proskurnina E. Free radicals and cell chemiluminescence. Biochemistry (Moscow). 2009;74(13):1545-66.

304. Motsenbocker M, Ichimori Y, Kondo K. Metal porphyrin chemiluminescence reaction and application to immunoassay. Anal Chem. 1993;65(4):397-402.

305. Liu X, Li A, Zhou B, Qiu C, Ren H, others. Chemiluminescence determination of surfactant triton X-100 in environmental water with luminol-hydrogen peroxide system. Chemistry Central Journal. 2009;3(7).

306. Huang Z, Xu H, Meyers AD, Musani AI, Wang L, Tagg R, et al. Photodynamic therapy for treatment of solid tumors–potential and technical challenges. Technol Cancer Res Treat. 2008;7(4):309-20.

307. Bredell MG, Besic E, Maake C, Walt H. The application and challenges of clinical PD–PDT in the head and neck region: a short review. J Photochem Photobiol B: Biol. 2010;101(3):185-90.

308. Wilson B, Madsen S. Intracranial photodynamic therapy. Optical Methods and Instrumentation in Brain Imaging and Therapy. 2013:207-33.

309. Sinha BK, Bhattacharjee S, Chatterjee S, Jiang J, Motten AG, Kumar A, et al. Role of nitric oxide in the chemistry and anticancer activity of etoposide (VP-16,213). Chem Res Toxicol. 2013;26(3):379-87.
310. Kim Y, Daniel W, Xia Z, Xie H, Mirkin C, Rao J. Bioluminescent nanosensors for protease detection based upon gold nanoparticle-luciferase conjugates. Chemical Communications. 2010;46(1).
311. Theodossiou T, Sideratou Z, Tsiourvas D, Paleos C. A novel mitotropic oligolysine nanocarrier: Targeted delivery of covalently bound d-luciferin to cell mitochondria. Mitochondrion. 2011.

LIST OF PUBLICATIONS

1. **Ting Luo**, Brian C Wilson, and Qing-Bin Lu. Evaluation of one-and two-photon activated photodynamic therapy with pyropheophorbide-a methyl ester in human cervical, lung and ovarian cancer cells. *Journal of Photochemistry and Photobiology B: Biology* 132 (**2014**), 102-110.
2. **Ting Luo**, Jianqing Yu, Jenny Nguyen, Chun-Rong Wang, Robert G. Bristow, David A. Jaffray, Xiao Zhen Zhou, Kun Ping Lu, and Qing-Bin Lu. Electron transfer-based combination therapy of cisplatin with tetramethyl-p-phenylenediamine for ovarian, cervical, and lung cancers. *Proceedings of the National Academy of Sciences* (**PNAS**) 109 (**2012**), 10175-10180.
3. Jenny Nguyen, Yuhan Ma, **Ting Luo**, Robert G. Bristow, David A. Jaffray, and Qing-Bin Lu. Direct observation of ultrafast-electron-transfer reactions unravels high effectiveness of reductive DNA damage. **PNAS** 108 (**2011**), 11778-11783.
4. Chun-Rong Wang, **Ting Luo** (**co-first author**), and Qing-Bin Lu. On the lifetimes and physical nature of prehydrated electrons in liquid water. *Physical Chemistry Chemical Physics* (Phys. Chem. Chem. Phys.) 10 (**2008**), 4463-4470.
5. Chun-Rong Wang, Kristine Drew, **Ting Luo**, Mei-Jun Lu, and Qing-Bin Lu. Resonant dissociative electron transfer of the presolvated electron to CCl_4 in liquid: direct observation and lifetime of the CCl_4^{*-} transition state. *Journal of Chemical Physics.* (J. Chem. Phys.) 128 (**2008**), 041102 (4 pages).